

Role of Orbital Hybridization in the Magnetism of Nanoscale Oxides

by

Vinod Kumar Paidi

A thesis submitted to
The Faculty of Graduate Studies of
The University of Manitoba
in partial fulfillment of the requirements
of the degree of

Doctor of Philosophy

Department of Physics and Astronomy
The University of Manitoba
Winnipeg, Manitoba, Canada
September 2019

© Copyright 2019 by Vinod Kumar Paidi

Thesis advisor

Author

Dr. Johan van Lierop

Vinod Kumar Paidi

Role of Orbital Hybridization in the Magnetism of Nanoscale Oxides

Abstract

Orbital degrees of freedom, coupled with the spin of an electron, play a fundamental role in magnetism. In this dissertation, I present an answer to an open question in the magnetism of nanoscale oxide systems: When oxygen ions surround a metal ion, what is the role of metal ions hybridized with oxygen in the magnetism? To begin with, two different classes of materials that are mixed valent in nature were chosen (d electron rich and d^0 systems) for this study, and their electronic structure and magnetism probed using atomic, elemental, and bulk sensitive techniques.

Using x-ray absorption spectroscopy and x-ray magnetic circular dichroism of Fe_3O_4 and CoFe_2O_4 (d electron rich) the origin of magnetic moment is associated to the spin of the electrons. The orbital angular momentum was mostly quenched due to the crystal field splitting of the d orbitals. *In-situ* magnetic susceptibility measurements performed under oxygen rich and oxygen deficient environments showed that partial pressure of oxygen disrupts the exchange pathway of $\text{Fe/Co} - \text{O}^{2-} - \text{Fe/Co}$, leading to an enhancement of magnetization in CoFe_2O_4 compared to Fe_3O_4 . In d^0 systems (CeO_2 shapes) the *in-situ* magnetic susceptibility measurements showed that depending on the amount of oxygen present in the lattice and surface of the nanoce-

ria a redox transformation ($\text{Ce}^{4+} \leftrightarrow \text{Ce}^{3+}$) occurred via oxygen vacancy formation and provided a window to quantify the defects. Electronic structure and element specific magnetism studies showed that in nanoscale CeO_2 the Ce $4f$ – O $2p$ states are hybridized. A comparison between the element sensitive and overall magnetism shined light on the origin of magnetism in these nanoscale systems evidencing that hybridized states captured in the vacancy orbitals play a critical role in mediating the long-range magnetism. This work demonstrates that this hybridization concept may be a solid foundation for understanding the weak ferromagnetic-like response that is observed in several non-magnetic oxides (where O $2p$ hole states are key players, and their hybridization with host or guest metal ions changes the density of states) that present similar magnetism.

Contents

Abstract	ii
Table of Contents	vii
List of Figures	viii
List of Tables	xix
Acknowledgments	xxi
Dedication	xxiv
1 Introduction	1
1.1 Paramagnetism	2
1.2 Ferromagnetism, Antiferromagnetism, and Ferrimagnetism	6
1.3 Nanoparticle Magnetism	9
1.4 Electron Correlation and Hybridization	10
1.5 Oxygen's Role in the Magnetism of Transition Metal Oxides	13
1.5.1 Superexchange	15
1.5.2 Double exchange	16
1.6 Catalytic Properties of Nanoparticle Oxides	17
1.7 Progress and Open Questions	19
1.8 Organization	23
2 Experimental Methods	24
2.1 Synthesis of Nanoparticles	25
2.1.1 Synthesis of Fe_3O_4 and CoFe_2O_4 nanoparticles	25
2.1.2 Synthesis of CeO_2 nanoshapes	26
2.1.3 Synthesis of CeO_2 nanoparticles	27
2.1.4 Synthesis of Fe and Co decorated nanoparticles	27
2.2 X-ray Diffraction	28
2.3 Transmission Electron Microscopy	33
2.4 Brunauer – Emmett – Teller Analysis	35
2.5 ICP OES	36
2.6 Activity Measurements	36
2.7 X-ray Spectroscopy	37

2.7.1	Soft x-ray absorption spectroscopy	40
2.7.2	Hard x-ray absorption spectroscopy	46
2.7.3	Experiments	47
2.7.4	The transmission geometry	48
2.7.5	The fluorescence geometry	50
2.7.6	The total electron yield	52
2.8	Mössbauer Spectroscopy	54
2.8.1	Recoilless emission and absorption of γ -rays	54
2.8.2	Hyperfine interactions	57
2.8.3	Isomer shift	58
2.8.4	Quadrupole shift	60
2.8.5	Magnetic hyperfine splitting	62
2.8.6	Application of ^{57}Fe Mössbauer spectroscopy in this thesis	64
2.8.7	Experiments	64
2.9	Magnetometry	69
3	Oxygen rich and oxygen deficient magnetism of nanoscale Fe_3O_4 and CoFe_2O_4	76
3.1	Introduction	77
3.1.1	Spinel structure	77
3.1.2	Aim of this chapter	79
3.2	Structure and Composition	79
3.3	Local Environment and Cation Distribution	81
3.3.1	Fe K edge of Fe_3O_4 nanocrystallites	83
3.3.2	Fe and Co K edges of CoFe_2O_4 nanocrystallites	84
3.4	Electronic Structure and Cation Distribution	88
3.4.1	Qualitative analysis of Fe_3O_4 and CoFe_2O_4 nanoparticles	88
3.4.2	Modelling parameters for Fe_3O_4 and CoFe_2O_4 nanoparticles	90
3.4.3	Quantitative XAS and XMCD analysis of Fe_3O_4 nanoparticles	91
3.4.4	Quantitative XAS and XMCD analysis of CoFe_2O_4 nanoparticles	92
3.5	Mössbauer Spectroscopy and Cation Distribution	97
3.5.1	Cation distribution from Mössbauer spectroscopy of CoFe_2O_4	100
3.5.2	Cation distribution from XAS and XMCD of CoFe_2O_4	101
3.6	Comparison of Cation Distributions from XAS and XMCD and Mössbauer Spectroscopy of Fe_3O_4 and CoFe_2O_4	101
3.7	The Magnetism and Oxygen Connection	101
3.7.1	Magnetic susceptibility as a probe to redox mechanism in Fe_3O_4 and CoFe_2O_4 nanocrystallites	105
3.8	Conclusions	109

4	Oxygen rich and oxygen deficient magnetism of CeO₂ nanoshapes	111
4.1	Introduction	112
4.1.1	Aim of this chapter	114
4.2	Structure, Composition, and Morphology	115
4.3	Magnetism of Nanoceria Cubes, Rods, and Spheres	120
4.4	The Catalysis and Oxygen Connection	127
4.5	Conclusions	130
5	Oxygen's function on the magnetism of nanoscale CeO₂, Fe - CeO₂, and Co - CeO₂	131
5.1	Introduction	132
5.1.1	<i>d</i> ⁰ magnetism	132
5.1.2	Aim of this chapter	133
5.2	Structure and Composition	133
5.3	Overall Magnetism	138
5.3.1	Curie – Weiss analysis of Fe and Co decorated CeO ₂ nanocrystallites	139
5.3.2	Field dependent magnetic response of CeO ₂ , Fe and Co decorated CeO ₂ nanocrystallites	142
5.4	Local Environment and Electronic Structure	145
5.4.1	Concentration of Ce ³⁺ content	146
5.4.2	Identifying the local environment of Ce, Fe and Co	147
5.4.3	Determining the oxidation state and local environment of Fe	148
5.4.4	Quantifying the <i>f</i> electron occupancy	151
5.5	Elemental and Overall Magnetism	157
5.5.1	Quantifying the spin and orbital magnetic moments	159
5.6	Conclusions	160
6	Discussion	162
6.1	Fe ₃ O ₄ and CoFe ₂ O ₄ Nanoparticles	163
6.1.1	Quantifying the <i>e_g</i> and <i>t_{2g}</i> orbital fraction	164
6.1.2	<i>In-situ</i> magnetic susceptibility measurements identify the magnetic exchange pathways	167
6.2	CeO ₂ Nanoshapes	170
6.2.1	Nanoceria shapes surface Ce ³⁺ concentration	171
6.2.2	Lattice oxygen and adsorbed surface oxygen dynamics in nanoceria	173
6.2.3	Quantifying the intrinsic oxygen storage capacity and defects	175
6.2.4	Surface localized Ce ³⁺ is the key to catalytic activity	180
	Ce ³⁺ surface density calculations	181
6.3	CeO ₂ <i>d</i> ⁰ Magnetism	183
6.3.1	Ce 4 <i>f</i> – O 2 <i>p</i> hybridization role in the <i>d</i> ⁰ magnetism	184

6.3.2 Vacancy orbitals are the key to understand d^0 magnetism . . .	187
7 Conclusions and Future work	191
Bibliography	220

List of Figures

1.1	M vs H and χ vs T plots of a paramagnet are shown. Susceptibility χ is positive and larger than diamagnetic susceptibility. χ is inversely proportional to the temperature, which is known as Curie's law.	3
1.2	(a) Spin arrangement in an ordered ferromagnet. (b) Magnetization as a function of an applied field in a ferromagnet is shown. Magnetic saturation is the maximum moment that can be achieved in a magnetic field (H_{sat}). (c) Magnetization as a function of temperature in a ferromagnet is shown, where T_C is the Curie temperature. (d,e) Spin arrangement in a ferrimagnet and antiferromagnet are shown respectively. (f) Temperature dependent susceptibility shows antiferromagnetic transition.	8
1.3	A schematic of Mott-Hubbard and charge transfer models. In the Mott-Hubbard model, an electron hops between transition metal ions and the energy cost is U . In the charge transfer model, the charge fluctuations are from oxygen ligand to metal sites, and the energy cost is Δ . Here E_F denotes the Fermi energy level[13; 14; 15].	12
1.4	A metal ion atom in a cubic, tetrahedral, spherical, and octahedral coordination are shown. The d_{xy}, d_{yz} , and d_{zx} are grouped together as t_{2g} level. The d_{z^2} and $d_{x^2-y^2}$ are grouped together as e_g level. Δ_c , Δ_t , and Δ_o are crystal-field splitting energies for cubic, tetrahedral and octahedral coordination respectively.	14
1.5	A schematic of superexchange mechanism is shown. The superexchange interaction is strong for 180° $M_1 - O - M_2$ bonds as discussed in the text.	16
1.6	A graphical representation of NO reduction by CO is proposed on the nanoceria (111) plane. In the first step two NO molecules adsorb on the Fe sites and decompose to N_2O . In the second step, CO molecules adsorb onto the Fe ions and take up the excess oxygen and form N_2 and CO_2 . The excess oxygens are neutralized by the oxygen vacancies of ceria supports.	18

2.1	Geometric diagram of Bragg diffraction by adjacent planes. X-ray originating from the source and reaching the detect are shown.	29
2.2	Bruker D8 DaVinci diffractometer using a Bragg-Brentano geometry. Components corresponding to the source and detector arms are shown.	31
2.3	Left: A layout of optical components in a transmission electron microscopy. Right: FEI Talos F200X transmission electron microscope at Manitoba Institute for Materials. TEM Photo credit: Lief Norman	35
2.4	(a) Schematic of the excitations corresponding to the K, $L_{3,2,1}$, and $M_{3,2,1}$ are shown and the arrows are indicative of energy differences. (b) X-ray absorption as a function of incident photon energy with four different edges are shown (K, $L_{3,2,1}$). (c) The three different regions: pre-edge, edge, and EXAFS oscillations are shown[61].	38
2.5	(a) The impact of spin-orbit coupling on the spectra is shown. For Co^{4+} , Fe^{3+} , and Mn^{2+} the d electron count are the same, and the atomic number (Z) changes. The spectra are spread out with an increase in Z , due to strong repulsion effects between nuclear charge. (b) Spectral line shapes of Co^{2+} ions in three different environments (isolated, octahedral and tetrahedral) is shown. Figure evidence that XAS spectra is strongly dependent on the crystal field environment ($10Dq$) of an atom. For comparison purposes energies are shifted to 0 eV and binding energies are not taken into account.	41
2.6	XMCD principles illustrated for the case of L edge absorption in a d band Fe metal. When d band is split into spin-up and spin-down with different occupation. The absorbed light of RCP (LCP) excites spin-up (spin-down) electrons with different occupation. Because spin flips are forbidden the measured resonance intensity quantify the empty d band states of a given spin. Reprinted with permission from [65]. Copyright 2006 Springer Science and Business Media.	44
2.7	A representation of central storage ring and corresponding experimental end stations are shown. Along the ring, magnets are used to steer and confine the beam along a circular track. Each end-station is equipped with optics, sample holders, and detectors to facilitate a particular experiment. Photo by Bruce Ravel/CC BY-SA 3.0 (https://creativecommons.org/licenses/by-sa/3.0/).	48
2.8	(a) Transmission geometry experimental setup at sector 20-BM-B at the Advanced Photon Source. Sample is placed in between the source and detector. (b) A photograph of samples prepared for the transmission geometry experiments are shown. Five samples are mounted on the sample holder.	50

2.9	A photograph of experimental setup for total fluorescence yield is shown. Detector is mounted perpendicular to the source to reduce the elastic scatter as discussed in the text. Photo by Bruce Ravel/CC BY-SA 3.0 (https://creativecommons.org/licenses/by-sa/3.0/).	51
2.10	A photograph of the 7 Tesla magnet at 4-ID-C at the Advanced Photon Source. (b) Samples are mounted on a carbon conductive tape, and stuck to a Cu cold finger for TEY experiments. A diagram illustrates the total electron measurement. Reprinted with permission from [65]. Copyright 2006 Springer Science and Business.	53
2.11	(a) Representation of momentum conservation of nucleus of mass M is shown. Linear momenta of nucleus (p_n) and the γ -photon (p_γ) are opposite in direction. (b) The emission and absorption lines of a free atom of mass M suffers recoil effect with energy E_R . In a free atom or molecule the emission and absorption lines shifted by $2E_R$ and makes resonance overlap less probable. Reprinted with permission from [76]. Copyright 2010 Springer Science and Business Media.	55
2.12	Nuclear decay scheme of ^{57}Fe Mössbauer resonance is shown. By electron capture ^{57}Co decays to ^{57}Fe with nuclear spin quantum number $I = 5/2$. $I = 3/2$ and $I = 1/2$ are the nuclear spin quantum numbers of the excited state and the ground state of 14.4 keV γ -rays that are used in ^{57}Fe Mössbauer spectroscopy.	57
2.13	Three kinds of hyperfine interactions observed using Mössbauer parameters are shown. (a) Electric monopole interaction between protons of nucleus and electrons penetrating the nucleus shifts the energy of the nuclear states and gives the isomer shift (δ). (b) Electric quadrupole interaction between nuclear quadrupole moment and electric field gradient at the nucleus is responsible for the quadrupole splitting (Δ). (c) Magnetic dipole interaction between the nuclear magnetic moment and a magnetic field around the nucleus due to neighbouring electrons is responsible for the hyperfine field (B_{hf}). Reprinted with permission from [76]. Copyright 2010 Springer Science and Business Media.	59
2.14	Ranges of ^{57}Fe compounds Mössbauer isomer shifts (δ) observed relative to α -Fe at room temperature. Reprinted with permission from [76]. Copyright 2010 Springer Science and Business Media.	65
2.15	Schematic representation of a transmission Mössbauer spectrometer.	67
2.16	(a) The sample to be measured is powdered and spread across two x-ray mylar films mounted on a brass holder. (b) A photograph of experimental setup for transmission geometry is shown. Sample is placed in between the source and detector.	68

2.17 (a) A SQUID consisting of two Josephson junctions arranged on a superconducting ring (b) Voltage a function of flux shows the period of flux quantisation (c) A schematic representation of a gradiometer with two pickup coils is shown.	70
2.18 The Quantum Design MPMS-XL5	72
2.19 Experimental setup of oxygen rich and oxygen deficient magnetic susceptibility measurements. NMR tubes are sealed with low temperature epoxy (ECO-BOND) to seal the tubes[84].	75
3.1 Schematic of the spinel crystal structure: 1/3 of cations are located in available 1/8 of the available tetrahedral (T_d) sites, and 2/3 of the cations are located in 1/2 of the available octahedral (O_h) sites. In normal spinel all Fe^{2+} ions are in T_d sites and Fe^{3+} ions are located in O_h sites. In an inverse spinel all Fe^{2+} ions are located in O_h sites whereas Fe^{3+} ions are located in O_h and T_d spinels equally. Structures created using VESTA[85]	78
3.2 Room temperature x-ray diffraction patterns of Fe_3O_4 and $CoFe_2O_4$ are shown. The (hkl) indices of the structure are labeled. Refinement (solid lines) of Fe_3O_4 and $CoFe_2O_4$ and residuals are presented; the short vertical bars indicate the position of Bragg reflections used in the refinement.	80
3.3 Fourier transformed modulus ($ \chi(R) $) of the $k\chi(k)$ experimental data (open circles) and theoretical fits (solid line) of Fe_3O_4 nanoparticles are shown. Inset shows $k\chi(k)$ experimental data (open circles) and theoretical fits (solid lines). $ \chi(R) $ represents raw data without correcting for phase shifts and the window used to select the coordination shell includes single scattering paths as discussed in text.	82
3.4 Fourier transformed modulus ($ \chi(R) $) of the $k\chi(k)$ experimental data (open circles) and theoretical fits (solid line) of $CoFe_2O_4$ nanoparticles are shown. Inset shows $k\chi(k)$ experimental data (open circles) and theoretical fits (solid lines). $ \chi(R) $ represents raw data without correcting for phase shifts and the window used to select the coordination shell includes single scattering paths as discussed in text.	84
3.5 Fourier transformed modulus ($ \chi(R) $) of the $k\chi(k)$ experimental data (open circles) and theoretical fits (solid line) of $CoFe_2O_4$ nanoparticles are shown. Inset shows $k\chi(k)$ experimental data (open circles) and theoretical fits (solid lines). $ \chi(R) $ represents raw data without correcting for phase shifts and the window used to select the coordination shell includes single scattering paths as discussed in text.	86

-
- 3.6 (a) Fe $L_{3,2}$ edge XAS/XMCD experimental spectra of Fe_3O_4 and CoFe_2O_4 nanoparticles. The XMCD spectra consists of two peaks that are pointing downwards and one upward peak that is pointing upwards. The downward peaks are due to Fe ion O_h sites and upward peaks are due to T_d sites. (b) Co $L_{3,2}$ edge XAS/XMCD experimental spectrum of CoFe_2O_4 nanoparticles are shown. The downward and upward peaks are due to O_h and T_d sites respectively. 89
- 3.7 (a) Fe L_3 edge XAS experimental spectra and simulations of Fe_3O_4 nanoparticles. The calculated Fe^{3+} (T_d), Fe^{3+} (O_h) and Fe^{2+} (O_h) components of the XAS spectra and theoretical resulting summed spectrum are shown. (b) Fe L_3 edge XMCD experimental spectrum and simulations are shown. The spin arrangement is shown at each T_d and O_h sites. The Fe^{3+} spins on the T_d and O_h sites cancel out their moments due to antiparallel alignment and their net ferrimagnetic moment is caused by the Fe^{2+} T_d spins. 91
- 3.8 Fe $L_{3,2}$ edge XMCD spectrum (left axis) together with integrated XMCD (right axis) are shown. The integrated XMCD intensities p and q are labeled, where p is the integrated XMCD intensity over the L_3 edge, and q is the integrated XMCD intensity over combined L_3 and L_2 edges. The XMCD simulation of the Fe L_3 edge is shown in Fig. 3.7. 93
- 3.9 (a) Co L_3 edge XAS experimental spectra and simulations of CoFe_2O_4 nanoparticles. The calculated Co^{2+} (T_d), Co^{2+} (O_h) and Co^{3+} (O_h) components of the XAS spectra and theoretical resulting summed spectrum are shown. (b) Co L_3 edge XMCD experimental spectrum and simulations are shown. The spin arrangement is shown at each T_d and O_h sites. In CoFe_2O_4 we also identify a small fraction ($\sim 20\%$) of Co^{3+} in O_h location as described in the text. 94
- 3.10 (a) Fe L_3 edge XAS experimental spectra and simulations of CoFe_2O_4 nanoparticles. The calculated Fe^{3+} (T_d), Fe^{3+} (O_h) and Fe^{2+} (O_h) components of the XAS spectra and theoretical resulting summed spectrum are shown. (b) Fe L_3 edge XMCD experimental spectrum and simulations are shown. The spin arrangement is shown at each T_d and O_h sites. Note that the difference between the simulation and experiment in the energy range of ~ 712 - 714 eV is because for oxides the edge jump is difficult to model due to the s-p intermixing effects. 95
- 3.11 Fe $L_{3,2}$ edge XMCD spectrum (left axis) together with integrated XMCD (right axis) are shown. The integrated XMCD intensities p and q are labeled, where p is the integrated XMCD intensity over the L_3 edge, and q is the integrated XMCD intensity over combined L_3 and L_2 edges. The XMCD simulations of the Co and Fe edges (L_3) are shown in Figs. 3.9 and 3.10, respectively. 96

- 3.12 Mössbauer spectrum of Fe_3O_4 measured (dotted line) and fit spectrum at room temperature are shown. The spectrum is fit with independent linewidth sextets where $\Gamma = \Gamma_{Nat} + \Delta\Gamma$ (Natural linewidth $\Gamma_{Nat} = 0.133$ mm/s). Three different sites are used to fit the spectrum with three components ($\text{Fe}^{3+} T_d$, $\text{Fe}^{3+} O_h$, and $\text{Fe}^{2+} O_h$) to quantify the cation distribution. 97
- 3.13 Mössbauer spectrum of Fe_3O_4 measured (dotted line) at room temperature. The spectrum is fit with independent linewidth sextets where $\Gamma = \Gamma_{Nat} + \Delta\Gamma$ (Natural linewidth $\Gamma_{Nat} = 0.133$ mm/s). Spectrum is fit (solid line) with three components ($\text{Fe}^{3+} T_d$, $\text{Fe}^{3+} O_h$, and $\text{Fe}^{2+} O_h$) to quantify the cation distribution. 99
- 3.14 Geometry – 1: $3d$ ions interact via an O $2p$ states in-between (the 180° geometry), both $3d$ ions couple to the same p -orbital. In this configuration antiferromagnetic superexchange results. Geometry – 2: When the angle of the $3d - \text{O} 2p - 3d$ group is 90° , the $3d$ ions couple to O $2p$ -states, making it impossible for an electron on one $3d$ -ion to influence the $3d$ ion on the other site. In this case, ferromagnetic exchange develops. 103
- 3.15 Five d orbitals d_{xy} , d_{xz} , d_{yz} , $d_{x^2-y^2}$, and d_{z^2} are shown. In octahedral coordination the metal e_g orbitals ($d_{x^2-y^2}$ and d_{z^2}) are pointed towards the O $2p$ ligands and results in higher energy compared to t_{2g} orbitals (d_{xy} , d_{xz} , and d_{yz}). 104
- 3.16 Oxygen K edge of (a) Fe_3O_4 and (b) CoFe_2O_4 are shown. The hybridization region of O $2p - \text{Fe} 3d$ (Fe_3O_4) and O $2p - \text{Fe/Co} 3d$ (CoFe_2O_4) are shaded in blue, * at 535 eV is due to vicinal oxygen from carbon conductive tape[102] and the broad peaks above 536 eV are due to O $2p - \text{Fe/Co} 4s4p$ orbitals. 105
- 3.17 (a,b) Zero-field cooled (ZFC) and field cooled (FC) $\chi(T)$ (Fe_3O_4 and CoFe_2O_4) of O_2 deficient systems. (c,d) ZFC and FC of $\chi(T)$ (Fe_3O_4 and CoFe_2O_4) of O_2 rich systems systems. (e) A comparison between $\Delta\chi_{FC-ZFC}$ (difference between FC and ZFC) of O_2 deficient and O_2 rich of Fe_3O_4 is shown. (f) A comparison between $\Delta\chi_{FC-ZFC}$ of O_2 deficient and O_2 rich of CoFe_2O_4 is shown. Note that in Fe_3O_4 , O_2 rich $<$ O_2 deficient and in CoFe_2O_4 , O_2 rich $>$ O_2 deficient as discussed in the text. 106
- 3.18 Catalytic activity as a function of temperature of Fe_3O_4 and CoFe_2O_4 are shown. Nanocrystallites of Fe_3O_4 are inactive and CoFe_2O_4 are active. 109

4.1	Crystal structure of CeO ₂ before (left) and after (right) vacancy (\square) formation. In CeO ₂ each Ce ⁴⁺ ion (white sphere) is surrounded by eight O ²⁻ ions (red spheres) and each O ²⁻ ion is surrounded by four Ce ⁴⁺ ions. The Ce ⁴⁺ -to-Ce ³⁺ transformation is due to \square formation and the released oxygen in the fluorite lattice is intrinsic oxygen. The lattice expansion of nanoceria is as described in the text.	113
4.2	TEM (a) and HRTEM images (b-c) images of nanocubes. TEM (d) and HRTEM (e-f) images of nanorods. TEM (g) and HRTEM (h-i) images of nanospheres.	117
4.3	Room temperature XRD patterns of CeO ₂ nanocubes (bottom, +10 ³ counts), nanorods(+10 ⁴ counts), and nanospheres (top, +1.5×10 ⁴ counts). The (hkl) indices of the structure are labeled. Refinement of different CeO ₂ shapes (solid lines) and nanospheres residuals is presented; the short vertical bars indicate the position of Bragg reflections used in the refinement.	118
4.4	CeO ₂ unit cell with the (111), (110), and (100) surfaces planes identified in blue. Schematic of the crystal lattice configurations produced using the VESTA software package[130]	119
4.5	Susceptibility as a function of temperature for nanocubes, nanorods and nanospheres in an O ₂ rich atmosphere.	121
4.6	Inverse susceptibility as a function of temperature for nanocubes, nanorods and nanospheres in an O ₂ rich atmosphere. The solid lines are fits of χ^{-1} vs T above 10 K as described in the text. The low temperature region of the nanoshape's susceptibilities show the maxima associated with magnetic order below ~ 7 K, and the low temperature spin flop transition under high fields of the O ₂ rich atmosphere measurements are shown by the M vs $\mu_0 H$ data of the nanocubes, nanorods, and nanospheres at 2 K, with the Brillouin function the solid lines (described in the text).	122
4.7	Temperature dependence of magnetic susceptibility for O ₂ deficient systems are shown. With the O ₂ deficient atmosphere nanoceria presents no low temperature transition compared to the O ₂ rich system measurements, and an additional 'transition' above 50 K. The inset shows the magnitude of the temperature dependent magnetism due to the released oxygen from the system (intrinsic CeO ₂ $\chi(T)$ subtracted data) of the O ₂ deficient environment.	125
4.8	Temperature dependence of field cooled ($\chi_{FC}(T)$) and zero field cooled ($\chi_{ZFC}(T)$) magnetic susceptibility for O ₂ deficient nanocubes, nanorods, and nanospheres are shown. With the FC measurement ($\mu_0 H=10$ mT) the magnetic signature from the O ₂ is removed in all shape dependent ceria nanoparticles.	126

4.9	(a) NO conversion as a function of time during steady-state NO reduction by CO at 300 and 350 °C over the various nanoceria shapes. (b)Activity ($\mu\text{mol/g/s}$) of cubes, spheres, and rods at 350 °C.	127
5.1	Room temperature XRD patterns of nanoceria, Fe-CeO ₂ and Co-CeO ₂ nanocrystals. The (hkl) indices of the structure are labeled. Refinement of nanoceria, Fe-CeO ₂ and Co-CeO ₂ crystallites (solid lines) are presented; the short vertical bars indicate the position of Bragg reflections used in the refinement.	134
5.2	Transmission electron micrographs of CeO ₂ and Fe – CeO ₂ are presented.	135
5.3	HAADF images acquired in the STEM mode of Ce atoms in Fe – CeO ₂ nanoparticles are shown.	136
5.4	HAADF images acquired in the STEM mode of Fe atoms in Fe – CeO ₂ nanoparticles are shown.	137
5.5	HAADF images acquired in the STEM mode of O atoms in Fe – CeO ₂ nanoparticles are shown.	138
5.6	$\chi(T)$ of CeO ₂ , Fe – CeO ₂ , and Co – CeO ₂ nanocrystallites measured in $\mu_0H = 2.5$ mT are presented. The inset shows $\chi(T)^{-1}$ data and Curie Weiss model fits (solid lines) of Fe – CeO ₂ and Co – CeO ₂ nanoparticles after subtracting CeO ₂ background. Fe – CeO ₂ and Co – CeO ₂ nanocrystallites $1/\chi(T)$ data is divided into two regions as discussed in the text. For Fe – CeO ₂ the high temperature component (> 350 K) is fit to Curie Weiss model and for Co – CeO ₂ the high temperature (> 250 K) component is temperature independent.	141
5.7	(a, c, e) Magnetization curves (corrected for diamagnetic background) for CeO ₂ , Fe – CeO ₂ , and Co – CeO ₂ are presented at 2, 5, 10, 100, 200, and 300 K. (b) In CeO ₂ the magnetic saturation (M_s) values are relatively comparable at 100, 200 and 300 K. (d) In Fe – CeO ₂ at 100, 200, and 300 K the M_s values are temperature independent. (f) In Co – CeO ₂ at 200 and 300 K the magnetization curves are temperature independent.	144
5.8	(a) The normalized XANES spectra were fitted with Gaussian functions. To exclude the effects of the edge jump from fits, an arctan function was included, as shown. (b) Fourier transforms represent raw data without correcting for phase shifts. Theoretical fits are the solid lines.	145
5.9	Fourier transformed magnitudes and fits of Fe-CeO ₂ and Co-CeO ₂ EXAFS data is shown.	149

- 5.10 Fe L_3 edge XAS experimental spectra and simulations of Fe – CeO₂ nanoparticles. The calculated Fe²⁺ (O_h) and Fe³⁺ (T_d) components of the XAS spectra and theoretical resulting summed spectrum are shown. (b) Co L_3 edge XMCD experimental spectrum and simulations are shown. Co ions exists in Co²⁺ T_d and Co³⁺ O_h environments. 150
- 5.11 Mössbauer spectra of Fe-decorated CeO₂ systems. The solid lines represent the fitted spectra (left) and subspectra components (right) used for the undistorted (site-I) and distorted (site-II) are shown. As identified by the ICP wt% the Fe decorations are very low and which is why the statistics are poor. 151
- 5.12 Ce $M_{4,5}$ edge XAS data and simulation with ionic limit. Higher energy satellite peaks region is shaded to show that the spectra could not be modeled successfully with $3d^{10}4f^0$ (initial) and $3d^94f^1$ (final) states and charge-transfer effects needs to be included. 152
- 5.13 (a) Ce $M_{4,5}$ edge XAS data and the simulation. Charge transfer effects with $4f^0+4f^1$ \underline{L} ground and $4f^1+4f^2$ \underline{L} final states are included in order to match the experimental spectra as discussed in the text. (b) Representation of charge transfer effect between O $2p$ ligand and Ce $4f$ are shown; \underline{c} is core hole on Ce. 154
- 5.14 Oxygen K edge XAS spectra of the nanoscale CeO₂, Fe – CeO₂, and Co – CeO₂ nanoparticles are shown. The three main transitions are due to O $2p$ hybridized with the $4f$, $5de_g$, and $5dt_{2g}$ states are shown. 156
- 5.15 Ce $M_{5,4}$ TEY(surface) and TFY(bulk) XMCD spectra evidencing the magnetic moment at Ce $4f$ sites. (a) Co-CeO₂ TEY XMCD and simulation are shown. The absence of the negative peak ~ 886 eV in the experiment is an indication that $4f$ electrons are hybridized as discussed in the text. (b,c) A comparison of Ce $M_{5,4}$ XAS and XMCD is shown. The origin of the energy axis of the simulated spectra has been chosen to align with the maximum intensity peak of the M_5 edge and the simulated spectra is reduced by a factor of twelve to match the experimental intensity of nanoceria. 158
- 6.1 A schematic diagram of superexchange (SE) and double exchange (DE) interactions are shown. SE is mediated between tetrahedral (T_d) and octahedral (O_h) sites via central lattice oxygen, and DE is mediated between two O_h sites via lattice oxygen as shown[65]. 164

- 6.2 Oxygen K edge of (a) Fe_3O_4 and (b) CoFe_2O_4 are shown. The hybridization region of O $2p - \text{Fe } 3d$ (Fe_3O_4) and O $2p - \text{Fe/Co } 3d$ (CoFe_2O_4) are shaded in blue, * at 535 eV is due to vicinal oxygen from carbon conductive tape[102] and the broad peaks above 536 eV are due to O $2p - \text{Fe/Co } 4s4p$ orbitals. The normalized XAS spectra were fitted with Gaussian functions to quantify the e_g and t_{2g} orbitals occupancy. To exclude the effects of the edge jump from fits, an arctan function was included for Fe_3O_4 and CoFe_2O_4 , as shown. Solid lines are fit to the O K edge XAS data. (c) Oxygen K edge of Fe_3O_4 is fit with two components: 23% t_{2g} and 77% e_g . (d) CoFe_2O_4 is fit with 39% t_{2g} and 61% e_g . The change in area of O K edge prepeak is an indication that in CoFe_2O_4 the $3d$ ions are pointing away from O $2p$ orbitals as discussed in the text. 166
- 6.3 (a) $\Delta\chi_{FC-ZFC}$ of Fe_3O_4 in O_2 rich and O_2 deficient conditions (b) $\Delta\chi_{FC-ZFC}$ of CoFe_2O_4 in O_2 rich and O_2 deficient conditions (c) Difference in O_2 rich and O_2 deficient magnetic susceptibility of $\Delta\chi_{FC-ZFC}$ of Fe_3O_4 and CoFe_2O_4 are shown. 168
- 6.4 (a) Temperature dependence of magnetic susceptibility for O_2 deficient systems are shown. The inset shows the magnitude of the temperature dependent magnetism due to the released oxygen from the system (intrinsic CeO_2 $\chi(T)$ subtracted data) of the O_2 deficient environment. (b) M vs $\mu_0 H$ curve of O_2 deficient systems at 2 K with Brillouin function fits to calculate the number of Ce^{3+}/g 174
- 6.5 $d\chi/dT$ vs T of O_2 deficient cubes, rods, and spheres. 175
- 6.6 Temperature dependence of field cooled ($\chi_{FC}(T)$) and zero field cooled ($\chi_{ZFC}(T)$) magnetic susceptibility for O_2 deficient nanospheres is shown. With the FC measurement ($\mu_0 H=10$ mT) the magnetic signature from the O_2 is removed in all shape dependent ceria nanoparticles. The $\Delta\chi_{FC-ZFC}$ vs T susceptibility of cubes, rods, and spheres identify the number of available excess Ce^{3+} ions due to the released oxygen as described in the text. 178
- 6.7 Ce^{3+}/O formation as a function of temperature. 179
- 6.8 (a) Activity ($\mu\text{mol}/\text{g}/\text{s}$) as a function of Frenkel and oxygen vacancies. (b) Activity as a function of oxygen vacancies. 180
- 6.9 SSA-normalized activity as a function of the surface density of Ce^{3+} sites determined by the magnetic susceptibility analysis in O_2 deficient conditions. The solid line is a straight line fit to the data (slope = $0.038 \pm 0.008 \frac{\mu\text{mol } NO/\text{m}^2/\text{s}}{\text{Ce}^{3+}/\text{nm}^2}$; intercept = $0.0014 \pm 0.0005 \mu\text{mol } NO/\text{m}^2/\text{s}$) as described in the text. 183

6.10	O K -edge XAS of the CeO ₂ , Fe – CeO ₂ , Co – CeO ₂ nanocrystallites are shown. The three main peaks are due to hybridized O $2p$ – Ce $4f$, O $2p$ – Ce $5de_g$, and O $2p$ – Ce $5dt_{2g}$ states.	184
6.11	$M(\mu_0H)$ of CeO ₂ , Fe-CeO ₂ and Co-CeO ₂ nanocrystallites measured at room temperature. $M(\mu_0H)$ of nanocerria shows a coercivity of ~ 50 mT and saturation magnetization (M_s) of ~ 4 Am ⁻¹ . Fe-CeO ₂ and Co-CeO ₂ nanocrystallites shows coercivity of ~ 50 mT and ~ 0 mT and M_s ' were ~ 7 Am ⁻¹ and ~ 4 Am ⁻¹	185
6.12	CeO ₂ crystal structure is shown in space filling style. Ce-lattice is FCC and V_{orb} -lattice is simple cubic. Each Ce-lattice consists of 4 Ce's per unit cell and V_{orb} -lattice consists of 1 V_{orb} per unit cell.	187
6.13	The lower and upper bounds of V_{orb} are shown. In the lower bound the radius of V_{orb} is defined as the distance at which neighboring atoms. Upper bound is the distance at which the V_{orb} fills all space.	188
6.14	Graphical illustration of the magnetic model. Ce $4f$ magnetic states, V_{orb} , and hybridized Ce $4f$ and O $2p$ states are shown. Ce $4f$ states captured in the V_{orb} polarizes the hybridized states and provides a channel to mediate the ferromagnetism. Shaded region illustrates the magnetic exchange process as discussed in the text.	189

List of Tables

2.1	Mössbauer hyperfine parameters for binary oxides.	66
3.1	Crystalline (nanoparticle) size (nm) and lattice constant (Å) of Fe ₃ O ₄ and CoFe ₂ O ₄ from XRD pattern refinements. The crystallographic site occupancies are fixed to 0.08333 for <i>O_h</i> sites and 0.04166 for <i>T_d</i> [87].	81
3.2	Parameters from the shell fitting of Fe <i>K</i> edge EXAFS analysis of Fe ₃ O ₄ . Coordination number (<i>N</i>), energy shift (<i>E</i> ₀), Debye-Waller factors (σ^2), average interatomic distances (<i>R</i>) are presented. The overall reduction <i>S</i> ₀ ² was obtained for Fe ₃ O ₄ as 1 by fitting to a bulk standard and the uncertainties are presented in parenthesis.	83
3.3	Parameters from the shell fitting of Fe <i>K</i> edge EXAFS analysis of CoFe ₂ O ₄ . Coordination number (<i>N</i>), energy shift (<i>E</i> ₀), Debye-Waller factors (σ^2), average interatomic distances (<i>R</i>) are presented. The overall reduction <i>S</i> ₀ ² was obtained for CoFe ₂ O ₄ as 0.71 by fitting to a bulk standard and the uncertainties are presented in parenthesis.	85
3.4	Parameters from the shell fitting of Co <i>K</i> edge EXAFS analysis of CoFe ₂ O ₄ . Coordination number (<i>N</i>), energy shift (<i>E</i> ₀), Debye-Waller factors (σ^2), average interatomic distances (<i>R</i>) are presented. The overall reduction <i>S</i> ₀ ² was obtained for CoFe ₂ O ₄ as 0.71 by fitting to a bulk standard and the uncertainties are presented in parenthesis.	87
3.5	Mössbauer hyperfine parameters of Fe ₃ O ₄ at room temperature. The spectrum is fit with independent linewidth sextets where Γ is set to 0.13 mm/s. Here $\Delta\Gamma$ is the broadened linewidth, δ is the isomer shift, and <i>B_{hf}</i> is the hyperfine field. Three different sites are used to fit the spectrum and the uncertainties are presented in parenthesis.	98
3.6	Mössbauer hyperfine parameters of CoFe ₂ O ₄ at room temperature. The spectrum is fit with independent linewidth sextets where Γ is set to 0.13 mm/s. Here $\Delta\Gamma$ is the broadened linewidth, δ is the isomer shift, and <i>B_{hf}</i> is the hyperfine field. Three different sites are used to fit the spectrum and the uncertainties are presented in parenthesis.	100

3.7	A comparison of cation distributions obtained from EXAFS, Mössbauer spectroscopy, and XAS/XMCD measurements are shown. EXAFS identifies the fraction of the Fe and Co ions that are O_h coordinated to oxygen as opposed to T_d coordinated (but is not sensitive to oxidation state). Mössbauer spectroscopy is sensitive to Fe ions (oxidation state and local environment) and quantifies the O_h and T_d sites. XAS/XMCD provides T_d and O_h cation distributions of both Fe and Co (sensitive to oxidation states).	102
4.1	Crystalline (nanoparticle) size (nm), lattice constant (Å) and preferred orientation (P_{hkl}) of crystal planes from XRD pattern refinements. Lattice constant (Å) from HRTEM image analysis. BET measurements for CeO_2 nanocubes, nanorods, and nanospheres.	118
4.2	O_2 rich systems' data: Ce^{3+}/g from χ^{-1} vs T fits with the total number of Ce^{3+}/g based on the full crystal field effect analysis, and thermal excitation energies (Θ) of CeO_2 nanocubes, nanorods, and nanospheres.	123
4.3	Comparison of NO conversion per plane for $1\text{ m}^2/g$.	130
5.1	Crystalline (nanoparticle) size (nm) and lattice constant (Å) from XRD pattern refinements. ICP wt%'s of Fe and BET measurements for nanoceria and Fe- CeO_2 and Co- CeO_2 are presented.	135
5.2	Comparison of Curie constant C , Curie-Weiss temperature θ , and $\mu_{eff}(\mu_B)$ measurements of Fe – CeO_2 and Co – CeO_2 are shown.	140
5.3	Parameters from the shell fitting of Ce L_3 edge EXAFS analysis of CeO_2 , Fe- CeO_2 and Co- CeO_2 nanocrystallites.	147
5.4	Parameters from the shell fitting of Fe K edge EXAFS analysis of Fe- CeO_2 .	148
5.5	Parameters from the shell fitting of Co K edge EXAFS analysis of Co- CeO_2 .	149
5.6	Mössbauer hyperfine parameters (line width (Γ), isomer-shift (δ) and quadrupole splitting (Δ) are presented.	150
5.7	Contributions of the z-component of the orbital and spin magnetic moments obtained from the TEY (surface) XMCD simulations of Co- CeO_2 and TFY (bulk) XMCD of CeO_2 , Fe- CeO_2 and Co- CeO_2 nanocrystallites.	159
6.1	O_2 deficient systems' data: Number of Ce^{3+} identified by the 2 K M vs $\mu_0 H$ data and excess Ce^{3+} ions from $\chi_{FC-ZFC}(T)$ along with the % of \square , Frenkel pair defects and Ce^{3+}/nm^2 .	176

Acknowledgments

The research work described in the thesis would not have been possible without the unconditional support and guidance of my advisor Prof. Johan van Lierop. I sincerely thank him for giving me the opportunity to pursue my graduate studies in his research lab. Johan is a passionate researcher, and I was fortunate to work with him during my PhD studies. His ability to focus on details with keeping the big picture in mind is still enigmatic to me, and his work ethic is exceptional. Thank you, Johan, for providing financial contributions, introducing me to the world-class experts in research and cutting edge experimental techniques to foster my scientific research career.

In the thesis, the samples I have studied are all synthesized by Dr. Charles A. Roberts (Chip) and his catalysis team at Toyota Motor Engineering and Manufacturing North America, Inc, Ann Arbor, USA. I sincerely want to thank Chip for introducing me to the exciting material CeO_2 , the physics and chemistry of CeO_2 are fascinating. Chip's approach to catalysis is interdisciplinary, and the discussions with him helped me appreciate the finer details of heterogeneous catalysis. I would also like to thank Dr. Kimber Stamm Masias and Dr. Krishna Gunugunuri for their discussions on catalysis of oxide systems. Special thanks to Prof. Justin Notestein research's group at Northwestern University, Evanston, USA, for providing CeO_2 nanoshapes and discussions on ceria catalysis.

Much of my efforts in exploring the physics and chemistry of metal oxides came from synchrotron studies at Advanced Photon Source (Argonne National Laboratory) using both soft and hard x-ray beamlines. I thank the beamline staff Dr. John Free-

land, Dr. Dale L. Brewé, Dr. David J. Keaveny, Dr. Yong Choi and Dr. Steve M. Heald who helped me with beamline experiments. I am thankful of Dr. John Free-land's help with XAS and XMCD simulations and data interpretation of nanoceria. I acknowledge Dr. Dale L. Brewé's help with discussions on the XANES and EXAFS analysis.

I thank Prof. Byron Southern, Prof. Viktor Nemykin, and Dr. Jacob Burgess for serving on my committee. I enjoyed statistical mechanics lectures by Prof. Southern, and I thank him for being on my committee since 2014. I am grateful to Prof. Viktor Nemykin for allowing me to work on some of his exciting chemistry projects through which I have learned some interesting aspects of inorganic and organometallic systems' molecular magnetism. I want to take this opportunity to thank Gillis Roy and Peiqing Wang for help with the instrumentation and its maintenance. Peiqing is excellent to work with, and his mastery of every instrument astounds me. A special thanks to the office staff Wanda Klassen, Christine McInnis, Susan Beshta, Aynsley Bishop-Mahon, and Robyn Beaulieu for their support during my graduate studies, and Maiko Langelaar for IT support. I sincerely thank Prof K. S. Sharma and Prof. R. L. Stamps for serving as department heads and offering their help during my grad studies.

I want to thank all past and present group members of Nanomagnetism Research Lab. I had the great fortune to interact and work with all of you. Ryan Desautels, Elizabeth Skoroapata, Yaroslav Wroczynskyj, Palash Manna, Kelly Newman, Rachel Nickel, Mike Shepit, Dustin Nevenon, Bassel Alkadour, Elif Demerci, Christopher Rutley, Subhasish Pattanaik, Richard Jones, Jyotirmay Dwivedi, Yuliia Mankovska,

Joann Hilmann, Christina Balanduk, Katyrna Fast, and Carlos Verbeno. Thanks to Ryan, Liz, and Yaro for helping me with magnetometry, Mössbauer spectroscopy, and data analysis in the beginning days of my graduate studies. Thanks to Ryan, Liz, Rachel and Mike for their help at the Argonne National Laboratory. I thank Mike for his help with *in-situ* Mössbauer spectrometer setup and catalytic reactor design. I want to thank some other friends who made my stay at Manitoba fun: Reddy, Lucky, Pavan, Suraksh, Vinutha, Bob, Kelvin, Gerd, Ashwini, Gopi, and Gaffar, thank you for all your support.

I have had the pleasure to work with amazing people during my PhD. I have tremendous gratitude for all those remarkable teachers, colleagues and friends, I have not named all of them, but to everyone, thank you. My sincere thanks to the University of Manitoba, Natural Sciences and Engineering Research Council of Canada (NSERC) and the Canada Foundation for Innovation for their financial support. The US DOE supported the use of the Advanced Photon Source at Argonne National Laboratory under contract DE-AC02-06CH11357.

To my brother and my parents

Chapter 1

Introduction

Orbital and spin angular momenta of the electrons are fundamental to the origins of magnetism. Depending on how the atoms in a material respond to an applied field, the magnetism can be classified into five major groups: Diamagnetism, paramagnetism, ferromagnetism, antiferromagnetism and ferrimagnetism[1]. In this thesis, we mainly are concerned with paramagnetism, ferromagnetism, antiferromagnetism, and ferrimagnetism.

1.1 Paramagnetism

In a paramagnetic material, the atoms with magnetic moments tend to align parallel to each other in an applied field to lower the energy. If the magnetization¹ (M) as a function of an applied field (H) is measured, the slope known as the *magnetic susceptibility* (χ), is positive as shown in Fig. 1.1. The inclination of the magnetic moments to align in parallel to the applied field is opposed by the thermal motion, which tends to make the direction of the moments random. A typical temperature dependent magnetic susceptibility plot of a paramagnet is shown in Fig. 1.1.

There are two main reasons behind the paramagnetic response in a system: 1. The magnetic moment from the ions (Curie's law) and 2. The spatial motion of the conduction electrons inside a material (Pauli paramagnetism). A brief discussion of both the reasons are below.

Pauli paramagnetism: In a free electron gas, electrons can respond to an externally applied magnetic field. The Hamiltonian that describes this process can be

¹Defined as the magnetic moment per unit volume.

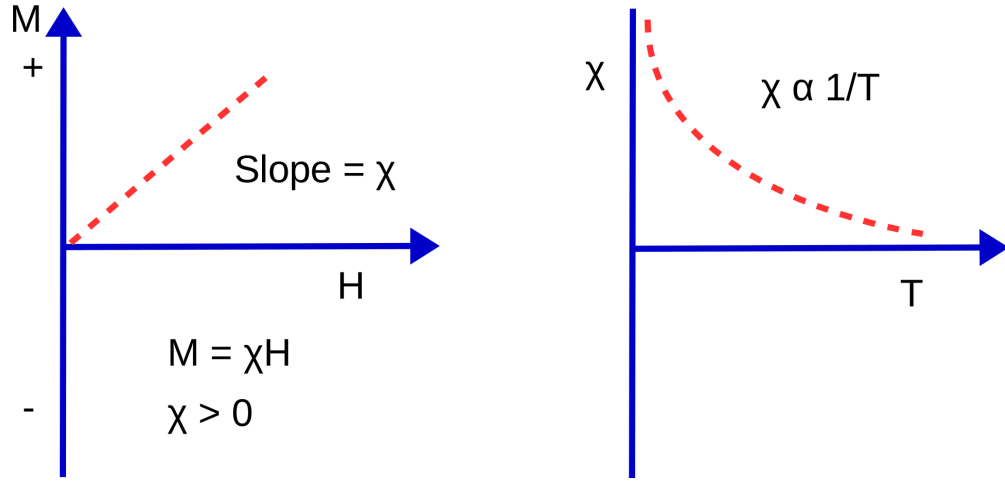


Figure 1.1: M vs H and χ vs T plots of a paramagnet are shown. Susceptibility χ is positive and larger than diamagnetic susceptibility. χ is inversely proportional to the temperature, which is known as Curie's law.

written as

$$\mathcal{H} = \frac{\mathbf{p}^2}{2m} + g\mu_B \mathbf{B} \cdot \sigma \quad (1.1)$$

where $\mathbf{p} = \hbar\mathbf{k}$ is the momentum of the electron², m is the mass of the electron, $g = 2$ is the g -factor of the electron, μ_B is the Bohr magneton, \mathbf{B} is the magnetic field, and σ is the spin of the electron with eigenvalues $\pm 1/2$. In an applied magnetic field, the energy (ϵ) of an electron with spin up (\uparrow) or spin down (\downarrow) configuration is

$$\epsilon(\mathbf{k}, \uparrow) = \frac{\hbar|\mathbf{k}|^2}{2m} + \mu_B|B| \quad (1.2)$$

$$\epsilon(\mathbf{k}, \downarrow) = \frac{\hbar|\mathbf{k}|^2}{2m} - \mu_B|B|. \quad (1.3)$$

At $T = 0$ with $B = 0$, both spin up and spin down states are filled up to the Fermi energy (E_F). Near the Fermi level the density of states $g(E_F)$ of the spin up (and spin down) electrons are $g(E_F)/2$. When the $B \neq 0$ the energy of the spin up electrons

² \hbar is the reduced Planck's constant and \mathbf{k} is the wave vector.

will increase by $\mu_B B$, thus the number of spin up electrons per unit volume decreases by $(g(E_F)/2)\mu_B B$. Similarly, the spin down electrons per unit volume increase by $(g(E_F)/2)\mu_B B$. Thus the magnetization is given by^[2]

$$M = g(E_F)\mu_B^2 B \quad (1.4)$$

and hence the magnetic susceptibility $\chi = \partial M / \partial H$ at $T = 0$ K is given by

$$\chi_{Pauli} = \frac{dM}{dH} = \mu_0 \frac{dM}{dB} = \mu_0 \mu_B^2 g(E_F) \quad (1.5)$$

where μ_0 is the permeability of free space.

Curie's law: In this case, atoms possess magnetic moment and are non-interacting with their neighbours above transition temperatures (T_C or T_N). Here T_C is the Curie temperature³ and T_N is the Néel temperature⁴. The Hamiltonian which describes the magnetic moment energy in an applied field is

$$\mathcal{H} = -\tilde{g}\mu_B \mathbf{B} \cdot \mathbf{J} \quad (1.6)$$

where \tilde{g} is the Landé g -factor⁵ and \mathbf{J} is total angular momentum. If we consider the z direction as the direction of the applied field, equation 1.6 becomes

$$\mathcal{H}_z = -\tilde{g}\mu_B B J_z. \quad (1.7)$$

The effect of magnetic interactions split the J state into its $2J + 1$ Zeeman components, and the magnetic susceptibility is written as^[3]

$$\chi = \frac{N g^2 \mu_B^2 J(J+1)}{V 3k_B T} = \frac{C}{T} \quad (1.8)$$

³Ferromagnetic to paramagnetic transition

⁴Antiferromagnetic to paramagnetic transition

⁵From the Wigner-Eckart theorem, the effective g -factor is $\tilde{g} = \frac{3}{2} + \frac{1}{2} \left[\frac{S(S+1) - L(L+1)}{J(J+1)} \right]$; where L and S are the orbital and spin angular momenta

where N/V is the number of magnetic atoms per unit volume and C is the Curie constant. The Curie constant can be used experimentally to quantify the effective magnetic moments (in Bohr magnetons) by

$$\mu_{eff} = \sqrt{\frac{3k_B C}{(N/V)\mu_B^2}}. \quad (1.9)$$

From equations 1.8 and 1.9 we can obtain effective moment

$$\mu_{eff} = g\sqrt{J(J+1)} \quad (1.10)$$

Most of the transition metals have S as a “good quantum number” (as discussed below in section 1.5), so for transition metals $g\sqrt{S(S+1)}$ describes moments in good agreement with the μ_{eff} values. However, if the energy spacing (Δ) between the ground and excited states is small enough ($\Delta \sim k_B T$, where k_B is the Boltzmann constant) the Van Vleck paramagnetism term should be taken into account to estimate μ_{eff} properly.

From perturbation theory the Van Vleck susceptibility (χ_{VV}) is obtained as [4]

$$\chi_{VV} = \frac{2\mu_0\mu_B^2}{V} \sum_n \frac{|\langle 0 | \mathbf{L}_z + g\mathbf{S}_z | n \rangle|^2}{E_n - E_0}. \quad (1.11)$$

In this thesis, because the Ce^{3+} ground state is an admixture of different doublets, we use Van Vleck susceptibility to calculate the concentration of Ce^{3+} in different nanoshapes. The description of the angular momentum quantum number J multiplet being widely spaced from the ground state compared to the thermal energy does not apply to Ce^{3+} as we know that the energy level diagram (from theory and experiment[5; 6]) is crystal field split from its $^2F_{\frac{5}{2}}$ state into three Kramer doublets with $J_z = \pm\frac{1}{2}$, $\pm\frac{5}{2}$, and $\pm\frac{3}{2}$. At low temperatures, only the $\pm\frac{1}{2}$ level is populated,

and with increasing temperature, $\pm\frac{5}{2}$ (at 10 K) and $\pm\frac{3}{2}$ (at 150 K) levels are also populated[7]. In these cases of J multiplet intervals are comparable to kT . That is $E_J^* - E_J \sim kT$, so it is necessary to use the complete expression of paramagnetic susceptibility (Curie and Van Vleck).

The full formalism for $\chi(T)$ for rare-earth ions in a paramagnetic state, such as Ce^{3+} , with the $J=\pm 1/2$, $\pm 5/2$ and $\pm 3/2$ states becoming occupied with warming from below 10 K is

$$\chi = \frac{N \sum_J \{ [g_J^2 J(J+1) \mu_B^2 / 3kT] + \alpha(J) \} (2J+1) e^{-E_J^0/kT}}{\sum_J (2J+1) e^{-E_J^0/kT}}. \quad (1.12)$$

Here E_J^0 is the energy of state J in zero field, $\alpha(J)$ is the temperature-independent term[8].

1.2 Ferromagnetism, Antiferromagnetism, and Ferrimagnetism

When cooling from a paramagnetic state a spontaneous magnetic order develops in ferro-, antiferro-, and ferrimagnetic materials, even with the absence of an external magnetic field. For example, in transition metal oxides where the strong interaction between electrons prevents hopping between the sites (e.g. Mott insulators), in zero applied field the model Hamiltonian is[2]

$$\mathcal{H} = -\frac{1}{2} \sum_{i,j} J_{i,j} \mathbf{S}_i \cdot \mathbf{S}_j. \quad (1.13)$$

Here \mathbf{S}_i is the electron spin on site i and $J_{i,j} \mathbf{S}_i \cdot \mathbf{S}_j$ is the interaction energy between spin i and spin j . In general, ferromagnetic materials exhibit two distinct properties: a spontaneous magnetization and an ordering temperature. Spontaneous magnetization exists in ferromagnets even without an applied field. Another related term

is the magnetic saturation; that is, the maximum moment that can be achieved in a magnetic field (H_{sat}). Above H_{sat} there is no further increase in magnetization as shown in Fig. 1.2b.

Although the electronic exchange interaction J is strong, eventually the thermal energy overcomes and randomizes the spins. The temperature at which this phenomenon occurs is called the Curie-temperature (T_C), as shown in Fig. 1.2c. Below T_C ferromagnets can retain their “memory” of an applied field once it is removed and this is due to the existence of magnetic domains. A magnetic domain is a region in which all moments point in the same direction. If all the neighbouring spins are aligned (Fig. 1.2a) in the ground state then $J > 0$ (equation 1.13).

On the other hand, if $J < 0$, then the neighbouring spins point in opposite directions, as shown in Fig. 1.2e – this is antiferromagnetism. A simple antiferromagnet consists of two A and B sublattices of equal moments in opposite directions and shows zero net magnetization. By examining the susceptibility as a function of temperature, one can identify the antiferromagnetism (Fig. 1.2f). Above the Néel temperature (T_N) the susceptibility obeys the Curie-Weiss law for paramagnets as shown in Fig. 1.2f.

Although the exchange is antiferromagnetic, when the atoms have different magnetic moments, they show ferrimagnetism. In ferrimagnets, two sublattices A and B of dissimilar magnetic moments result in a net magnetization (Fig. 1.2d). Fe_3O_4 is an example of a ferrimagnet where oxygens separate the two Fe magnetic sublattices as discussed in Chapter 3. The oxygen anions mediate the exchange interactions. Ferrimagnets exhibit the properties of ferromagnets such as a spontaneous magnetization, Curie temperatures, hysteresis, etc.

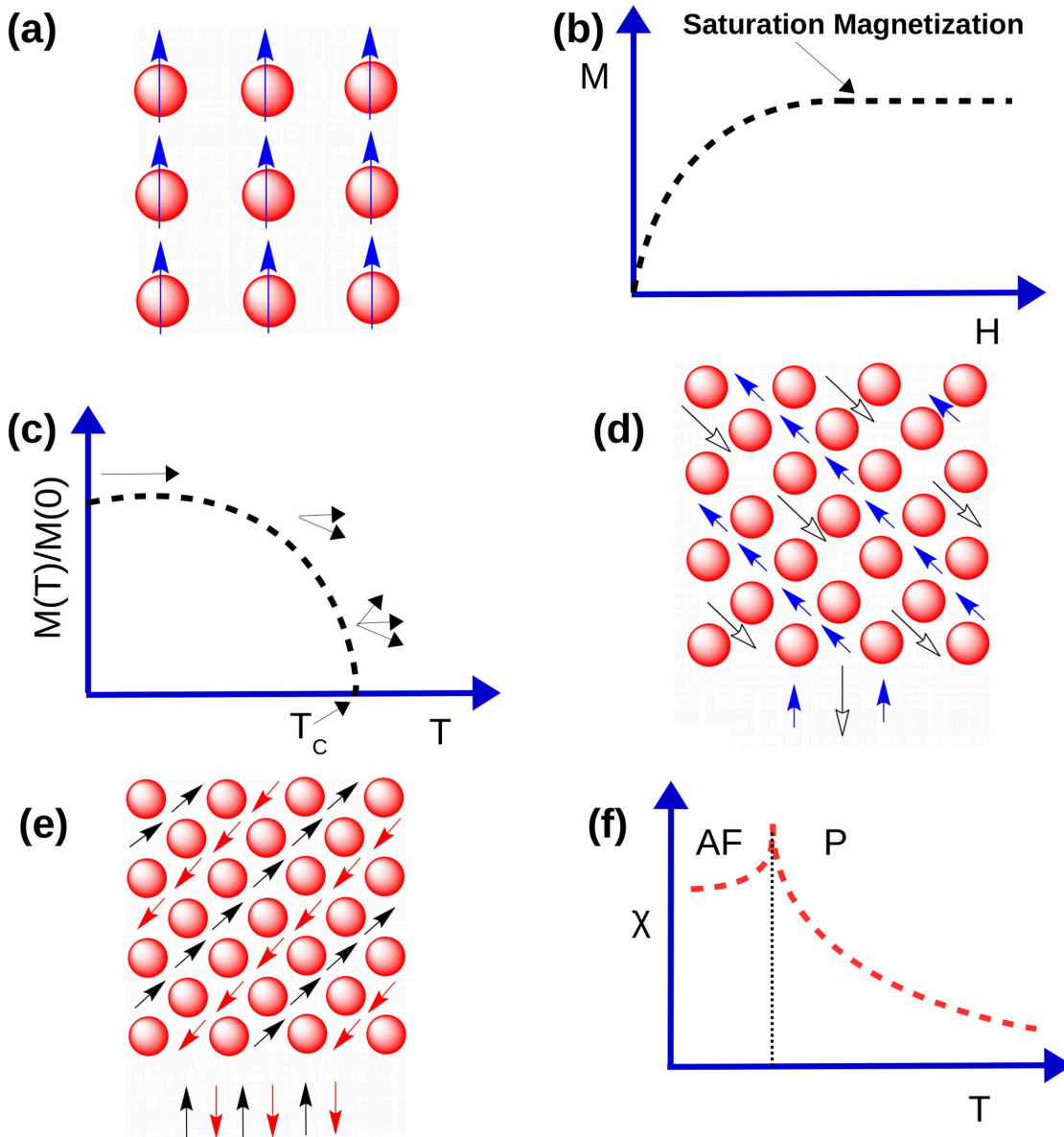


Figure 1.2: (a) Spin arrangement in an ordered ferromagnet. (b) Magnetization as a function of an applied field in a ferromagnet is shown. Magnetic saturation is the maximum moment that can be achieved in a magnetic field (H_{sat}). (c) Magnetization as a function of temperature in a ferromagnet is shown, where T_C is the Curie temperature. (d,e) Spin arrangement in a ferrimagnet and antiferromagnet are shown respectively. (f) Temperature dependent susceptibility shows antiferro-paramagnetic transition.

1.3 Nanoparticle Magnetism

The basic physics behind the magnetism of nanoparticles is described below. In bulk-sized magnetic materials, the alignment of the magnetic moment creates a region called a magnetic domain. However, in a single-domain nanoparticle, all of its internal magnetization is pointed in the same direction, with the largest possible magnetic moment (“super moment”). In a single-domain nanoparticle, the magnetization is often considered to lie parallel or anti-parallel to a particular direction. In the absence of an applied magnetic field, a particle of volume V and with an anisotropy constant K the energy associated with magnetization reversal of a non-interacting assembly is described by $E = KV \sin^2(\theta)$. A particle needs an activation energy $\Delta E = KV$ to flip its magnetization orientation from $\theta = 0$ to $\theta = \pi$. Because the order of $V \sim 10^{-19} \text{ cm}^3$ and $K = 10^5 - 10^6 \text{ erg/cm}^3$, $\Delta E \sim 2 \times 10^{-25} \text{ erg}$. In the limit of $k_B T \gg KV$, the particle⁶ can be freely fluctuating. In a single domain nanoparticle the transition time τ between the equilibrium positions is described by Néel-Brown model[9; 10]

$$\tau = \tau_0 \exp\left(\frac{\Delta E}{k_B T}\right) \quad (1.14)$$

where τ_0 represents the attempt frequency to flip orientation. As the temperature is cooled down the fluctuations slow down (τ decreases) and this behaviour is one of the reasons why nanoscale magnetism is significantly different from bulk materials. A consequence to this temperature dependent τ behaviour is that measured magnetization depends on the measuring time (τ_m) of the technique used. When the energy barrier (ΔE) is comparable to the thermal energy, $k_B T$, the ferromagnetic

⁶At 300 K, the thermal energy $k_B T \sim 4 \times 10^{-14} \text{ erg}$

nanoparticle is defined as superparamagnetic. The system appears static when the superparamagnetic relaxation time $\tau \gg \tau_m$ (experimental measuring time). Only when $\tau < \tau_m$, one may observe an average value of the magnetization. When the $\tau \sim \tau_0$ the magnetic behaviour of the particle is “blocking” and below which (blocking temperature (T_b)) the particle moments appear frozen in the limit of $\tau_m \sim \tau$. Equation 1.14 can be rewritten as

$$T_B \sim \frac{KV}{k_B \ln(\tau_m/\tau_0)}. \quad (1.15)$$

1.4 Electron Correlation and Hybridization

In transition metals, the $3d$ electrons localize near the atoms and tend to participate relatively weakly in the chemical bonding. Although $3d$ electrons in an atom are localized in a solid, there is interaction with the neighbouring atoms. The Coulomb and exchange interactions between localized electrons cause a collective behaviour called electron correlation. To first order if one assumes an atomic like picture, then an atom with n electrons in a $3d$ shell (10 states are available) have $\frac{10!}{(10-n)!n!}$ (${}^{10}C_n$) different ways to arrange the n electrons within the orbitals. So depending on the oxidation state of the element, for an isolated atom, there are ${}^{10}C_n$ eigenstates, although some can be degenerate. The eigenstates are called *multiplets*[11], and their energies are sensitive to the number of d electrons. The same logic applies to rare-earths valence $4f$ electrons. However, in Chapter 5 we see that if we only consider the atomic-like picture, that is, Coulombic, exchange and spin-orbit coupling interactions due to isolated atoms, the x-ray absorption spectra cannot be explained properly, and interactions with the neighbouring atoms must be taken into account.

The Mott-Hubbard[12; 13] theory proposes that the hopping of an electron from one site to another involves large Coulomb and exchange interaction energies (7 - 10 eV for the late transition metals) and the material will be insulating. For example, the energy required to move an electron from $d_i^n d_j^n \leftrightarrow d_i^{n-1} d_j^{n+1}$ (where i and j label transition metal ions) is given by

$$U = E(d^{n-1}) + E(d^{n+1}) - 2E(d^n) \quad (1.16)$$

where U is the Coulomb and exchange interaction energies of the transition metal $3d$ electrons. Although the model was successful in explaining the $d - d$ gap for Ti and V it was challenging to explain that why NiS, CuS, and CoS were not insulators, and the reduction of U from 7 - 10 eV in oxides to 1 - 2 eV in sulfides was puzzling. Later in the 1980s, for a large number of systems, it was shown that charge-transfer energies associated with ligand electrons hopping to metal sites should be included[13]. The charge-transfer energy (Δ) is then defined as

$$\Delta = E(d^{n+1}\underline{L}) - E(d^n) \quad (1.17)$$

where \underline{L} refers to a hole in the anion (ligand) valence band. The competition between the Mott-Hubbard U energy gained when an electron jumps between metal sites and the charge transfer Δ gained between ligand band to metal sites dictates which fluctuation lowers the energy and defines the band gap.

Figure 1.3 shows these ideas in a schematic of the density of states in a transition metal oxide. In transition metal ions, the metal cation donates electrons to complete the oxygen $2p$ shells, so the density of states near the Fermi level consists of metal $3d$ states and O $2p$ states. Because the oxygen $2p$ states are full, there is a strong

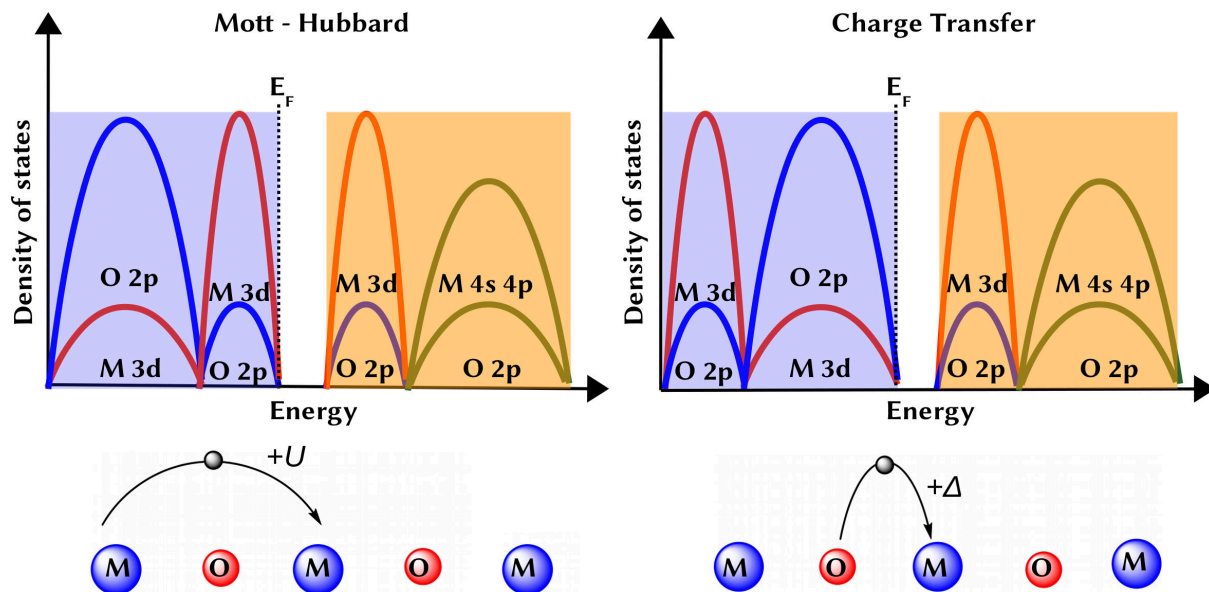


Figure 1.3: A schematic of Mott-Hubbard and charge transfer models. In the Mott-Hubbard model, an electron hops between transition metal ions and the energy cost is U . In the charge transfer model, the charge fluctuations are from oxygen ligand to metal sites, and the energy cost is Δ . Here E_F denotes the Fermi energy level[13; 14; 15].

presence of $2p$ states in the valence band. Similarly, because the $3d$ states are partially full, the occupied valence band and unoccupied conduction bands are separated by metal $3d$ states with a Mott-Hubbard energy U .

The charge-transfer energy Δ comes into play as a result of bonding between metal $3d$ and oxygen $2p$ states in the transition metal oxides. The mixing of O $2p$ states with the metal $3d$ states is hybridization. Figure 1.3 shows the charge transfer process between an oxygen ligand and a metal ion. The hole in the oxygen $2p$ ligand pushes the occupied $3d$ states to the bottom of the valence band, and the top of the valence band has primarily $2p$ character. For this reason, the magnitude of the band gap is defined by Δ rather than U .

1.5 Oxygen's Role in the Magnetism of Transition Metal Oxides

Metal ions placed in the crystal environment of oxides show interesting magnetic properties due to the oxygen neighbours. If the metal ion consists of $3d$ and $4d$ electrons, crystal field effects are dominant. On the other hand, for rare earths the $4f$ electrons, which are shielded by the large filled $5s$ and $5p$ shells, the crystal field effects can be neglected[16]. Therefore, for the rare earths, J , is a good quantum number. Contrarily, for the transition metals, because the crystal field effects are usually larger than the spin-orbit coupling, the orbital moment should be quenched. As a result, for transition metal ions, S is a good quantum number. If the ion is located at a site with cubic symmetry, its basis set of eigenfunctions are[16]

$$\begin{aligned}
 \psi_{xy} &= \left(\frac{-i}{\sqrt{2}}\right)(\psi_2 - \psi_{-2}) \\
 \psi_{yz} &= \left(\frac{i}{\sqrt{2}}\right)(\psi_1 + \psi_{-1}) \\
 \psi_{zx} &= \left(\frac{-1}{\sqrt{2}}\right)(\psi_1 - \psi_{-1}) \\
 \psi_{x^2-y^2} &= \left(\frac{1}{\sqrt{2}}\right)(\psi_2 + \psi_{-2}) \\
 \psi_{z^2} &= \psi_0
 \end{aligned} \tag{1.18}$$

where ψ_0 , $\psi_{\pm 1}$, and $\psi_{\pm 2}$ are free ion eigenfunctions, and the subscripts denote the magnetic quantum numbers m_l . Figure 1.4 shows the crystal field splitting of the ion in different coordinations. Crystal field effects play a major role in understanding the origin of magnetism in oxides. The origin of exchange interactions lies in the Coulomb interactions that couple electronic spins. In general, Hund's rule exchange

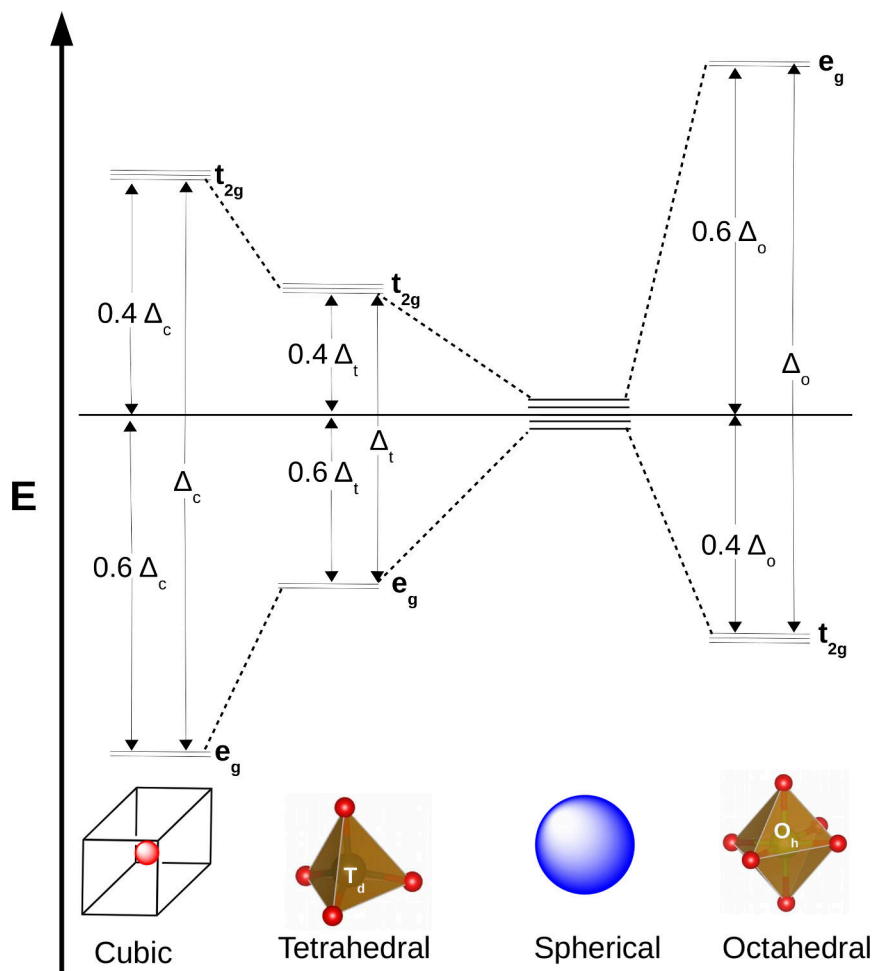


Figure 1.4: A metal ion atom in a cubic, tetrahedral, spherical, and octahedral coordination are shown. The d_{xy}, d_{yz} , and d_{zx} are grouped together as t_{2g} level. The d_{z^2} and $d_{x^2-y^2}$ are grouped together as e_g level. Δ_c , Δ_t , and Δ_o are crystal-field splitting energies for cubic, tetrahedral and octahedral coordination respectively.

(\mathcal{J}_H) maximizes the total spin of an ion with a partially filled shell. In the majority of cases, the crystal field energy (CFE) of oxides is smaller than \mathcal{J}_H and spin up orbitals are filled first, favouring a high-spin configuration[16]. If the $\text{CFE} > \mathcal{J}_H$ then the ion is in a low-spin configuration. Some examples of exchange interactions in oxides are discussed below.

1.5.1 Superexchange

In the oxide systems of interest, the superexchange interaction happens via hybridization between metal $3d$ and oxygen $2p$ states. Oxygen acts as a central bridge between metal ions and makes the superexchange interaction possible. A schematic diagram of the superexchange interaction case is shown in Fig. 1.5. An electron in O $2p^6$ transfers to an adjacent metal ion M_1 , leading to a d^{n+1} state. The energy required to making this transition is given by the Coulomb energy U . The hole in the O $2p$ ligand is filled by another adjacent metal ion M_2 which overlaps with the O $2p$ bridge. Because the superexchange interactions involve virtual transfer of electrons from one state to the other with a formation of $3d^{n+1}2p^5$ states, the exchange energy \mathcal{J} is $\sim -t^2/2U$ where t is the $p-d$ hopping integral[17]. \mathcal{J} strongly depends on the $M_1 - O - M_2$ bond angle and interatomic separation. The d orbital occupancy and degeneracy are the critical factors in determining the strength and sign of the exchange constant \mathcal{J} , given by the Goodenough-Kanamori rules[18] presented below.

1. When two cations of partially filled $3d$ orbitals point toward each other that gives a large overlap and hopping integral. The exchange interaction is strong and antiferromagnetic ($\mathcal{J} < 0$). For example, this is the case for $180^\circ M_1 - O - M_2$ bonds.
2. When two cations overlap at 90° with zero symmetry, the exchange interaction is relatively weak and ferromagnetic. For example, this is the case for $90^\circ M_1 - O - M_2$ bonds.
3. When two cations of partially filled $3d$ orbitals overlap with empty or doubly-occupied orbitals, the exchange interaction is weak and ferromagnetic.

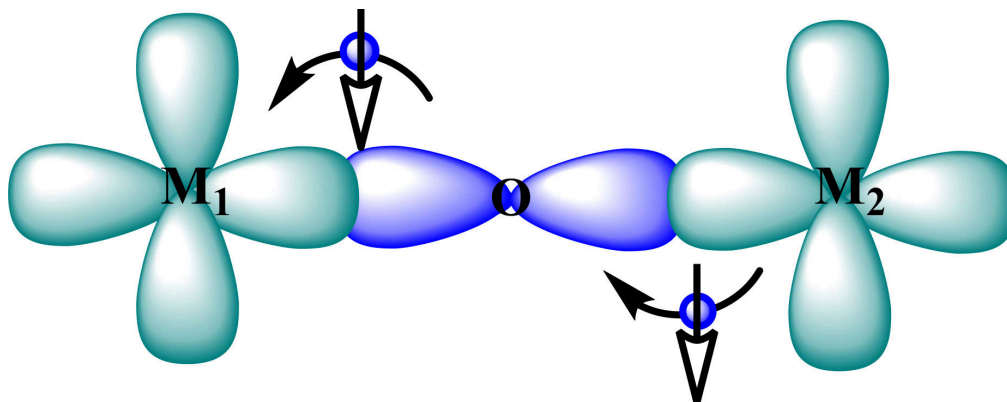


Figure 1.5: A schematic of superexchange mechanism is shown. The superexchange interaction is strong for 180° $M_1 - O - M_2$ bonds as discussed in the text.

1.5.2 Double exchange

When cations of the same element exist in two different oxidation states (mixed valence), a double exchange interaction arises between $3d$ ions that involves both localized and localized electrons. In mixed valence systems an electron may hop from a site i with $n + 1$ electrons to an adjacent site j with n electrons. Zener suggested this mechanism of electron spin interaction in mixed valence manganites of perovskite structure such as $(La_xCa_{1-x})(Mn_x^{III}Mn_{1-x}^{IV})O_3$ [19]. Magnetite (Fe_3O_4) is another example that shows double exchange ferromagnetism. In Fe_3O_4 , Fe^{3+} and Fe^{2+} ions have d^5 and d^6 ions respectively. The d^5 configuration is a half-filled, in d^6 configuration the sixth d electron occupies the bottom of a $t_{2g} \uparrow$ band when the Fe is octahedrally coordinated by oxygen, where it can hop directly from one $d^5 \uparrow$ core to another. The fundamental difference between the double and superexchange mechanisms is that in double exchange electrons do not hop between the two metal cations (localized), with double exchange, electrons hop between the positive ions via

the oxygen ligands resulting in properties like electrical conductivity.

1.6 Catalytic Properties of Nanoparticle Oxides

Metal oxides have a long history in heterogeneous catalysis and found a wide range of applications[20], for example in automotive exhaust. For context, in this thesis we are dealing with a solid catalyst and the gaseous reactants and products. In general a catalyst is a substance that speeds up a chemical reaction by decreasing the activation energy or changing the reaction mechanism, while emerging from the process unchanged. For metal oxide catalysts, the surface plays a fundamental role because of O^{2-} surface defects and the different environments of metal cations[21] compared to the bulk. At the nanoscale, engineering the shape and size of a catalyst is of great importance to control the surface chemistry and enhance the catalytic properties.

Rare earth and transition metal oxides have made a significant impact on the modern world by enabling the catalytic oxidation of carbon monoxide (CO) and reduction of nitrogen oxides (NO_x). They are widely used in automotive catalytic converters to remove poisonous gases from engine exhaust; reduction of NO_x and oxidation of CO simultaneously. One of the fundamental properties that makes a material excellent for NO_x reduction over CO oxidation catalysis is its ability to release and uptake oxygen depending on the partial pressure of the surroundings, that is its oxygen storage capacity (OSC). Nanoscale CeO_2 is the prototypical system for studying the NO_x reduction catalysis. A schematic representation of the reaction mechanism[22] on Fe and Na supported CeO_2 nanocatalysts is shown in Fig. 6.2.2.

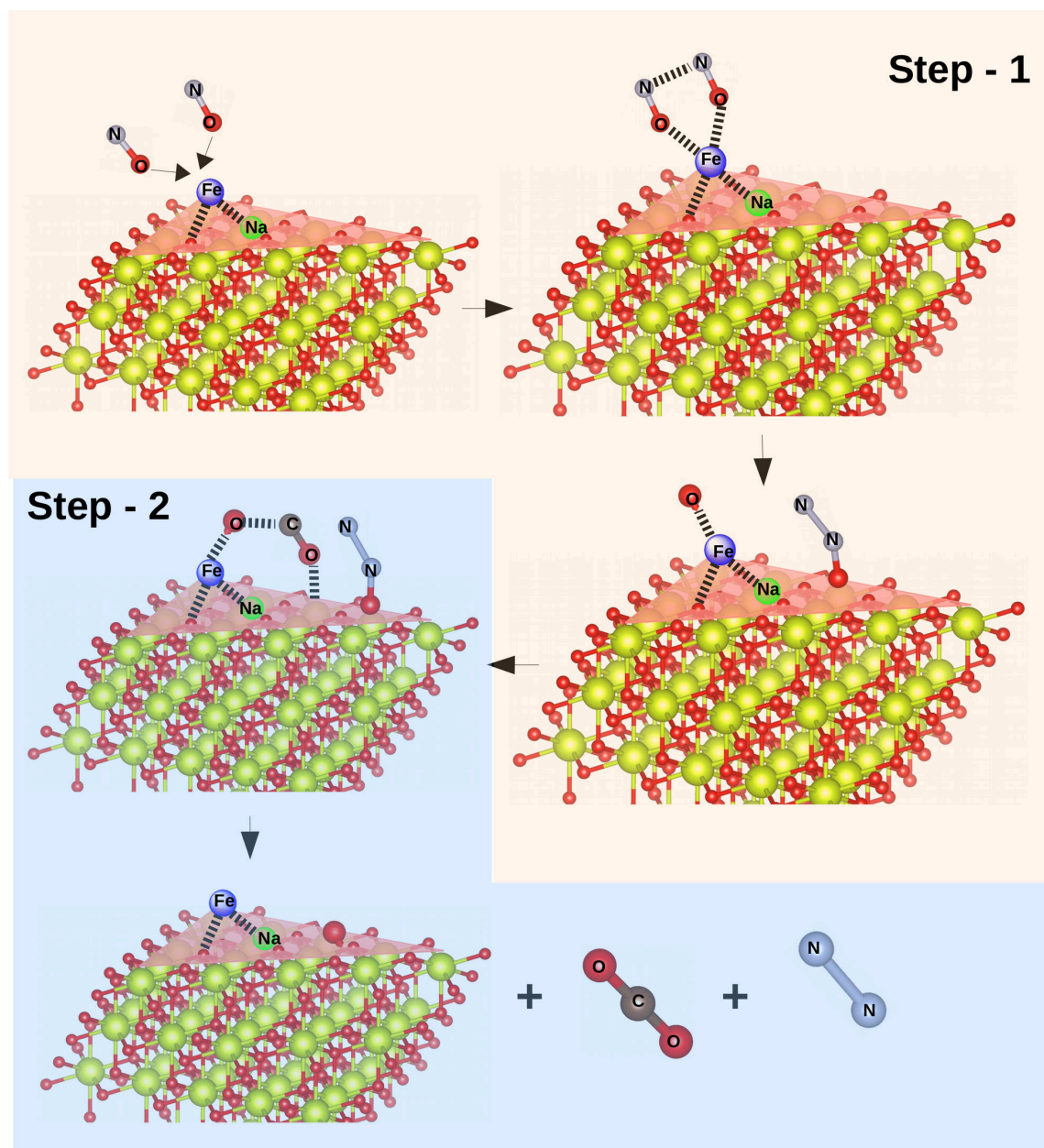
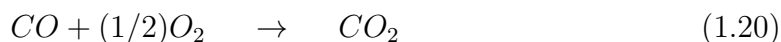
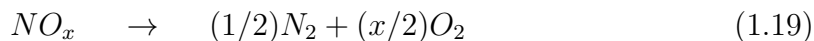
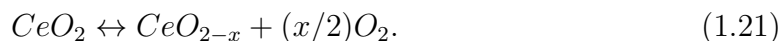


Figure 1.6: A graphical representation of NO reduction by CO is proposed on the nanoceria (111) plane. In the first step two NO molecules adsorb on the Fe sites and decompose to N₂O. In the second step, CO molecules adsorb onto the Fe ions and take up the excess oxygen and form N₂ and CO₂. The excess oxygens are neutralized by the oxygen vacancies of ceria supports.

The above chemical reactions involve processes such as



that takes place on the Ce (metal) ions over a narrow and specific range of oxygen partial pressures[23]. The primary role of the CeO₂ is to maintain the local partial pressure by the reaction



The reason that nanoceria is so successful at catalysis is that CeO₂ nanocrystallites have a very high OSC compared to other heterogeneous catalysts for the same NO_x reduction and CO oxidation[24]. Nanoceria's high OSC makes it a powerful catalyst for the oxidation-reduction (redox) catalytic process.

In this thesis, my goal was not to focus on the reaction pathways to understand the catalysis. Instead, I used the redox mechanism as a probe to understand the impact of lattice and surface oxygen on the magnetism of metal oxide nanoparticles.

1.7 Progress and Open Questions

Magnetism in nanoscale oxide systems differs significantly compared to that of their corresponding bulk oxides[25]. These differences arise mainly due to the dimensions being comparable to the size of the magnetic domains, the reduced atomic coordination number at the surface, and broken exchange bonds at the surface. Unlike bulk systems, at the nanoscale the majority of the atoms can be located on the surface.

Nanoscale spinel oxides, especially those containing transition metal ions Fe, Co, Cu, Cr, Mn, or Ni, have shown applications in the field of information technology for data storage, magnetic sensing, and electronics for spintronic devices[26]. Spinel oxides are briefly described as AB_2O_4 , where metal A occupies centres of tetrahedral (T_d) sites and metal B occupies centres of octahedral O_h positions. Based on the cation distributions, spinels are classified into three different groups: normal, inverse, and mixed spinels. A more convenient format to distinguish spinels is $(A_\lambda B_{1-\lambda})[A_\lambda B_{2-\lambda}]O_4$, where () and [] refers to T_d and O_h sites respectively; $\lambda = 0$ is regarded as “normal” spinel, $\lambda = 1$ is the “inverse” spinel, and $0 < \lambda < 1$ is the “mixed” spinel[26]. Several factors affect the cation distributions in spinels such as cation radius, Coulomb interaction between the cations, and crystal field effects of the cations. Any subtle changes in these factors impact the stoichiometry and cause significant changes in the properties of the magnetism[26]. Oxygen vacancy defects on the surface of these nanoscale spinel oxides are majorly responsible for the non-stoichiometry. In a wide class of nanoscale spinel oxides, it has been shown that oxygen vacancies play a fundamental role in tuning the magnetism. For example, $Co_{0.5}Cu_{0.5}Fe_2O_4$ nanoparticles calcined at different temperatures (450 – 600 °C range) showed changes in the crystallinity/oxygen vacancies and impacted the magnetic saturation (M_S)[27]. Similarly, $NiFe_2O_4$ spinels that were prepared using pulsed laser deposition with different oxygen partial pressures (0.2×10^{-6} Torr to 500 mTorr) showed reduction in oxygen vacancies and strengthened exchange interactions between $Fe^{3+} - O^{2-} - Fe^{3+}$ [28]. Authors showed that oxygen vacancies are possibly responsible for the higher M_S . Additionally, studies on $MnFe_2O_4$, $CuFe_2O_4$, and $CoFe_2O_4$ thin films reported that oxygen

vacancies led to a large change in the coercivity[29; 30; 31], speaking to changes in the spin-orbit coupling mechanisms and superexchange through the lattice oxygen. Density functional studies with on-site Hubbard U calculations on $\text{Ni}_x\text{Co}_{3-x}\text{O}_4$ ($0 < x < 1$) showed that Ni and $\text{Co}(T_d)$ $3d$ states hybridized with oxygen $2p$ orbitals. It was also been predicted that oxygen vacancies occur more frequently at sites coordinated to a larger number of Ni ions[32]. As discussed above, oxygen vacancies defects and non-stoichiometry are strongly connected where charge imbalance due to the oxygen vacancies are compensated by the mixed valence ions (contain ions of the same element in two different formal states of oxidations). One of the open questions in these systems is how is the magnetism is affected in the stoichiometric (O_2 rich) and non-stoichiometric (O_2 deficient) environments (so far the reported literature studies are in the *ex-situ* conditions)⁷.

Nanoscale CeO_2 (nanoceria) is another mixed valence system (exists in Ce^{3+} and Ce^{4+} oxidation states). Unlike the nanoscale spinels oxides that are d electron rich, nanoceria is a d^0 system. Ferromagnetism at room temperature is usually found in materials rich in $3d$ electrons[33]. In oxides, their spontaneous magnetic order is due to exchange interactions that involve unpaired electrons in their $3d$ shells. Very few oxides order ferromagnetically with $T_C > 500$ K. At the beginning of 21st century a new class of magnetic materials were discovered, known as dilute magnetic oxides. Dilute magnetic oxides garnered special attention from physicists because of the surprisingly ferromagnetic-like response even without magnetic cations (also known as d^0 magnets). Thin films of the oxides TiO_2 , HfO_2 , In_2O_3 , MgO , ZnO and Cu_2O are some early examples that showed d^0 magnetism[34]. Later, nanoparticles

⁷The experimental setup details for the *in-situ* magnetometry are discussed in Chapter 2

of oxides such as CeO_2 , Al_2O_3 , ZnO , In_2O_3 , and SnO_2 all showed a ferromagnetic-like response at room temperature, and the magnetism was removed when the samples were sintered[35]. This indicated that d^0 magnetism could be from surface oxygen vacancy defects. Nanoscale CeO_2 (nanoceria) is considered a prototypical system for studying d^0 magnetism due to the ability to synthesize phase pure nanostructures with different shapes[24], thin films[36], and straight-forward doping with nonmagnetic cations[34]. The physics of the origin of this ferromagnetism has been enigmatic. At first, the magnetism was attributed to the most obvious candidate, exchange interactions between localized electron spin moments resulting from the oxygen vacancies [37]; first-principles calculations revealed that the vacancies (especially those at the surface) could induce magnetic moments in nanoceria[38; 39]. Later, the ferromagnetism was attributed to only sub-20 nm nanoceria with no obvious dependence on oxygen vacancies[40]. Others reported that mixed valence $\text{Ce}^{3+}/\text{Ce}^{4+}$ pairs on the surface were responsible[41]. Recently, a model based on a giant orbital paramagnetism phenomenon[42] that occurs in a mesoscopic quasi-two-dimensional configuration with dilute magnetically active sites has been proposed. Despite d^0 behaviour in nanoceria being widely reproducible[43; 37; 40; 38; 44; 45; 46; 42; 33], an understanding of the physics behind the nanomagnetism with the defects, disorder and non-stoichiometry is still lacking. In this thesis, one of our primary goals is to focus on the fundamental problem related to identifying the origin of the magnetism in nanoceria and ascertaining the mechanisms that affect the magnetic properties. We use local probes of the electronic structure and magnetism (x-ray spectroscopy and Mössbauer spectroscopy) combined with conventional magnetometry to provide in-

sights into the underlying physics. Although there are earlier reports on the element specific magnetism of nanoceria[45; 46; 47], because of the weak x-ray magnetic circular dichroism signal, explicit evidence of the spin and orbital contributions to the magnetic moments of the Ce $4f$ states were still lacking and no quantitative analysis had been done. Using electronic structure, surface and bulk magnetism measurements and simulations we unambiguously demonstrate that vacancy orbitals (V_{orb}), Ce $4f$ – O $2p$ hybridization, and their effect on the Ce³⁺ spin and orbital angular momenta are fundamental to understanding the origins of the long range ferromagnetic order.

1.8 Organization

The organization of this thesis is as follows. This introduction provided a brief description of the magnetic interactions, hybridization, and heterogeneous catalysis concepts. Chapter 2 describes the experimental techniques that were used to identify the structure, composition, and magnetism of the systems that were studied in this thesis. Chapter 3 presents how oxygen rich and oxygen deficient magnetism plays a key role in understanding the d electron rich nanosystems such as Fe₃O₄ and CoFe₂O₄ nanocrystallites. Chapter 4 presents oxygen rich and oxygen deficient magnetism of CeO₂ nanoshapes and how surface defects impact the magnetism in d^0 systems. Chapter 5 presents electronic structure and magnetism studies of d electron rich and d^0 systems and give insights into the orbital hybridization role in the ferromagnetism. Chapter 6 presents a summary for the results and provides a discussion of the role of the vacancy orbitals and hybridization in understanding the origin of ferromagnetism. Conclusions and propositions for future work are provided in Chapter 7.

Chapter 2

Experimental Methods

To understand the role of orbital hybridization in the magnetism of nanoscale oxides, complementary experimental techniques were used to gain a fundamental understanding of the structure, composition and magnetism. Phase purity, morphology, the average crystallite sizes and specific surface areas were identified by powder x-ray diffraction, transmission electron microscopy, high-angular annular diffraction field images, and Brunauer – Emmett – Teller analysis. Inductively coupled plasma optical emission spectroscopy was used to identify the composition of surface decorated ions. Electronic structure, local environments, and element sensitive magnetism of the nanocrystallites were probed using soft and hard x-ray absorption spectroscopy and x-ray magnetic circular dichroism techniques. The overall contribution to the magnetism was identified using a superconducting quantum interference device (SQUID) magnetometry and susceptometry. Further, the local environment of Fe ions and their contribution to the magnetism was probed by Mössbauer spectroscopy. In this chapter, the experimental methods used to investigate the surface and bulk properties of the nanocrystallites are discussed.

2.1 Synthesis of Nanoparticles

2.1.1 Synthesis of Fe_3O_4 and CoFe_2O_4 nanoparticles

The commercial spinel oxide nanoparticles Fe_3O_4 and CoFe_2O_4 were obtained from our collaborators at Toyota. Samples were brought from Sigma Aldrich and sintered at 400 °C for four hours by Dr. Charles A. Roberts's research group.

2.1.2 Synthesis of CeO₂ nanoshapes

Nanoscale CeO₂ (nanoceria) shapes studied in this thesis were synthesized by Prof. Justin M. Notestein's research group at Northwestern University. All reagents were obtained from Sigma-Aldrich and used as received. Water was purified to 18 MΩ-cm resistivity by a Barnstead NanoPure system.

Ceria nanocubes were synthesized following a previously reported method [48; 49]. 2.0 mmol of Ce(NO₃)₃ · 6H₂O was dissolved in 5 mL water, mixed with 35 mL of 5 M NaOH, and stirred in a Teflon container for 30 minutes. The Teflon container was put in a stainless steel autoclave and heated for 24 h at 180 °C in an electric oven. The snow-white solid was separated by centrifuge and washed with alternating water and ethanol three times. Nanocubes were dried overnight at 70 °C in air. Their color remained white after drying. Total yield was 0.26 g (76%).

The synthesis of ceria nanorods was based on a previously reported microwave hydrothermal method [50]. 41.9 mmol of cerium (III) nitrate hexahydrate (Ce(NO₃)₃ · 6H₂O, 99.9% purity) was dissolved in 105 mL water, the solution mixed with 105 mL of 5 M sodium hydroxide (NaOH), stirred for 30 minutes, and split evenly into four Teflon containers. The containers were heated in a Milestone EthosEZ Microwave at 10 °C/min to 160 °C, held at 160 °C for 1 hour, and cooled to room temperature. A light purple solid was separated by centrifuge and washed with alternating water and ethanol three times. Nanorods were dried overnight at 70 °C in air, and became yellow after drying. Total yield was 7.07 g (98% yield).

The synthesis of ceria nanospheres was based on a previously reported microwave hydrothermal method [50; 51]. 5.0 mmol of cerium (IV) ammonium nitrate

$((\text{NH}_4)_2\text{Ce}(\text{NO}_3)_6$, 98.5% purity) was dissolved in 25 mL water, mixed with 25 mL of 5 M NaOH in a Teflon container and stirred for 3 hours. The container was heated in a Milestone EthosEZ Microwave at 10 °C/min to 100 °C, held at 100 °C for 10 minutes, and cooled to room temperature. The creamy yellow solids were separated by centrifuge and washed with alternating DI water and ethanol three times. Nanospheres were dried at 70 °C in air overnight, and stayed light yellow after drying. Total yield was 0.91 g (106% yield, indicating a small amount of retained surface water or ethanol, as expected from the high surface areas).

2.1.3 Synthesis of CeO_2 nanoparticles

The commercial CeO_2 nanocrystallites were obtained from C. I. Kasei Co., Ltd., NanoTek powder company.

2.1.4 Synthesis of Fe and Co decorated nanoparticles

The Fe and Co decorated nanoparticles were prepared by Dr. Charles A. Roberts's research group at Toyota Motor Engineering and Manufacturing North America Incorporated using incipient wetness impregnation of an aqueous solution with varying concentrations of $\text{Fe}(\text{NO}_3)_3 \cdot 9\text{H}_2\text{O}$ (Sigma-Aldrich, 99.99%) or $\text{Co}(\text{NO}_3)_2 \cdot 6\text{H}_2\text{O}$ (Sigma-Aldrich, 99.99%) onto a nonporous CeO_2 supports with an as-received specific surface area of 55 m^2/g as described in Refs. [52; 53].

2.2 X-ray Diffraction

In a crystal lattice, x-ray diffraction occurs when the photons are scattered from a periodic array of atoms with long-range order, generating constructive interference at a specific incident angle. Bragg's law gives the condition for maximum intensity:

$$n\lambda = 2d\sin\theta \quad (2.1)$$

where n is an integer, λ is the wavelength of x-rays, d is the distance between planes, θ is the angle of diffraction. A geometric argument can be used to derive Bragg's law. Figure 2.1 shows the paths of 1, 2, 3, and 4 are parallel in the regions of SX and YD. We assume that the distance from the source (SX) and detector paths (YD) is large compared to the interplanar spacing d of the sample. The angle of incidence is congruent to all angles marked in Fig. 2.1 and the difference in path length XY for paths as $2d\sin\theta$. Similarly, the path difference between 1 and 3, 1 and 4 are $4d\sin\theta$ and $6d\sin\theta$ respectively. Assuming that two photons starting at source S, the condition for constructive interference at detector D is that the path difference XY is an integer number of wavelengths, or $n\lambda = 2d\sin\theta$.

The measured intensity as a function of the angle between scattered angle and the forward direction of the incident beam (2θ) gives information on the spacing between lattice planes and positions of atoms within the unit cell. In a crystal lattice, the relative intensity of diffraction patterns are mainly governed by the structure factor $F(hkl)$ given by^[54]

$$F(hkl) = \sum_1^N f_n \exp[2\pi i(hx_n + ky_n + lz_n)] \quad (2.2)$$

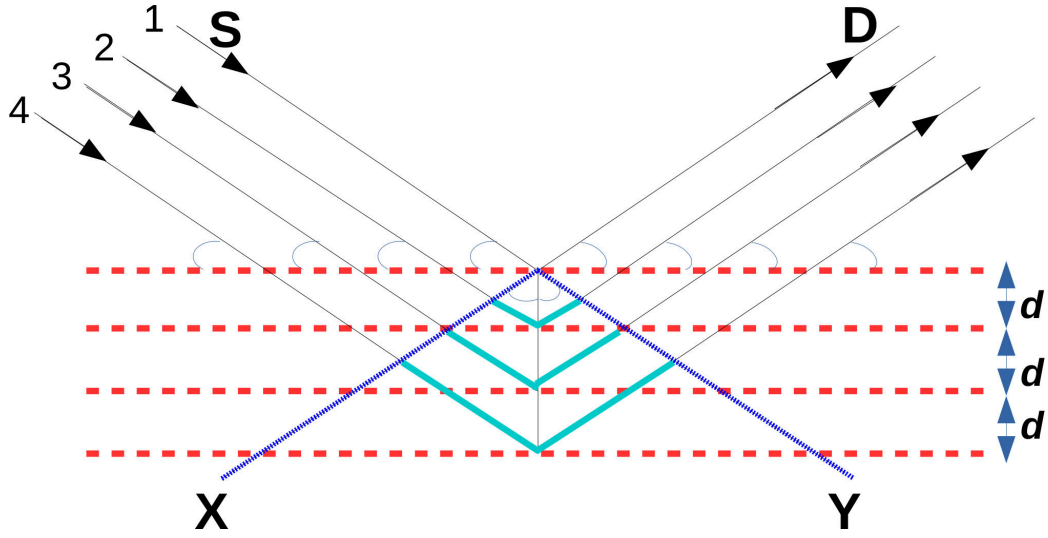


Figure 2.1: Geometric diagram of Bragg diffraction by adjacent planes. X-ray originating from the source and reaching the detect are shown.

where h, k, l are the Miller indices of scattering plane, and x_n, y_n, z_n are the coordinates of atoms expressed as fractions of the base vectors a, b, c of the unit cell. Here f_n (atomic scattering factor) is a measure for the ability of an atom to scatter x-rays relative to that of a single electron. The measured intensity is directly proportional to $|F(hkl)|^2$.

In this work, x-ray diffraction analysis was performed on all powder samples under ambient conditions using a Bruker D8 DaVinci with a Cu K_α x-ray source. The geometry is Bragg-Brentano in which incident angle θ_i is always half of the diffracted angle 2θ as shown in figure 2.2. X-rays are generated by an x-ray tube, where the tube consists of the cathode (tungsten filament), an anode (metal target) and Beryllium windows. For the generation of x-rays, high voltages and tube currents are required; typically we used 40 kV and 40 mA. When accelerated electrons collide with atoms of the metal target, because of the Cu anode metal characteristic x-rays K_α and K_β

x-rays are generated on a continuous background of Bremsstrahlung radiation. The emerged x-ray are channeled through primary and secondary optics to enhance the x-ray diffraction pattern quality. Primary and secondary optics consist of manual slits, filters, and Soller slits as shown in figure 2.2. For all the measurements presented in this thesis, primary optics consisted of 0.1 mm slit width, no filter; whereas secondary optics consisted of 5 mm slit width, Ni K_β filter. Soller slits were used for reducing the axial divergence of the x-ray beam and the Ni K_β filter used on secondary optics attenuated the Cu K_β x-rays. For the x-ray powder diffraction, we used a Si-based LYNXEYE 1-D detector. The active area of the detector is 14.4 mm by 16 mm, and 192 strips of the sensor acts as an individual detector. This detector allows operation at much higher count rates compared to gaseous detectors. We have used lower level (LL) = 0.11 V and upper level (UL) = 0.19 V for all measurements. A knife edge over the sample was used on a rotation stage to reduce air scattering.

All patterns were collected on dried nanoparticles on a zero-background quartz slide with an instrument resolution of 0.02° . X-ray diffraction patterns were analysed using full pattern Rietveld refinements[55] to identify the lattice constant, crystallite size, and any preferred orientation that is present. In Rietveld refinements, the best set of the parameters mentioned above are obtained by an iterative least square method that minimizes the difference between calculated and experimental diffraction patterns.

In Rietveld refinements, a structural model is required and $F(hkl)$ (see equation 2.2) is calculated from this model. For all the x-ray diffraction pattern refinements, a preliminary idea about the structural model is given by a diffraction pattern sourced

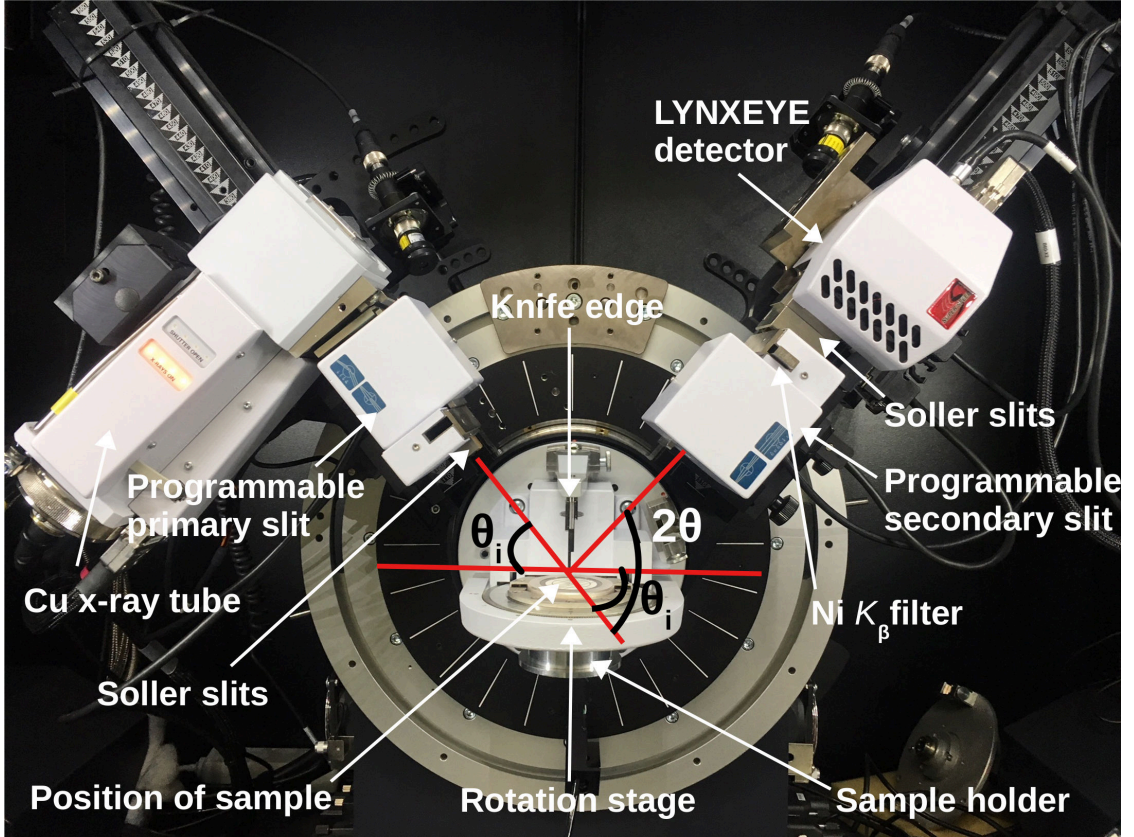


Figure 2.2: Bruker D8 DaVinci diffractometer using a Bragg-Brentano geometry. Components corresponding to the source and detector arms are shown.

from the Pearson's Crystal Structure Database[56]. In Rietveld refinement of powder diffraction patterns the intensity obtained at i -th step ($y_{obs(i)}$) is compared with corresponding intensity calculated by the modelling $y_{calc(i)}$. Here $y_{calc(i)}$ is obtained by summing the contribution from neighboring Bragg reflections plus background:

$$y_{calc(i)} = \sum_{\varphi} S_{\varphi} \sum_h I_{\varphi,h} \Omega(T_i - T_{\varphi,h}) + y_{bkg(i)} \quad (2.3)$$

here h labels the Bragg reflections and φ labels the phase (can vary from 1 to number of existing crystal structure phases), S_{φ} is the scale factor of phase φ , $\Omega(T_i - T_{\varphi,h})$ is the reflection profile function that models both instrumental and sample broadening

effects. In FullProf[55] $I_{\varphi,h}$ is the integrated intensity, and it depends on several factors that are described below. The general expression of $I_{\varphi,h}$ is[55]

$$I_{\varphi,h} = \left(L A P C F^2 \right)_{\varphi,h} \quad (2.4)$$

for a specific phase φ , the intensity I_h depends on Lorentz-polarization multiplicity factor for reflection (L_h), absorption correction (A_h), preferred orientation (P_h), specific corrections such as non-linearity (C_h), and structure factor (F_h). The Rietveld method minimizes the weight squared difference between observed and calculated patterns by

$$\chi^2 = \sum_i^n w_i \left(y_{obs(i)} - y_{calc(i)} \right)^2 \quad (2.5)$$

where the weights of the observations are calculated as

$$w_i = \frac{1}{\sigma_i^2} = \frac{1}{\sigma_{peak(i)}^2 + \sigma_{bkg(i)}^2} \quad (2.6)$$

$\sigma_{peak(i)}$ is the standard deviation associated with the Bragg peak and $\sigma_{bkg(i)}$ is that associated with background intensity $y_{bkg(i)}$. Another important parameter for the refinement is peak shape function. For determining nanocrystallites size and strain refinements the peak profiles are described by Thompson-Cox-Hastings pseudo-Voigt function[57]. Pseudo-Voigt is a simple approximation to the convolution of Gaussian and Lorentzian functions. The Full Width Half Maximum (FWHM) of the Gaussian and Lorentzian components of the peak depends on angle (θ):

$$\Gamma_G^2 = U \cdot \tan^2\theta + V \cdot \tan\theta + W + \frac{I_G}{\cos^2\theta} \quad (2.7)$$

$$\Gamma_L = X \cdot \tan\theta + \frac{Y}{\cos\theta} \quad (2.8)$$

here U , V , and W are the instrument broadening parameters¹ and I_G is Gaussian profile parameter. The remaining parameters X and Y are related to the strain and size, respectively. The volume-weighted average size can be calculated using the Scherrer formula:

$$\langle D \rangle = \frac{K \cdot \lambda}{\Gamma \cdot \cos\theta} \quad (2.9)$$

where K is Scherrer[58] constant (for spherical particles K is 0.94), λ is the wavelength of x-rays, and Γ is the FWHM. For Thompson-Cox-Hastings the FWHM is calculated as[57]:

$$\Gamma = (\Gamma_G^5 + 2.69269\Gamma_G^4\Gamma_L + 2.42843\Gamma_G^3\Gamma_L^2 + 4.47163\Gamma_G^2\Gamma_L^3 + 0.07842\Gamma_G\Gamma_L^4 + \Gamma_L^5)^{1/5} \quad (2.10)$$

XRD patterns presented in the thesis were refined using FullProf Suite. However, for CeO₂ nanoshapes preferred orientation² of the lattice planes and their fractions were quantified using GSAS-II[59].

2.3 Transmission Electron Microscopy

Transmission electron microscopy (TEM) provides information about the morphology and internal structure of nanocrystallites. In a TEM a high energy beam of electrons (~ 200 keV) is incident on the sample. During this process, the electrons interact with the sample giving rise to signals containing information about the internal structure, lattice spacing, and morphology. Lattice fringes observed are an example of interfer-

¹These values are obtained by refining a standard XRD pattern e.g. BaF₂

²In GSAS program EXPGUI (Graphical User Interface) is very intuitive, and it allows refinement of a preferred-orientation parameter concerning a specific crystallographic vector based on the March-Dollase model

ence between incident and diffracted beam that is observed in high-resolution TEM images. Analogous to a conventional optical microscope a TEM consists of an illumination stage, specimen system, and imaging stage. A schematic diagram showing the TEM optical components are shown in figure 2.3. The illumination stage consists of an electron source, acceleration column and condenser lenses. The primary role of the illumination stage is to project the electron beam on a specimen sample, and the condenser lenses provide a parallel beam of convergent electrons at the sample. The electron beam interacts with the sample, and the transmitted beam is collected by a charge coupled device detector.

Prof. Justin M. Notestein's group collected TEM images of the CeO₂ nanoshapes (cubes, rods, spheres) at the EPIC facility of the NUANCE Center at Northwestern University using a JEOL-2100F (0.16 nm resolution and 0.92 eV energy resolution). CeO₂ commercial nanoparticles and Fe dispersed on CeO₂ nanoparticles TEM and high-angular annular diffraction field images were collected by Dr. Abdul Khan at the Manitoba Institute for Materials facility of the University of Manitoba using the FEI Talos F200X transmission electron microscopy. Nanocrystallites were dispersed in ethanol and sonicated for 30 min. The resulting suspension was pipetted on to a Cu-coated holey carbon grid and dried overnight at room temperature. TEM and electron diffraction data were taken at a 200 kV accelerating voltage, 140 μ A emission, and 0.5 Å probe size.

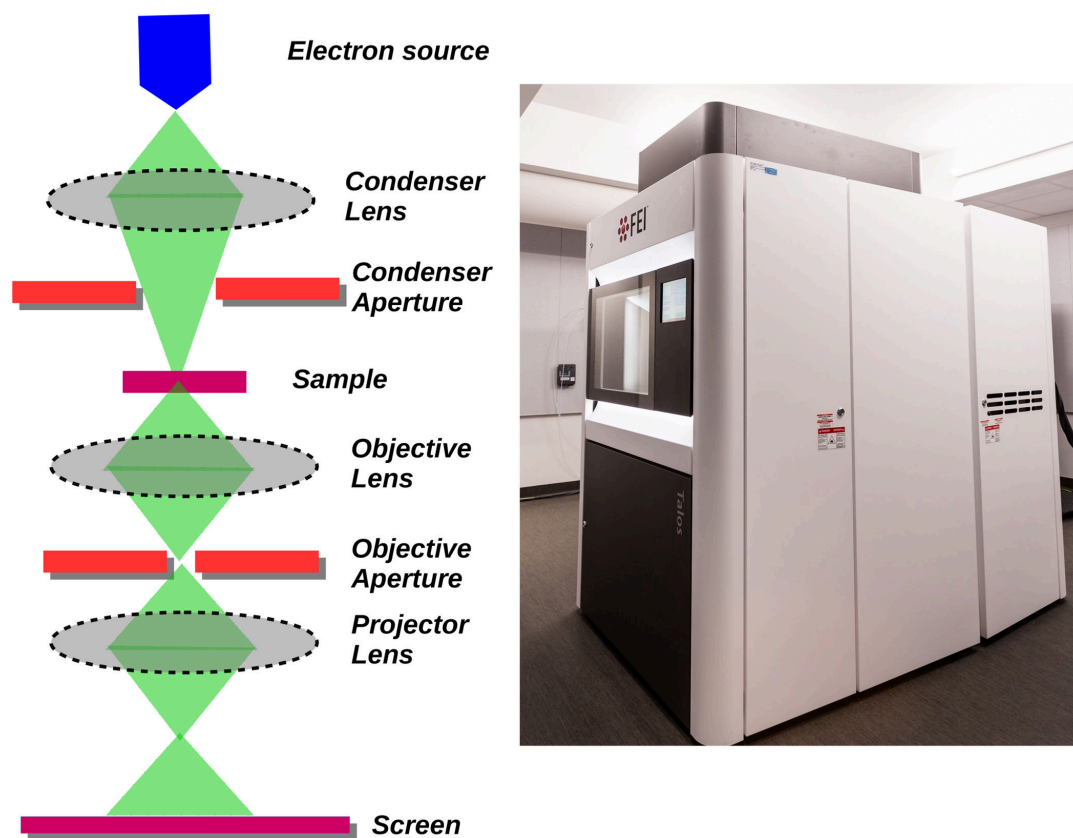


Figure 2.3: Left: A layout of optical components in a transmission electron microscopy. Right: FEI Talos F200X transmission electron microscope at Manitoba Institute for Materials. TEM Photo credit: Lief Norman

2.4 Brunauer – Emmett – Teller Analysis

The specific surface area (m^2/g) of all the samples were measured using Brunauer – Emmett – Teller (BET) analysis. The physical adsorption of a gas on the surface of the solid is the basis for the BET theory[60]. BET surface area is calculated by measuring the adsorbate gas corresponding to a monomolecular layer on the surface of a solid. N_2 physisorption isotherms were obtained using a Micrometrics ASAP 2010 instrument. Using the BET equation[60] N_2 physisorption isotherms were utilised

to determine the specific surface areas of all the samples. Before measurements, all the materials were degassed 12 h at < 5 mTorr and 150 °C. All of the BET measurements and analysis was performed by Dr. Charles A. Roberts research group at Toyota Motor Engineering and Manufacturing North America Incorporated, Ann Arbor, Michigan, USA.

2.5 ICP OES

Elemental analysis was performed using a Varian MPX ICP-OES instrument. Samples were prepared by dissolving 50 mg of solids in 1 mL of HF and subsequently diluting to 50 mL with H₂O. Metal contents were quantified by comparison against standards of known concentration[52]. All of the ICP measurements and analysis was performed by Dr. Charles A. Roberts.

2.6 Activity Measurements

Steady-state catalytic activities were measured using a fixed bed quartz tubular reactor with temperature and gas flow control. The reactor was loaded with 50 mg of catalyst powder that was mixed with quartz sand as a diluent in order to achieve a constant gas hourly space velocity (GHSV) of $\sim 15,000$ hr⁻¹. The catalyst was first pretreated in 30 sccm of 10% O₂/He at 500°C for 30 min, and then cooled in flowing UHP He. The reduction of NO by CO was monitored at 300°C and 350 °C for 45 min each at a total flow rate of 100 sccm with a stoichiometric composition of 4000 ppm NO, 4000 ppm CO, 8000 ppm Ar, and He balance. Mass spectrometry of the gas phase product stream was obtained continuously using a quadrupole mass spectrome-

ter (MKS Instruments, Inc. Cirrus-2). The Ar present in the reactant stream acted as tracer of constant concentration and the Ar signal at $m/z = 40$ was used to normalize each of the mass spectrum traces.

The 100% and 0% conversion of NO was defined as the normalized mass spectrum intensity at $m/z = 30$ under inert flow, and under NO+CO reaction mixture flow while bypassing the reactor, respectively. Linear interpolation determined the resulting NO conversions at steady-state temperatures. Rates ($\mu\text{mol NO/s}$) at 350°C were calculated from differential NO conversions ($\leq 15\%$). Mass-normalized activity ($\mu\text{mol NO/g/s}$) and SSA-normalized activity ($\mu\text{mol NO/m}^2/\text{s}$) were calculated using the mass of catalyst and the BET-determined specific surface area, respectively[52]. All of the catalytic activity measurements and analysis was performed by Dr. Charles A. Roberts.

2.7 X-ray Spectroscopy

X-ray spectroscopy provides unambiguous detection of magnetic species in a multi-element system, as well as identification of oxidation state, site symmetry, and quantitative information of the local environment. Element specificity is at the heart of the x-ray spectroscopy measurements, because of the absorption coefficient $\mu(E) \propto Z^4$, where Z is the atomic number. Due to the Z^4 dependence of $\mu(E)$ a strong contrast is observed between different elements of the periodic table by adjusting the x-ray energies.

As a result of the absorption resonances near the $1s$ to $3d$, $1s$ to $2p$, $3p$ to $3d$, and $3d$ to $4f$ transitions, soft (~ 0.5 keV to 3.0 keV) and hard (~ 3.0 keV to 50 keV) x-ray

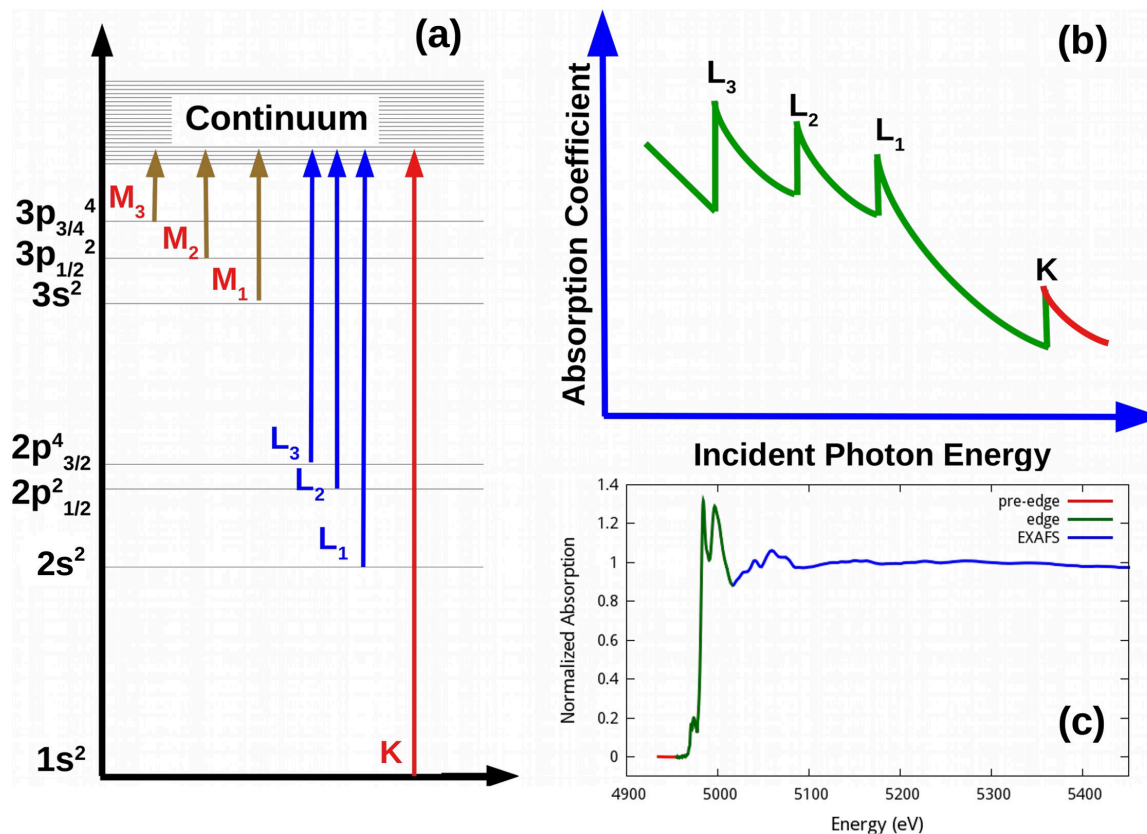


Figure 2.4: (a) Schematic of the excitations corresponding to the K, $L_{3,2,1}$, and $M_{3,2,1}$ are shown and the arrows are indicative of energy differences. (b) X-ray absorption as a function of incident photon energy with four different edges are shown (K, $L_{3,2,1}$). (c) The three different regions: pre-edge, edge, and EXAFS oscillations are shown[61].

probes are ideal for the transition and rare-earth metal oxides. In this thesis soft x-ray absorption spectroscopy (XAS) and x-ray magnetic circular dichroism (XMCD) measurements were performed at the 4-ID-C sector and x-ray absorption near edge spectroscopy (XANES) and extended x-ray absorption near edge spectroscopy (EXAFS) at 20-BM-B and 20-ID-B,C sectors at the Advanced Photon Source located within Argonne National Laboratory.

X-ray absorption fine structure (XAFS) refers to the oscillatory nature of the

x-ray absorption coefficient (μ) just above the x-ray absorption edge. In XAFS an edge results when a core electron absorbs energy equal to or greater than its binding energy. The edges are labelled according to the shell the core electron originates from. If the absorption coefficient (μ) is measured as a function of energy E , the experimental spectrum (Fig. 2.4) shows three distinct features: (1) A region with a decrease in $\mu(E)$ as a function of increasing E called the pre-edge; (2) a region with sharp increase in absorption coefficient called the edge; (3) a series of oscillatory wiggles that modulate the $\mu(E)$. The pre-edge feature is illustrative of interactions of photons with electrons, and the edge is a unique feature to the absorbing atom and reflects the excitation of core-shell electrons. The edge is due to quantum-mechanical transitions that excite the core electrons to free or unoccupied continuum levels (Fig. 2.4). The oscillatory wiggles above the absorption edge are known as EXAFS and identify the detailed local atomic level information such as the number of neighboring atoms and interatomic distances. The XAFS spectrum is typically divided into two regions (Fig. 2.4c): The x-ray absorption near edge spectra (XANES) and extended x-ray absorption near edge spectra (EXAFS). Note that x-ray absorption fine-structure spectroscopy (XAFS), x-ray absorption near edge spectroscopy (XANES), extended x-ray absorption fine-structure spectroscopy (EXAFS), near-edge x-ray absorption fine structure (NEXAFS) and some other variation of the techniques, all come under the common umbrella of x-ray absorption spectroscopy (XAS). In all these cases variations in the x-ray absorption coefficient are measured as a function of energy, and related to the electronic structure and local environment.

2.7.1 Soft x-ray absorption spectroscopy

The absorption coefficient due to the transition between the initial and final state in an electromagnetic field is proportional to the initial ground state and final excited state of the electron. Transition metal ion $L_{3,2}$ edge XAS excites the $2p$ core electrons, whereas rare earth ions $M_{5,4}$ edge XAS excites the $3d$ core electrons to unoccupied states. Because of the dipole selection rules ($\Delta l = \pm 1$, where l is the orbital angular momentum quantum number) only the s and d states for transition metal ions, and p and f states are allowed for rare earth ions. One of the primary reasons behind the compatibility of the XAS technique to study the electronic structure and magnetism of transition metal and rare earth compounds is their electrons are well localised. Because of the localization, in transition metal ions there is a strong overlap of the $2p$ core wavefunction containing an unpaired electron and the $3d$ valence wavefunction. Additionally, Coulomb and exchange interaction between $3d$ electrons are further responsible for multiplet effects[62].

Several advantages come naturally with the dominance of multiplet effects. Even though the number of d and f electrons is the same, due to the change in the increase in the repulsion factor between the nucleus and electrons the multiplet features are revealed. Figure 2.5a shows the simulated³ XAS spectra (using Xclaim: A graphical interface for the calculation of core-hole spectroscopies[63]) of Co^{4+} , Fe^{3+} , and Mn^{2+} . The spectral shapes are the same (d electron count) and spin-orbit coupling effects get stronger as the atomic number increases. For transition metal ions if we keep the number of d electrons constant, with a change in the local coordination we see

³10 $Dq = 1.0$ for O_h and Slater integrals are scaled to 80% of Hartree-Fock values

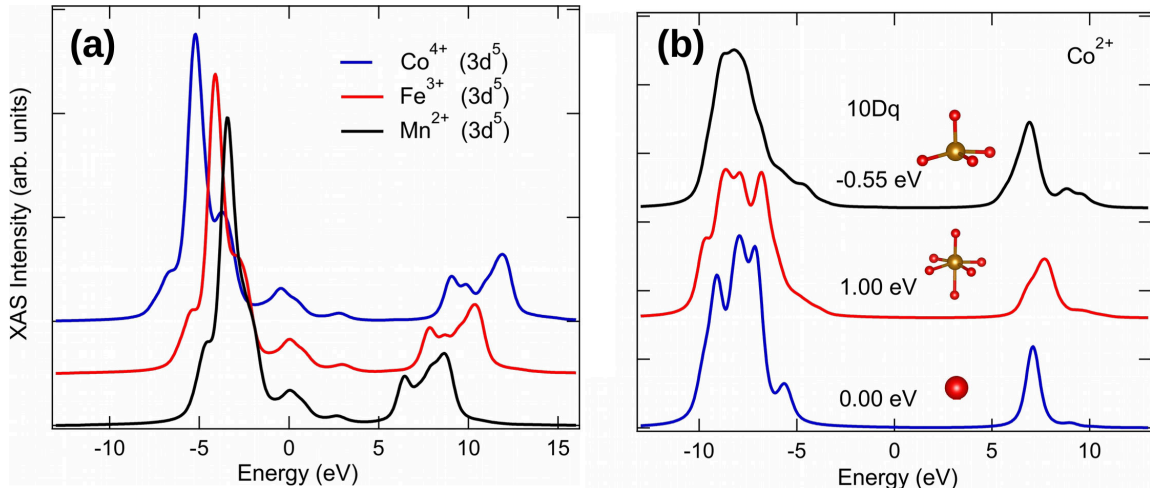


Figure 2.5: (a) The impact of spin-orbit coupling on the spectra is shown. For Co^{4+} , Fe^{3+} , and Mn^{2+} the d electron count are the same, and the atomic number (Z) changes. The spectra are spread out with an increase in Z , due to strong repulsion effects between nuclear charge. (b) Spectral line shapes of Co^{2+} ions in three different environments (isolated, octahedral and tetrahedral) is shown. Figure evidence that XAS spectra is strongly dependent on the crystal field environment ($10Dq$) of an atom. For comparison purposes energies are shifted to 0 eV and binding energies are not taken into account.

changes in the spectral shapes as shown in figure 2.5b. They indicate that XAS spectral shapes are also governed by the crystal fields produced by the neighboring ligands. Due to the smaller atomic radii of the rare-earths, the crystal field effects are negligible. However, hybridization with the ligands plays a significant role as we discuss in Chapter 5.

In this thesis soft x-ray absorption spectroscopy simulations were performed using CTM4XAS5.5[62] and Xclaim[63]. In an x-ray spectroscopy measurement monochromatic x-rays cause a transition from initial state $|i\rangle$ to final state $|f\rangle$. For a one-photon (where the photon is absorbed) process using Fermi's golden rule the transition prob-

ability is given as

$$I(\omega) = \sum_f |\langle f|T|i\rangle|^2 \delta(E_f - E_i - \hbar\omega) \quad (2.11)$$

where E_i and E_f are the energies of the initial $|i\rangle$ and final states $|f\rangle$, respectively; $\hbar\omega$ is the incident energy, T is the transition operator (e.g. dipole transition $T = \vec{\epsilon} \cdot \vec{r}$). For core-level excitations equation 2.11 can be reexpressed as the Green's function of the final state[63]

$$I(\omega) = -\frac{1}{\pi} \text{Im} \langle i|T^\dagger \frac{1}{E_i + \hbar\omega - H_f + i\Gamma} T|i\rangle \quad (2.12)$$

Γ is the broadening due to the lifetime of the core-hole, in the calculation first the lowest-energy eigenstate $|i\rangle$ of the initial-state Hamiltonian is obtained and the Green's function of the final-state Hamiltonian is calculated by using a continued fraction expansion[63].

To gain atomic level insights into the materials studied in the thesis, spectra were modelled using a Hamiltonian approach. Three different terms are included

$$H = H_{atomic} + H_{CF} + H_{hybridization}. \quad (2.13)$$

For atomic model the Hamiltonian of central atom (H_{atomic}) takes the form

$$H_{atomic} = H_{ke} + H_{n-e} + H_{e-e} + H_{so} \quad (2.14)$$

$$= \sum_i \frac{\vec{p}_i^2}{2m} - \sum_i \frac{Ze^2}{r_i} + \sum_{i<j} \frac{e^2}{|r_i - r_j|} + \sum_i \xi(r_i) \vec{l}_i \cdot \vec{s}_i \quad (2.15)$$

where the indices i and j run over all electrons of the ion. The four terms represent electron kinetic energy (\vec{p}_i is the momentum and m of electrons respectively), nucleus-electron energy (potential energy of nucleus, Z is the atomic number), electron-electron energy (Coulomb interaction between electrons), and spin-orbit coupling

($\xi(r_i)$ is the radial part of spin-orbit interaction, \vec{l}_i and \vec{s}_i are the orbital and spin momentum operators).

In 3d transition materials, beyond the atomic model crystal field effects (H_{CF}) are introduced to understand solid-state phenomena. An atom in a solid is modelled considering neighboring atoms as point charges. The effect of crystal field is to lower the symmetry by splitting of the states that are obtained in a spherical symmetry. For crystal field effects the Hamiltonian takes the form

$$H_{CF} = -eV(\vec{r}) \quad (2.16)$$

where e is charge of electron and V is the potential.

The inclusion of crystal field effects lead to satisfactory explanation of spectral line shapes in x-ray absorption spectroscopy for ionic compounds. However, for strongly covalent materials as shown in Chapter 5 such an interpretation fails and the charge transfer from ligands need to be included explicitly. The final term in equation 2.13 describes the hybridization of a central ion with the surrounding ligands. The hybridization term is written as[63]

$$H_{hybridization} = \sum_{\Gamma_\gamma} T_{dL}(\Gamma)(d_\gamma^\dagger L_\gamma + L_\gamma^\dagger d_\gamma) + \sum_{\Gamma_\gamma} \epsilon_L(\Gamma) L_\gamma^\dagger L_\gamma \quad (2.17)$$

$\epsilon_L(\Gamma)$ is the energy of electrons in the ligand shell (L). d_γ^\dagger and L_γ^\dagger are the creation operators of an electron in the d and ligand shells. $T_{dL}(\Gamma)$ are the written in terms of the Slater-Koster parameters[64].

The nature of the ligands such as oxygen in transition metal and rare earth oxides can be probed by soft x-ray absorption spectroscopy. Unlike the transition metal ions ($L_{2,3} : 2p \rightarrow 3d$ transition) and rare earth ions ($M_{4,5} : 3d \rightarrow 4f$ transition),

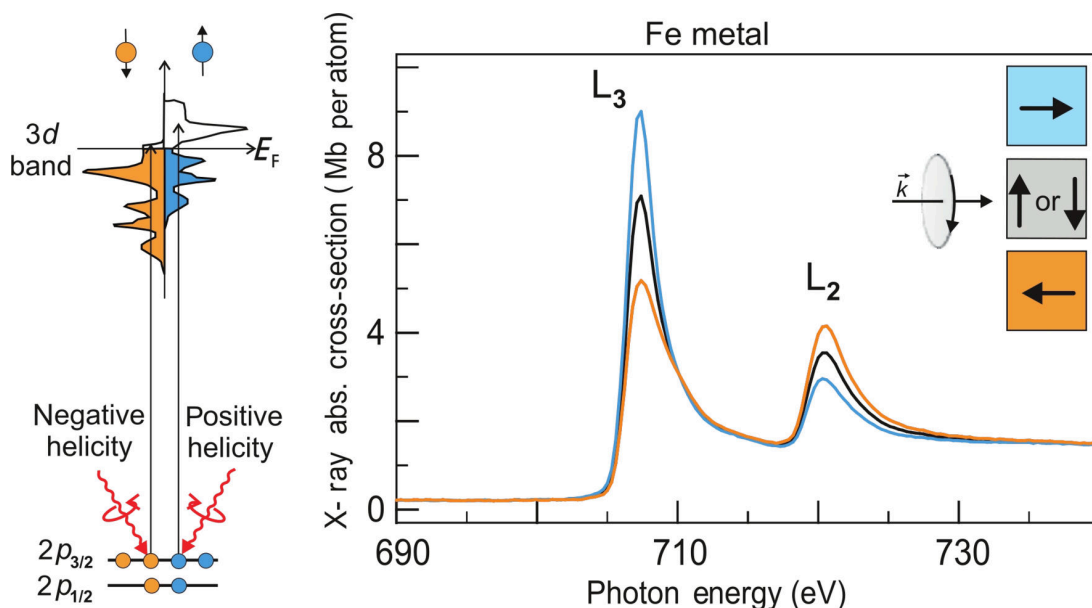


Figure 2.6: XMCD principles illustrated for the case of L edge absorption in a d band Fe metal. When d band is split into spin-up and spin-down with different occupation. The absorbed light of RCP (LCP) excites spin-up (spin-down) electrons with different occupation. Because spin flips are forbidden the measured resonance intensity quantify the empty d band states of a given spin. Reprinted with permission from [65]. Copyright 2006 Springer Science and Business Media.

oxygen K edge excites $1s$ core level into states of primarily $2p$ character. In $L_{2,3}$ and $M_{4,5}$ edges XAS spectra the electrons are mostly localized in character, whereas, for oxygen K edge the $2p$ electrons are delocalized. As a result, the oxygen K edge can be viewed from a single electrons' point of view and provides significant information on the unoccupied density of states of the oxygen $2p$ ligands. Experimental spectra of transition metal oxides O K edge show changes in the $3d$ states splitting into e_g and t_{2g} bands as discussed in Chapter 3. Further, the higher energy region provides information of the O $2p$ states hybridized with the $4s$ and $4p$ states of the transition metal ions.

Synchrotron sources are often considered to be the best choices for the x-ray

spectroscopy measurements because of their high flux and the polarized nature of photons. Depending upon the beamline the transmitted radiation can be linearly polarized or circularly (both right and left) polarized. For right circularly polarised (RCP) mode the electric field (E) rotates clockwise if viewed in the direction of propagation vector (k) and E rotates counter-clockwise if viewed in the direction of k for left circularly polarised light (LCP). RCP (LCP) photons carry an angular momentum of $+\hbar(-\hbar)$. Using this fundamental difference between the RCP and LCP, x-ray magnetic circular dichroism (XMCD) was technique was developed by Schütz et al.[66], as shown figure 2.6 for Fe metal ion. In ferromagnetic metal Fe the $3d$ shell has a magnetic moment due to the imbalance in spin up and spin down electrons below the Fermi energy (E_F) level. The absorption of RCP (LCP) photons excites the spin up (spin down) electrons and transfers the spin or angular momentum, or both. If the photoelectron emerges from a spin-orbit split level such as $2p_{3/2}$, as shown in figure 2.6, the angular momentum of the photon can be transferred to spin through the spin-orbit coupling. In a Fe metal $2p_{3/2}$ (L_3) and $2p_{1/2}$ (L_2) levels have opposite spin-orbit coupling ($l + s$ and $l - s$ respectively), so the spin polarization will be opposite at the two edges. As spin flips are forbidden and $\Delta l = \pm 1$ in the x-ray absorption process, the spin-up (spin-down) photoelectrons from $2p$ core-shell are excited into spin-up (spin-down) $3d$ core hole states. For this reason, probing $2p \rightarrow 3d$ and $3d \rightarrow 4f$ with polarised photons gives valuable information on the magnetic species of transition and rare earth elements by measuring the resonance intensity directly from XMCD measurements. In this thesis for the Fe_3O_4 and CoFe_2O_4 nanoparticles XMCD spectra (Fe and Co $L_{3,2}$ edges), sum rule analysis was performed to quantify

the L_z/S_z , where L_z and S_z are the orbital moment and spin moment. The ratio of orbital to spin moment $L_z/S_z = \frac{2p}{3p-6q}$, where p is the integrated XMCD intensity over the L_3 -edge, and q is the integrated intensity over the L_3 and L_2 -edges[67; 68; 69]. The XMCD measurements were performed at sector 4-ID-C of Argonne National Laboratory.

2.7.2 Hard x-ray absorption spectroscopy

Hard x-ray absorption spectroscopy probe the transition metal ions K edge, rare earths K and L edges, and provides complementary information on the coordination and local environment of absorption species. Rare earth (Ce) and transition-metal K edge spectra (Fe, Co) were acquired in transmission mode from powder samples, and detectors were ionization chamber based. Since the Ce L_2 and L_3 emission lines are close in energy (5262 and 4869 eV, respectively), only Ce L_3 edge spectra were acquired, and analysis was performed. All spectra were analysed using the Athena and Artemis programs[70]. For normalization, a linear fit of the pre-edge line was subtracted from the spectrum, and a fourth-order knot-spline polynomial was used to fit the post-edge line to remove the background contribution. Before the Fourier transforms, the EXAFS was multiplied by a Hanning window⁴. The EXAFS equation, which describes the EXAFS ($c_i(k)$) of a component i as a function of the photoelectron wavevector k , is given by

$$\chi_i(k) = N_i S_0^2 (F_i(k)/kR_i^2) e^{(-2R_i/\lambda(k))} e^{(-2k^2\sigma_i^2)} \sin(2kR_i + \delta_i(k)) \quad (2.18)$$

⁴A window function goes from 0 to 1 and back to 0. Hanning has good frequency resolution and reduced spectral leakage

where $R_i = R_0 + \Delta R$, $k^2 = \frac{2m_e(E-E_0)}{\hbar}$, m_e is the mass of photoelectron and \hbar is reduced Plank's constant; the parameters $F_i(k)$ (effective scattering amplitude), $\delta(k)$ (effective scattering phase shift), $\lambda(k)$ (mean free path length) and R_0 (initial path length) are all calculated using the FEFF[71] program from crystallography data of the rare earth and transition metal oxides under study as well as structural analogues. The parameters N (degeneracy of path), S_0^2 (amplitude reduction factor), E_0 (energy shift), ΔR_0 (change in half-path length) and σ^2 (mean squared displacement) are all fit parameters in Artemis. For all the spectra analyzed in this thesis the amplitude reduction factor S_0^2 was obtained by fitting experimental bulk standards Fe_3O_4 , CoFe_2O_4 , and CeO_2 .

2.7.3 Experiments

Soft or hard x-ray spectroscopy measurements require a very good measure of absorption coefficient ($\mu(E)$). In a nut shell one simply needs an x-ray source and a detector to measure absorption coefficient $\mu(E)$. X-ray sources are usually synchrotron facilities, which provide a full range of x-rays and one use a monochromator made from silicon to select and tune the energies using Bragg diffraction. In addition to monochromator, pre-mono slits are other components used to control the stability, resolution and divergence of the x-ray beam. For the most part, these features are maintained by the beamlines designed for the x-ray experiments. A schematic diagram of x-rays produced from beamlines is shown in figure 2.7. Several factors decide (such as concentration of samples, penetration of x-rays, surface or bulk sensitive interests) what type of measurement mode is best suitable for a set of systems. Below

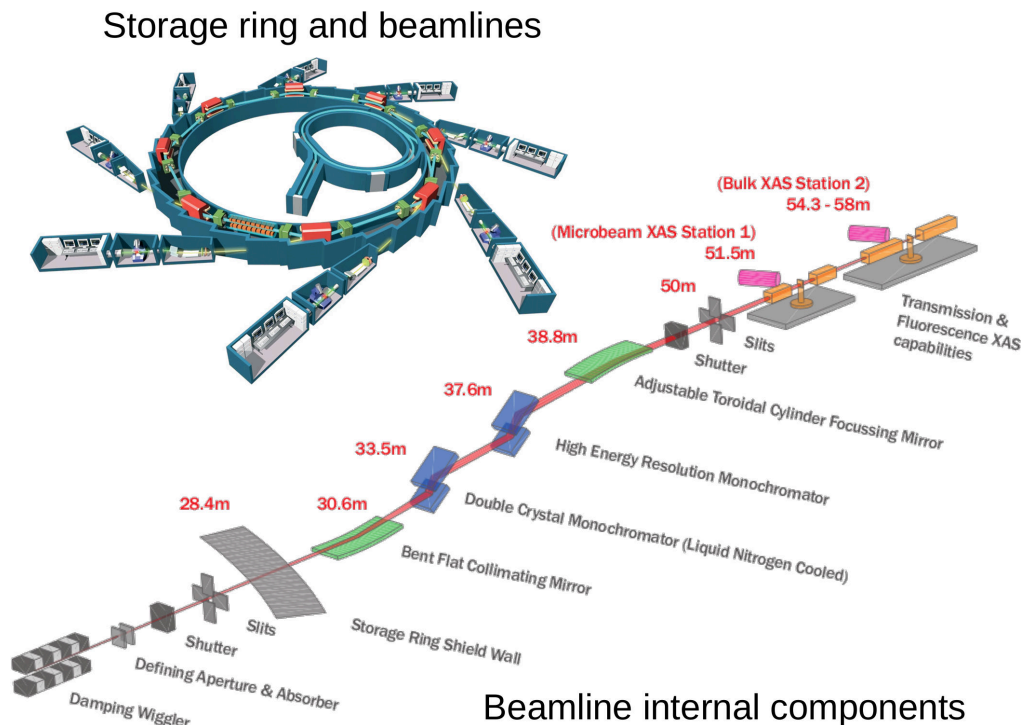


Figure 2.7: A representation of central storage ring and corresponding experimental end stations are shown. Along the ring, magnets are used to steer and confine the beam along a circular track. Each end-station is equipped with optics, sample holders, and detectors to facilitate a particular experiment. Photo by Bruce Ravel/CC BY-SA 3.0 (<https://creativecommons.org/licenses/by-sa/3.0/>).

I will explain three common techniques used in this thesis for $\mu(E)$ measurements.

- Transmission geometry
- Fluorescence geometry
- Total electron yield geometry

2.7.4 The transmission geometry

The transmission geometry is used for concentrated samples where the element of interest is major component (e.g. Ce in CeO_2). Figure 2.8 shows the transmission

geometry experimental setup, in this case photons pass through the sample and the attenuation of photons from the sample is directly measured. The process is simply described by the Beer-Lambert law, described mathematically by

$$I_T = I_0 e^{-\mu(E)t} \quad (2.19)$$

I_T is attenuation of the beam, I_0 is the incident beam, $\mu(E)$ is the energy dependent absorption coefficient, and t is the thickness of the sample. By simply rearranging the equation one can obtain the absorption coefficient as

$$t\mu(E) = \ln\left(\frac{I_0}{I_T}\right). \quad (2.20)$$

In a typical XAS experiment one measures $\mu(E)$. In transmission mode, ion chambers are usually used as detectors. X-rays pass through a parallel plate capacitor filled with an inert gas and a high voltage is applied across. Each photon ionizes many molecules and resulting current is amplified and converted to a voltage. The voltage is converted to measure the intensity of the detector. If a sample is homogeneous, free of pinholes, and the thickness is appropriate, transmission geometry is ideal for all XAS measurements. In this thesis the hard x-ray measurements done on Ce L_3 edge, Fe and Co K edges are all performed using transmission mode. In spite of all the advantages, transmission geometry is not appropriate when $t\mu(E) \gg 1$, then photons cannot penetrate through the sample. Additionally, transmission experiments are not suitable for very dilute samples. For example, in the thesis Fe and Co K edges of Fe-CeO₂ and Co-CeO₂ samples we could not measure XAS spectrum in a transmission geometry because the total absorption in the sample from the resonant element was less than 2%. In such cases the signal to noise ratio from

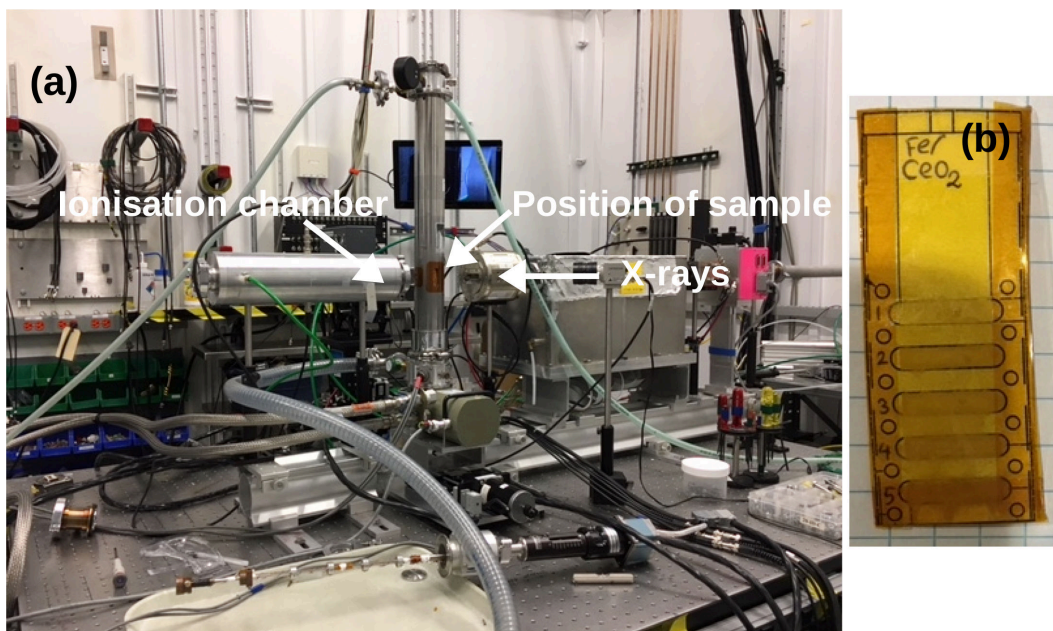


Figure 2.8: (a) Transmission geometry experimental setup at sector 20-BM-B at the Advanced Photon Source. Sample is placed in between the source and detector. (b) A photograph of samples prepared for the transmission geometry experiments are shown. Five samples are mounted on the sample holder.

counting statistics determined that a fluorescence based experiment was appropriate.

2.7.5 The fluorescence geometry

The fluorescence geometry is appropriate for thick samples and low concentration samples. Fluorescence geometry setup is shown in figure 2.9. In this case, photons are incident on the face of the sample. The secondary photons that fill the core-hole fluoresce over the entire solid angle. However, because the photons are polarized in the plane of synchrotron the elastic scatter is significantly suppressed at 90° to the incident beam, in the horizontal plane. Therefore, the fluorescence detectors are usually placed perpendicular to the x-ray beam. In addition to the solid angle, another

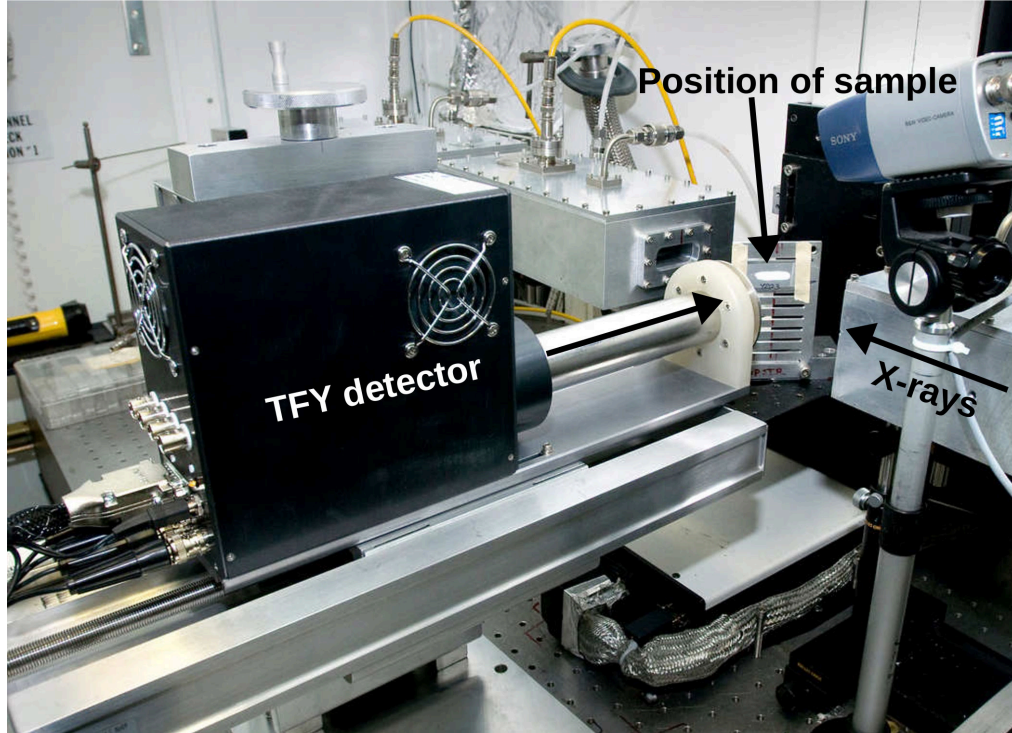


Figure 2.9: A photograph of experimental setup for total fluorescence yield is shown. Detector is mounted perpendicular to the source to reduce the elastic scatter as discussed in the text. Photo by Bruce Ravel/CC BY-SA 3.0 (<https://creativecommons.org/licenses/by-sa/3.0/>).

important consideration of fluorescence measurements is energy discrimination. It allows us to focus on the fluorescence lines of interest and suppress background intensity and scattering peaks to increase the signal-to-noise level. For the fluorescence measurements at hard x-rays, a 13 element solid-state detector was used to monitor the fluorescence x-rays, and for soft x-rays, a Si-based vortex detector was used. The measured fluorescence I_F [72] goes as

$$I_F = \frac{I_0 \beta(E) \mu_c(E)}{\mu''(E_F) + \mu_b(E) + \mu_c(E)} \quad (2.21)$$

$\mu_c(E)$ is the absorption of the element of interest, $\mu_b(E)$ is the absorption of all other atoms in the material and the electrons in the absorption atom that not the excited electron. $\mu''(E_F)$ is the total absorption of the material at the fluorescence energy. The multiplying factor β includes all the factor affecting the detector (such as solid angle, gain) and fluorescence efficiency of the absorbing atom. In the limit where $\mu''(E_F) + \mu_b(E) \gg \mu_c(E)$ then

$$I_F = I_0(E)\beta(E)\mu_c(E) \quad (2.22)$$

$$\mu(E) \propto \frac{I_F}{I_0}. \quad (2.23)$$

For very concentrated samples one important consideration is self-absorption. Self-absorption is due to the escape depth for the fluoresced x-ray is generally much longer than the penetration depth. For this reason, all absorbed x-rays cause a fluoresced x-ray and this sometimes severely dampens the x-ray absorption spectra[73]. The absorption peaks vanish and some emerge in the fluorescence geometry[74]. This may not be a big challenge with hard x-rays, but for soft x-rays, because their penetration depth is low, there total electron yield measurements more suitable.

2.7.6 The total electron yield

In total electron yield, one measures the drain current to obtain the absorption coefficient. Incident photons excite the core electrons to empty states above the Fermi level. The created core holes are filled by Auger decay. As the Auger electrons leave they create scattered secondary electrons. A cascade of these scattering events originates from an average depth of t and generates current (see figure 2.10b). The electrons created deep in the sample do not have sufficient energy to overcome the

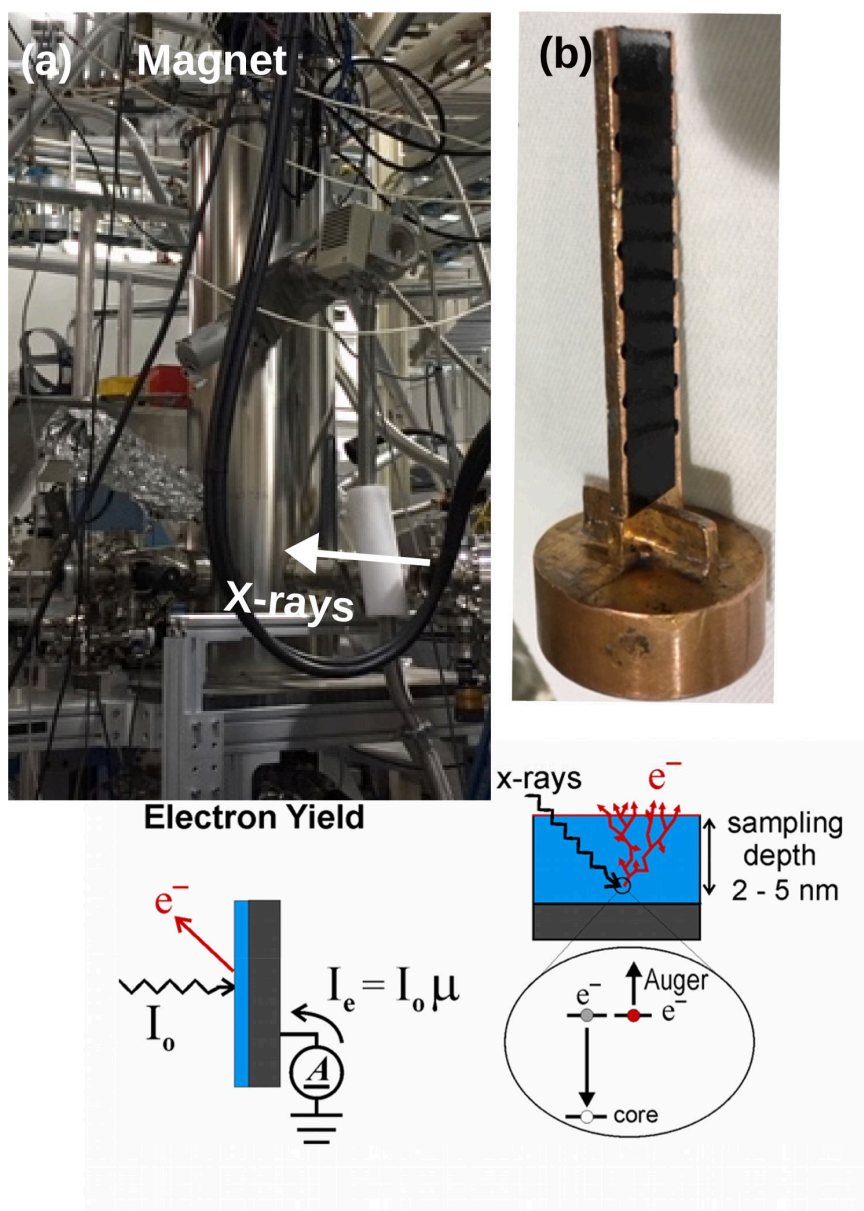


Figure 2.10: A photograph of the 7 Tesla magnet at 4-ID-C at the Advanced Photon Source. (b) Samples are mounted on a carbon conductive tape, and stuck to a Cu cold finger for TEY experiments. A diagram illustrates the total electron measurement. Reprinted with permission from [65]. Copyright 2006 Springer Science and Business.

work function and contribute to the total electron yield signal (TEY). TEY measurements are surface sensitive and probe the topmost $\sim 2 - 5$ nm surface of the

systems[65]. A diagram of the Cu sample holder and TEY experimental setup are shown in figure 2.10a,c. In the thesis, soft x-ray absorption spectroscopy and x-ray magnetic circular dichroism measurements were collected in TEY mode.

2.8 Mössbauer Spectroscopy

The nucleus is at the heart of an atom. Mössbauer spectroscopy is a technique that targets the nuclei of probe atom and provides valuable information on the local structure, bonding properties and magnetism. Rudolf Mössbauer discovered the phenomenon of recoil-free nuclear resonant absorption of γ -radiation in 1957[75]. The extreme local sensitivity of the technique proves an excellent opportunity to probe the nanoscale systems.

2.8.1 Recoilless emission and absorption of γ -rays

A free atom that emits γ -ray must recoil due to the law of conservation of momentum. Thus, the recoil free energy:

$$E_R = \frac{Mv^2}{2} = \frac{p^2}{2M} = \frac{E_\gamma^2}{2Mc^2} \quad (2.24)$$

where E_γ is the photon energy, M is the mass of the atom, c is the velocity of light. In a free atoms (or molecules in gaseous or liquid state) the recoil effect (Fig. 2.11a) reduces the transition energy E_R for the emission process and increases the transition energy by E_R for the absorption process as shown in figure 2.11b. Hence at a given point the emission and absorption lines are shifted away from each other by $2E_R \sim$

$10^6 \Gamma_0$, where Γ_0 is the natural linewidth⁵, and this difference makes the overlap of resonance impossible.

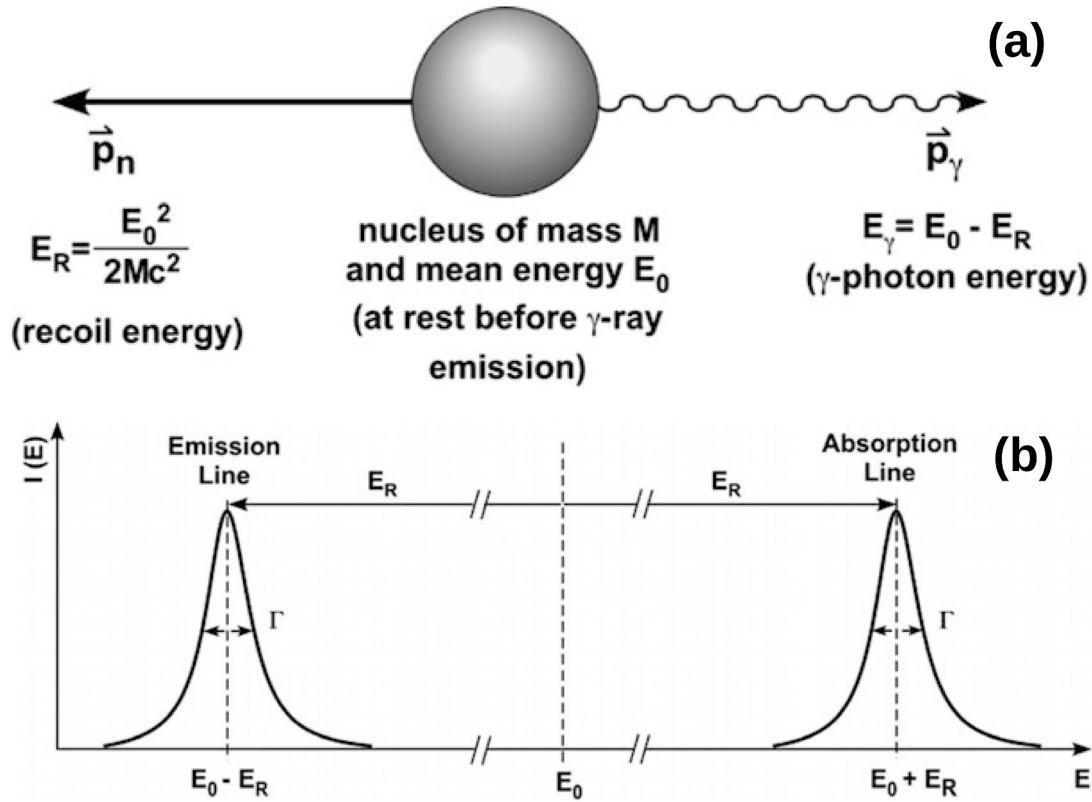


Figure 2.11: (a) Representation of momentum conservation of nucleus of mass M is shown. Linear momenta of nucleus (p_n) and the γ -photon (p_γ) are opposite in direction. (b) The emission and absorption lines of a free atom of mass M suffers recoil effect with energy E_R . In a free atom or molecule the emission and absorption lines shifted by $2E_R$ and makes resonance overlap less probable. Reprinted with permission from[76]. Copyright 2010 Springer Science and Business Media.

Here comes the brilliant discovery of resonant recoil-free emission effect also known as Mössbauer effect. If the atom is bounded by the crystal lattice and the binding energy of the lattice is much larger than the recoil energy (~ 1 -10 eV) the momentum

⁵For 14.4 keV level of ^{57}Fe $E_R \sim 2 \times 10^{-3}$ eV and from Heisenberg uncertainty principle $\Gamma_0 \sim \hbar / (2\pi \times 97 \text{ ns})$; 97 ns is the lifetime of excited state.

is transferred to the whole crystal. Because the mass M in equation 2.24 is at least $\sim 10^{15}$ atoms and the E_R is significantly smaller compared to Γ_0 , a recoilless emission and absorption of gamma quanta possible as shown in figure 2.11b. Note that the crystal lattice is not completely rigid and the atoms vibrate from their mean positions as phonons. The recoil energy of the γ -ray can still be transferred to the crystal lattice as a quantised lattice vibration, or phonon. Only if the recoil energy is less than the lowest quantisation mode a recoilless event occurs, this is also known as f -factor. The f -factor is a certain probability that no phonon excitation takes place due to emission or absorption of γ -rays. The Mössbauer effect is observable for only this recoil-free event f , which is given as

$$f \propto \exp\left(\frac{-E_\gamma^2 \langle x^2 \rangle}{\hbar c^2}\right) \quad (2.25)$$

where $\langle x^2 \rangle$ is mean square vibrational amplitude of nucleus in the direction of x and E_γ is energy of γ -ray radiation. If Debye-model is used for temperature $T \ll \Theta_D$:

$$f = \exp\left[-\frac{E_R}{3k_B\Theta_D}\left(\frac{3}{2} + \frac{\pi^2 T^2}{\Theta_D^2}\right)\right] \quad (2.26)$$

where k_B is Boltzmann constant and $\Theta_D = \hbar\omega_D/k_B$ is the Debye-temperature. f is inversely proportional to E_R , T and directly proportional to θ_D . That means the higher the Debye-temperature, the stronger the bond-strength of the material and the higher the recoil-free fraction. Because of the constraints (e.g. lifetime of the excited state) on the f -factor only a limited number of elements in the periodic table are suitable for Mössbauer spectroscopy. Some examples of the Mössbauer isotopes are ^{57}Fe , ^{129}I , ^{119}Sn , and ^{121}Sb . In this thesis, all the Mössbauer spectroscopy studies were performed using a ^{57}Fe source. The abundance of ^{57}Fe is $\sim 2\%$ of natural iron. The decay scheme of the source ^{57}Co is shown in figure 2.12. In the whole process, only

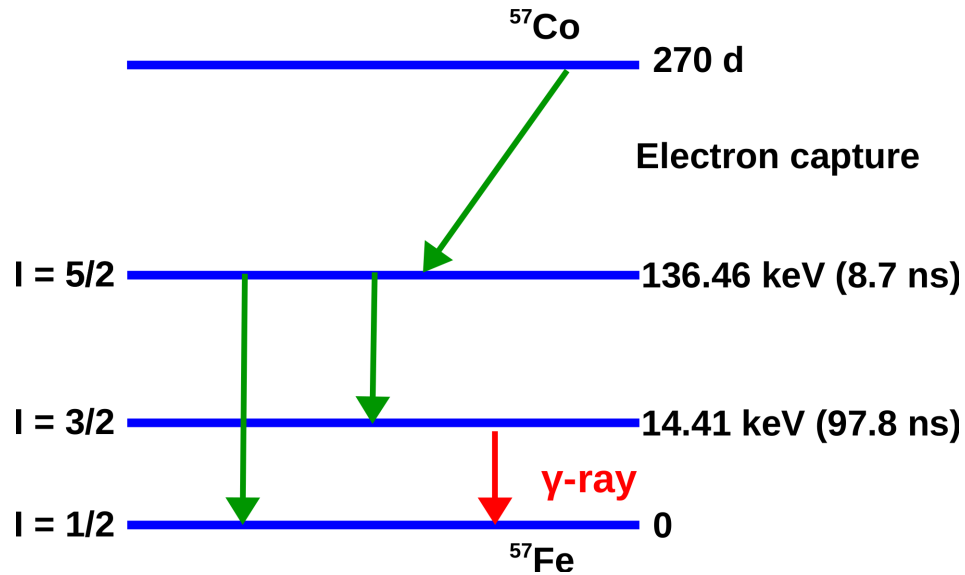


Figure 2.12: Nuclear decay scheme of ^{57}Fe Mössbauer resonance is shown. By electron capture ^{57}Co decays to ^{57}Fe with nuclear spin quantum number $I = 5/2$. $I = 3/2$ and $I = 1/2$ are the nuclear spin quantum numbers of the excited state and the ground state of 14.4 keV γ -rays that are used in $^{57}\text{Mössbauer}$ spectroscopy.

about 11% of the decay will emit the desired 14.4 keV Mössbauer radiation through the $\frac{3}{2}$ to $\frac{1}{2}$ transition. The nuclear energy levels can be shifted and sometimes split by hyperfine interactions (discussed below). To still have resonance, in an actual transmission Mössbauer experiment, the radioactive source is Doppler shifted. Because of the Doppler effect the motion modulates the energy of γ photons by $E_\gamma = E_0(1 \pm \frac{v}{c})$.

2.8.2 Hyperfine interactions

Hyperfine interactions are the interactions between nuclei and electrons neighboring Mössbauer atom itself and by other atoms in the neighbourhood. The electric and magnetic fields produced by the electrons interact with the Mössbauer nuclei and per-

turb its nuclear energy levels. Usually, there are three main hyperfine interactions; the electric monopole interaction, the electric quadrupole interaction, and the magnetic dipole interaction. The electric monopole interaction shifts the energy scale; it is also called as *isomer shift* δ . The electric quadrupole interaction induces partial splitting of the degenerate levels, and the magnetic quadrupole interaction completely lifts the degeneracy, and they are called the *quadrupole shift* (Δ) and the *hyperfine field* (B_{hf}), respectively.

2.8.3 Isomer shift

The nucleus is very small in an atom; however, it has a finite size, and there is a probability that the density of electron at the nucleus is non-zero. The isomer shift (δ) arises due to the electrons (mainly *s*-electrons) penetrating the nuclear field. The volume of the nucleus in its ground state and excited state are different, and *s*-electron densities are affected by the chemical environment⁶. The relation between the *s*-electron density and the nuclear radius is given by

$$\delta = \frac{2}{3}\pi Ze^2 \left\{ |\psi_S(0)_E|^2 - |\psi_S(0)_A|^2 \right\} \left\{ \langle R_e^2 \rangle - \langle R_g^2 \rangle \right\} \quad (2.27)$$

where $\langle R_e^2 \rangle$ and $\langle R_g^2 \rangle$ are the mean square radii of the ground and excited nuclear states, $|\psi_S(0)_E|^2$ and $|\psi_S(0)_A|^2$ are the electron densities at the emitting and absorbing nuclei and Z is the atomic number.

Isomer shift (Fig. 2.13a) values give information about the oxidation state. For example, Fe^{+1} , Fe^{2+} and Fe^{3+} ions have electronic configurations of $3d^7$, $3d^6$, and

⁶In a typical Mössbauer experiment source is located in different environment (e.g. ^{57}Co source in Rh matrix) than absorber(sample) material (e.g. Fe is decorated on CeO_2 surface or CoFe_2O_4)

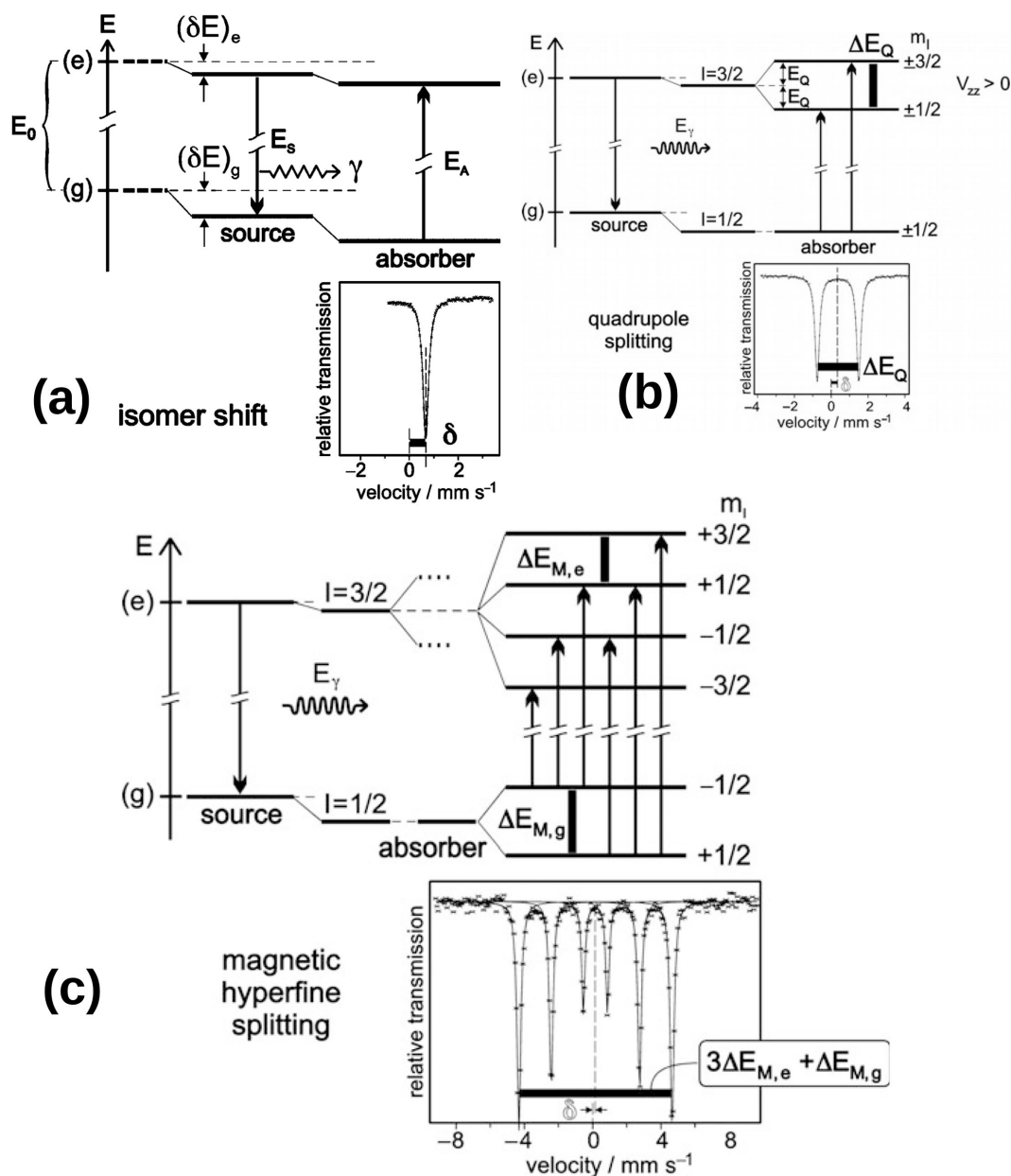


Figure 2.13: Three kinds of hyperfine interactions observed using Mössbauer parameters are shown. (a) Electric monopole interaction between protons of nucleus and electrons penetrating the nucleus shifts the energy of the nuclear states and gives the isomer shift (δ). (b) Electric quadrupole interaction between nuclear quadrupole moment and electric field gradient at the nucleus is responsible for the quadrupole splitting (Δ). (c) Magnetic dipole interaction between the nuclear magnetic moment and a magnetic field around the nucleus due to neighbouring electrons is responsible for the hyperfine field (B_{hf}). Reprinted with permission from [76]. Copyright 2010 Springer Science and Business Media.

$3d^5$, respectively. The Fe^{1+} ions have 7 d -electrons, and they exert a very strong shielding of the s -electrons towards the nuclear charge, this reduces greatly the s -electron density $|\psi_S(0)_A|$ giving a strongly negative quantity $|\psi_S(0)_E|^2 - |\psi_A(0)_A|^2$. Because the $\langle R_e^2 \rangle - \langle R_g^2 \rangle$ of Fe nucleus (only for Fe) is negative it makes the δ strongly positive (see equation 2.27). For this reason among these three ions, the most positive isomer shift occurs with Fe^{1+} . The isomer shift also gives valuable information about spin state and bonding properties such as covalency and electronegativity.

Additionally, an effect called the second-order Doppler shift also affects the energy shift of a spectrum. All atoms in a crystal vibrate at a temperature above 0 K. The period of oscillation ($\sim 10^{-13}$ s) is much shorter than the lifetime of Mössbauer nucleus ($\sim 10^{-8}$ s) resulting in an average displacement of zero. However, the second term in the Doppler shift depends on v^2 leading to the mean square displacement being non-zero⁷. This energy shift is^[76]:

$$\frac{\delta E_\gamma}{E_\gamma} = -\frac{\langle v^2 \rangle}{c^2} \quad (2.28)$$

2.8.4 Quadrupole shift

Electric quadrupole interaction occurs if at least one of the nuclear states involved in the Mössbauer atom possesses a quadrupole moment eQ (for $I > \frac{1}{2}$) and if electric field at the nucleus (e.g. via crystal field effects) is inhomogeneous⁸. The nuclear quadrupole moment is defined as:

$$eQ = \int \rho r^2 (3\cos^2\theta - 1) d\tau \quad (2.29)$$

⁷Doppler effect change the frequency of emitted γ -ray as: $\nu' = \nu \sqrt{1 - (\frac{v}{c})^2}$

⁸For ^{57}Fe first excited state is $I = \frac{3}{2}$ so possesses an electric quadrupole moment

where e is the proton charge, ρ is the charge density, r is the distance from the center of the nucleus, and θ is the angle to the nuclear spin quantisation axis, and $d\tau$ is the volume element. The sign of Q is positive if the nucleus is elongated and negative if it is flattened.

A nucleus that is present in anisotropic crystallographic surroundings experiences an electric field gradient. The electric field gradient is defined as the $E = -\nabla V$ and is given by $V_{ij} = (\partial V / \partial i \partial j)$; ($i, j, k = x, y, z$) of a 3×3 second rank tensor. If a suitable coordinate system is chosen the electric field gradient can be defined because of the symmetry form of tensor only five components are independent, i.e. $V_{ij} = V_{ji}$ and $\Sigma V_{ii} = 0$ due to Laplace's equation and an asymmetry parameter results:

$$\eta = \frac{V_{xx} - V_{yy}}{V_{zz}}. \quad (2.30)$$

In the principal axis system with z as the quantisation axis, the interaction between electric field gradient and electric quadrupole moment is described by a Hamiltonian

$$H = \frac{eQV_{zz}}{4I(2I-1)} \left\{ 3\hat{I}_z^2 - I(I+1) + \eta(\hat{I}_x^2 - \hat{I}_y^2) \right\}. \quad (2.31)$$

For an $I = \frac{3}{2}$ state, of e.g. ^{57}Fe the splitting between two sublevels (powder average) is

$$\Delta E_Q = \frac{eQV_{zz}}{2} \left(1 + \frac{\eta^2}{3} \right)^{1/2}. \quad (2.32)$$

Lattice contribution from charges to distant ions and valence contribution due to incompletely filled shells are the two main contributors to the electric field gradient. The quadrupole shift (Fig. 2.13b) gives information on the oxidation state, spin state and local asymmetry of the probe atom.

2.8.5 Magnetic hyperfine splitting

A nucleus state with $I > 1/2$ possesses a magnetic moment μ . Magnetic hyperfine splitting occurs because the magnetic dipole moment will also interact with the magnetic field B . The magnetic hyperfine field (B_{hf}) originates from the interaction between the magnetic field of the nucleus and spins of the electrons of the same atom. This internal magnetic field is present even without an applied field for Fe one can measure the internal magnetic field in the absence of an external field.

In ^{57}Fe the ground state is $I = 1/2$ and the first excited state is $I = 3/2$. The magnetic dipole interaction leads to splitting of the states $|I, m_I\rangle$ into $2I + 1$ substates, where m_I is the magnetic spin quantum number. Thus, the degeneracy is lifted and the ground state $I = 1/2$ is divided into two substates and $I = 3/2$ is divided into four substates. From first-order perturbation theory⁹, the energy of sublevels is given by

$$E_M(m_I) = -\mu B m_I / I = -g_N \beta_N B m_I \quad (2.33)$$

where g_N is Landé g-factor, and β_N is the nuclear Bohr-magneton. Dipole selection rules govern the transition between the states by $\Delta I = \pm 1$ and $m_I = 0, \pm 1$ and six allowed transitions are possible as shown in figure 2.13c. For ^{57}Fe the relative transmission probabilities of randomly oriented powders are 3:2:1:1:2:3 as determined by Clebsch-Gordon coefficients. Among the six lines, the separation between lines 2 and 4 (also between 3 and 5) is magnetic dipole splitting of the ground state. The separation between lines 5 and 6 (also between 1 and 2, 2 and 3, 4 and 5) is magnetic dipole splitting of the excited $I = 3/2$ state. The magnetic hyperfine field (Fig.

⁹As long as $\Delta \ll B_{hf}$; if $\Delta \sim B_{hf}$ then full Hamiltonian should be used

2.13c) enables one to determine the effective magnetic field acting at the nucleus. This hyperfine field can be an applied field as well; sometimes many of the materials can also create a magnetic field of their own field. A general expression for the magnetic field at the nucleus is:

$$B_{int} = B_C + B_D + B_L + B_{ext} \quad (2.34)$$

where B_C is the Fermi contact interaction, B_D is the spin dipolar term, B_L is the orbital magnetic term, B_{ext} is contributions from a Zeeman term, Lorentz field, demagnetizing field, etc.

The Fermi-contact term originates from the polarization of electrons whose wavefunctions overlap with the nucleus, e.g. s -electrons. This polarization is due to the unpaired electrons in d and f orbitals and gives an imbalance in the s electron spin-density at the nucleus. For transition metal ions the dominant term is the Fermi contact term described as

$$B_C = \frac{-16\pi}{3} \mu_B \left\langle \sum \left(\rho_S(\uparrow) - \rho_S(\downarrow) \right) \right\rangle. \quad (2.35)$$

The spin dipolar term B_D arises due to the interaction between the nucleus and the magnetic moment of electron spin of $3d$ and $4f$ electrons and can be described as

$$B_D = -2\mu_B \langle \mathbf{S} \rangle \langle r^{-3} \rangle \langle 3 \cos^2 \theta - 1 \rangle \quad (2.36)$$

where θ is the angle between spin \mathbf{S} and principle axis z for axial symmetry.

The orbital magnetic term, B_L , arises from the net orbital moment at the nucleus caused by the orbital motion of electrons in partially filled shells. In transition metal ions the net orbital magnetic moment is quenched by interactions with the crystal

field, but in Rare Earth ions it is substantial, and B_L is given as

$$B_L = \frac{2\mu_0\mu_B}{4\pi} \langle r^{-3} \rangle \langle \mathbf{L} \rangle \quad (2.37)$$

2.8.6 Application of ^{57}Fe Mössbauer spectroscopy in this thesis

Overall ^{57}Fe Mössbauer spectroscopy is extensively used to examine the oxidation state of iron atoms, which are found in a Fe^0 (metal), Fe^{2+} , Fe^{3+} , and Fe^{4+} electronic coordination, as well as the type of coordination environment occupied by iron atoms (tetrahedral, octahedral, etc.). Figure 2.14 shows the approximate representation of the range of δ (mm/s) values found in iron complexes. Additionally, Mössbauer spectroscopy is also used in the identification of solid state Fe-oxide phases on the basis of their hyperfine parameters and the site assessments (stiochiometry) based on the relative spectral absorptions, and providing additional valuable information[77] about individual Fe sites in the solid (e.g. level of disorder and distortion via Δ and Γ). Table 2.1 presents a list of Mössbauer hyperfine parameters of some binary oxides.

2.8.7 Experiments

A schematic diagram showing the primary components of Mössbauer spectrometer are shown in figure 2.15. In this thesis, all measurements on the Fe contained nanocrystallites were performed using a ^{57}Fe source embedded in Rh matrix mounted on a Wissel MDU MR-360 transducer. The transducer is controlled by a Wissel DFG-1200 function generator which provides a triangular waveform yielding linear Doppler-shifted γ -rays used to study Fe in the sample. The transmitted γ -rays are detected through a LND model 45431 Ar/Xe gas proportional counter. The pulses from the detector are

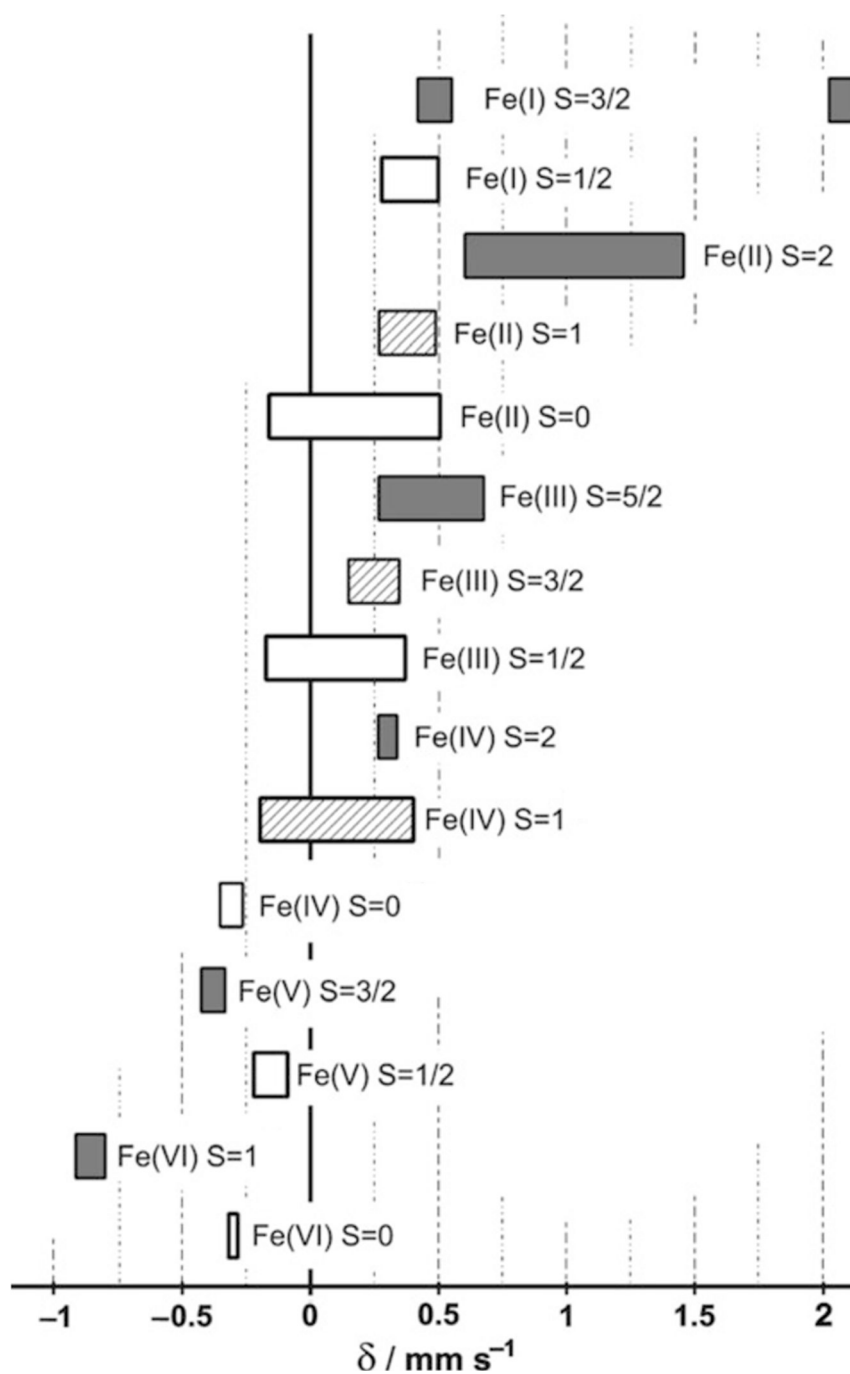


Figure 2.14: Ranges of ^{57}Fe compounds Mössbauer isomer shifts (δ) observed relative to $\alpha\text{-Fe}$ at room temperature. Reprinted with permission from [76]. Copyright 2010 Springer Science and Business Media.

	T (K)	Δ (mm/s)	B_{hf} (T)	Site	$\delta(\text{Fe})$ (mm/s)	Reference
$\alpha\text{-Fe}_2\text{O}_3$	298	0.12	51.5		0.38	[78]
$\gamma\text{-Fe}_2\text{O}_3$	RT	–	48.8	A-site	0.27	[79]
		–	49.9	B-site	0.41	
$\text{Fe}_{0.93}\text{O}$	297	0.46	0	A-site	0.91	[80]
		0.78	0	B-site	0.86	
Fe_3O_4	300	–	49.1	A-site	–	[81]
		–	45.3	B-site	–	
	82	-0.05	49.1	A-site Fe^{3+}	0.37	[82]
		0.50	45.3	B-site Fe^{3+}	0.77	
		-0.02	49.1	B-site Fe^{3+}	0.59	
		0.95	45.3	B-site Fe^{2+}	0.71	
		-2.62	45.3	B-site Fe^{2+}	1.20	

Table 2.1: Mössbauer hyperfine parameters for binary oxides.

amplified, and pass through through an ORTEC single channel analyser (SCA). The SCA acts as a discriminator where most of the non-resonant background radiation is rejected by appropriately choosing the lower level and upper-level window settings to select 14.4 keV γ -rays. The discriminated pulses are fed into ORTEC multi-channel analyser with 512 different channels, where each channel correspond to one single velocity. The velocity scale was set by a calibration measured using a 6 μm $\alpha\text{-Fe}$ at room temperature using the known B_{hf} (300 K) = 33 T, and all δ (mm/s) are relative to $\alpha\text{-Fe}$ at 300 K.

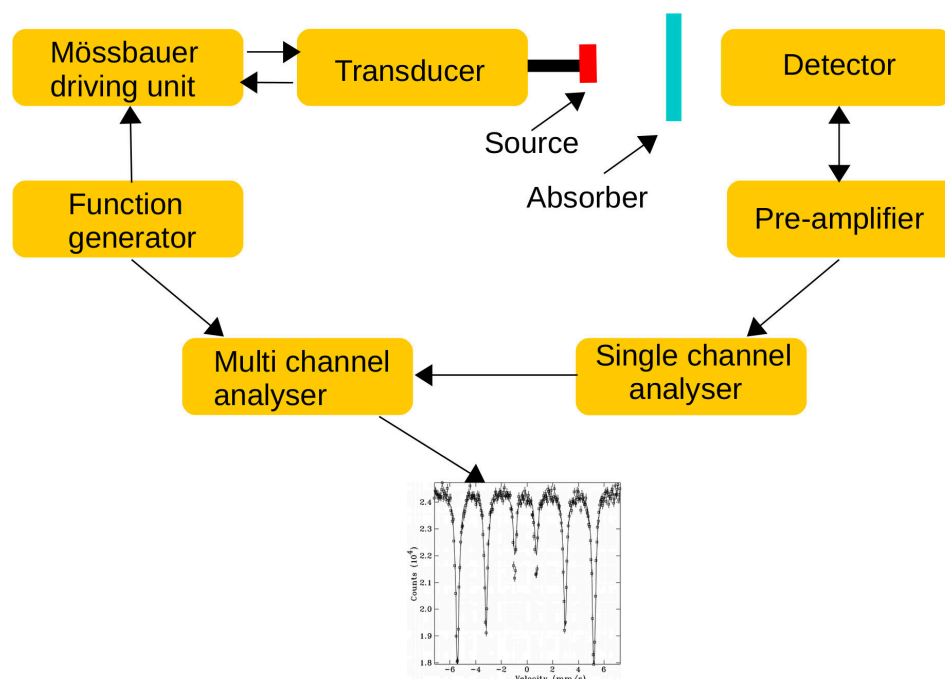


Figure 2.15: Schematic representation of a transmission Mössbauer spectrometer.

All measurements reported in this thesis were performed on powder samples (as shown in Fig. 2.16a) spread across a sample holder. The ground powders were held between two x-ray mylar films mounted in a brass holder with a diameter equal to that of the window in the detector (Fig. 2.16). All measurements were performed in a transmission geometry, where the sample is between the source and the detector, as shown in Fig. 2.16b. Fe_3O_4 , CoFe_2O_4 , and Fe-decorated CeO_2 nanoparticles' spectra were measured at room temperature. The measured Mössbauer spectrum was analysed using a non-linear least squares fitting method with Lorentzian line-shapes, and a first-order perturbation treatment of the Hamiltonian to calculate the transition energies. The transition (relative) absorptions were determined from the probabilities set by the powder average values (i.e. $3:R:1:1:R:3$ for lines 1 through 6, respectively,

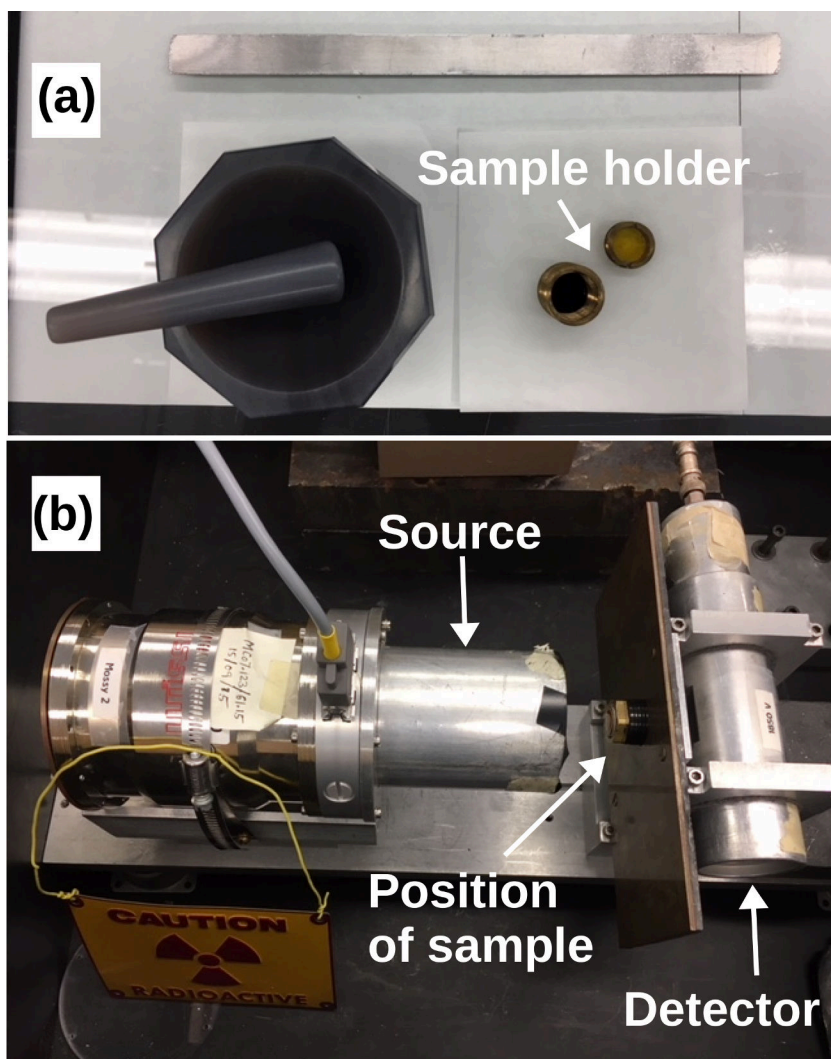


Figure 2.16: (a) The sample to be measured is powdered and spread across two x-ray mylar films mounted on a brass holder. (b) A photograph of experimental setup for transmission geometry is shown. Sample is placed in between the source and detector.

with $R = 2$).

2.9 Magnetometry

X-ray magnetic circular dichroism (see Section 2.7.1) and Mössbauer spectroscopy (see Section 2.8) discussed above are element sensitive probes and advantageous to determine the magnetic contribution from different ions and different sites as Fe^{2+} and Fe^{3+} ions on A and B sites on Fe_3O_4 and Co^{2+} and Co^{3+} ions on A and B sites on CoFe_2O_4 as discussed in Chapter 3. However, these techniques cannot give overall information on the magnetism of the system. In addition to Ce^{3+} and Ce^{4+} in CeO_2 , electrons polarised in the vacancy orbitals cannot be probed. Furthermore, measurements in oxygen-rich and deficient measurements are possible using magnetometry (a technique developed[83] during my PhD work to distinguish and quantify various defects as discussed in Chapter 4). Additionally, magnetometry measurements can identify the total moment by varying the magnetic field and temperature and provides complementary information to x-ray spectroscopy and Mössbauer spectroscopy. Because the magnetic response of the CeO_2 is very small ($\sim 10^{-6}$ Am²/kg¹⁰ at 10 milli Tesla at 300 K) a superconducting quantum interference device (SQUID) based magnetic properties measurement system (MPMS) is required. SQUID magnetometry uses a combination of superconductivity, flux quantisation and a Josephson Junction to measure magnetic fields up to a resolution of 10^{-15} Tesla¹¹.

In 1911 Heike Kamerlingh Onnes first discovered that mercury became a superconductor when cooled down to liquid helium temperature at 4.2 K. Afterwards, many elements, for example, Sn, Pb and Nb and an enormous number of alloys showed

¹⁰1 emu/g = 1 Am²/kg

¹¹One femtotesla corresponds to $1/10^{11}$ of the earth's magnetic field

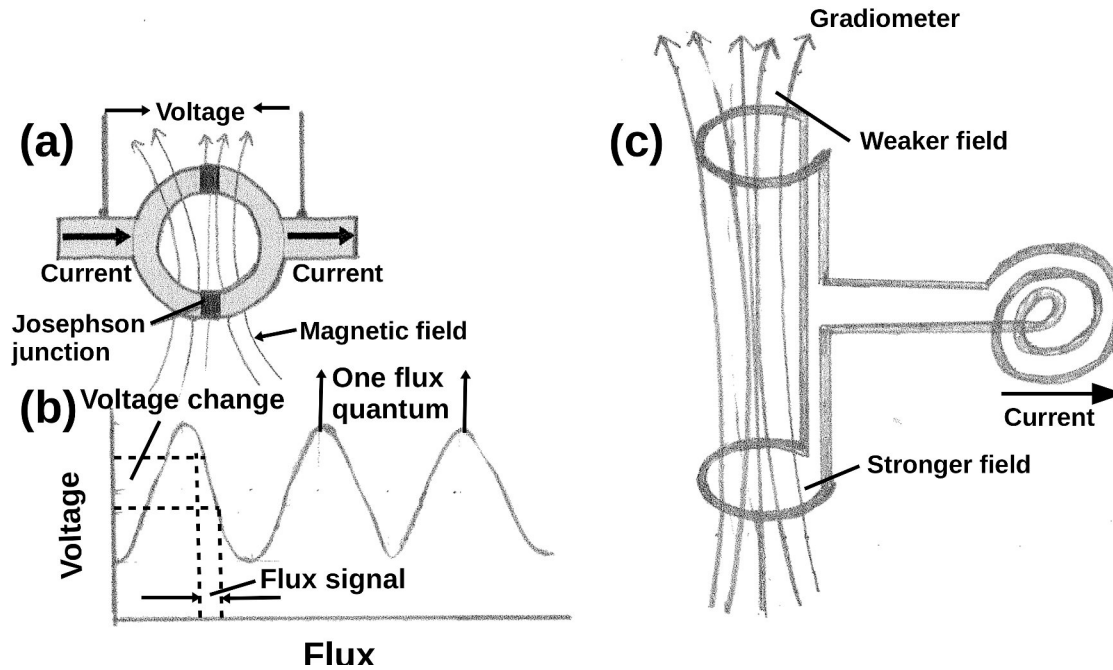


Figure 2.17: (a) A SQUID consisting of two Josephson junctions arranged on a superconducting ring (b) Voltage a function of flux shows the period of flux quantisation (c) A schematic representation of a gradiometer with two pickup coils is shown.

zero resistance to an applied current. Later, in 1957 Bardeen, Leon N. Cooper and J. Robert Schrieffer's theory (also known as BCS theory) was published to explain the superconductivity via Cooper pair formation (two electrons with opposite spin and opposite momentum bound together). One of the exciting aspects is that a single wavefunction can explain the entire collection of Cooper pairs. Following that in 1962 Brian D. Josephson predicted that when two superconducting materials are placed between an insulator the superconducting wavefunction of Cooper pairs tunnel through, and the junction acts a weak superconductor for a finite thickness. Besides, superconductivity and the Josephson effect, a principle called flux quantisation was

also discovered. Flux quantisation suggests that if current flows through a superconducting ring the product of magnetic field produced and the area enclosed by the ring is equal to an integer multiple of an arbitrary value: $\Phi_0 = \frac{2\pi\hbar}{2e}$. This quantum is termed a *fluxon*.

In a SQUID two Josephson junctions are arranged on a superconducting ring as shown in figure 2.17a. When a bias current is applied to the SQUID, the current is divided between the coils and only for values higher than critical current is voltage produced in the SQUID. Steadily increasing the flux (by bringing in a magnet) changes the critical current to decrease and increase successively, as shown in figure 2.17b. The critical current is maximum for an integer number of quanta and minimum for half-integer number of quanta. In a SQUID the interference between the two wavefunctions at Josephson junction produces the current and voltage oscillations.

The magnetic properties of the systems studied in this thesis are all measured using a Quantum Design SQUID-based magnetic properties measurement system (MPMS-XL5). A measurement is performed by moving the sample through the superconducting detection coils that are located at the center of the magnet and outside the sample chamber. As the sample moves through the superconducting detection coils, the change in flux produces a change in the detection current. Because SQUID functions as a highly linear current to voltage converter, the variation in the superconducting persistent current produce variations in the voltage and that are proportional to the magnetic moment of the sample. The detection coils are usually second-order gradiometers as shown in figure 2.17c, configured to minimise the background drifts in the SQUID detection system caused by the fluctuations in the magnetic fields of



Figure 2.18: The Quantum Design MPMS-XL5

a superconducting magnet. Because of its extreme sensitivity a SQUID sensor is surrounded by a superconducting shield to eliminate the fluctuations in the ambient field of the laboratory and high magnetic fields produced by the superconducting magnet. The magnetic field is applied to a sample through a superconducting magnetic solenoid configuration that surrounds the SQUID coils. A picture of MPMS system components is shown in figure 2.18. In the MPMS a sample space is maintained at low pressure (5 mm Hg) with helium gas. At the top of a sample space, an airlock valve is located, and that can be used to purge the sample space with clean helium gas. The MPMS system consists of a high precision temperature control system, al-

lowing measurements between 2 K and 400 K, and superconducting magnet, giving a field in the range of ± 5 Tesla. All magnetometry measurements were performed using a Reciprocating Sample Option (RSO). In contrast to DC measurements where the sample is moved through discrete steps¹², in the RSO measurements sample is moved using servo motor which oscillates the sample. The RSO measurements sensitivity is of the order of 5×10^{-9} A.m²¹³. MPMS Multi-View software is used to control all aspects of the SQUID electronics, sample measurement parameters, field, and temperature.

Magnetic susceptibility (χ) is a versatile probe to identify the presence of a phase transition, the magnetic moment, magnetic exchange interaction strength, and magnetization dynamics. Magnetic susceptibility is defined as:

$$\chi = \lim_{H \rightarrow 0} \frac{M}{H} = \frac{\partial M}{\partial H}. \quad (2.38)$$

For $\chi \ll 1$, $B = \mu_0(H + M) \simeq \mu_0 H$ and equation 2.38 can be written as:

$$\chi = \lim_{B \rightarrow 0} \frac{\mu_0 M}{B} = \frac{\delta M}{\delta B} \quad (2.39)$$

DC susceptibility (χ_{dc}) measurements determine the equilibrium magnetization and generally are made in field-cooled (FC) and zero-field cooled (ZFC) regimes as a function of temperature. In ZFC measurements, a sample will be cooled in zero field to base temperature and $\delta M(T)$ is measured in an applied field at a fixed temperatures on the first warming cycle. For FC measurements magnetization is measured in an applied field in a cooling cycle.

¹²MPMS XL standard transport system has a range of 0-32 points

¹³1 Am² = emu

In AC susceptibility (χ_{ac}), a time varying, sinusoidal magnetic field of amplitude H_{ac} (typically ~ 0.25 mT) is applied to the sample. The AC susceptibility is given as:

$$\chi_{ac}(\nu, T) = \chi'_{ac}(\nu, T) + i\chi''_{ac}(\nu, T) \quad (2.40)$$

where ν is the oscillating field and typically in the range of $0.1 - 10^4$ Hz, $\chi'_{ac}(\nu, T)$ and $\chi''_{ac}(\nu, T)$ are in-phase and out-of-phase components respectively. In low frequency limit χ' is dM/dH . The out-of-phase component is non-zero for relaxation and irreversibility in the sample.

All samples were mounted in low background NMR (Norell high resolution S-5-20-8) tubes. Magnetic susceptibility measurements were done using 10 mT applied field. To cool the nanoparticles in zero field the degauss shield¹⁴ and magnet reset¹⁵ options from the MPMS were used.

A new method was introduced to distinguish the magnetism from oxygen-rich, and oxygen-deficient magnetism of several metal oxide systems studied in this thesis[83]. During the measurement, MPMS pumps the sample space to 5 mm Torr He atmosphere. As a consequence of this, all measurements performed with NMR tubes are oxygen deficient systems (open system) as shown in figured 2.19. Whereas for oxygen-rich measurements the NMR tubes are sealed with ECO-BOND under the ambient condition to create oxygen-rich (closed system) environment. During each magnetic measurement, the temperature was held at a fixed setpoint. NMR tubes are sensitive

¹⁴Degaussing is a method to decrease or eliminate remnant magnetic field. $M(\mu_0 H)$ measurements curves were measured from 2 K to 300 K from ± 5 T after cooling samples in a 5 T field. In MPMS-XL5 degauss shield option alternates positive and negative field polarity from the maximum 1 T to zero in sequentially smaller field steps.

¹⁵Magnet reset option purges the trapped fields by quenching the magnets from a high field. During this operation superconducting magnet is warmed above its T_C (~ 9.5 K) and releases the trapped fields

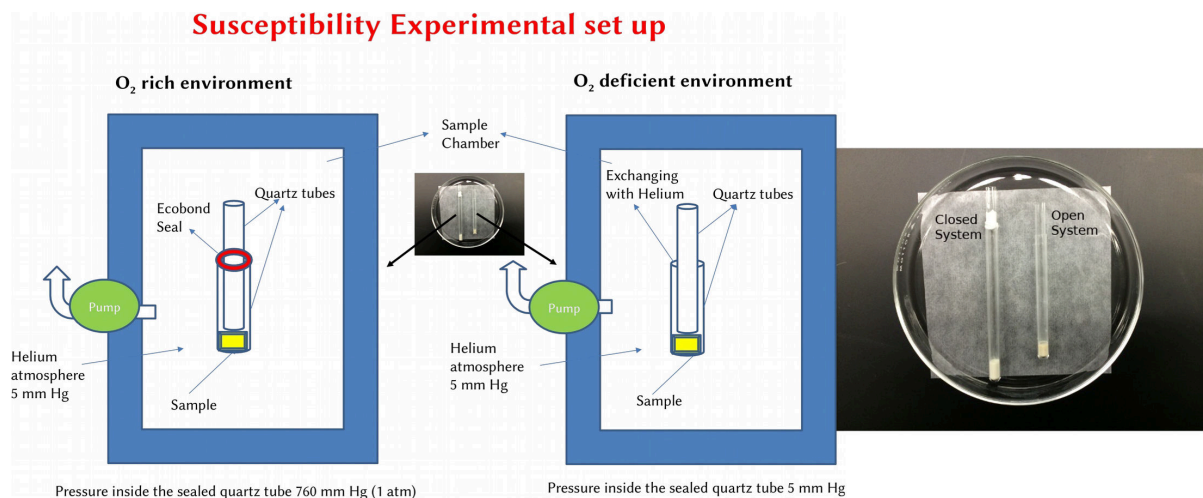


Figure 2.19: Experimental setup of oxygen rich and oxygen deficient magnetic susceptibility measurements. NMR tubes are sealed with low temperature epoxy (ECOBOND) to seal the tubes[84].

to thermal gradients, so during the temperature scan between measurements, a scan rate of 1 K/min below 100 and 2 K/min above that was used during heating and cooling to avoid thermal cycling effects breaking the tubes.

Chapter 3

Oxygen rich and oxygen deficient magnetism of nanoscale Fe_3O_4 and CoFe_2O_4

3.1 Introduction

The oxygen rich and oxygen deficient magnetic susceptibility studies are used in this thesis to identify the role of oxygen in the magnetism of metal oxides systems[83]. To demonstrate that the investigation is suitable to more complicated nonmagnetic oxides systems such as CeO_2 and transition metal decorated CeO_2 (as discussed in Chapter 4) we benchmarked this methodology on a prototypical spinel structure.

3.1.1 Spinel structure

The general molecular formula of spinel oxide structure is AB_2O_4 where A sites are tetrahedral sites and B sites are octahedral sites. The unit cell consists of 32 oxygen atoms, i.e. $A_8B_{16}O_{32}$. In this configuration, the close packed lattice of oxygen ions with interstitial octahedral (O_h) and tetrahedral (T_d) sites can accommodate a wide variety of cations. The spinel structure is based on a unit cell of 32 O^{2-} ions where 16 of the 32 available octahedral (B), and 8 of the 64 available tetrahedral (A) sites may be occupied as shown in Fig. 3.1. The charges of A and B in the prototypical spinel structure are +2 and +3, respectively ($A^{2+}B_2^{3+}O_4$), but other combinations incorporating monovalent and tetravalent cations from the s , p , and d -blocks can also be found in the spinel. The crystal structure is *normal* if all +2 cations occupy the T_d sites, and *inverse* if all the +2 cations occupy O_h sites.

Fe_3O_4 (magnetite) has a completely inverse spinel crystal structure. The magnetic structure of Fe_3O_4 is as follows: Fe^{3+} cations on the O_h and T_d sites are coupled antiferromagnetically via the superexchange interaction and the Fe^{2+} and Fe^{3+} on the O_h sites couple ferromagnetically through the magnetic double exchange interaction.

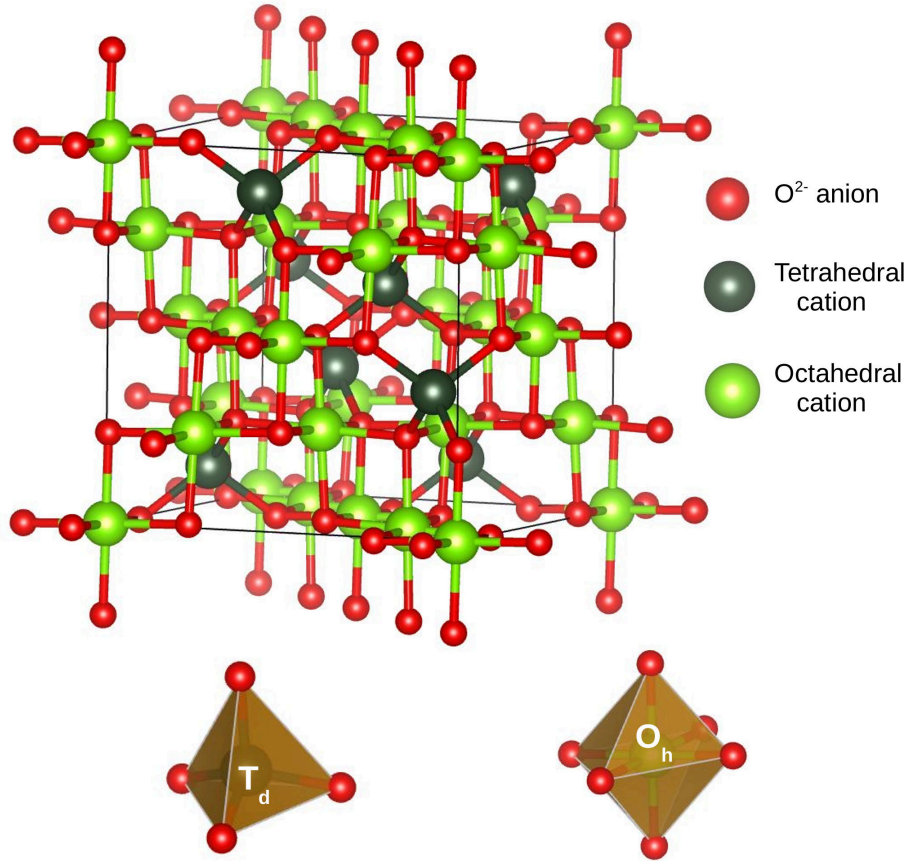


Figure 3.1: Schematic of the spinel crystal structure: $1/3$ of cations are located in available $1/8$ of the available tetrahedral (T_d) sites, and $2/3$ of the cations are located in $1/2$ of the available octahedral (O_h) sites. In normal spinel all Fe^{2+} ions are in T_d sites and Fe^{3+} ions are located in O_h sites. In an inverse spinel all Fe^{2+} ions are located in O_h sites whereas Fe^{3+} ions are located in O_h and T_d spinels equally. Structures created using VESTA[85]

Due to the resulting net magnetic moment of O_h and T_d sites, Fe_3O_4 is expected to show ferrimagnetic behaviour with a bulk magnetic moment of $4.1 \mu_B/\text{formula unit(f.u)}$ [86]. $CoFe_2O_4$ is similar to Fe_3O_4 , except that divalent Fe ions are replaced by Co^{2+} ions. Because of various reasons¹ the structure is no longer fully inverse like Fe_3O_4 , and there is a preference for a small fraction ($\sim 10\%$) of Co^{2+} ions to also

¹Relative sizes of cations, ligand-field stabilization energies of T_d and O_h , covalency effects, etc.

occupy T_d sites. The Fe^{3+} cations are antiferromagnetically coupled with O_h and T_d sites, whereas Fe^{3+} and Co^{2+} ions are coupled ferromagnetically, resulting in a ferrimagnet and the experimentally determined spin magnetic moment of $CoFe_2O_4$ is $3.7 \mu_B/f.u.$ [86].

3.1.2 Aim of this chapter

This chapter aims to identify the structure, composition, electronic structure and magnetism of nanoscale spinel Fe_3O_4 and $CoFe_2O_4$. Whether a spinel is normal, inverse or mixed², the lattice oxygen (O^{2-}) mediates the magnetism via double exchange or superexchange mechanisms. We identify that the magnetism can be altered by the oxygen rich and oxygen deficient environments. Further, we show that the magnetic susceptibility in oxygen rich and oxygen deficient magnetism differs and factors responsible for their impact on the redox process, and oxygen vacancy dynamics are presented.

3.2 Structure and Composition

X-ray diffraction (XRD) patterns of Fe_3O_4 and $CoFe_2O_4$ nanoparticles are shown in Fig. 3.2. Rietveld refinements with FullProf yielded identical $Fd\bar{3}m$ space group structures for Fe_3O_4 and $CoFe_2O_4$ as expected. The spinels are phase pure, and broadening of reflections are from the nanocrystallite sizes, i.e. Scherrer broadening. Lattice parameters and estimates of crystallite sizes calculated from the Rietveld refinements are provided in table 3.1. Results show that the lattice constant stays the same, and

²In mixed spinels, $2+$ ions are located at both O_h and T_d sites

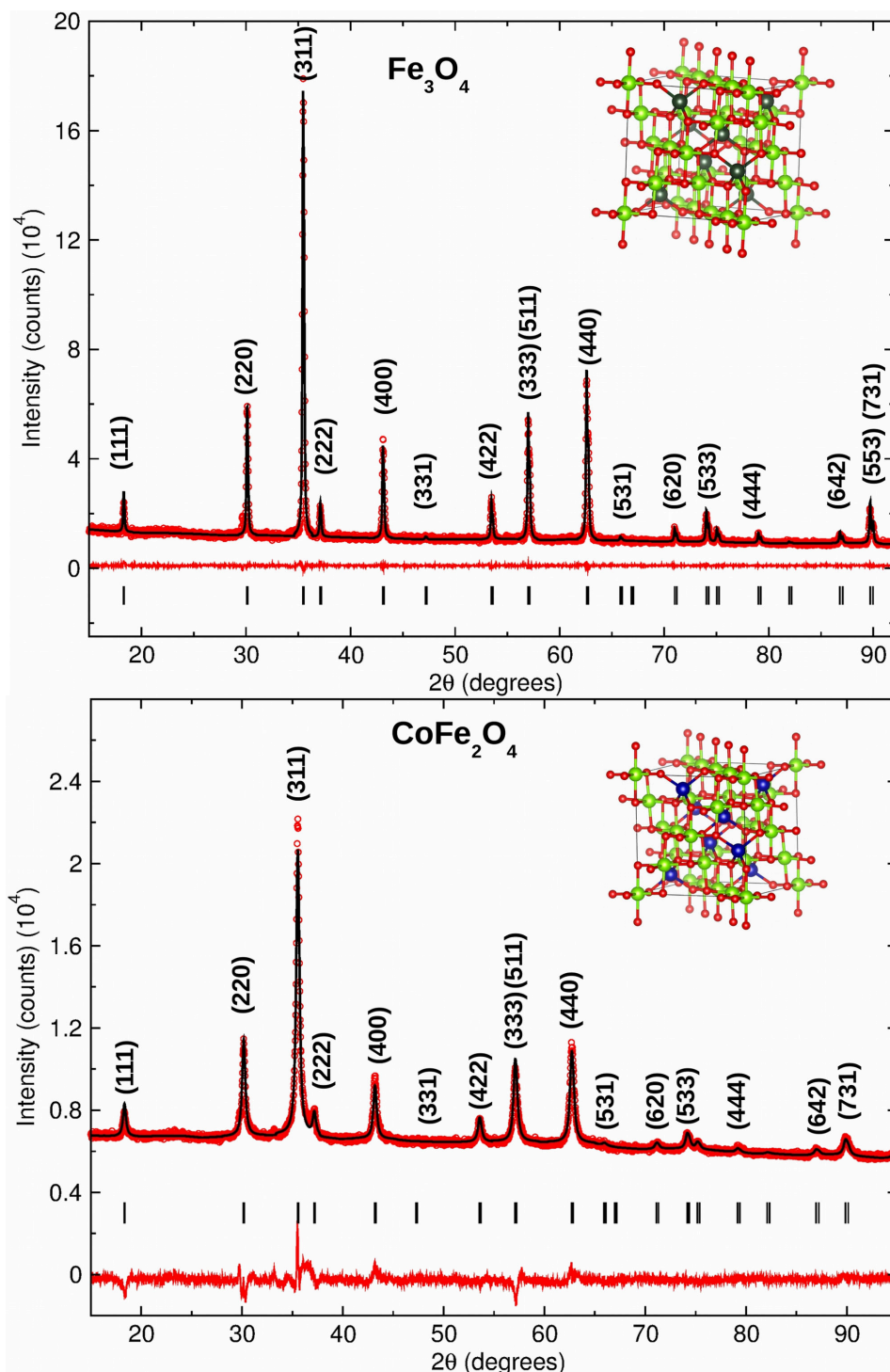


Figure 3.2: Room temperature x-ray diffraction patterns of Fe_3O_4 and CoFe_2O_4 are shown. The (hkl) indices of the structure are labeled. Refinement (solid lines) of Fe_3O_4 and CoFe_2O_4 and residuals are presented; the short vertical bars indicate the position of Bragg reflections used in the refinement.

Table 3.1: Crystalline (nanoparticle) size (nm) and lattice constant (\AA) of Fe_3O_4 and $CoFe_2O_4$ from XRD pattern refinements. The crystallographic site occupancies are fixed to 0.08333 for O_h sites and 0.04166 for T_d [87].

	size (nm)	a (\AA , XRD)
Fe_3O_4	17 ± 1	8.378 ± 0.001
$CoFe_2O_4$	17 ± 1	8.379 ± 0.001

the crystallite sizes are of the order of ~ 17 nm. The identified lattice constant values are in agreement with previously reported bulk Fe_3O_4 [87] and $CoFe_2O_4$ [88] systems. At first glance, the XRD refinement results illustrate that $CoFe_2O_4$ is plausibly an inverse spinel, like Fe_3O_4 . However, due to broadening of the reflections, XRD patterns may not be indicative of a change in spinel lattice parameter or T_d and O_h site occupancy. To better identify the cation site occupancies and electronic structures, x-ray absorption spectroscopy measurements were performed.

3.3 Local Environment and Cation Distribution

Extended x-ray absorption fine structure (EXAFS) spectroscopy is ideally suited for determination of local environment (e.g. coordination number, bond distances and cation site occupancies) of absorbing atoms due to photoabsorption processes. EXAFS spectra were measured at room temperature on Fe_3O_4 and $CoFe_2O_4$ systems up to $\sim 15 \text{\AA}^{-1}$ in wave vector k range to analyze the data. Background subtracted EXAFS spectra were analyzed using the ATHENA and ARTEMIS software programs[70]. The theoretical calculation of the phase shifts and backscattering amplitudes for specific atom pairs were obtained using the FEFF program[71] based on the crystallo-

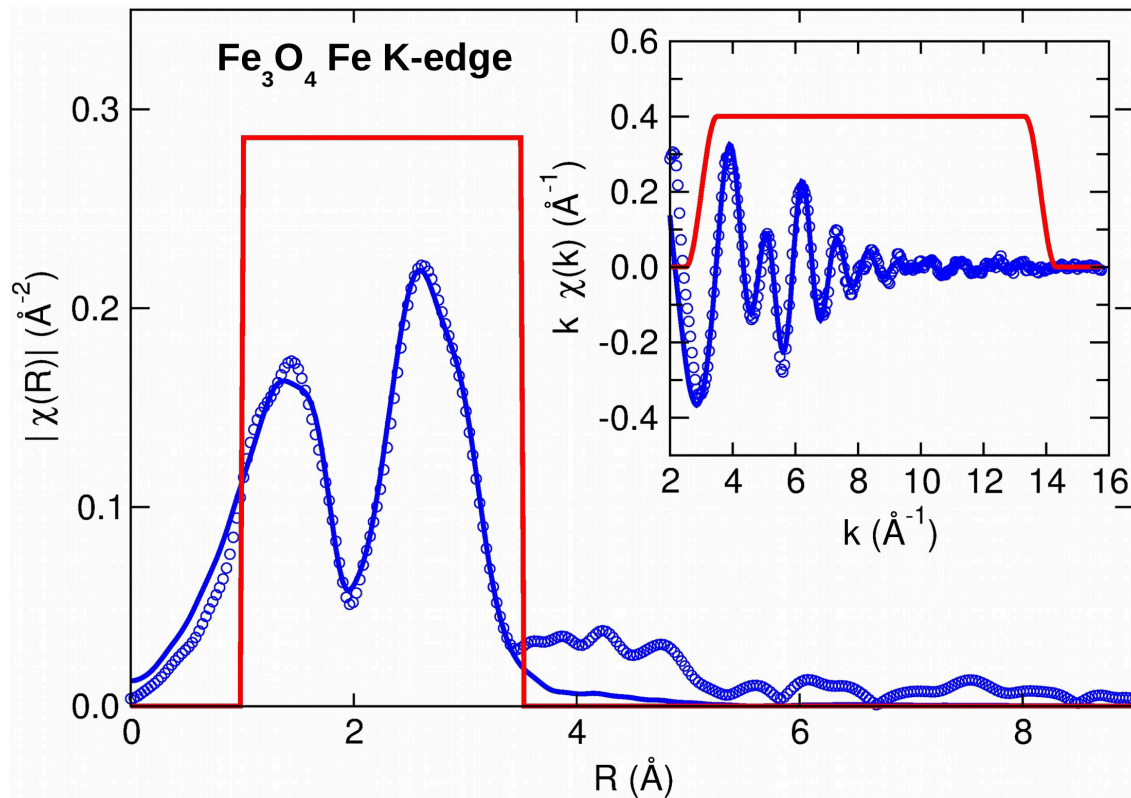


Figure 3.3: Fourier transformed modulus ($|\chi(R)|$) of the $k\chi(k)$ experimental data (open circles) and theoretical fits (solid line) of Fe_3O_4 nanoparticles are shown. Inset shows $k\chi(k)$ experimental data (open circles) and theoretical fits (solid lines). $|\chi(R)|$ represents raw data without correcting for phase shifts and the window used to select the coordination shell includes single scattering paths as discussed in text.

graphic data of Fe_3O_4 and CoFe_2O_4 . The model used to fit the Fe K and Co K edges data included single scattering paths up to 4\AA (to include first and second coordination shells). For Fe K edge of Fe_3O_4 and CoFe_2O_4 two different absorber atoms were used (Fe in O_h and T_d sites). Similarly, for Co K edge analysis of CoFe_2O_4 , Co in O_h and T_d sites were used to calculate the scattering paths.

Table 3.2: Parameters from the shell fitting of Fe K edge EXAFS analysis of Fe_3O_4 . Coordination number (N), energy shift (E_0), Debye-Waller factors (σ^2), average inter-atomic distances (R) are presented. The overall reduction S_0^2 was obtained for Fe_3O_4 as 1 by fitting to a bulk standard and the uncertainties are presented in parenthesis.

Shell	N	E_0 (eV)	$\sigma^2(\text{\AA}^2)$	R (\AA)
$Fe_{T_d} - O$	3.8(3)	-8(1)	0.007(2)	1.887(9)
$Fe_{O_h} - O$	5.7(4)	-8(1)	0.007(2)	2.061(9)
$Fe_{O_h} - Fe_{O_h}$	5.7(4)	-8(1)	0.010(1)	2.970(9)
$Fe_{O_h} - Fe_{T_d}$	5.7(4)	-8(1)	0.010(1)	3.482(9)
$Fe_{T_d} - Fe_{O_h}$	11.5(9)	-8(1)	0.010(1)	3.482(9)

3.3.1 Fe K edge of Fe_3O_4 nanocrystallites

Figure 3.3 shows the Fourier transformed ($|\chi(R)|$) EXAFS spectrum (inset shows in k space) of Fe_3O_4 . Two main peaks are observed, one at ~ 1.5 \AA and other ~ 3.5 \AA . The peak at ~ 1.5 \AA is due to the first oxygen coordination shell (O_h and T_d) and peak at ~ 3 \AA is related to the Fe_{O_h/T_d} [89]. The quantified local environment parameters (N , E_0 , σ^2 , and R) are in the Table 3.2.

The first peak (Fig. 3.3) has two different oxygen atoms located near Fe at 1.887 \AA (T_d environment) and 2.061 \AA (O_h environment) and their coordination numbers are consistent with the expected (T_d and O_h environments)[89]. From the second peak (Fig. 3.3) three different Fe ions are identified; $Fe_{O_h} - Fe_{O_h}$, $Fe_{O_h} - Fe_{T_d}$, and $Fe_{T_d} - Fe_{O_h}$ with slightly higher Debye-Waller factors compared to the Fe - O (Table 3.2). The disorder parameters (DW factors) obtained for Fe - O and Fe - Fe of nanocrystalline Fe_3O_4 are marginally higher than those in bulk Fe_3O_4 [89] as expected

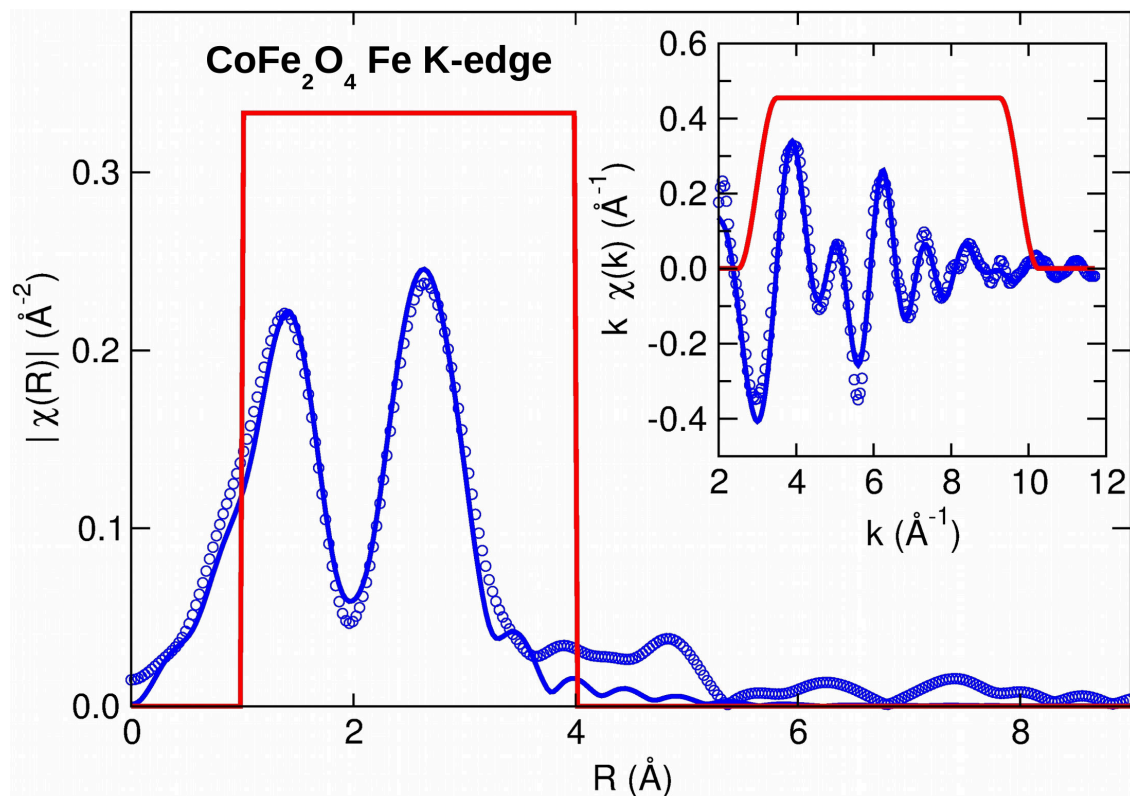


Figure 3.4: Fourier transformed modulus ($|\chi(R)|$) of the $k\chi(k)$ experimental data (open circles) and theoretical fits (solid line) of CoFe_2O_4 nanoparticles are shown. Inset shows $k\chi(k)$ experimental data (open circles) and theoretical fits (solid lines). $|\chi(R)|$ represents raw data without correcting for phase shifts and the window used to select the coordination shell includes single scattering paths as discussed in text.

due to increased disorder at the nanoscale. The EXAFS spectra fits revealed the nanocrystalline Fe_3O_4 to have $40 \pm 5\%$ Fe cations in T_d sites and $60 \pm 5\%$ Fe cation in O_h sites.

3.3.2 Fe and Co K edges of CoFe_2O_4 nanocrystallites

Figure 3.4 shows the Fe K edge EXAFS spectrum and the modulus of the Fourier transform of CoFe_2O_4 measured at room temperature. CoFe_2O_4 structure is similar

Table 3.3: Parameters from the shell fitting of Fe K edge EXAFS analysis of $CoFe_2O_4$. Coordination number (N), energy shift (E_0), Debye-Waller factors (σ^2), average interatomic distances (R) are presented. The overall reduction S_0^2 was obtained for $CoFe_2O_4$ as 0.71 by fitting to a bulk standard and the uncertainties are presented in parenthesis.

Shell	N	E_0 (eV)	σ^2 (\AA^2)	R (\AA)
$Fe_{O_h} - O(1)$	4(1)	-7(2)	0.007(4)	1.99(2)
$Fe_{T_d} - O(1)$	6(1)	-7(2)	0.007(4)	2.00(2)
$Fe_{O_h} - Fe_{O_h}$	6(1)	-7(2)	0.004(1)	2.970(2)
$Fe_{T_d} - Co_{O_h}$	13(2)	-7(2)	0.007(5)	3.48(3)
$Fe_{T_d} - O(2)$	13(2)	-7(2)	0.007(4)	3.52(2)

to Fe_3O_4 except that the majority of Fe^{2+} cations are replaced by Co^{2+} cation. Two main peaks are observed; one at ~ 1.5 \AA and another at ~ 3 \AA . The peak at ~ 1.5 \AA is due to the first oxygen coordination shell (O_h and T_d) and the peak at ~ 3 \AA is due to both Co_{O_h}/Fe_{O_h} and O atoms. The quantified local environment parameters (N , E_0 , σ^2 , and R) are reported in the Table 3.3.

In $CoFe_2O_4$ the bond distances, Debye-Waller factors of $Fe_{O_h} - O$ and $Fe_{T_d} - O$ are similar to that Fe_3O_4 . In the second coordination shell, the Fe ion is surrounded by Co and Fe ions. In $CoFe_2O_4$ (Table. 3.3) the interatomic distance of $Fe_{O_h} - Fe_{O_h}$ is smaller than that of Fe_3O_4 's (Table. 3.2) suggesting that the Co substitution decreases the disorder around Fe_{O_h} sites. EXAFS spectrum fit results identify the nanocrystalline $CoFe_2O_4$ to have $60 \pm 10\%$ Fe cations in T_d sites and $40 \pm 10\%$ Fe cations in O_h sites. Note that Fe cation distribution combined with Co (shown below) quantify the full cation distribution of $CoFe_2O_4$. This observation is consistent with

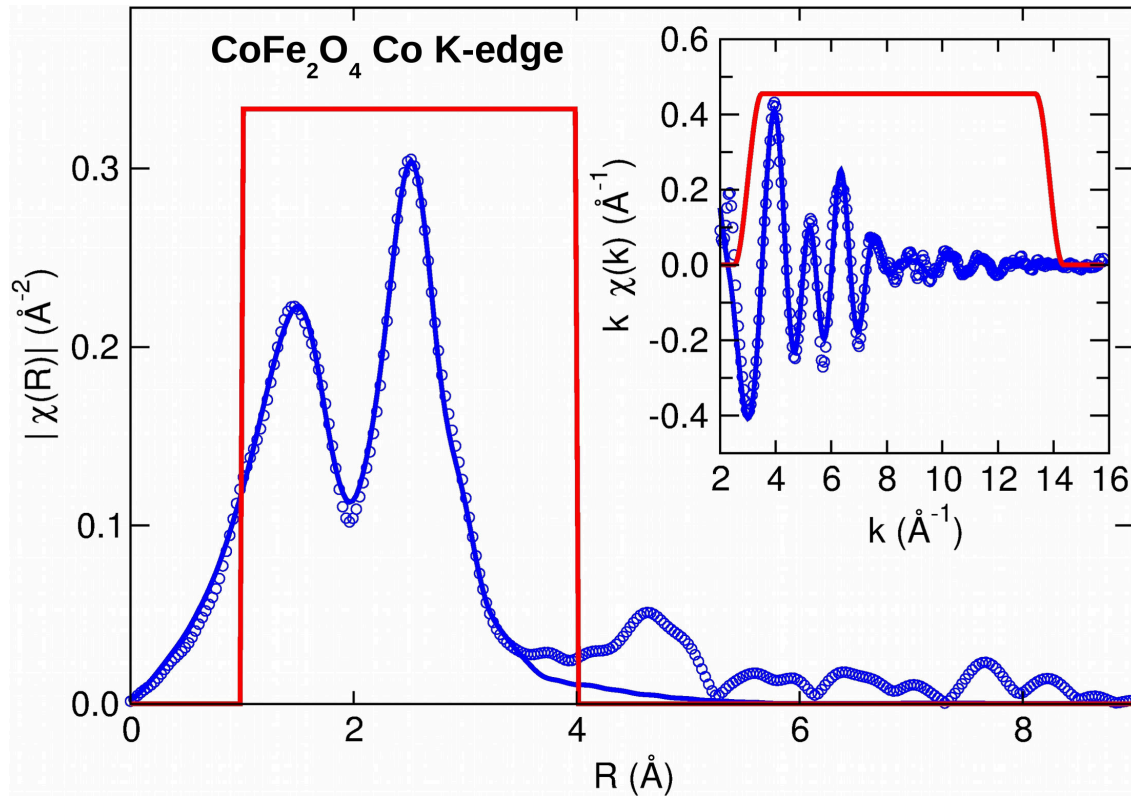


Figure 3.5: Fourier transformed modulus ($|\chi(R)|$) of the $k\chi(k)$ experimental data (open circles) and theoretical fits (solid line) of $CoFe_2O_4$ nanoparticles are shown. Inset shows $k\chi(k)$ experimental data (open circles) and theoretical fits (solid lines). $|\chi(R)|$ represents raw data without correcting for phase shifts and the window used to select the coordination shell includes single scattering paths as discussed in text.

our shell fitting results of $CoFe_2O_4$ that majority of Co ions are located at O_h sites since the $Fe_{T_d} - Fe_{O_h}$ sites in Fe_3O_4 are replaced with $Fe_{T_d} - Co_{O_h}$ bonds.

To further quantify the local environment around Co and cation distributions, we performed EXAFS spectroscopy on the Co K edge of the nanoscale $CoFe_2O_4$. Fig. 3.5 shows the $\chi(k)$ and Fourier transform modulus of the $k\chi(k)$ at the Co K edge. EXAFS shell fitting results are presented in Table. 3.4. The first peak consists of scattering amplitudes from Co ions from nearest neighboring oxygen in T_d and

Table 3.4: Parameters from the shell fitting of Co K edge EXAFS analysis of $CoFe_2O_4$. Coordination number (N), energy shift (E_0), Debye-Waller factors (σ^2), average interatomic distances (R) are presented. The overall reduction S_0^2 was obtained for $CoFe_2O_4$ as 0.71 by fitting to a bulk standard and the uncertainties are presented in parenthesis.

Shell	N	E_0 (eV)	$\sigma^2(\text{\AA}^2)$	R (\AA)
$Co_{T_d} - O(1)$	5(1)	-4(1)	0.012(1)	1.966(7)
$Co_{O_h} - O(1)$	8(1)	-4(1)	0.012(1)	2.003(7)
$Co_{O_h} - Co_{O_h}$	8(1)	-4(1)	0.007(1)	2.970(6)
$Co_{O_h} - O(2)$	3(1)	-4(1)	0.012(1)	3.460(7)
$Co_{O_h} - Fe_{T_d}$	16(1)	-4(1)	0.015(1)	3.483(9)
$Co_{T_d} - Fe_{O_h}$	16(1)	-4(1)	0.015(1)	3.483(9)
$Co_{T_d} - O(2)$	16(1)	-4(1)	0.012(1)	3.52(7)

O_h environments at a distance of 1.966 and 2.003 \AA , respectively. The second peak consists of scattering amplitudes of Co – Co and Co – Fe in O_h and T_d environments. Results clearly identify that compared to Fe – O bonds (Table. 3.3) the Debye-Waller factors of Co – O bonds are greater, indicating that there is some distortion at the Co sites in these $CoFe_2O_4$ nanoparticles (Table. 3.4). The cation distribution of Co sites are identified at $40 \pm 10\%$ available in T_d and $60 \pm 10\%$ available in O_h sites.

Although EXAFS is successful in quantifying the local environment and site occupancies, it does not provide information on the oxidation state of the cations (e.g. what is the % of +2 and +3 in Fe and Co ions). In order to quantify the cation occupancies we performed soft x-ray spectroscopy of Co and Fe $L_{3,2}$ edges of Fe_3O_4 and $CoFe_2O_4$.

3.4 Electronic Structure and Cation Distribution

X-ray absorption spectroscopy (XAS) and x-ray magnetic circular dichroism (XMCD) are element-selective as it involves analysis of the K and $L_{3,2}$ edge absorptions, which occurs at specific photon energy for each element (as discussed in Chapter 2.9). XMCD measures the difference between the core-level XAS using left and right circularly polarized x-rays in the vicinity of an absorption edge. XAS and XMCD results will provide information on the oxidation state (including mixed states), site symmetry, spin state, and crystal-field splitting of the absorbing $3d$ metal ions. Further, XMCD gives insights into the magnetic structure[69]. For example, in Fe_3O_4 the spin arrangement is identified (discussed below) as $(Fe^{3+} \downarrow)_A [Fe^{3+} \uparrow Fe^{2+} \uparrow]_B O_4$ where \uparrow and \downarrow refers to the relative direction of spin moments, $()_A$ and $[]_B$ are T_d and O_h sites respectively.

3.4.1 Qualitative analysis of Fe_3O_4 and $CoFe_2O_4$ nanoparticles

The $L_{3,2}$ edge XMCD spectra for different polarization directions of Fe and Co at 10 K and in ± 1 T applied fields were used to determine the Fe and Co cation distribution in Fe_3O_4 and $CoFe_2O_4$. Figures 3.6a,b show the measured Fe XAS/XMCD of Fe_3O_4 , $CoFe_2O_4$ and Co XAS/XMCD of $CoFe_2O_4$, which are divided into L_3 ($2p_{3/2}$) and L_2 ($2p_{1/2}$) regions. The comparison (Fig. 3.6a) shows that the Fe $L_{3,2}$ edges XAS and XMCD spectra of Fe_3O_4 and $CoFe_2O_4$ are very similar which is indicative that Fe ions occupy similar sites in the two systems. The two sharper and larger intensity of XMCD peaks that are pointing downwards are due to the O_h sites and the remaining peaks that are pointing upwards are due to the T_d sites in Fe_3O_4 and $CoFe_2O_4$ [90].

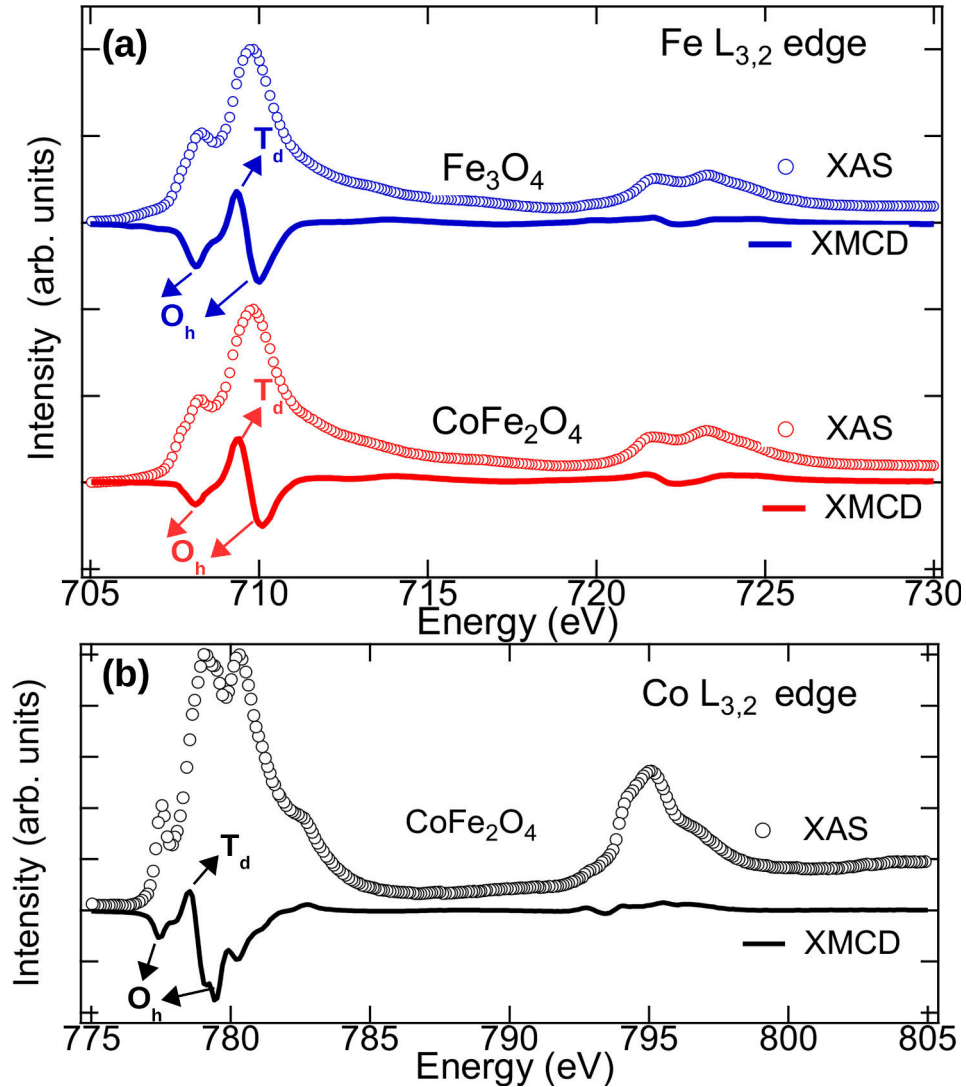


Figure 3.6: (a) Fe $L_{3,2}$ edge XAS/XMCD experimental spectra of Fe_3O_4 and $CoFe_2O_4$ nanoparticles. The XMCD spectra consists of two peaks that are pointing downwards and one upward peak that is pointing upwards. The downward peaks are due to Fe ion O_h sites and upward peaks are due to T_d sites. (b) Co $L_{3,2}$ edge XAS/XMCD experimental spectrum of $CoFe_2O_4$ nanoparticles are shown. The downward and upward peaks are due to O_h and T_d sites respectively.

Similar to Fe $L_{3,2}$ edge, Co $L_{3,2}$ edge also has two different down features and one up feature in the XMCD spectrum representative of O_h and T_d sites. These up and down orientations of the XMCD features in the L_3 absorption edges of Fe_3O_4 and

$CoFe_2O_4$ are due to the antiparallel spin orientations between O_h and T_d sites. The XAS/XMCD experimental spectra are modelled to quantify the cation occupancies and determine the cationic origin of the different spectral features.

3.4.2 Modelling parameters for Fe_3O_4 and $CoFe_2O_4$ nanoparticles

The L_3 edge XAS and XMCD spectra for the ground and final states were calculated using XCLAIM[63] in the atomic limit[91] which is appropriate for the $3d$ electrons. The Hamiltonian includes a spin-orbit interaction in the $2p$ and $3d$ orbitals and Coulomb interactions in the $3d$ shell and between the $3d$ shell and the $2p$ core hole. Parameters were obtained in the Hartree-Fock limit and the values for the Coulomb interaction were scaled down to 80% to account for interatomic screening effects. The initial to final state transitions identified for the Fe^{2+} , Fe^{3+} , Co^{2+} and Co^{3+} are $2p^63d^6 \rightarrow 2p^53d^7$, $2p^63d^5 \rightarrow 2p^53d^6$, $2p^63d^7 \rightarrow 2p^53d^8$, and $2p^63d^6 \rightarrow 2p^53d^7$, respectively. To simulate the spectra, for the O_h sites a crystal field of $10Dq = 1.2$ eV was used, and for the T_d sites a $10Dq = -0.6$ eV was used. Note that for well (ideally) localized systems such as molecules, $T_d = -4/9 \times 10Dq$ for O_h coordination, but in semimetals like these transition metal oxides, $10Dq$ values are affected by delocalization of the $3d$ states in the presence of core holes, as expressed by Carolyn et al.[92] and Patrick et al.[93]. The simulated spectra were described by a Lorentzian of $\Gamma = 0.5$ eV to account for intrinsic linewidth broadening of the excited states, and a Gaussian of $\sigma = 0.5$ eV to account for instrumental broadening (as per usual, and they alter the L_3 and L_2 lineshapes a bit differently[62]).

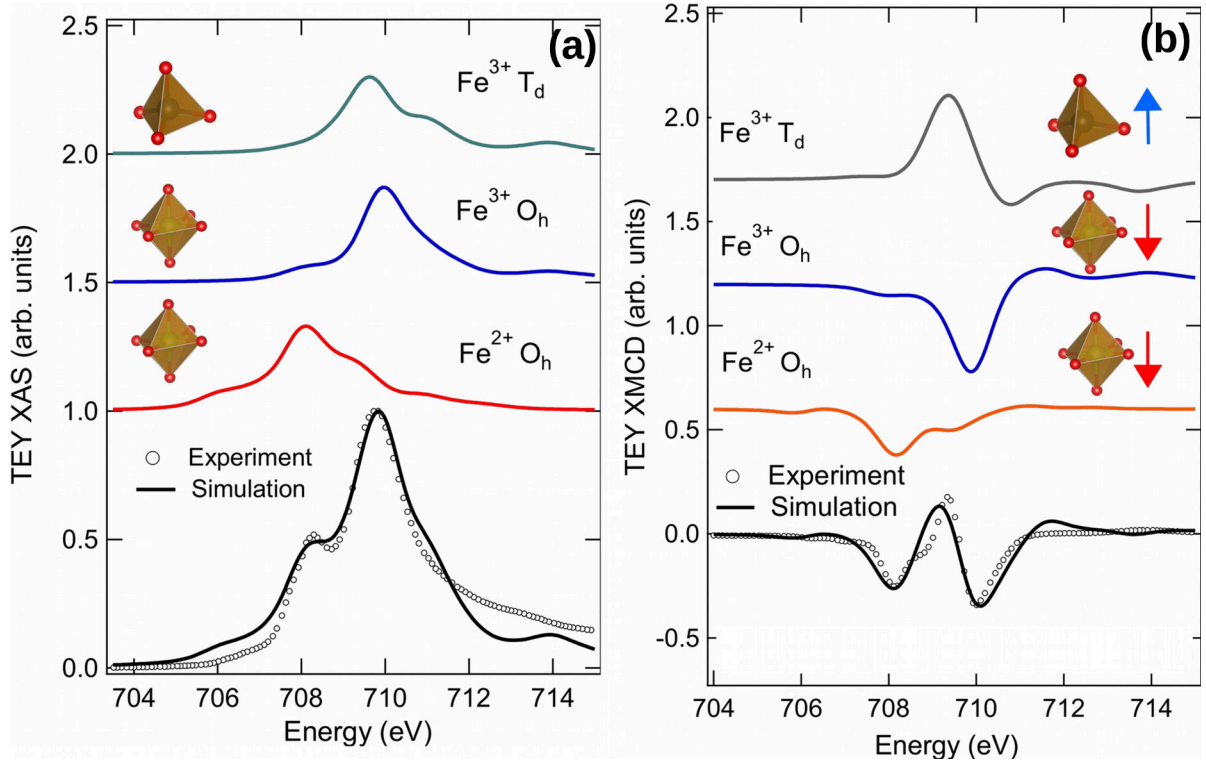


Figure 3.7: (a) Fe L_3 edge XAS experimental spectra and simulations of Fe_3O_4 nanoparticles. The calculated $Fe^{3+} (T_d)$, $Fe^{3+} (O_h)$ and $Fe^{2+} (O_h)$ components of the XAS spectra and theoretical resulting summed spectrum are shown. (b) Fe L_3 edge XMCD experimental spectrum and simulations are shown. The spin arrangement is shown at each T_d and O_h sites. The Fe^{3+} spins on the T_d and O_h sites cancel out their moments due to antiparallel alignment and their net ferrimagnetic moment is caused by the $Fe^{2+} T_d$ spins.

3.4.3 Quantitative XAS and XMCD analysis of Fe_3O_4 nanoparticles

Figure. 3.7a,b shows the XAS and XMCD experimental spectra and theoretical resulting summed spectrum of Fe_3O_4 . The XAS and XMCD spectrum of Fe_3O_4 (Fig. 3.7a) comprises three main components which are derived from the three sites occupied by $Fe^{2+} O_h$, $Fe^{3+} T_d$, and $Fe^{3+} O_h$. The sign of the XMCD is given by the direction of the spin moment of the O_h and T_d sites. The simulation shown here is

mainly focused on the three main transitions of interest in the L_3 region³ at ~ 708 , ~ 709 , and ~ 710 eV. The transition at ~ 707 eV is ascribed to Fe^{2+} in O_h sites, ~ 708 eV is attributed to Fe^{3+} in T_d and ~ 709 eV is related to Fe^{3+} in O_h sites. The relative energy positions of the calculated spectra for the three sites were shifted to obtain the theoretical spectrum compared to experimental spectrum. In Fe_3O_4 nanoparticles the relative distribution of the Fe-sites was found to be 30% Fe^{3+} T_d , 37% Fe^{3+} O_h , and 33% Fe^{2+} O_h from a best weighted sum of simulated Fe-sites. Figure. 3.8 shows the XMCD and the integrated XMCD of Fe ion in Fe_3O_4 nanocrystallites. XMCD sum-rules were used to determine the ratio of orbital (L_z) to spin (S_z) moment provided by the $L_z/S_z = 2q/(9p - 6q)$, where p and q are the integrated XMCD intensities over the L_3 edge, and L_3 and L_2 edges, respectively. For Fe_3O_4 : $L_z/S_z = 0.16$ was determined for Fe.

3.4.4 Quantitative XAS and XMCD analysis of $CoFe_2O_4$ nanoparticles

XAS and XMCD measurements were carried out to obtain information on the cations of Fe and Co in $CoFe_2O_4$ system. Figure 3.9a,b shows the Co L_3 edge XAS and XMCD experimental spectra and simulations. At first, the XAS and XMCD spectra were attempted to fit with only Co^{2+} in O_h and T_d sites assuming that only Co exists in +2 oxidation state as suggested by the thin film standard sample of $CoFe_2O_4$ [95]. However, this approach does not provide a good fit for the spectrum of nanocrystalline $CoFe_2O_4$, and a small fraction of Co^{3+} in T_d is needed, which leads to better agreement with the experimental results. The calculated spectra for the three individual

³Involving L_2 further complicates the process because for oxides the edge jump is difficult to take into account[94]

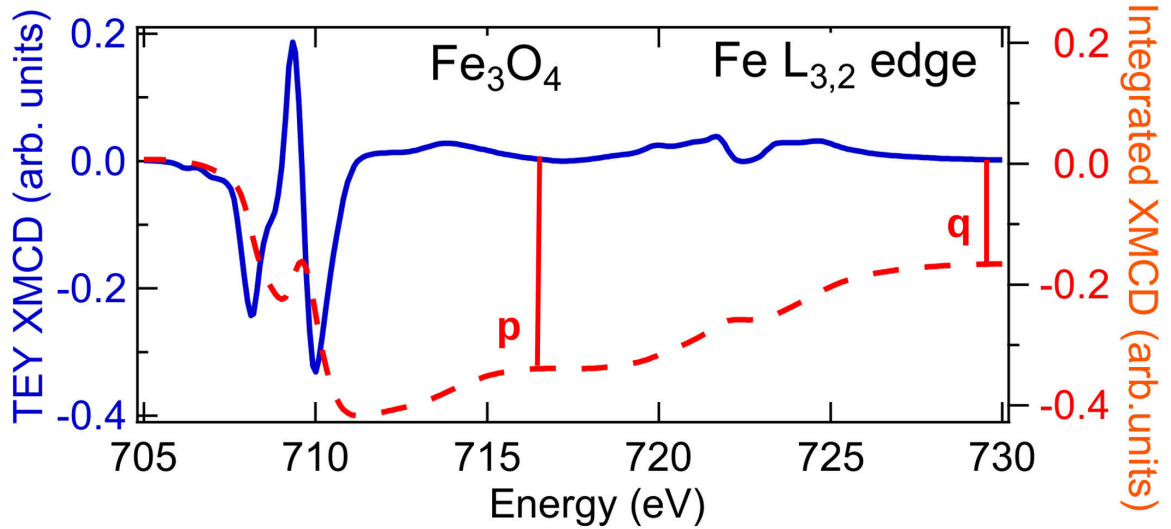


Figure 3.8: Fe $L_{3,2}$ edge XMCD spectrum (left axis) together with integrated XMCD (right axis) are shown. The integrated XMCD intensities p and q are labeled, where p is the integrated XMCD intensity over the L_3 edge, and q is the integrated XMCD intensity over combined L_3 and L_2 edges. The XMCD simulation of the Fe L_3 edge is shown in Fig. 3.7.

components are shown in Figs. 3.9a,b along with the total calculated spectrum of CoFe_2O_4 . The simulation shown is mainly focused on the three main transitions of interest in the L_3 region at ~ 778.5 , ~ 779 , and ~ 781 eV. The transition at ~ 778.5 eV is due to Co^{2+} in T_d sites, ~ 779 and ~ 781 eV is related to Co^{2+} in O_h and Co^{3+} in O_h sites. The relative energy positions of the calculated spectra for the three components were shifted to obtain the total theoretical spectrum. Note that the difference between the simulation and experiment in the energy range of ~ 782 - 784 eV is because for oxides the edge jump is difficult to model due to the s - p intermixing effects. The relative distribution of Co-sites was found to be 60% Co^{2+} O_h , 20% Co^{3+} O_h , and 20% Co^{2+} T_d from a best-weighted sum of simulated Co-sites.

The Fe L_3 edge XAS and XMCD spectra for the CoFe_2O_4 are shown in Fig. 3.10.

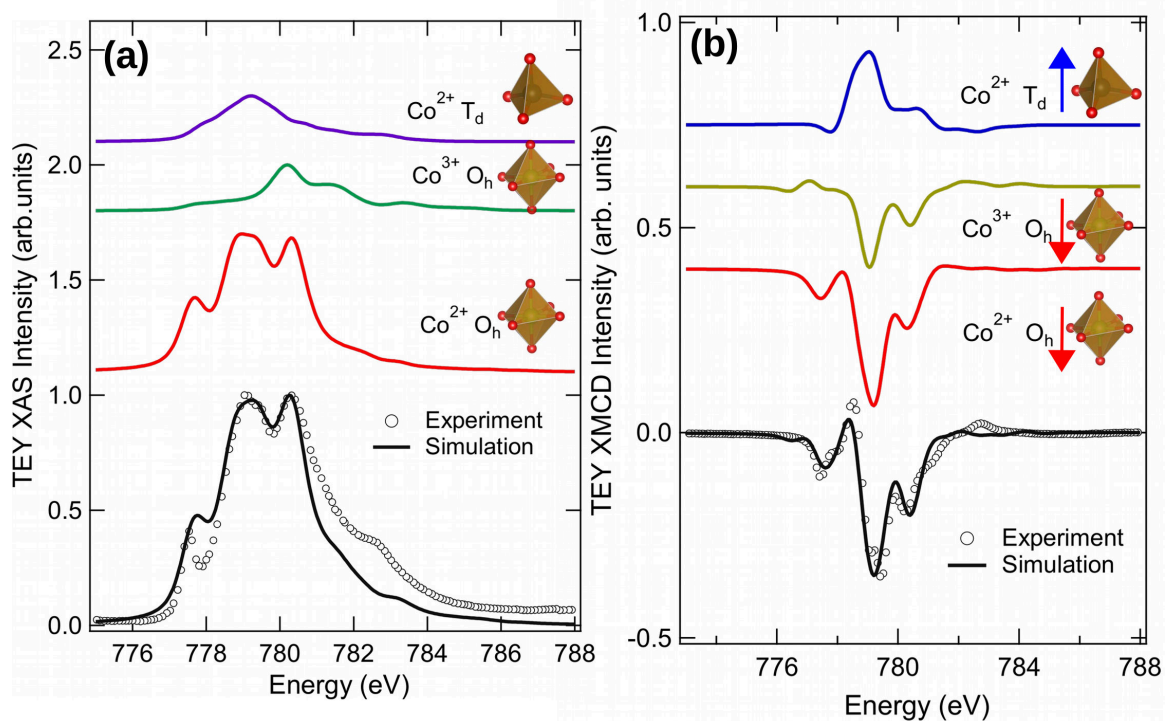


Figure 3.9: (a) Co L_3 edge XAS experimental spectra and simulations of $CoFe_2O_4$ nanoparticles. The calculated $Co^{2+} (T_d)$, $Co^{2+} (O_h)$ and $Co^{3+} (O_h)$ components of the XAS spectra and theoretical resulting summed spectrum are shown. (b) Co L_3 edge XMCD experimental spectrum and simulations are shown. The spin arrangement is shown at each T_d and O_h sites. In $CoFe_2O_4$ we also identify a small fraction ($\sim 20\%$) of Co^{3+} in O_h location as described in the text.

The Fe experimental spectra of $CoFe_2O_4$ are similar to that of Fe_3O_4 (see Fig. 3.7) where both Fe^{2+} and Fe^{3+} ions are present as anticipated. The explicit Fe site-occupancy ratios have been calculated using the theoretically derived $Fe^{2+} O_h$, $Fe^{3+} O_h$, and $Fe^{3+} T_d$ components. The cation distributions obtained by the Co^{2+} and Co^{3+} -sites in T_d and O_h sites are used to constrain the % of Fe-sites in T_d and O_h sites. The agreement with the experimental results obtained for the 40% Fe^{3+} in T_d , 44% Fe^{3+} in O_h , and 16% Fe^{2+} in O_h sites.

Figure. 3.11, shows the Fe and Co XMCD and the integrated XMCD of $CoFe_2O_4$

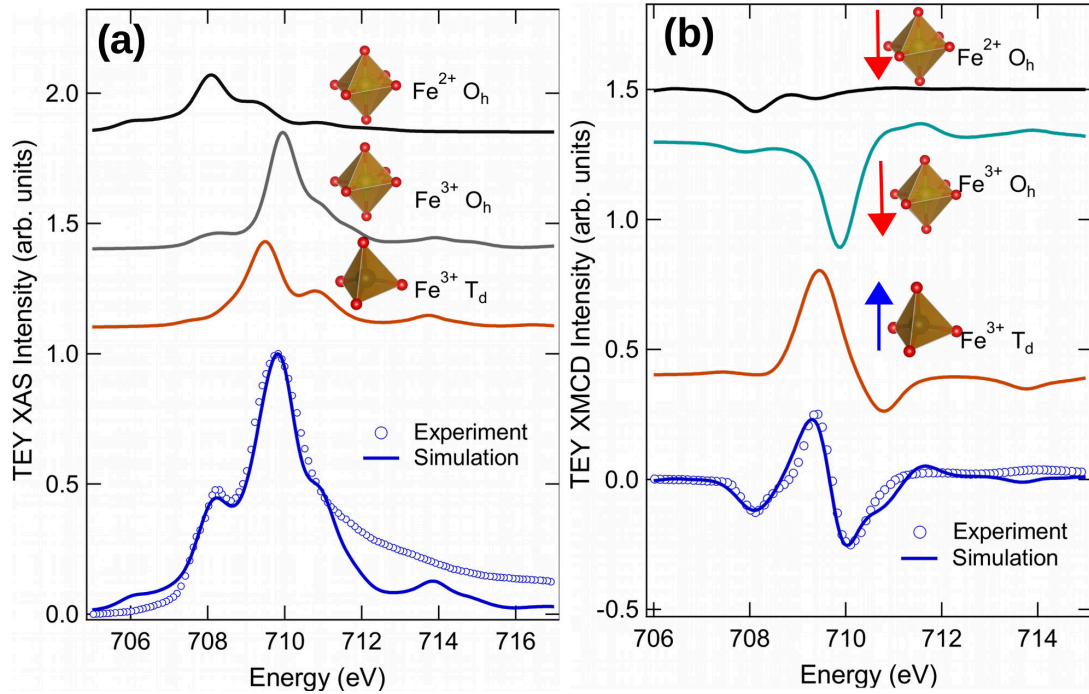


Figure 3.10: (a) Fe L_3 edge XAS experimental spectra and simulations of $CoFe_2O_4$ nanoparticles. The calculated Fe^{3+} (T_d), Fe^{3+} (O_h) and Fe^{2+} (O_h) components of the XAS spectra and theoretical resulting summed spectrum are shown. (b) Fe L_3 edge XMCD experimental spectrum and simulations are shown. The spin arrangement is shown at each T_d and O_h sites. Note that the difference between the simulation and experiment in the energy range of ~ 712 - 714 eV is because for oxides the edge jump is difficult to model due to the s-p intermixing effects.

nanocrystallites. For Fe the L_z/S_z was measured as -0.10 . Compared to Fe_3O_4 , the sign of L_z/S_z of $CoFe_2O_4$ is negative which is indicative that the orbital moment and spin moment are antiparallel to each other. The L_z/S_z of Co is determined as 0.46, four times that of Fe.

Note that the XAS and XMCD measurements of the Fe_3O_4 and $CoFe_2O_4$ nanoparticles are from surface sensitive total electron yield (TEY) measurements. TEY probes the first ~ 2 - 4 nm surface[96] of the nanoparticles as discussed in Section 2.7.1. To further identify whether the cation distribution by XAS and XMCD results are homo-

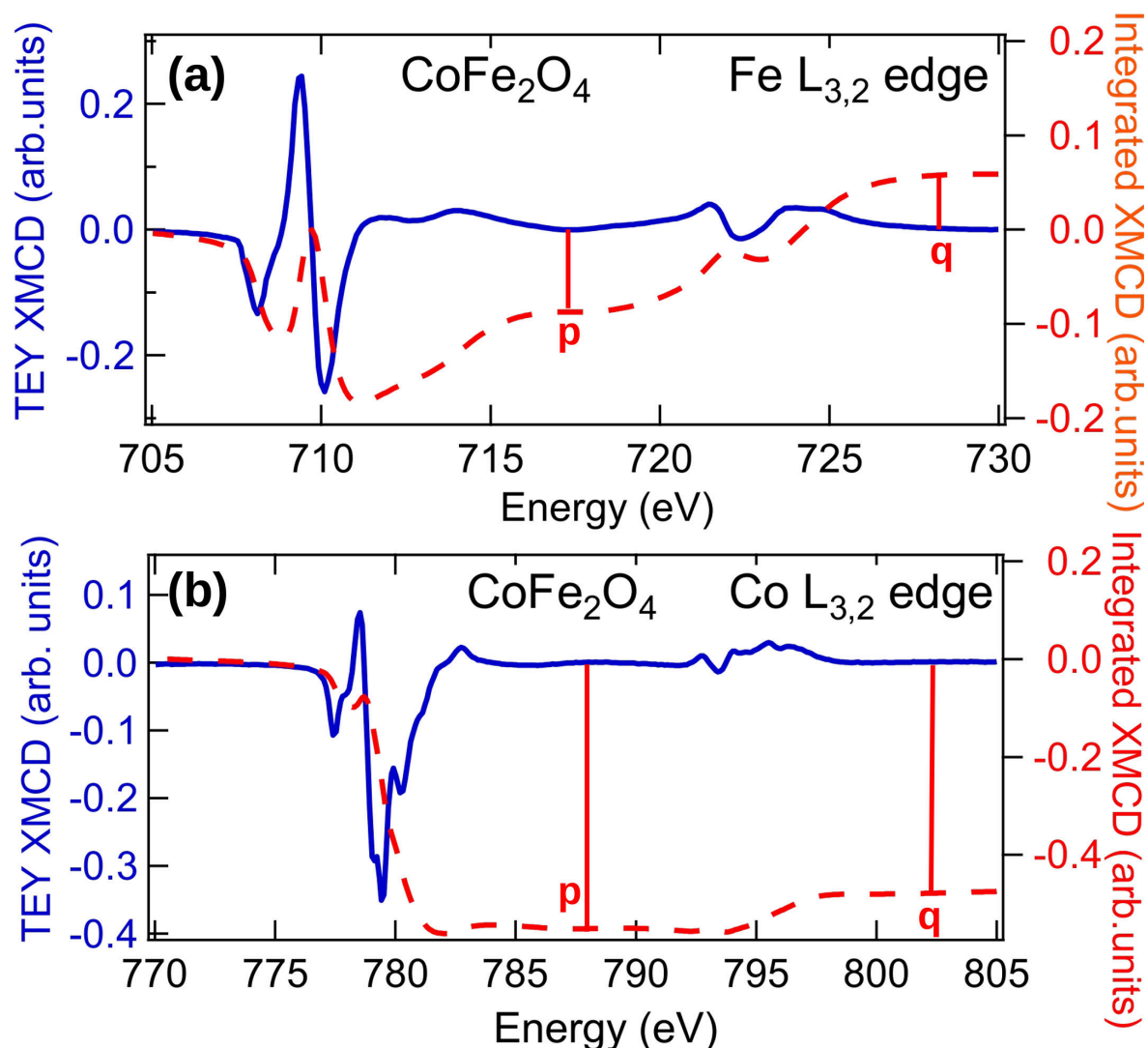


Figure 3.11: Fe $L_{3,2}$ edge XMCD spectrum (left axis) together with integrated XMCD (right axis) are shown. The integrated XMCD intensities p and q are labeled, where p is the integrated XMCD intensity over the L_3 edge, and q is the integrated XMCD intensity over combined L_3 and L_2 edges. The XMCD simulations of the Co and Fe edges (L_3) are shown in Figs. 3.9 and 3.10, respectively.

geneous throughout the nanoparticles, we compared our results with the transmission Mössbauer spectroscopy results.

3.5 Mössbauer Spectroscopy and Cation Distribution

Mössbauer spectroscopy is a local probe of Fe and quantifies the fraction of cations that are occupied in the O_h and T_d sites of Fe_3O_4 and CoFe_2O_4 by the hyperfine parameters (see Chapter 2.8). Figure. 3.12 shows the Mössbauer spectrum of Fe_3O_4 nanoparticles measured at room temperature. The spectrum shows a well-developed magnetic hyperfine splitting typical of magnetite with no trace of superparamag-

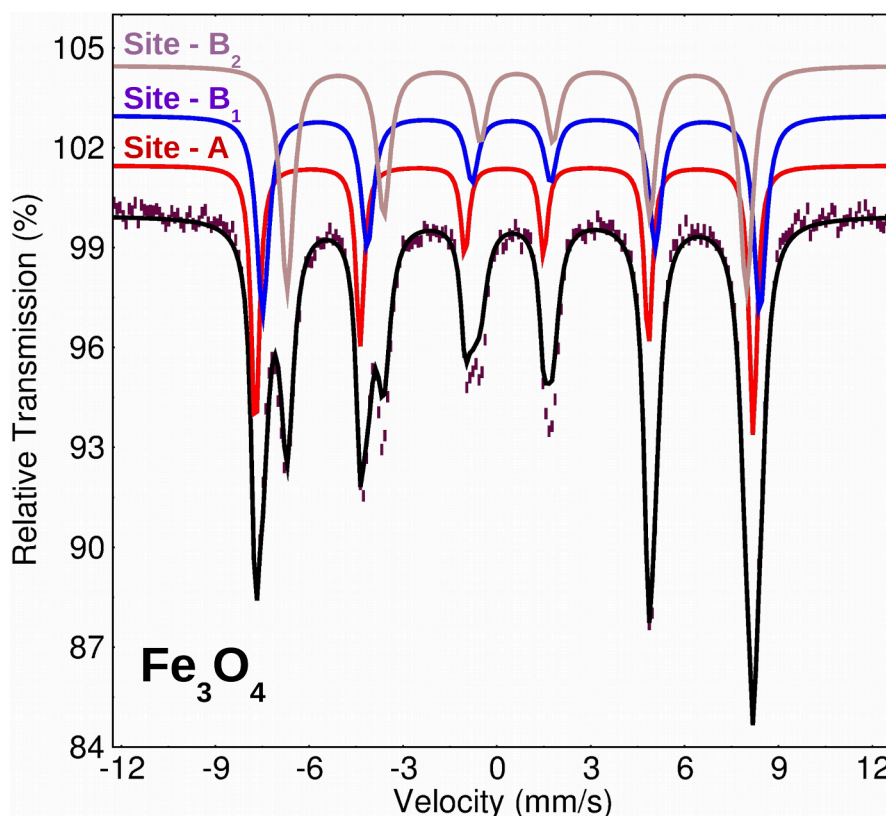


Figure 3.12: Mössbauer spectrum of Fe_3O_4 measured (dotted line) and fit spectrum at room temperature are shown. The spectrum is fit with independent linewidth sextets where $\Gamma = \Gamma_{Nat} + \Delta\Gamma$ (Natural linewidth $\Gamma_{Nat} = 0.133$ mm/s). Three different sites are used to fit the spectrum with three components ($\text{Fe}^{3+} T_d$, $\text{Fe}^{3+} O_h$, and $\text{Fe}^{2+} O_h$) to quantify the cation distribution.

Table 3.5: Mössbauer hyperfine parameters of Fe_3O_4 at room temperature. The spectrum is fit with independent linewidth sextets where Γ is set to 0.13 mm/s. Here $\Delta\Gamma$ is the broadened linewidth, δ is the isomer shift, and B_{hf} is the hyperfine field. Three different sites are used to fit the spectrum and the uncertainties are presented in parenthesis.

	$\Delta\Gamma$ (mm/s)	δ (mm/s)	B_{hf} (T)	Area (%)
Site - A ($Fe^{3+} T_d$)	0.03(1)	0.237(5)	49.44(3)	29(1)
Site - B ₁ ($Fe^{3+} O_h$)	0.11(1)	0.463(8)	49.39(6)	32(1)
Site - B ₂ ($Fe^{2+} O_h$)	0.13(1)	0.635(7)	45.62(1)	39(1)

netic behaviour. The Mössbauer spectrum was fit with three distinct, independent linewidth sextets to determine the linewidth $\Delta\Gamma$, magnetic hyperfine field B_{hf} , isomer shift δ , and quadrupole splitting Δ , with the relative abundance of each site proportional to the relative spectral area of the representative components. The spectrum consists of three sextets: Site – A, Site – B₁, and Site – B₂.

For Fe_3O_4 [97], Site – A is described with $\delta_A = 0.24$ mm/s, $\Delta\Gamma_A = 0.03$ mm/s, $B_{hf(A)} = 49.4$ T and identified as $Fe^{3+} T_d$. Whereas, Site – B₁ is described with $\delta_{B1} = 0.46$ mm/s, $\Delta\Gamma_{B1} = 0.11$ mm/s, $B_{hf(A)} = 49.4$ T and identified as $Fe^{3+} O_h$. Similarly, Site – B₂ is described with $\delta_{B2} = 0.63$ mm/s, $\Delta\Gamma_{B2} = 0.12$ mm/s, $B_{hf(B2)} = 49.6$ T and identified as $Fe^{2+} O_h$. The area of spectral components, 29(1)% $Fe^{3+} T_d + 32(1)\%$ $Fe^{3+} O_h + 39(1)\%$ $Fe^{2+} O_h$ are in excellent agreement with XAS and XMCD analysis discussed above and further evidence that Fe_3O_4 is inverse spinel like.

$CoFe_2O_4$ has near ideal inverse cation distribution in the bulk, however, research has shown that the cation distribution can be modified by heat treatment[98], and

nanoscale affects increases the occupancy of A-sites by Co^{2+} and possibly Co^{3+} . To identify the cation distributions in $CoFe_2O_4$, Mössbauer spectroscopy measurements were performed. Fig. 3.13 shows the Mössbauer spectrum collected at room temperature.

The spectrum of $CoFe_2O_4$ consists of three well defined sites and no trace of superparamagnetic behavior is observed. The A-site (T_d) is populated with Fe^{3+} ions (0.28 mm/s) with a hyperfine field, $B_{hf} = 48.7$ T. The B_1 and B_2 , O_h sites are Fe^{3+}

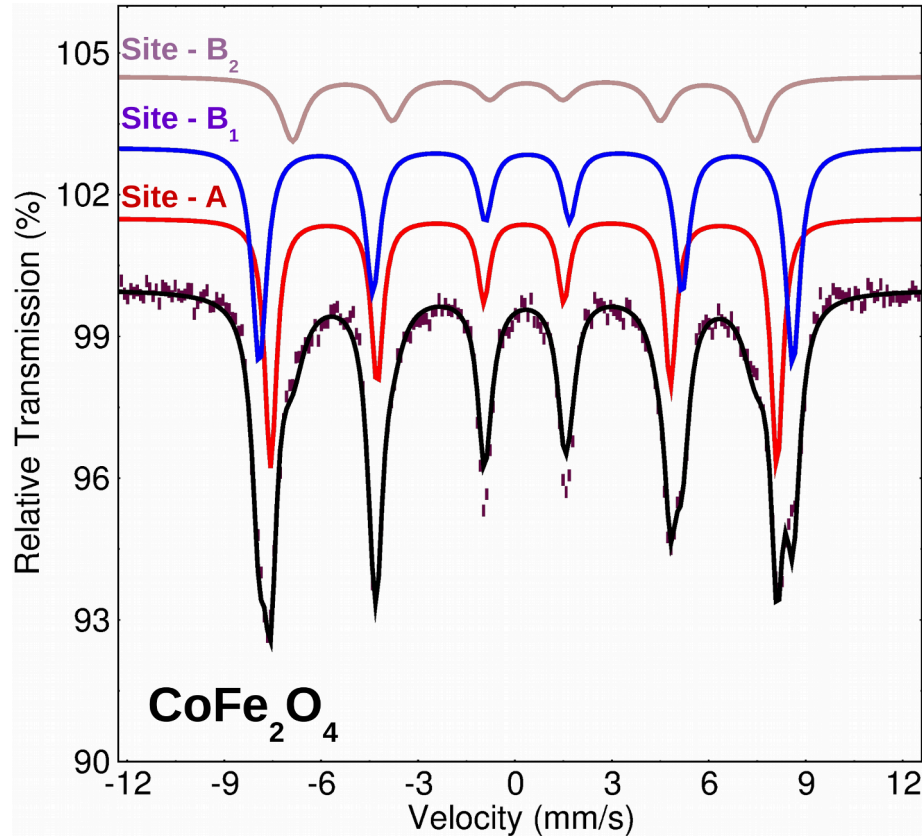


Figure 3.13: Mössbauer spectrum of Fe_3O_4 measured (dotted line) at room temperature. The spectrum is fit with independent linewidth sextets where $\Gamma = \Gamma_{Nat} + \Delta\Gamma$ (Natural linewidth $\Gamma_{Nat} = 0.133$ mm/s). Spectrum is fit (solid line) with three components ($Fe^{3+} T_d$, $Fe^{3+} O_h$, and $Fe^{2+} O_h$) to quantify the cation distribution.

Table 3.6: Mössbauer hyperfine parameters of $CoFe_2O_4$ at room temperature. The spectrum is fit with independent linewidth sextets where Γ is set to 0.13 mm/s. Here $\Delta\Gamma$ is the broadened linewidth, δ is the isomer shift, and B_{hf} is the hyperfine field. Three different sites are used to fit the spectrum and the uncertainties are presented in parenthesis.

	$\Delta\Gamma$ (mm/s)	δ (mm/s)	B_{hf} (T)	Area (%)
Site - A ($Fe^{3+} T_d$)	0.09(1)	0.28(1)	48.70(4)	39(1)
Site - B ₁ ($Fe^{3+} O_h$)	0.14(1)	0.37(1)	51.32(5)	41(1)
Site - B ₂ ($Fe^{2+} O_h$)	0.30(5)	0.31(3)	44.5(2)	19(1)

($\delta_{B1} = 0.37$ mm/s, $B_{hf(B1)} = 51.3$ T) and Fe^{2+} ($\delta_{B2} = 0.31$ mm/s, $B_{hf(B2)} = 44.5$ T) respectively; typical of a ferrite. The area of spectral components, 39(1)% $Fe^{3+} T_d$ + 41(1)% $Fe^{3+} O_h$ + 19(1)% $Fe^{2+} O_h$ are in agreement with XAS and XMCD analysis discussed above in Section 3.4.

From the area ratio $r = T_d/O_h$ of the T_d and O_h subspectra (e.g. XAS, EXAFS, and Mössbauer spectra) the parameter $x = (1 - r)/(1 + r)$ [99], which gives the Co^{2+} occupation of T_d -sites and therefore the cation distributions can be calculated.

3.5.1 Cation distribution from Mössbauer spectroscopy of $CoFe_2O_4$

From the Mössbauer spectroscopy fits fraction of Fe ions are quantified as:

$$39(1)\% Fe^{3+} T_d + 41(1)\% Fe^{3+} O_h + 19(1)\% Fe^{2+} O_h$$

With the obtained cation distribution, r (area ratio) and x are calculated as 0.65 (T_d/O_h) and 0.21 respectively (suggesting that Co^{2+} ions are occupying T_d and $CoFe_2O_4$ is not a completely inverse). Using the value of x the correlated cation

distribution⁴ becomes $(Co_{0.21(1)}Fe_{0.79(1)}^{3+})[Co_{0.79(1)}Fe_{0.83(1)}^{3+}Fe_{0.38(1)}^{2+}]O_4$.

3.5.2 Cation distribution from XAS and XMCD of $CoFe_2O_4$

From the XAS/XMCD simulations the fraction of Fe ions are quantified as:

$$40(2)\% Fe^{3+} T_d + 44(2)\% Fe^{3+} O_h + 16(2)\% Fe^{2+} O_h$$

With the above information, we obtain r (area ratio) = 0.66 and $x = 0.20$ (suggesting that Co^{2+} ions are occupying T_d sites. Based on the value of x the correlated cation distribution becomes $(Co_{0.20(2)}Fe_{0.80(4)}^{3+})[Co_{0.80(4)}Fe_{0.88(4)}^{3+}Fe_{0.32(4)}^{2+}]O_4$.

From the XAS and XMCD simulations the fraction of Co ions are quantified as:

$$20(2)\% Co^{2+} T_d + 20(2)\% Co^{3+} O_h + 60(2)\% Co^{2+} O_h$$

3.6 Comparison of Cation Distributions from XAS and XMCD and Mössbauer Spectroscopy of Fe_3O_4 and $CoFe_2O_4$

A comparison of the cation distributions obtained from EXAFS, XAS/XMCD, and Mössbauer spectroscopy are summarized in Table 3.7.

3.7 The Magnetism and Oxygen Connection

The cation distribution by electronic structure and local probes provides direct measure that in $CoFe_2O_4$, Co^{2+} ions are occupying both T_d and O_h sites. The majority ($\sim 60\%$) of Co^{2+} ions occupy Co^{2+} in O_h sites, and 20% of Co^{2+} occupy T_d sites. Additionally, we also identify a small fraction ($\sim 20\%$) of Co^{3+} ions in O_h sites.

⁴Note that T_d and O_h sites are represented by () and [] respectively.

Table 3.7: A comparison of cation distributions obtained from EXAFS, Mössbauer spectroscopy, and XAS/XMCD measurements are shown. EXAFS identifies the fraction of the Fe and Co ions that are O_h coordinated to oxygen as opposed to T_d coordinated (but is not sensitive to oxidation state). Mössbauer spectroscopy is sensitive to Fe ions (oxidation state and local environment) and quantifies the O_h and T_d sites. XAS/XMCD provides T_d and O_h cation distributions of both Fe and Co (sensitive to oxidation states).

Method	Fe_3O_4	$CoFe_2O_4$
EXAFS	$(Fe_{1.2(2)})[Fe_{1.8(2)}]O_4$	$(Co_{0.20(5)} Fe_{0.80(5)})[Co_{0.80(10)}Fe_{1.20(10)}]O_4$
Mössbauer spectroscopy	$(Fe_{0.87(1)}^{3+})[Fe_{0.96(1)}^{3+}Fe_{1.17(1)}^{2+}]O_4$	$(Co_{0.21(1)}Fe_{0.80(1)}^{3+})[Co_{0.79(1)}Fe_{0.83(1)}^{3+}Fe_{0.38(1)}^{2+}]O_4$
XAS/XMCD	$(Fe_{0.90(6)}^{3+})[Fe_{1.11(6)}^{3+}Fe_{0.99(6)}^{2+}]O_4$	$(Co_{0.20(2)}^{2+}Fe_{0.80(4)}^{3+})[Co_{0.60(4)}^{2+}Co_{0.20(2)}^{3+}Fe_{0.88(4)}^{3+}Fe_{0.32(4)}^{2+}]O_4$
	Inverse spinel	Mixed spinel

In Fe_3O_4 , O_h sites are occupied by Fe^{3+}/Fe^{2+} and T_d sites are occupied by only Fe^{3+} . Ions in O_h and T_d sites ($Fe^{3+}O_h \uparrow - O - Fe^{3+}T_d \downarrow$) are coupled antiferromagnetically via the superexchange interaction, and the $Fe^{3+}O_h$ and $Fe^{2+}O_h$ sites ($Fe^{3+}O_h \uparrow - O - Fe^{2+}O_h \uparrow$) are coupled ferromagnetically via double exchange interaction, here O is the lattice oxygen.

In $CoFe_2O_4$, O_h sites are occupied by $Co^{2+}/Co^{3+}/Fe^{2+}/Fe^{3+}$ and T_d sites are occupied by Co^{3+}/Fe^{3+} . In addition to $Fe^{3+}O_h \uparrow - O - Fe^{3+}T_d \downarrow$ coupled antiferromagnetically via the superexchange interaction; $Fe^{3+}O_h \uparrow - O - Co^{2+}O_h \uparrow$ are coupled ferromagnetically via double exchange interaction, and other combinations using Co^{2+} , Co^{3+} , Fe^{2+} , and Fe^{3+} are also possible via intermediate oxygen atoms. Much of the superexchange (antiferromagnetic) and double exchange (ferromagnetic) mechanisms are due to the oxygen that lies between two $3d$ orbitals, as shown in Fig. 3.14.

To gain insights into how the O $2p$ states interact with Fe and Co ions ($3d$ states)

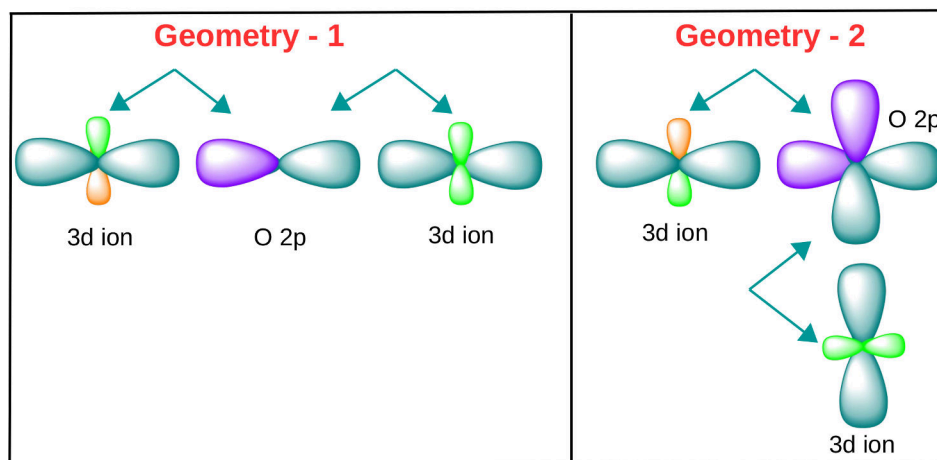


Figure 3.14: Geometry – 1: $3d$ ions interact via an O $2p$ states in-between (the 180° geometry), both $3d$ ions couple to the same p -orbital. In this configuration antiferromagnetic superexchange results. Geometry – 2: When the angle of the $3d - O 2p - 3d$ group is 90° , the $3d$ ions couple to O $2p$ -states, making it impossible for an electron on one $3d$ -ion to influence the $3d$ ion on the other site. In this case, ferromagnetic exchange develops.

in the Fe_3O_4 and $CoFe_2O_4$ systems we performed XAS on O K edge. The primary difference between the O K edge and the Fe/Co (K and L edge) XAS is that O $2p$ bands are delocalized and form wide bands. O K -edge of iron oxides and several $3d$ transition metal oxides have been studied by de Groot et al.[100] and they have shown that the shape of the spectrum is sensitive to the $3d$ electron count. Later, using full multiple-scattering approach Wu et al.[101] identified that the pre-peak structure is due to the transitions from the oxygen $1s$ core state to antibonding oxygen $2p$ states hybridized with Fe $3d$ orbitals. The pre-peak consists of two components and identified as t_{2g} and e_g symmetry bands separated by ligand field splitting. The t_{2g} orbitals (xy , xz , and yz) can hold six electrons and e_g orbitals ($x^2 - y^2$, z^2) can accommodate four electrons. For example, in transition metal oxides with O_h coordination, the transition metal ions are surrounded by six oxygen ions (O^{2-}) which

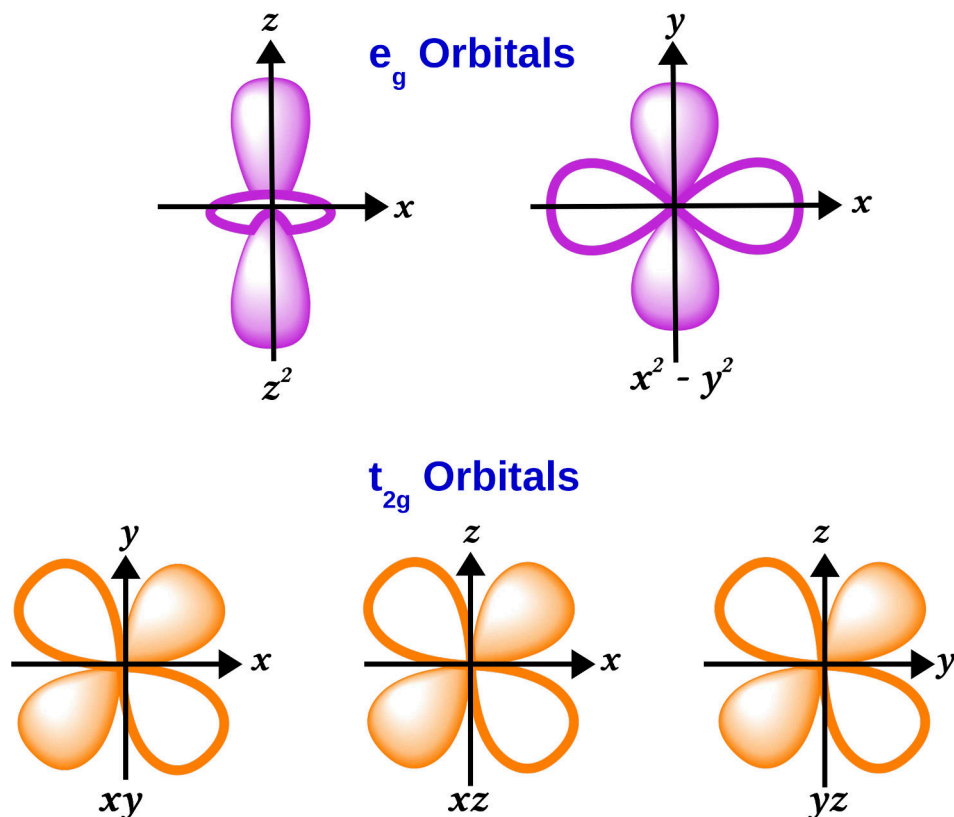


Figure 3.15: Five d orbitals d_{xy} , d_{xz} , d_{yz} , $d_{x^2-y^2}$, and d_{z^2} are shown. In octahedral coordination the metal e_g orbitals ($d_{x^2-y^2}$ and d_{z^2}) are pointed towards the O $2p$ ligands and results in higher energy compared to t_{2g} orbitals (d_{xy} , d_{xz} , and d_{yz}).

give rise to the crystal field splitting of d orbitals. Wave functions that are pointing toward O^{2-} ions have higher energy in comparison with wave functions pointing in between them. Figure 3.15 shows the two configurations of higher energy e_g and lower energy t_{2g} orbitals.

Oxygen K edge XAS of Fe_3O_4 and $CoFe_2O_4$ nanoparticles are shown in Figures 3.16a,b, respectively. The shaded region (530 – 533 eV) corresponds to the excitation from the O $1s$ to the hybridized O $2p$ – Fe and Co $3d$ orbitals, and the higher energy peaks (> 535 eV) corresponds to O $2p$ – Fe and Co $4s4p$ orbitals. In

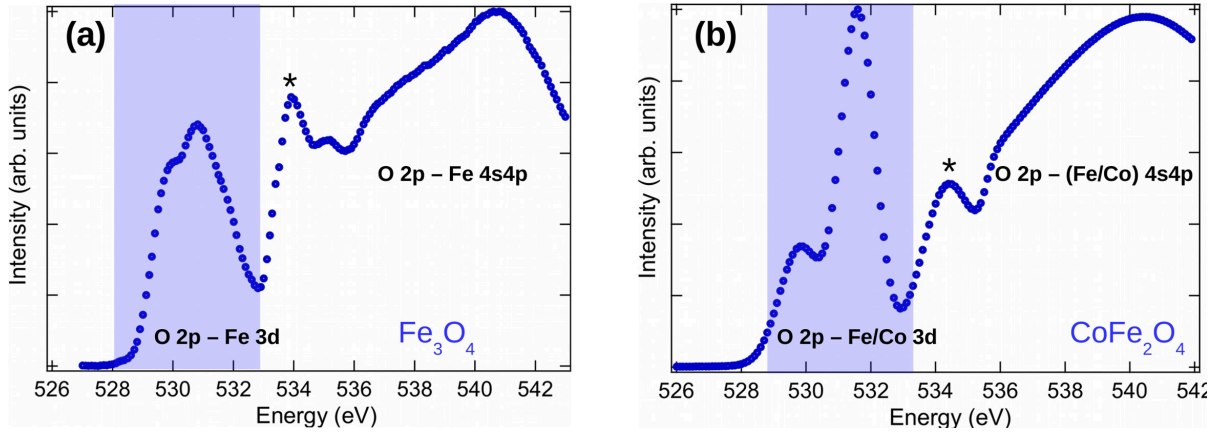


Figure 3.16: Oxygen K edge of (a) Fe_3O_4 and (b) CoFe_2O_4 are shown. The hybridization region of $\text{O } 2p - \text{Fe } 3d$ (Fe_3O_4) and $\text{O } 2p - \text{Fe/Co } 3d$ (CoFe_2O_4) are shaded in blue, * at 535 eV is due to vicinal oxygen from carbon conductive tape[102] and the broad peaks above 536 eV are due to $\text{O } 2p - \text{Fe/Co } 4s4p$ orbitals.

Fe_3O_4 nanoparticles the first peak is due to $\text{O } 2p - \text{Fe } 3d$ hybridization. Similarly, in CoFe_2O_4 nanoparticles it is due to $\text{O } 2p - \text{Fe}$ and $\text{Co } 3d$ orbitals. The experimental spectra shows significant differences (Figs. 3.16a,b) in both the shape and peak intensities of Fe_3O_4 and CoFe_2O_4 , indicating that the oxygen occupancy of t_{2g} and e_g orbitals are different. Because the nature of bonding between the oxygen and transition metals are important in the magnetism, to elucidate the role of oxygen we performed magnetic susceptibility measurements.

3.7.1 Magnetic susceptibility as a probe to redox mechanism in Fe_3O_4 and CoFe_2O_4 nanocrystallites

Figure 3.17a,c shows the zero-field-cooled (ZFC) and field-cooled (FC) $\chi(T)$ curves of Fe_3O_4 measured in O_2 deficient and O_2 rich environments. The nanoparticles were first cooled from 300 to 2 K under zero field, and then a 5 mT field was applied. In

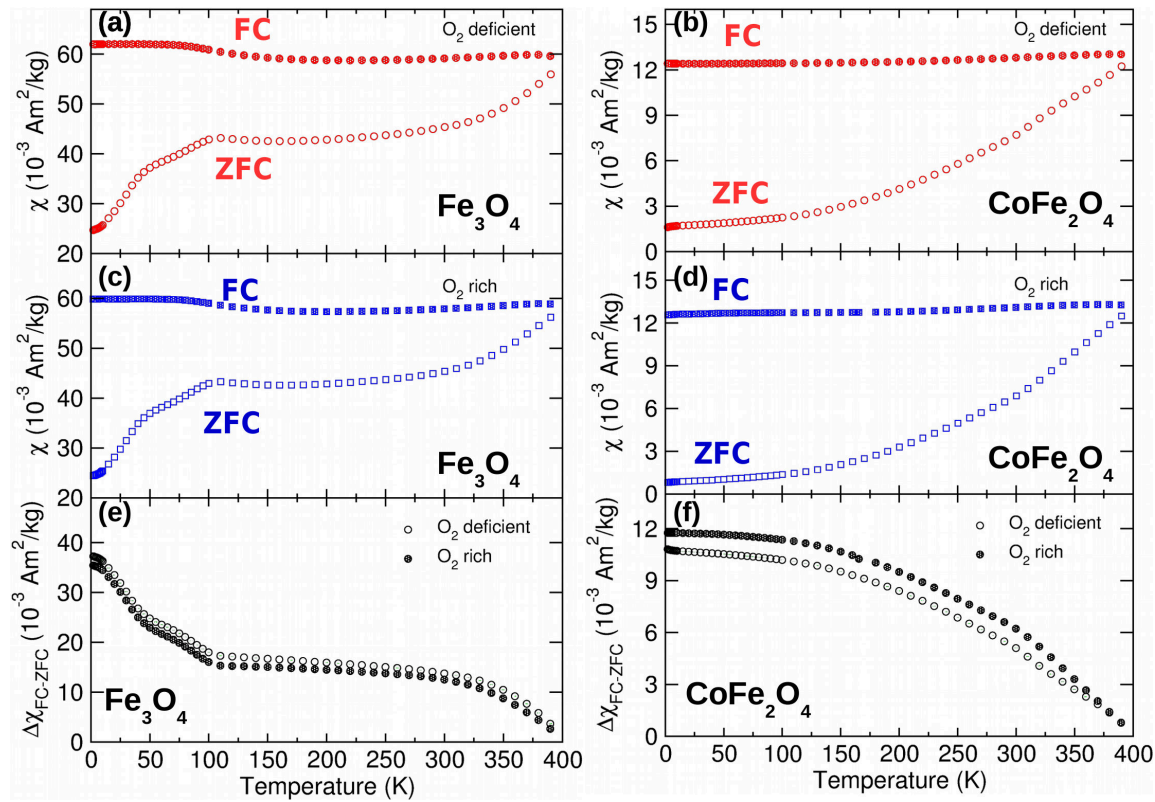


Figure 3.17: (a,b) Zero-field cooled (ZFC) and field cooled (FC) $\chi(T)$ (Fe_3O_4 and CoFe_2O_4) of O_2 deficient systems. (c,d) ZFC and FC of $\chi(T)$ (Fe_3O_4 and CoFe_2O_4) of O_2 rich systems. (e) A comparison between $\Delta\chi_{FC-ZFC}$ (difference between FC and ZFC) of O_2 deficient and O_2 rich of Fe_3O_4 is shown. (f) A comparison between $\Delta\chi_{FC-ZFC}$ of O_2 deficient and O_2 rich of CoFe_2O_4 is shown. Note that in Fe_3O_4 , O_2 rich $<$ O_2 deficient and in CoFe_2O_4 , O_2 rich $>$ O_2 deficient as discussed in the text.

the warming cycle, $\chi(T)$ was measured – i.e., $\chi_{ZFC}(T)$. The $\chi(T)$ was measured in the cooling cycle keeping the magnetic field constant, giving rise to the $\chi_{FC}(T)$ curve. In both O_2 deficient and O_2 rich conditions the ZFC and FC susceptibilities for the Fe_3O_4 nanoparticles remained separate even at 400 K, indicating that their blocking⁵ temperature is above 400 K. In magnetic nanoparticles, the irreversibility in FC and

⁵It is the temperature where the ZFC and FC magnetizations diverge

ZFC profiles arises from the collective excitations of the equilibrium directions of nanoparticle magnetization. The $\chi(T)$ measurements of both O_2 deficient and O_2 rich samples are similar (see Fig. 3.17a,c). The $\chi(T)$ of ZFC curve increases and FC curve decreases rapidly at ~ 105 K, that corresponds to the Verwey transition in Fe_3O_4 , close to the bulk[103] and nanoparticles[104] of 120 K. Earlier, Fe_3O_4 thin films studied by Yang et al.[105] and Balakrishna et al.[106] observed such a decrease in Verwey transition temperature and attributed this to Fe vacancies on B sites and interfacial strain.

Figure 3.17b,d shows the $\chi_{ZFC}(T)$ and $\chi_{FC}(T)$ of $CoFe_2O_4$ nanoparticles in O_2 deficient and O_2 rich environments. The crystal structure, crystallite size, and lattice constants are similar (see Fig. 3.2 and Table. 3.1) to Fe_3O_4 and gives further insights into the relationship between the oxygen vacancy defects and magnetism. The temperature dependent susceptibility (FC/ZFC) of $CoFe_2O_4$ resembles to that of Fe_3O_4 with blocking temperature above 400 K. Unlike Fe_3O_4 , $CoFe_2O_4$ does not show Verwey transition (Fig. 3.17b,d). In Fe_3O_4 the origin of metal – insulator transition is still under debate and identifying the sources that are responsible for its origin is beyond the scope of this thesis, however, it is worth noting that one of the widely reported explanation is that rapid electron exchange between the Fe^{2+} and Fe^{3+} ions at the O_h sites are responsible for this transition. In $CoFe_2O_4$, because Co^{2+} ions replace Fe^{2+} in O_h and Co^{3+} ions replace Fe^{3+} in O_h (Table. 3.7) the relatively higher electron negativity Co^{2+} do not prefer to transform to Co^{3+} , suppressing the Verwey transition. Earlier, Abellä et al.[107] has shown that $Fe_{3-x}Co_xO_4$ ($x \leq 5\%$) is sufficient to remove the transition.

The magnetometry measurements performed in O_2 rich and O_2 deficient samples have an analogy to some of the catalysts that work under cyclic conditions of oxygen rich and lean conditions. For example, noble metal supported oxides catalysts are widely used in automotive three-way catalytic converters to remove toxic gases from the automotive engine exhaust[108]. The converters perform adverse tasks such as reducing nitrogen oxides (NO_x) and oxidizing carbon monoxide (CO). Chemical reactions, like $2NO_x \rightarrow N_2 + xO_2$ and $2CO + O_2 \rightarrow 2CO_2$ takes place on the surface of *active* sites, but only within a specific narrow range of oxygen partial pressures. The fundamental role of these oxide catalyst supports is that of oxygen reservoirs. Redox couple mechanisms are excellent at creating and annihilating oxygen vacancies and provides a window of opportunity to maintain oxygen partial pressure in oxygen rich and lean conditions. For instance a general formula for simple metal oxide can be written as $MO_x \leftrightarrow MO_{x-y} + (y/x)O_x$ where M is a metal ion. By identifying whether a system undergoes a redox reaction or not, to the first order, we can estimate its NO_x reduction catalytic activity.

Embracing this idea, we compared the NO_x reduction catalytic activity of the Fe_3O_4 and $CoFe_2O_4$ during O_2 lean and rich periods to see any common features. Figure 3.18 shows the NO_x reduction catalytic activity of both inverse spinel Fe_3O_4 and mixed spinel $CoFe_2O_4$ as a function of temperature. Results show that Fe_3O_4 is not active for direct nitric oxide (NO) decomposition possibly because (as identified by O_2 rich and O_2 deficient magnetic susceptibility measurements) it cannot undergo a redox couple reaction by maintaining local oxygen partial pressure. Remarkably, $CoFe_2O_4$ shows excellent activity for direct NO_x decomposition, as shown in Fig. 3.18.

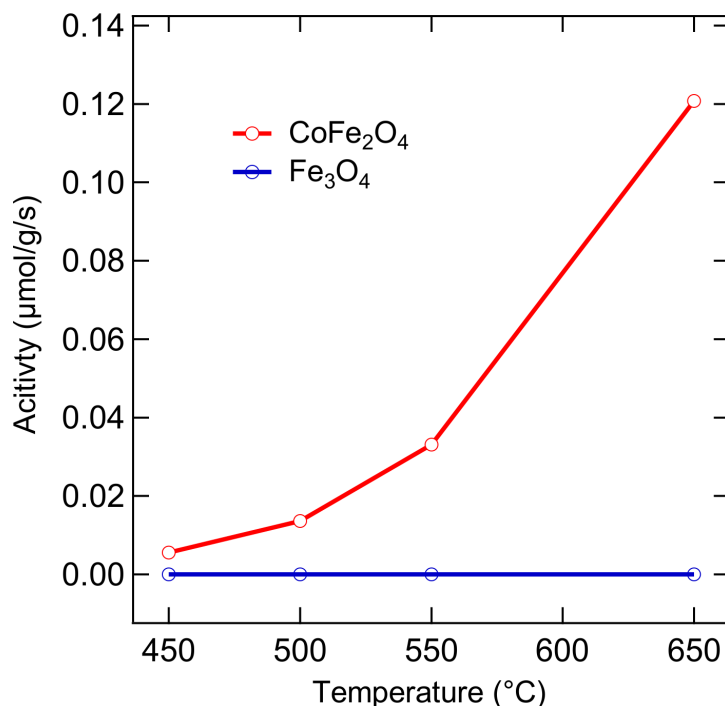


Figure 3.18: Catalytic activity as a function of temperature of Fe_3O_4 and $CoFe_2O_4$ are shown. Nanocrystallites of Fe_3O_4 are inactive and $CoFe_2O_4$ are active.

The reasons behind this are mostly due to the surface oxygen mobility of $CoFe_2O_4$ catalyst as evidenced by the magnetic susceptibility measurements. The difference in $\Delta\chi(T)_{FC-ZFC}$ is an indication that the replacement of Fe ions by Co ions favor the redox reaction in $CoFe_2O_4$, thereby refining the surface oxygen mobility.

3.8 Conclusions

In this Chapter, we have performed a comprehensive study on nanoscale oxide systems Fe_3O_4 and $CoFe_2O_4$. The two systems are phase pure and consists of an identical space group of $Fd\bar{3}m$ with comparable lattice constants and crystallite sizes. Local environment probe EXAFS on Fe and Co K edges were used to quantify the co-

ordination number, bond distances, Debye-Waller factor (disorder parameter), and the fraction of O_h and T_d components. XAS/XMCD measurements and ligand field multiplet theory calculations on Fe, Co $L_{3,2}$ edge quantified the oxidation states of Fe, Co and their relative sign ($|\uparrow\rangle$ or $|\downarrow\rangle$) of their magnetic moment. Mössbauer spectroscopy measurements further complemented the ion distributions allowing identification of their overall cation distribution as as $(Fe_{0.90(6)}^{3+})[Fe_{1.11(6)}^{3+}Fe_{0.99(6)}^{2+}]O_4$ and $(Co_{0.20(2)}^{2+}Fe_{0.80(4)}^{3+})[Co_{0.60(4)}^{2+}Co_{0.20(2)}^{3+}Fe_{0.88(4)}^{3+}Fe_{0.32(4)}^{2+}]O_4$ for Fe_3O_4 (inverse spinel) and $CoFe_2O_4$ (mixed spinel) respectively. Oxygen K edge XAS measurements were very distinct from each other; indicating that the transition metal $3d$ – oxygen $2p$ hybridization strengths are different ($3d - 2p$ bonding is weaker in $CoFe_2O_4$ nanocrystallites). As a consequence of this hybridization, to probe the $3d$ localized electrons effect on the delocalized oxygen orbitals, we performed magnetic susceptibility measurements in O_2 rich and O_2 deficient environments. In comparison to Fe_3O_4 , we showed that $CoFe_2O_4$ shows excellent redox property via the mobility of surface lattice oxygen and oxygen vacancies. To further understand the relationship between the redox mechanism and surface oxygen (vacancies), we performed nitric oxide (NO) reduction catalysis measurements. Results showed that the catalytic activity of $CoFe_2O_4$ (a system that showed excellent redox properties) is remarkably high compared to Fe_3O_4 indicating that O_2 rich and O_2 deficient measurements play a key role in providing insights into the magnetism of oxide systems.

Chapter 4

Oxygen rich and oxygen deficient magnetism of CeO₂ nanoshapes

4.1 Introduction

In the previous Chapter we established a connection between the defects and magnetism via O₂ rich and O₂ deficient susceptibility of strongly ferromagnetic and ferrimagnetic systems such as Fe₃O₄ and CoFe₂O₄ nanocrystallites. In this Chapter, we apply the principles to nanoscale dilute magnetic semiconducting oxide CeO₂ (nanoceria). Nanoceria exhibits a growing popularity in the magnetism[42; 109] and catalysis[110; 111; 84] research. It is often used as a prototypical system due to the intrinsic structural and redox properties. The crystallographic defect structure of nanoceria is predominately oxygen vacancy based, where an oxygen ion is removed from a lattice position, and a vacancy is created. In ceria's structure (Figure 4.1), the defect formation is explained by the reaction $4\text{Ce}^{4+} + \text{O}^{2-} \rightarrow 4\text{Ce}^{4+} + 2\text{e}^-/\square + \frac{1}{2}\text{O}_2 \rightarrow 2\text{Ce}^{4+} + 2\text{Ce}^{3+} + \square + \frac{1}{2}\text{O}_2$, where \square is an oxygen vacancy and O²⁻ and O₂ represent lattice and molecular oxygen, respectively[108]. The valence change of Ce⁴⁺ to Ce³⁺ with concomitant oxygen vacancy formation significantly modifies the reactivity of nanoceria. Esch et al.[112] proposed that these oxygen vacancies cluster and expose the Ce³⁺ ions to gas phase reactants such as CO and NO. Campbell et al.[111] specifically reported that reactive Ce³⁺ are formed when three oxygen ions are removed, consisting of a surface dimer plus a subsurface oxygen. Much of the interest in ceria materials is because of its high oxygen storage capacity from being able to form and eliminate these oxygen vacancies rapidly. Because of this fast Ce⁴⁺/Ce³⁺ redox cycle, CeO₂ can store oxygen during operation in oxygen-rich conditions[113] and release oxygen to the surroundings in oxygen-lean conditions[114], as used in

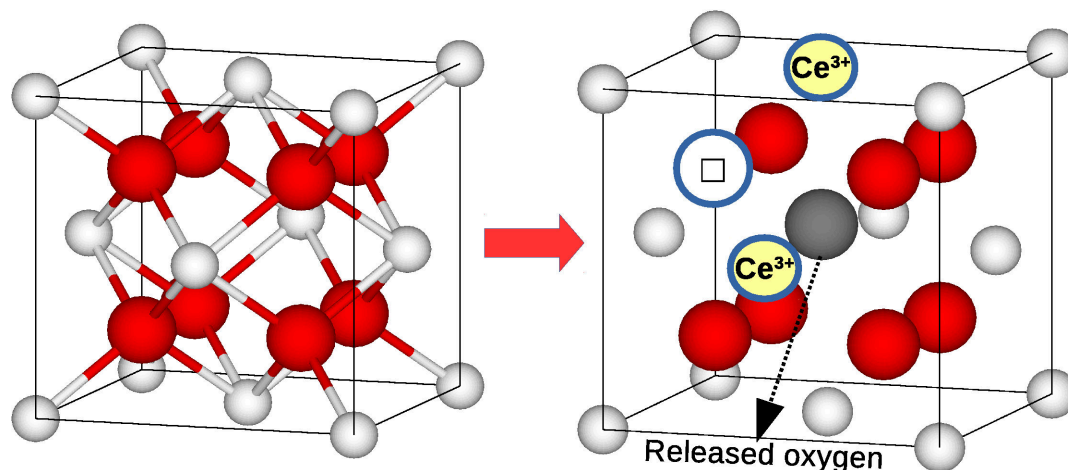


Figure 4.1: Crystal structure of CeO₂ before (left) and after (right) vacancy (\square) formation. In CeO₂ each Ce⁴⁺ ion (white sphere) is surrounded by eight O²⁻ ions (red spheres) and each O²⁻ ion is surrounded by four Ce⁴⁺ ions. The Ce⁴⁺-to-Ce³⁺ transformation is due to \square formation and the released oxygen in the fluorite lattice is intrinsic oxygen. The lattice expansion of nanoceria is as described in the text.

modern catalysis for automotive emissions abatement. The path towards the rational improvement of the properties of these materials, such as the oxygen storage capacity of the ceria nanoparticles, requires a fundamental understanding of the Ce⁴⁺ \leftrightarrow Ce³⁺ redox cycle. Techniques such as x-ray photoelectron spectroscopy[115], x-ray absorption spectroscopy[116], electron paramagnetic resonance[117], and Fourier transform infrared spectroscopy[117] have shown clear evidence of Ce⁴⁺-to-Ce³⁺ reduction, and earlier research on ceria materials also demonstrated that the oxygen diffusion rate is dependent on the whole of the nanocrystal[118], and not just its surface. All of these studies have consolidated researcher's appreciation that the Ce⁴⁺/Ce³⁺ redox cycle, \square creation and annihilation, and oxygen storage and release processes, are strongly coupled.

Several challenges make attains a fundamental understanding of the processes

described above difficult. Feng et al.[116] reported that high-vacuum spectroscopy studies of CeO₂ over-estimate the Ce³⁺ concentration due to the enhanced surface reduction of ceria in the sample measurement environment. Furthermore, during temperature programmed reaction (TPR) techniques, some artifacts can interfere in the interpretation of measurements, e.g. TPR does not take into account the reduction of impurities (nitrates, carbonates)[119]. As opposed to most measurements that have motivated and driven current understanding of catalysis in CeO₂, magnetic measurements can provide quantitative results concerning the Ce³⁺ ions arising from both surface and bulk reduction. Insight into oxygen vacancy creation and annihilation mechanisms is also gained because of the unique magnetic signatures of released and stored O₂.

4.1.1 Aim of this chapter

In this Chapter, we examine nanoceria under O₂ rich (in air) and deficient (in He) conditions to determine its intrinsic oxygen storage and release properties. In magnetometry, one measures the direct response of the intrinsically present Ce³⁺ and oxygen ions (figure 4.1).

The main advantages of using magnetometry are: (i) the ability to determine the number of Ce³⁺ and oxygen vacancies at any given temperature or atmosphere, and free of sample preparation and gas-transport limitations, (ii) the identification of oxygen from both surface and bulk contributions, and the observation of the dynamics of the transformation $O_{\text{lattice}} \leftrightarrow O_{2,\text{ads}}$. Neutron diffraction studies by Mamontov et al.[23] on nanoceria identified that the missing intrinsic oxygen ions occupy interstitial

sites and are weakly bound in the fluorite lattice, enabling additional defects in the form of anion-Frenkel pairs. Much of the earlier experimental work and density functional theory calculations[120; 121] were devoted to understanding the effects of extrinsic oxygen on the surface of nanoceria; that is, how externally adsorbed oxygen reacts. Currently, the lack of clarity on the interstitial oxygen ions' interactions and dynamics (figure 4.1) significantly hinders understanding of nanoceria's unusual magnetism and catalytic reactivity.

4.2 Structure, Composition, and Morphology

Shape selected nanoceria (cubes, rods, and spheres) were synthesized with well-defined crystallographic surface planes (low index planes (111), (110) and (100)) of different stability and Ce:O coordination number[122], thereby changing the concentration of Ce^{3+} and vacancies. Figures 4.2a, 4.2d, and 4.2g show transmission electron micrographs of the nanocubes (25 ± 3 nm), nanorods (length 50 ± 10 nm and width 8 ± 2 nm), and nanospheres ($\varnothing 2 \pm 1$ nm) respectively. Figures 4.2b and 4.2c show the images resulting from high resolution transmission electron microscopy (HRTEM) of the cubes bound by (100) and (110) facets with lattice spacings of 0.27 and 0.19 nm, respectively. Figures 4.2e and 4.2f show HRTEM images of rods defined by (100) and (111) facets with lattice spacings of 0.27 and 0.31 nm. Figures 4.2h and 4.2i show the (111) facet dominated spheres with a lattice spacing of 0.31 nm. The observed HRTEM images are in agreement with previous reports on nanoceria cubes and spheres[49; 123; 124], but it is still an open question as to what planes should be exposed in nanorod ceria. Earlier reports suggest that nanorods expose (100)

and (110) planes[49]. However, our results indicate clearly that the (100) and (111) surface planes are exposed, which is in agreement with Datya et al. and Liu et al.'s work[125; 126]. They proposed that the (110) plane is unstable, and the exposure of the (110) or (111) planes is extremely dependent on the synthesis technique.

To further confirm the structure and surface terminations of the different shaped nanoceria, x-ray diffraction (XRD) experiments under ambient conditions were performed followed by full pattern Rietveld refinements using GSAS-II[59] to determine the lattice constants, overall crystallite sizes, and preferred crystal lattice orientation that indicated the stable, exposed surface planes. Room temperature XRD patterns (Fig. 4.3) clearly show that the three different shaped nanoceria have identical CeO₂ cubic $Fm\bar{3}m$ structures. The preferred orientation (P_{hkl}) due to the stable planes of the nanoceria were described in the refinements using the March-Dollase function. In agreement with previous reports, refinements indicated preferred facets along the (100) planes for nanocubes and nanorods, and the (111) plane for nanospheres[49; 125; 123; 124]. The XRD refinements revealed the nanocubes consisted of (100) and (110) crystal planes in a 64% and 36% ratio, and nanorods were (100) and (111) plane dominant at 90% and 10%, respectively. Nanospheres were (111) plane oriented, as expected. The lattice expansion (compared to 5.414 Å of bulk ceria[108], Table 4.1) is due to the Ce³⁺ valance being favored (4f localized behavior) via electrostatic force reduction[127; 128] due to finite size effects.

The Brunauer-Emmett-Teller (BET) method was used with N₂ physisorption at 77 K to quantify the specific surface areas of the nanoceria shapes (see Table 4.1). The specific surface areas (m²/g) calculated with the BET method are consistent

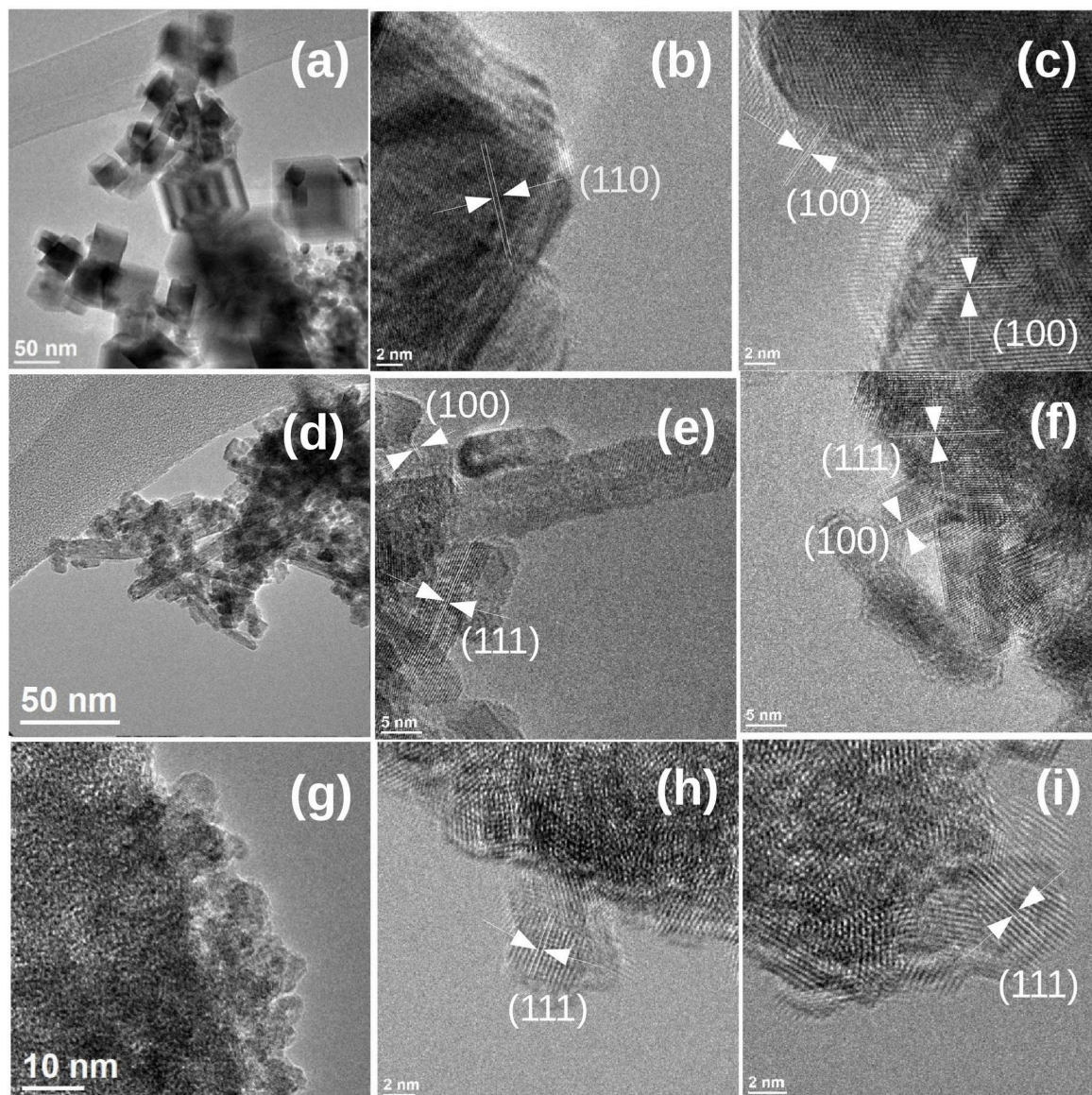


Figure 4.2: TEM (a) and HRTEM images (b-c) images of nanocubes. TEM (d) and HRTEM (e-f) images of nanorods. TEM (g) and HRTEM (h-i) images of nanospheres.

with the observed nanoparticle surface-to-volume ratios and their bulk density. In the unit cell fluorite structure of CeO_2 each Ce ion has eight surrounding oxygen ions, and each oxygen ion has four surrounding Ce ion, thus the Ce:O coordination number

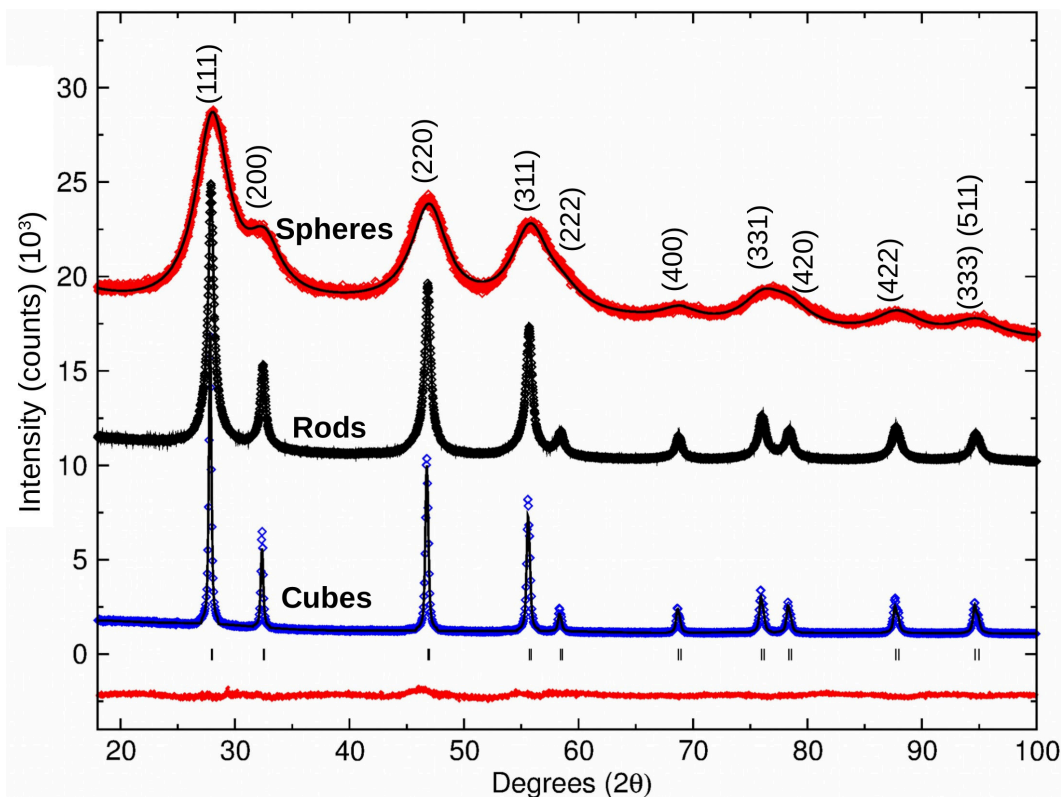


Figure 4.3: Room temperature XRD patterns of CeO_2 nanocubes (bottom, $+10^3$ counts), nanorods ($+10^4$ counts), and nanospheres (top, $+1.5 \times 10^4$ counts). The (hkl) indices of the structure are labeled. Refinement of different CeO_2 shapes (solid lines) and nanospheres residuals is presented; the short vertical bars indicate the position of Bragg reflections used in the refinement.

Table 4.1: Crystalline (nanoparticle) size (nm), lattice constant (\AA) and preferred orientation (P_{hkl}) of crystal planes from XRD pattern refinements. Lattice constant (\AA) from HRTEM image analysis. BET measurements for CeO_2 nanocubes, nanorods, and nanospheres.

shape	size (nm)	a (\AA , XRD)	preferred orientation (P_{hkl})	a (\AA , HRTEM)	BET (m^2/g)
Nanocubes	$\square 28.0 \pm 1.5$	5.426 ± 0.001	(100) 64% + (110) 36%	5.45	35
Nanorods	N.A.	5.427 ± 0.001	(100) 90% + (111) 10%	5.45	167
Nanospheres	$\varnothing 1.6 \pm 0.1$	5.420 ± 0.001	-	5.40	214

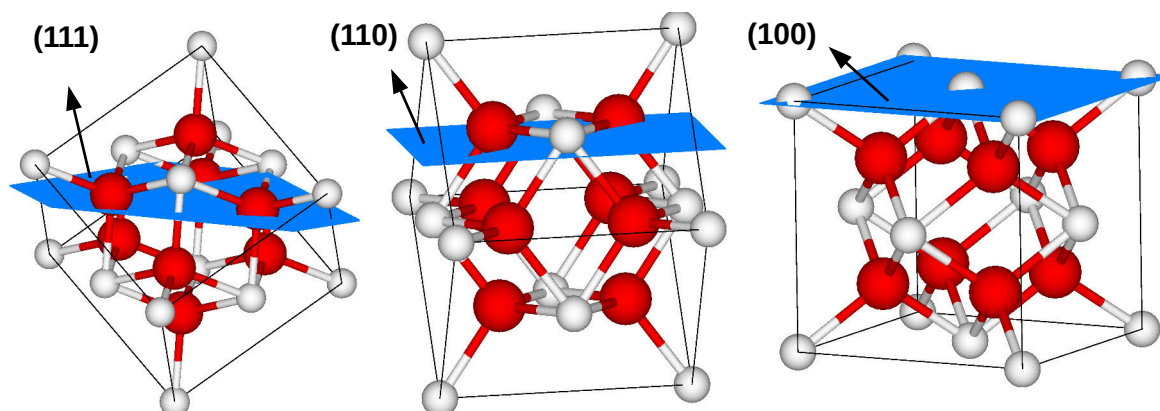


Figure 4.4: CeO_2 unit cell with the (111), (110), and (100) surfaces planes identified in blue. Schematic of the crystal lattice configurations produced using the VESTA software package[130]

ratio is 8:4 as shown in Fig. 4.1. The number of nearest bonded neighbors on a surface is a function of the surface termination by different planes. The CeO_2 (111) surface is terminated with threefold coordinated oxygen and sevenfold coordinated cerium atoms. The CeO_2 (110) surface is terminated by threefold coordinated oxygen and sixfold coordinated cerium atoms. The CeO_2 (100) surface is terminated by twofold coordinated oxygen atoms and sixfold coordinated cerium atoms[129].

The above coordination number ratios provide a metric to ascertain the number of oxygen vacancies on a given structure's surface from the relevant termination (Figure 4.4). The (111) surface termination has a 7:3 Ce-to-O coordination number ratio that involved $1\frac{1}{4}$ oxygen vacancies per unit cell. (110) surface termination results in a 6:3 Ce-to-O coordination number ratio that has $2\frac{1}{4}$ oxygen vacancies per unit cell. The (100) surface termination has Ce-to-O coordination ratio of 6:2 that has $2\frac{1}{2}$ oxygen vacancies associated with each unit cell along this surface. These coordination number and vacancy configurations can be seen in Figure 4.4.

4.3 Magnetism of Nanoceria Cubes, Rods, and Spheres

In general, a paramagnetic substance with its atom's unpaired electron spins has a magnetization arising from the orbital and spin angular momenta. Figure 4.5 shows $\chi(T)$ plots of nanoceria cubes, rods, and spheres in oxygen rich environment. Because the energy level diagram of Ce³⁺ is crystal field split from its $^2F_{\frac{5}{2}}$ state into three Kramer doublets with $J_z = \pm\frac{1}{2}$, $\pm\frac{5}{2}$, and $\pm\frac{3}{2}$ the description of the angular momentum quantum number J multiplet being widely spaced from the ground state compared to the thermal energy does not apply to Ce³⁺ as we discussed in the Chapter 1 and the Van Vleck susceptibility is used to calculate the concentration.

For the occupation of J states with $\pm 1/2$, $\pm 5/2$, and $\pm 3/2$, the magnetic susceptibility becomes

$$\chi = \chi_0 + \frac{N\mu_B^2}{4kT} \left[\frac{g_{1/2}^2 + g_{5/2}^2 e^{-\Delta_1/T} + g_{3/2}^2 e^{-\Delta_2/T}}{1 + e^{-\Delta_1/T} + e^{-\Delta_2/T}} \right] \quad (4.1)$$

with, as previously, N the number of Ce³⁺ ions. The energy separation of the states[7] is $\Delta_1 = 10$ K and $\Delta_2 = 150$ K, and $g_{1/2} = 2.07$, $g_{5/2} = 2.80$, and $g_{3/2} = 2.30$. $\chi_0 = N\alpha(J)$ describes the ever present temperature-independent diamagnetism[8]

Figure 4.6 shows the data and fits (solid lines) to the above expression of the susceptibility, χ^{-1} vs T , measured for the ceria nanocubes, nanorods, and nanospheres when sealed in air (oxygen-rich conditions, see Fig. 2.19). In the high temperature region above Δ_2 , an additional term $A \exp(-\Theta/T)$ (A is a constant and Θ arises for the thermal excitation of nearby excited levels) is incorporated to describe the effects of thermal expansion of the lattices and its effect on the crystal field splittings[131]. The calculated Ce³⁺ ions/g are identified by incorporating crystal field effects. The

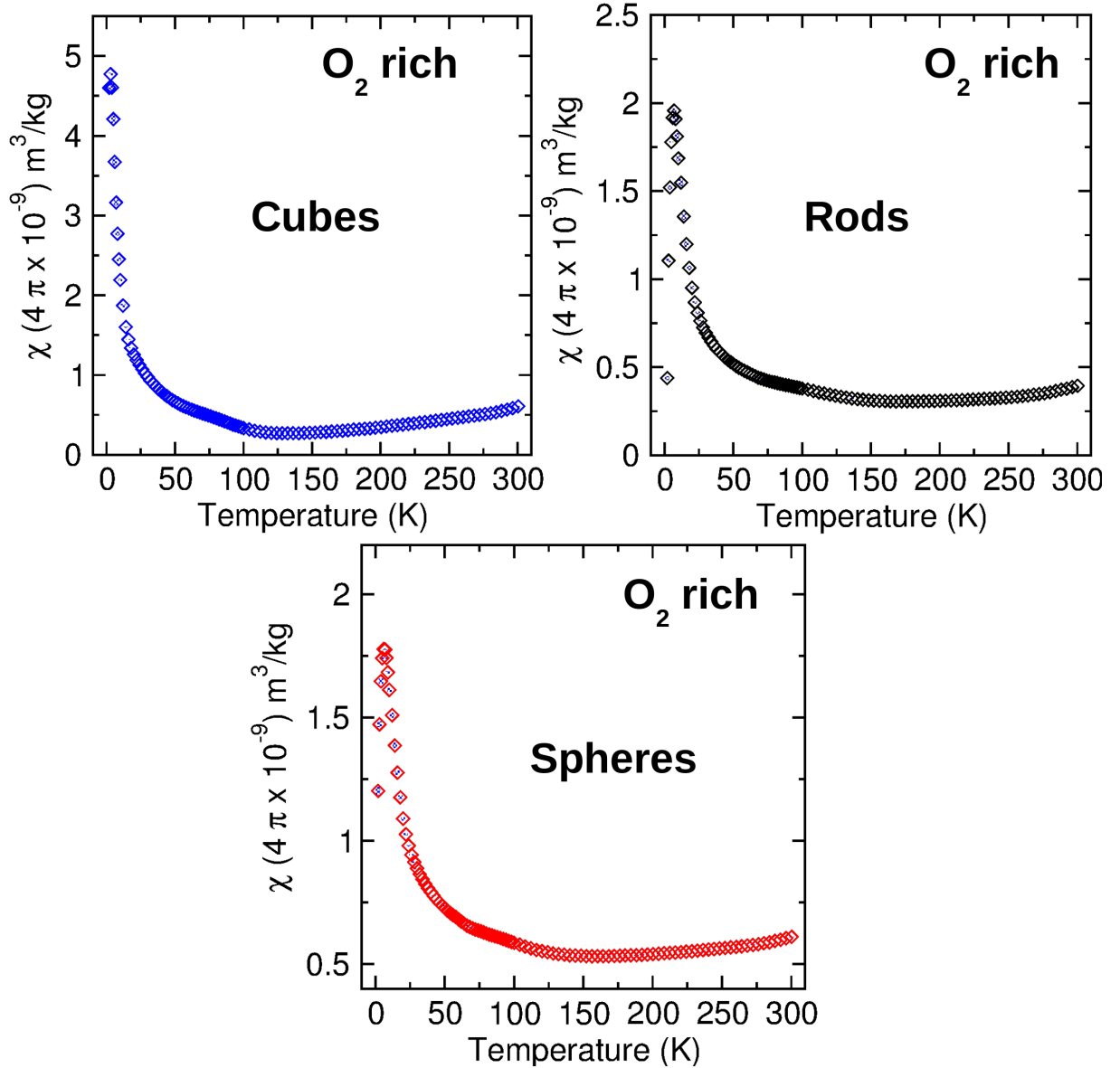


Figure 4.5: Susceptibility as a function of temperature for nanocubes, nanorods and nanospheres in an O_2 rich atmosphere.

relative ordering of Ce^{3+} ions tracks with spheres < rods < cubes, going from $\sim 1.3 \times 10^{19} \text{ Ce}^{3+}/\text{g}$ to $\sim 1.9 \times 10^{19} \text{ Ce}^{3+}/\text{g}$ (see table 4.2). The number of Ce^{3+}/g are consistent with the M vs $\mu_0 H$ susceptibility analysis at 10 K above the antiferromag-

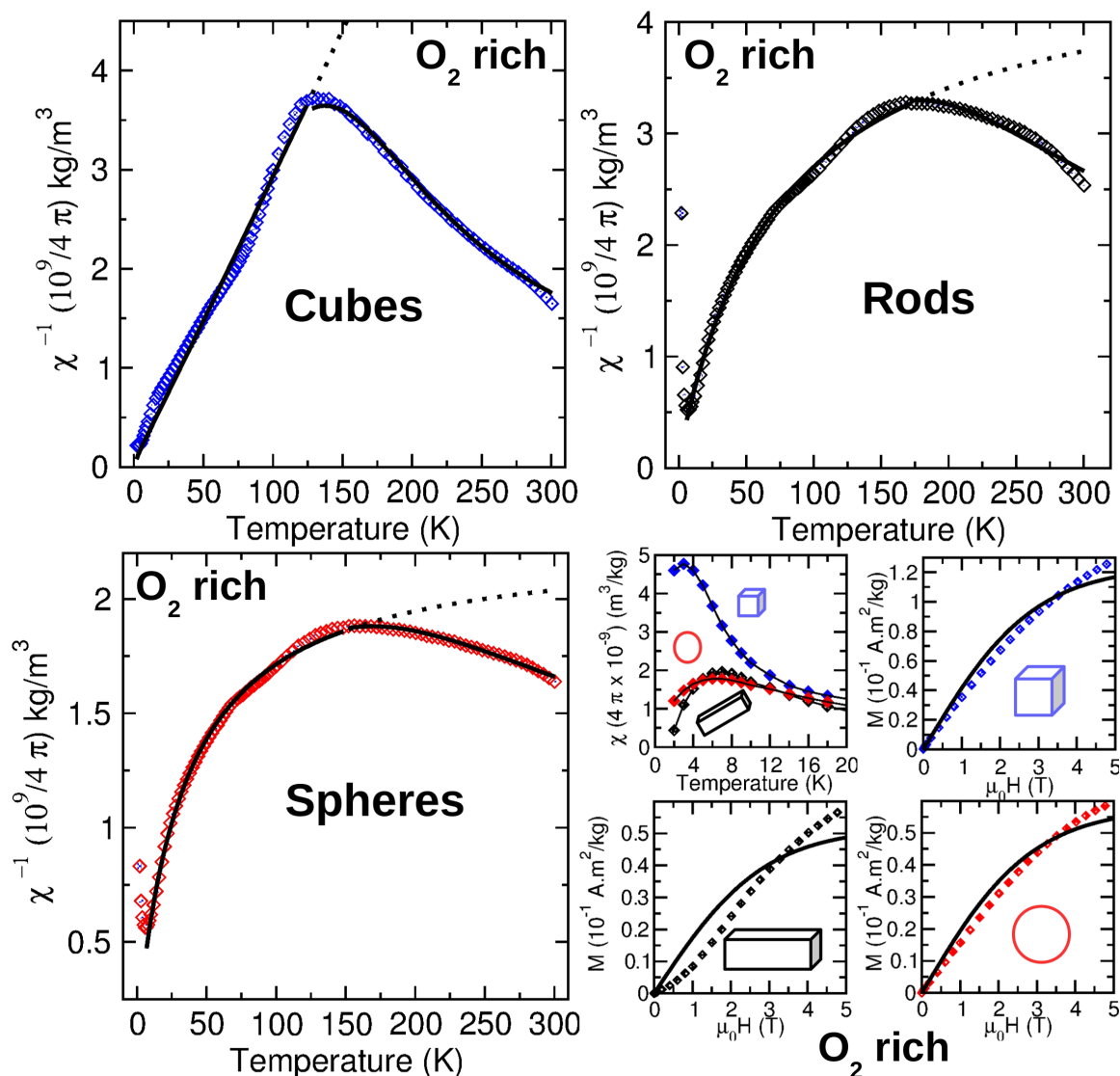


Figure 4.6: Inverse susceptibility as a function of temperature for nanocubes, nanorods and nanospheres in an O_2 rich atmosphere. The solid lines are fits of χ^{-1} vs T above 10 K as described in the text. The low temperature region of the nanoshape's susceptibilities show the maxima associated with magnetic order below ~ 7 K, and the low temperature spin flop transition under high fields of the O_2 rich atmosphere measurements are shown by the M vs $\mu_0 H$ data of the nanocubes, nanorods, and nanospheres at 2 K, with the Brillouin function the solid lines (described in the text).

Table 4.2: O₂ rich systems' data: Ce³⁺/g from χ^{-1} vs T fits with the total number of Ce³⁺/g based on the full crystal field effect analysis, and thermal excitation energies (Θ) of CeO₂ nanocubes, nanorods, and nanospheres.

shape	Ce ³⁺ /g	Θ
Nanocubes	$1.94 \pm 0.05 \times 10^{19}$	500 ± 30
Nanorods	$1.68 \pm 0.02 \times 10^{19}$	600 ± 60
Nanospheres	$1.28 \pm 0.01 \times 10^{19}$	600 ± 40

netic transition temperature (discussed below). The origin behind the Ce⁴⁺ \rightarrow Ce³⁺ reduction is due to the removed lattice oxygen (\square) where the excess electrons localize on two cerium atoms turning Ce⁴⁺ to Ce³⁺. Because the experiments were carried out with the nanoceria sealed in air, the oxygen vacancies in the nanoceria responsible for Ce⁴⁺-to-Ce³⁺ are intrinsic and formed during sample synthesis. The low temperatures of the measurements further suggest that thermal excitations cannot be responsible for this transformation. Additional information is identified by Θ 's of 500 ± 30 K, 600 ± 60 K, and 600 ± 40 K for the nanoceria cubes, rods, and spheres, respectively. The excited level energies are crystal plane orientation dependent, and comparatively, indicate that the nanoceria cubes should have slightly expanded lattices at elevated temperatures that enable more O²⁻ to be incorporated into the crystalline lattice compared to the nanoceria rods and spheres.

Interestingly, for $T \leq 10$ K all nanoceria presented a maximum in their susceptibilities. We ascribe this $\chi(T)$ behaviour to an antiferromagnetic transition; $T_N \sim 6$ K, of the Ce³⁺ ions. It has been shown in Ce-based compounds that $4f$ localized Ce³⁺ ions have a tendency to show antiferromagnetism[132; 133; 134]. To further confirm its

presence, the field dependent magnetization, $M(\mu_0 H)$, of the nanocubes, nanorods, and nanospheres at 2 K (below T_N , shown in Figure 4.6) evidences a meta-magnetic transition. A model independent telltale is the change in slope at intermediate fields of $M(\mu_0 H)$, most visible in the nanorod system. The $M(\mu_0 H)$ data was poorly fit (Fig. 4.6) by a Brillouin function that describes the field dependent magnetization of a paramagnet ($M = Ng_{1/2}S\mu_B B_S(x)$ ¹), further evidence that the samples undergo an antiferromagnetic transition when measured encapsulated in air, and the Ce³⁺ ions experience superexchange coupling through intermediate O²⁻ ions. Experiments in this oxygen rich atmosphere probe only the intrinsic magnetism of the nanoceria.

To understand the Ce³⁺ \leftrightarrow Ce⁴⁺ redox transformation and the dynamics of released oxygen in the lattice, we direct our attention to the susceptibility measurements in an oxygen deficient environment (as shown in Fig. 2.19). $\chi(T)$ measurements of the nanoceria shapes in an oxygen deficient environment (active pumping with a He sweep) showed a significantly different susceptibility compared to the same measurements in air (see Fig. 4.7). No antiferromagnetic transitions are observed at low temperatures, and new broad maxima of $\chi(T)$ between 50 and 120 K are observed for all three shapes (Fig. 4.7). The differences indicate that the oxygen storage mechanism strongly depends on the surrounding atmosphere. First, the absence of antiferromagnetic transition indicates that the O²⁻ ions are no longer in their fixed lattice positions and cannot mediate the superexchange interactions of neighboring Ce³⁺ ions; O²⁻ ions are diffusing through the ‘bulk’ of the nanoceria to the surface.

The occurrence of the broad maximum in $\chi(T)$ under oxygen-deficient conditions

¹ N is the number of paramagnetic Ce³⁺/g from $\chi(T)$ fits. $g_{1/2} = 2.07$, $S = 1/2$, and $B_S(x) = [(2S + 1)/2S] \coth(2S + 1)x/2S - (1/2S) \coth(x/2S)$; $x = g\mu_B\mu_0 HS/kT$.

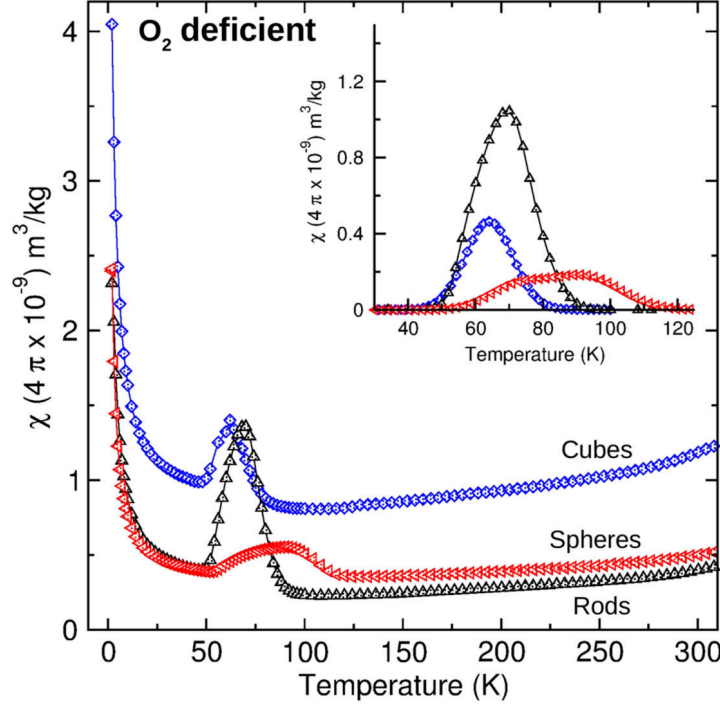


Figure 4.7: Temperature dependence of magnetic susceptibility for O_2 deficient systems are shown. With the O_2 deficient atmosphere nanocerium presents no low temperature transition compared to the O_2 rich system measurements, and an additional ‘transition’ above 50 K. The inset shows the magnitude of the temperature dependent magnetism due to the released oxygen from the system (intrinsic CeO_2 $\chi(T)$ subtracted data) of the O_2 deficient environment.

can be understood in the following way. In nanocerium, the carriers responsible for the magnetism are Ce^{3+} and \square [135]. At low temperatures, the $4f^1$ localized Ce^{3+} ions act as non-interacting dipoles, and their susceptibility decreases with increasing temperature. However, above ~ 50 K, the susceptibility rises monotonically with warming to a maximum and decreases with further warming (≤ 120 K). This response is due to the γ - β antiferro-to-paramagnetic transition of $S = 1$ O_2 [136]. Magnetic susceptibility studies of adsorbed O_2 (denoted $\text{O}_{2,ads}$) on vycor glass, graphite, and zeolites identified this transition and presented similar $\chi(T)$ behaviour[137; 138; 139;

140; 141; 142] that is observed herein. Also, $\chi(T)$ from $O_{2,ads}$ broadens depending on the amount of $O_{2,ads}$ surface coverage. Our $\chi(T)$ of nanoceria in an oxygen-deficient environment clearly indicates that $Ce^{3+} \leftrightarrow Ce^{4+}$ redox reactions result in an intrinsic supply of reactive lattice oxygen that combine to produce $O_{2,ads}$.

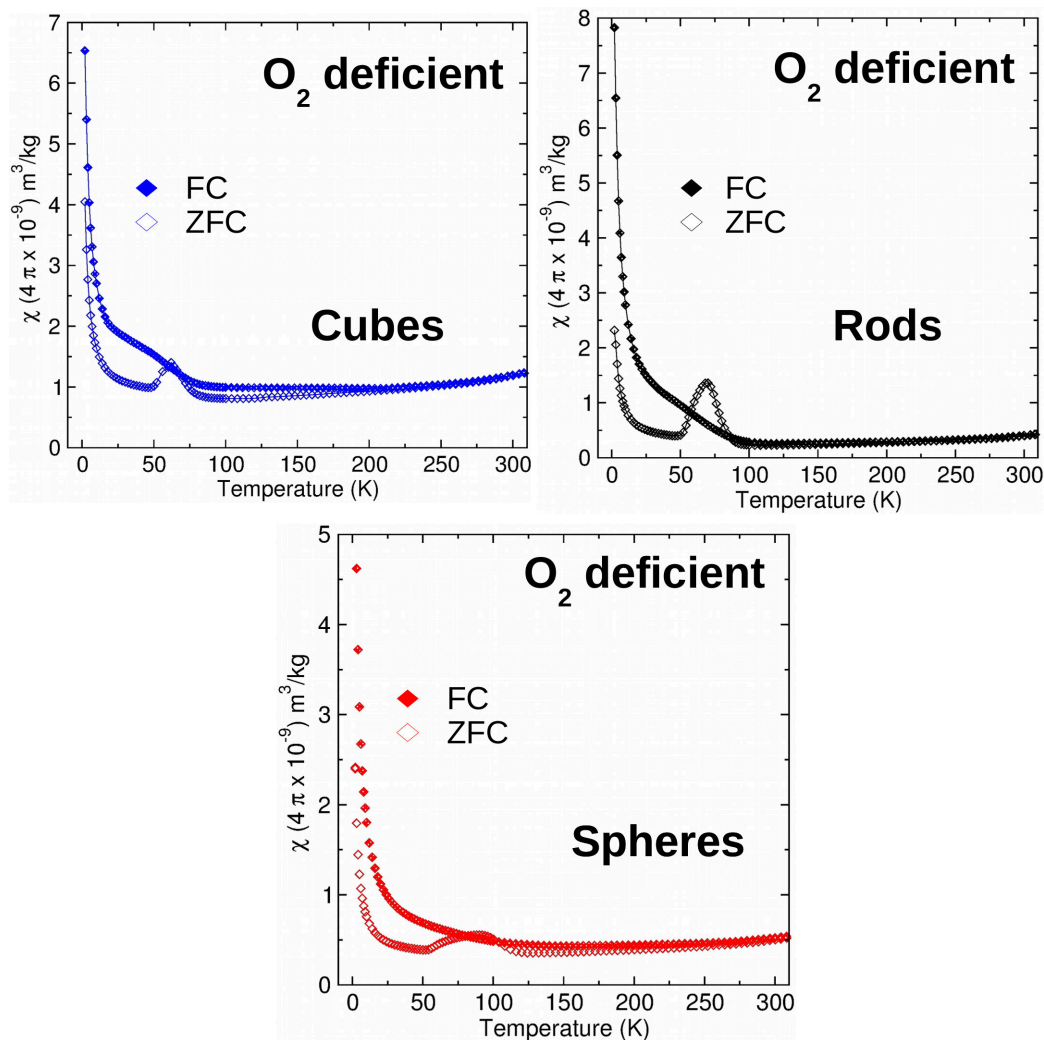


Figure 4.8: Temperature dependence of field cooled ($\chi_{FC}(T)$) and zero field cooled ($\chi_{ZFC}(T)$) magnetic susceptibility for O_2 deficient nanocubes, nanorods, and nanospheres are shown. With the FC measurement ($\mu_0 H = 10$ mT) the magnetic signature from the O_2 is removed in all shape dependent ceria nanoparticles.

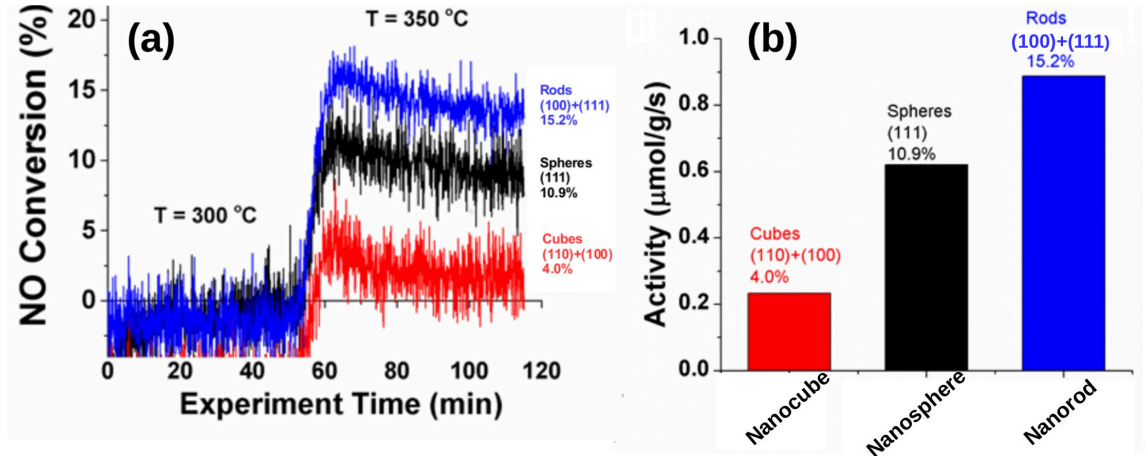


Figure 4.9: (a) NO conversion as a function of time during steady-state NO reduction by CO at 300 and 350 °C over the various nanoceria shapes. (b) Activity ($\mu\text{mol/g/s}$) of cubes, spheres, and rods at 350 °C.

Additionally, to gain insight into the kinetics of the O_{lattice} transformation, field-cooled $\chi_{FC}(T)$ measurements were performed on the nanoshapes under oxygen deficient atmospheric conditions. Unlike the experiments carried out with air encased samples where identical $\chi_{FC}(T)$ and $\chi_{ZFC}(T)$ were observed, the experiments under oxygen deficient conditions present an irreversibility between $\chi_{FC}(T)$ and $\chi_{ZFC}(T)$ below the respective O_2 T_N 's (shown in Fig. 4.8). The $\chi_{FC}(T)$ measurements identify that T_N is suppressed, and $\chi_{FC}(T)$ for temperatures below T_N was increased significantly, demarking the increased number of Ce^{3+} ions able to provide a measurable magnetization after the O_{lattice} migration to $O_{2\text{ads}}$ during the $\chi_{ZFC}(T)$ measurement.

4.4 The Catalysis and Oxygen Connection

Ceria is an important catalytic material, especially for automotive emissions control. Therefore, the relationship between the structure, Ce^{3+} , and catalytic activity of the

various nanoceria shapes were examined by performing the steady-state reduction of NO by CO at 350 °C to further confirm the presence of intrinsic oxygen and surface Ce³⁺. As shown in Figure 4.9a, the conversion was negligible below this reaction temperature but reached a stable steady state within 1h of achieving the reaction temperature. Conversions at 350 °C were deliberately maintained below ~15% by using a constant 50 mg of each catalyst, such that accurate reaction rates could be calculated without reactant depletion effects. The important role of the nanoceria shape is first seen in the 40% increase in rate (per g catalyst) comparing the rates (Fig. 4.9b) of the spherical nanoceria to that of the rod-shaped nanoceria; the cubes presented a much slower rate. Earlier, Dario et al.[143] have demonstrated that reaction rates over ceria-based materials scale with the amount of lattice oxygen removed during conventional temperature programmed reduction. Because the only difference between the three shapes (cubes, rods, and spheres) are exposed surface facets to gain further insights we compared nitric oxide (NO) conversion on (111), (110), and (100) planes.

From the XRD refinements (Fig. 4.3, Table. 4.1) and TEM (Fig. 4.2) the preferred orientation of the nanoshapes are:

- Cube surfaces expose 64% (100) planes and 36% (110) planes.
- Rod surfaces expose of 90% (100) planes and 10% (111) planes.
- Sphere surfaces exhibit no preferred overall geometric orientation but expose only (111) planes as facets.

With the above information, we can calculate the surface area of the planes for the different nanoshapes with the BET analysis.

Spheres: 214 m²/g is the surface area of the (111) planes.

Rods: Similarly, 90% and 10% of the total BET surface area of 167 m²/g of the (100) and (111) planes are 150.3 m²/g and 16.7 m²/g, respectively.

Cubes: The total BET surface area of 35 m²/g suggests the surface area of the (100) and (110) planes are (0.64)(35 m²/g)=22.4 m²/g and (0.36)(35 m²/g)=12.6 m²/g, respectively.

From the measured conversions of the cubes (4.0%), rods (15.2%) and spheres (10.9%) (see Fig. 4.9c).

Spheres: The total NO conversion is on the (111) planes, so the conversion per plane is (10.9%)/(214 m²/g) = 0.0509% conversion for (1 m²/g)_{(111)planes}.

Rods: The total 15.2% NO conversion is on the (100) and (111) planes that is shared as (150.3 m²/g)x + (16.7 m²/g)(0.0590%_{(111)planes}) = 15.2%. Thus, we find 0.0954% conversion for (1 m²/g)_{(100)planes}.

Cubes: The total 4.0% NO conversion is on the (100) and (110) planes this is shared by (22.4 m²/g) (0.0954%_{(100)planes}) + (9.6 m²/g)y = 4.0%. Thus, we find 0.1479% conversion for (1 m²/g)_{(110)planes}.

Comparing between rates on planes, (100) → (110) is 0.0590% → 0.1478%, so the reaction is ~190% faster on the (110) than the (111) plane. Similarly, (111) → (100) rates are ~90% faster (0.0509% → 0.0954%).

It is found that the reaction is 190% faster on the (110) surface than the (111) surface, and ~90% faster on the (100) surface than the (111) surface. This is in

Table 4.3: Comparison of NO conversion per plane for 1 m²/g.

Plane	Conversion % for 1 m ² /g
(111)	0.0509
(110)	0.1479
(100)	0.0954

agreement with the theoretical prediction that the relative activity of the surface planes are in the order (110) to (100) to (111)[144; 145].

4.5 Conclusions

In this Chapter, we studied structure, composition, morphology, and magnetism of nanoscale CeO₂ shapes. Three different nanoshapes (cubes, rods, and spheres) are chosen for the study because changing the morphology provides access to various crystallographic surface planes. X-ray diffraction measurements were performed to confirm the phase purity and quantify the lattice constants, average crystallite size, and preferred orientation of nanoshapes. Nanocubes, nanorods, and nanospheres have an identical space group of $Fm\bar{3}m$. HRTEM images further confirm that nanocubes consists of (100) and (110) planes, nanorods consist of (110) and (111) planes, nanospheres consists of (111) planes. Magnetic susceptibility measurements performed in O₂ rich and O₂ deficient conditions revealed the mechanism behind the Ce⁴⁺ ↔ Ce³⁺ redox reaction via an antiferro-to-paramagnetic transition. In summary, we showed that nanoscale CeO₂ acts as an oxygen buffer by supplying lattice oxygen and controlling the redox reaction via Ce³⁺ ↔ Ce⁴⁺.

Chapter 5

Oxygen's function on the magnetism of nanoscale CeO₂, Fe - CeO₂, and Co - CeO₂

5.1 Introduction

In the previous Chapters 3 and 4 we discussed the magnetism in two classes of materials ($Fe_3O_4/CoFe_2O_4$ rich in $3d$ electrons and CeO_2 with no unpaired $3d$ electrons) and demonstrated how oxygen rich and oxygen deficient environments impact the magnetism at the nanoscale. Whether a system is rich in d electrons or not (d^0), all the metal oxides discussed in this thesis have a common theme that is lattice oxygen. Lattice oxygen is the natural bridge between the metal ions to mediate the magnetism. Understanding d^0 magnetism in nanoscale oxides provides insights into the role of lattice oxygen (surface or bulk) in magnetism.

5.1.1 d^0 magnetism

d^0 magnets are the systems that display a weak ferromagnetic-like response to an applied magnetic field with low or no coercivity. Venkatesan et al. first reported that HfO_2 thin films show ferromagnetism at room temperature and suggested that it could be related to anion vacancies[146] with no magnetic cations. Later, TiO_2 and In_2O_3 films also showed room temperature ferromagnetism, whereas, their corresponding bulk samples were diamagnetic, indicating that vacancies are possibly responsible for the ferromagnetism[147]. First-principle calculations further suggested that intrinsic point defects are responsible for the origin of magnetism[148] in these materials. However, some challenged the phenomenon by pointing out that possible iron contamination while using stainless-steel tweezers in handling thin films is responsible for the magnetism[149]. To address this issue, nanoparticle powder samples were chosen for the study. The first unambiguous experimental evidence of d^0 ferromagnetism was

provided by Sundaresan et al. The authors suggested that non-magnetic nanoscale oxides such as CeO₂, Al₂O₃, ZnO, In₂O₃, and SnO₂ showed ferromagnetism while the corresponding bulk samples are diamagnetic, clearly indicating that it is a surface or interface phenomenon[35]. At the nanoscale (as discussed in Chapter 1), oxide systems exhibit emergent properties such as electrical conduction and ferromagnetism, indicative of the distinct electronic structure at the surface or interface.

5.1.2 Aim of this chapter

In this Chapter, we study the structure, composition, morphology, electronic structure and magnetism of CeO₂, Fe - CeO₂, and Co - CeO₂ nanoscale systems (Fe - CeO₂ and Co - CeO₂ refers to decoration of Fe and Co ions on the CeO₂ nanocrystallites) and identify the role of oxygen in the magnetism. These three systems were deliberately chosen for this study because they allow a combination of d^0 (no unpaired d electrons) and non- d^0 (rich in d electrons) magnetic systems and explore the mechanisms behind the magnetism[109]. Additionally, the surface magnetism probed by XMCD (total electron yield) measurements gives better signal, noting that ceria is a poor conductor, so adding Fe and Co on the surface increases the conductivity, which made it possible to measure a clean XMCD spectra in TEY for the Fe and Co and CeO₂ samples.

5.2 Structure and Composition

Nanoceria and Fe and Co decorated nanoceria were prepared as described in Ref. [52; 53]. X-ray diffraction patterns of CeO₂, Fe - CeO₂ and Co - CeO₂ nanoparticles are shown in Fig. 5.1. Rietveld refinements with FullProf[55] yielded the expected

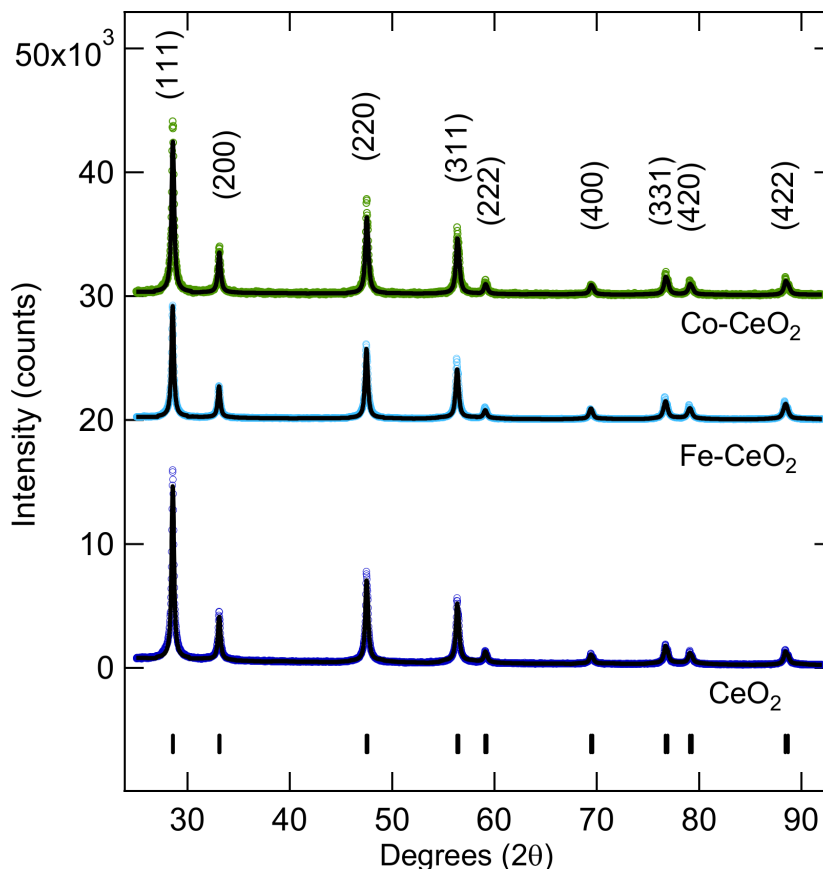


Figure 5.1: Room temperature XRD patterns of nanoceria, Fe-CeO_2 and Co-CeO_2 nanocrystals. The (hkl) indices of the structure are labeled. Refinement of nanoceria, Fe-CeO_2 and Co-CeO_2 crystallites (solid lines) are presented; the short vertical bars indicate the position of Bragg reflections used in the refinement.

cubic structure of the $Fm\bar{3}m$ space group and all three systems were phase pure (the presence of secondary phase, such as a metallic cluster or an oxide phase of Fe or Co, was not observed). The broadening of reflections was from the nanocrystallite sizes, i.e. Scherrer broadening. Lattice parameters and estimates of crystallite sizes are calculated from the Rietveld refinements (with fixed crystallographic site occupancies ($\text{Ce} = 0.02053$ and $\text{O} = 0.04116$)[56]) are provided in table 5.1. Refinements identified the average crystallite size as ~ 20 nm, and lattice constants stay the same

indicating that the Fe and Co ions are not merely substituting the Ce ions and they are decorating the surface[150]. The surface densities were quantified as 1.11 Fe/nm^2 and 3.57 Co/nm^2 [52; 53].

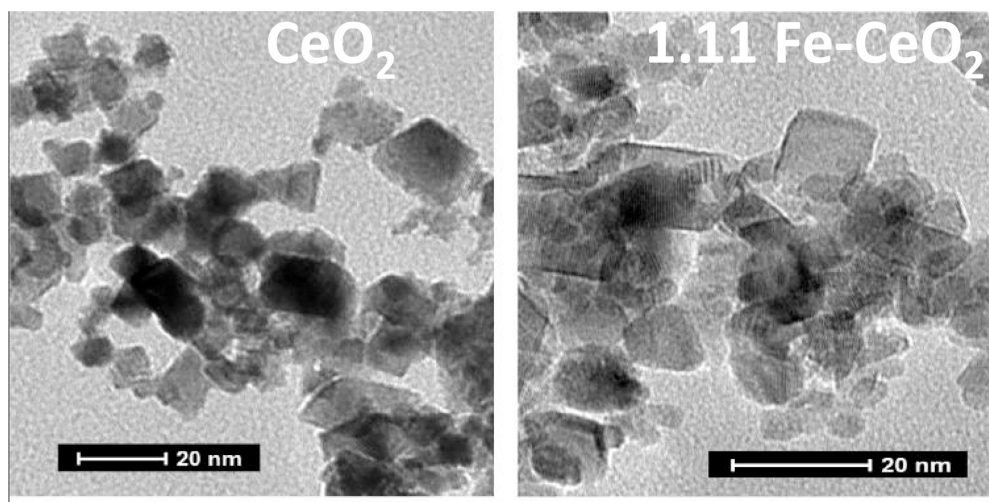


Figure 5.2: Transmission electron micrographs of CeO_2 and $\text{Fe} - \text{CeO}_2$ are presented.

Table 5.1: Crystalline (nanoparticle) size (nm) and lattice constant (\AA) from XRD pattern refinements. ICP wt%'s of Fe and BET measurements for nanoceria and Fe-CeO_2 and Co-CeO_2 are presented.

Sample	size (nm)	a (\AA , XRD)	ICP wt%	BET (m^2/g)
CeO_2	21.0 ± 0.3	5.412 ± 0.001	0	55
Fe-CeO_2	23.4 ± 0.5	5.412 ± 0.001	0.57	55
Co-CeO_2	20.0 ± 0.4	5.410 ± 0.001	3.57	55

Transmission electron micrographs (TEM) of CeO_2 and $\text{Fe} - \text{CeO}_2$ nanoparticles are shown in Fig. 5.2. The clear bright and dark fringes are indicative that atoms that within the nanoparticles exhibit highly crystalline order. Crystallite sizes were of the order of 20 nm in diameter consistent with the XRD analysis. Electron to-

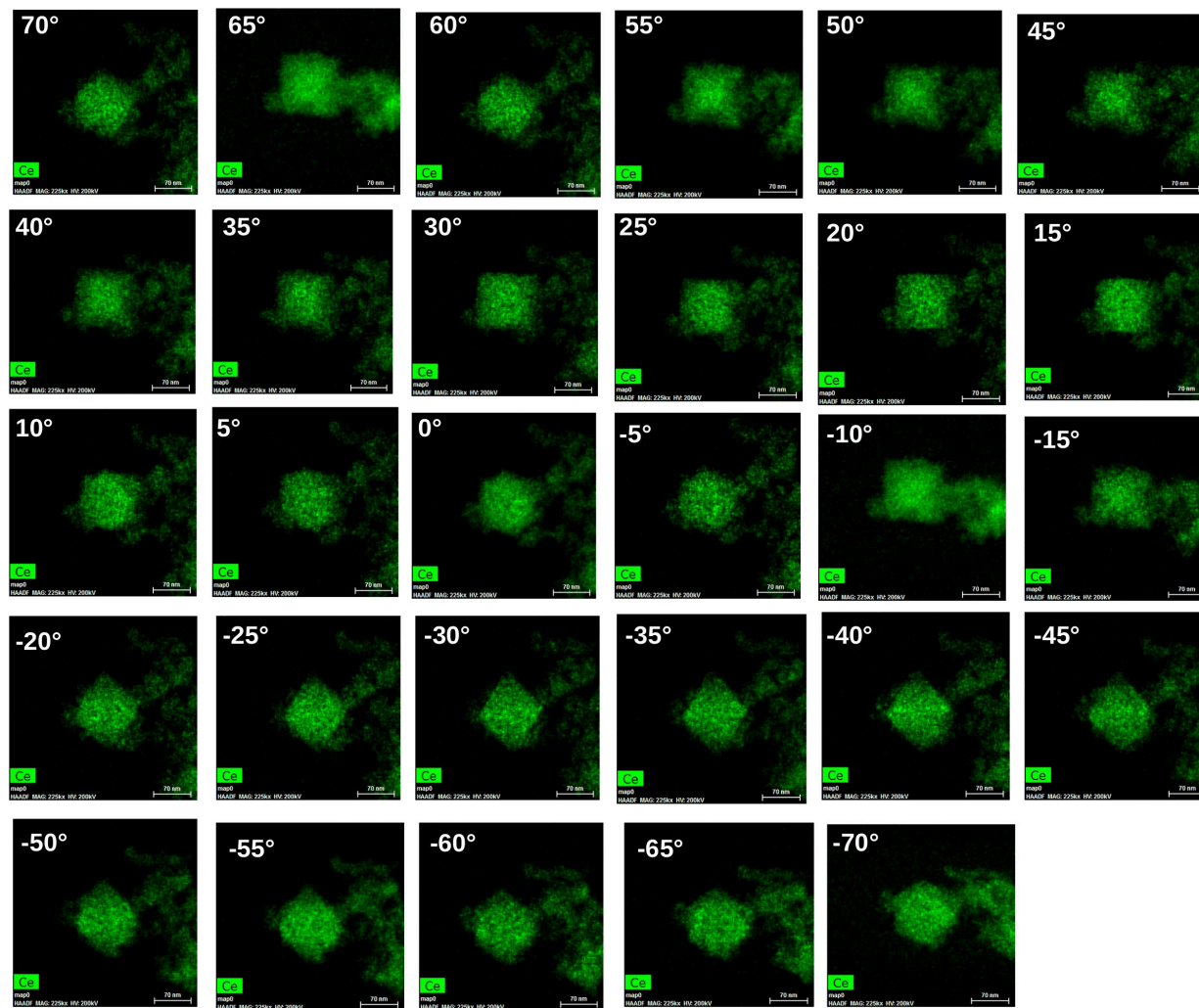


Figure 5.3: HAADF images acquired in the STEM mode of Ce atoms in Fe – CeO_2 nanoparticles are shown.

mography experiments were conducted on Fe – CeO_2 nanocrystallites in the TEM mode and scanning transmission electron microscopy (STEM) to further confirm the Fe decoration. The high angle annular dark field and bright field tilt series in the STEM were collected in the angular range of $\pm 70^\circ$ using an increment of 5° . Figures 5.3, 5.4, and 5.5 show the HAADF images of Ce, Fe, and O atoms in the Fe – CeO_2 nanoparticles. The elemental mapping using HAADF reveals the Fe decoration

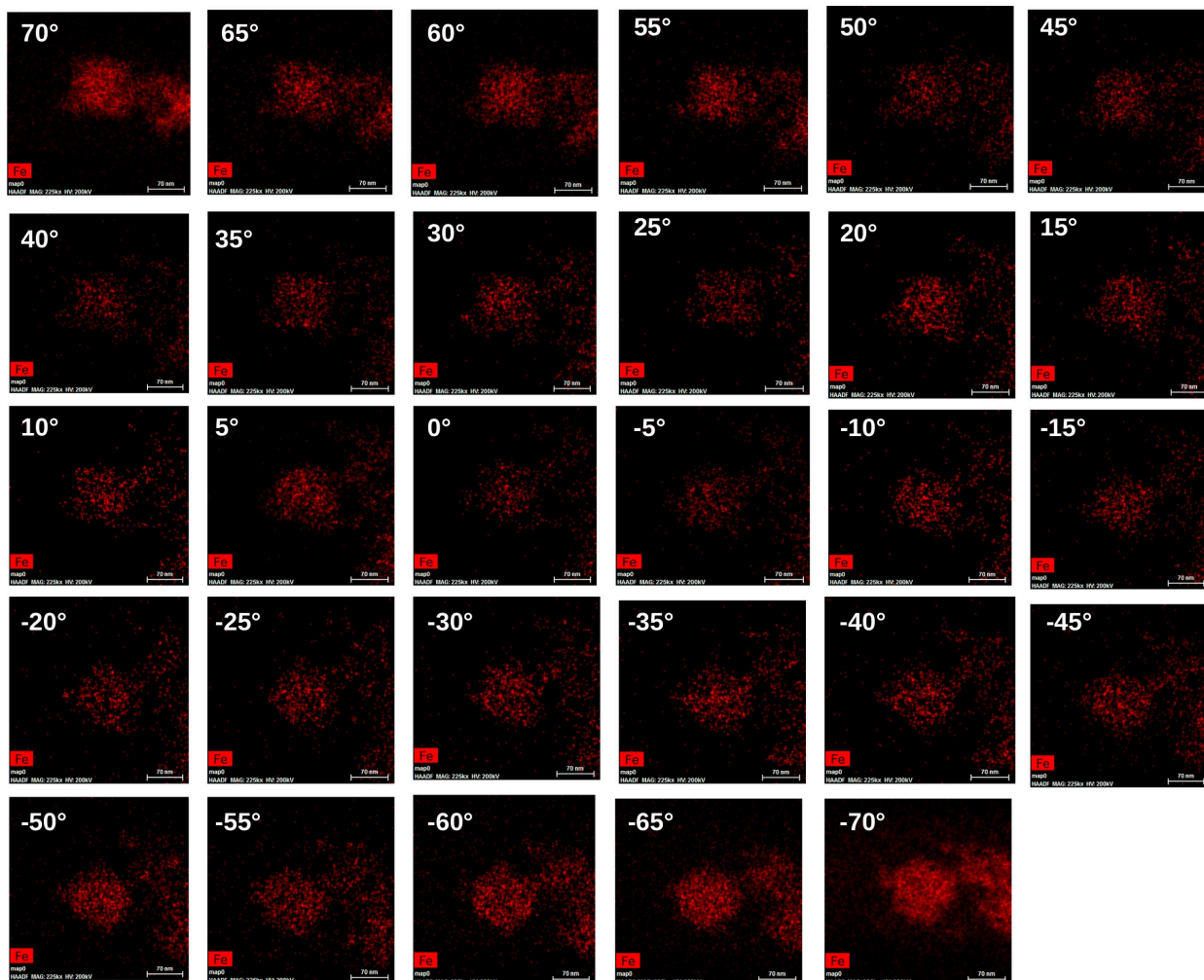


Figure 5.4: HAADF images acquired in the STEM mode of Fe atoms in Fe – CeO_2 nanoparticles are shown.

on CeO_2 particles. XRD, TEM, HAADF, and Mössbauer spectroscopy (discussed below) results confirmed that no secondary phases (e.g. metal oxides) were present, as do the x-ray absorption spectroscopy measurements discussed below.

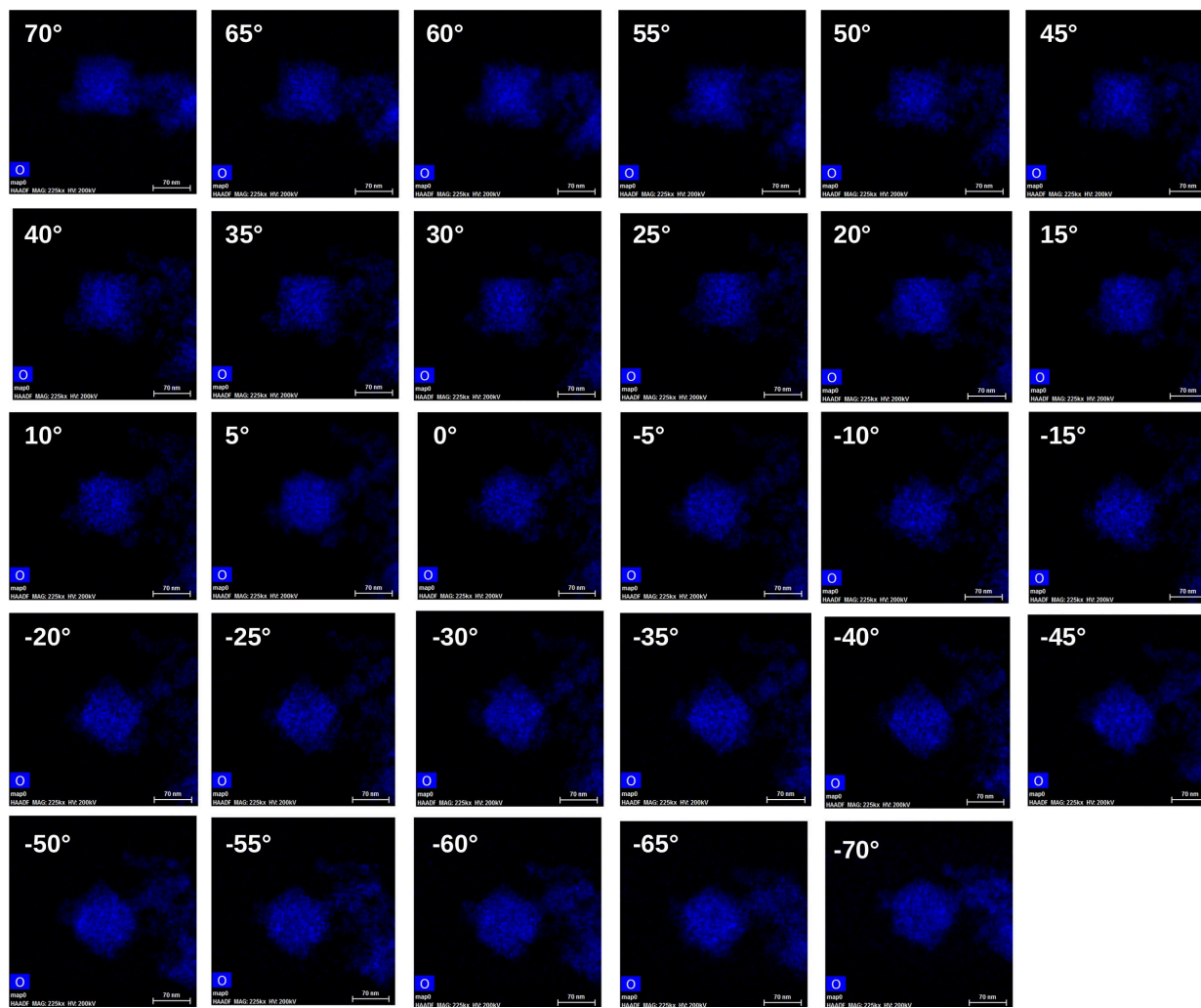


Figure 5.5: HAADF images acquired in the STEM mode of O atoms in Fe – CeO_2 nanoparticles are shown.

5.3 Overall Magnetism

The susceptibility of CeO_2 , $Fe - CeO_2$, and $Co - CeO_2$ nanocrystallites measured with 2.5 mT are shown in Fig. 5.6. The $\chi(T)$ of CeO_2 is relatively low compared to that $Co - CeO_2$ and $Fe - CeO_2$ nanocrystallites as expected because the decoration of Fe and Co contributes to the overall magnetism of the nanoparticles. Similar behaviour

between the $\chi(T)$ measurements of Fe - CeO₂ and Co - CeO₂ showed that there is no evidence of secondary magnetic phase down to 2 K. The significant change in the magnetization at the low temperatures of Fe - CeO₂ and Co - CeO₂ indicates the presence of a paramagnetic component.

5.3.1 Curie – Weiss analysis of Fe and Co decorated CeO₂ nanocrystallites

The spin moment of Fe and Co ions are obtained by standard Curie – Weiss analysis. The inverse susceptibility as a function of temperature $[\chi(T)]^{-1}$ is presented in the inset of Fig. 5.6; the $[\chi(T)]^{-1}$ was obtained by subtracting the CeO₂ support background from $\chi(T)$ for the decorated samples. From

$$1/\chi = [T - \theta]/C \quad (5.1)$$

where C is Curie constant and θ is Curie – Weiss temperature, fits to the data provided (see table 5.2) a measure of C , θ and the effective (ionic) moments $\mu_{eff} = \sqrt{\frac{3k_B C}{N}}/\mu_B$, where k_B is the Boltzmann constant and N is the number of magnetic ions¹ (as obtained by ICP wt% provided in table 5.1). An example calculation μ_{eff} calculation for Fe - CeO₂ in the low temperature region is shown below.

For² Fe - CeO₂ in the temperature range < 350 K:

$$C = (1.26 \pm 0.06) \times 10^{-4} \frac{emu \cdot K}{g \cdot Oe} \text{ and } \theta = -1.00 \pm 0.05 \text{ K.}$$

$$\mu_{eff} = \sqrt{\frac{3 \times 1.38 \times 10^{-16} \times (1.26 \pm 0.06) \times 10^{-4}}{6.147 \times 10^{19}}} \frac{1}{\mu_B} = 3.1 \pm 0.2 \mu_B/Fe \quad (5.2)$$

¹For example 0.57 wt% Fe corresponds to 6.417×10^{19} Fe/g (because $N_A \times 0.0057g/55.85g$)

²CGS units are used for this calculation

³ $1 \frac{emu \cdot K}{g \cdot Oe} = 4\pi \times 10^{-3} \frac{m^3 \cdot K}{kg}$

Table 5.2: Comparison of Curie constant C , Curie-Weiss temperature θ , and $\mu_{eff}(\mu_B)$ measurements of $Fe - CeO_2$ and $Co - CeO_2$ are shown.

Sample	T range (K)	ICP wt%	N	$C (\frac{emu K}{g Oe})$	θ (K)	$\mu_{eff} (\mu_B)$
$Fe - CeO_2$	10 - 350	0.57	6.147×10^{19} Fe/g	$(1.26 \pm 0.06) \times 10^{-4}$	-1.00 ± 0.05	$3.1 \pm 0.2/Fe$
$Fe - CeO_2$	350 - 400	0.57	6.147×10^{19} Fe/g	$(1.2 \pm 0.1) \times 10^{-5}$	320 ± 30	$0.98 \pm 0.09/Fe$
$Co - CeO_2$	10 - 250	3.57	3.649×10^{20} Co/g	$(2.57 \pm 0.05) \times 10^{-4}$	-34 ± 1	$1.84 \pm 0.04/Co$

Similarly, μ_{eff} of $Fe - CeO_2$ in the higher temperature region ($T > 350$ K) is calculated as $0.98 \pm 0.09 \mu_B/Fe$. μ_{eff} of $Co - CeO_2$ is $1.84 \pm 0.04 \mu_B/Co$. C and θ of $Fe - CeO_2$ and $Co - CeO_2$ samples are proved in table 5.2.

Because the magnetism of CeO_2 is taken into account (background) for the $Fe - CeO_2$ and $Co - CeO_2$ nanocrystallites the $1/\chi(T)$ analysis is expected to give insights into the magnetism of decorated Fe and Co ions. For $Fe - CeO_2$ nanocrystallites the $1/\chi(T)$ fits resulted in $3.1 \pm 0.1 \mu_B/Fe$ and $0.98 \pm 0.09 \mu_B/Fe$ in the low and high-temperature regions respectively. The reason between the difference in free ion moments of Fe^{3+} ions in the low and high-temperature regions are explained below.

XAS simulations (discussed in the section 5.4.3) of $Fe - CeO_2$ identified 30% Fe^{2+} in O_h and 70% Fe^{3+} in O_h ⁴. The number of valence electron in Fe^{2+} is six and in Fe^{3+} it is five. In Fe^{2+} the first three electrons occupy t_{2g} state with parallel spin ($3t_{2g} \uparrow$) followed by two electrons in the e_g state with parallel spin ($2e_g \downarrow$), resulting in a high spin system. The remaining electron occupies t_{2g} state in anti-parallel ($t_{2g} \downarrow$) configuration, giving rise a net spin of $S = 2$ and corresponding μ_{eff} of Fe^{2+} as $4.89 \mu_B$. For Fe^{3+} the first three electrons occupy t_{2g} state with parallel spin configuration ($3t_{2g} \uparrow$) and remaining two electrons occupy t_{2g} state in anti-parallel

⁴The Coulomb interaction of Fe with oxygen anions lifts the degeneracy of d orbitals and splits into lower energy t_{2g} and higher energy e_g states

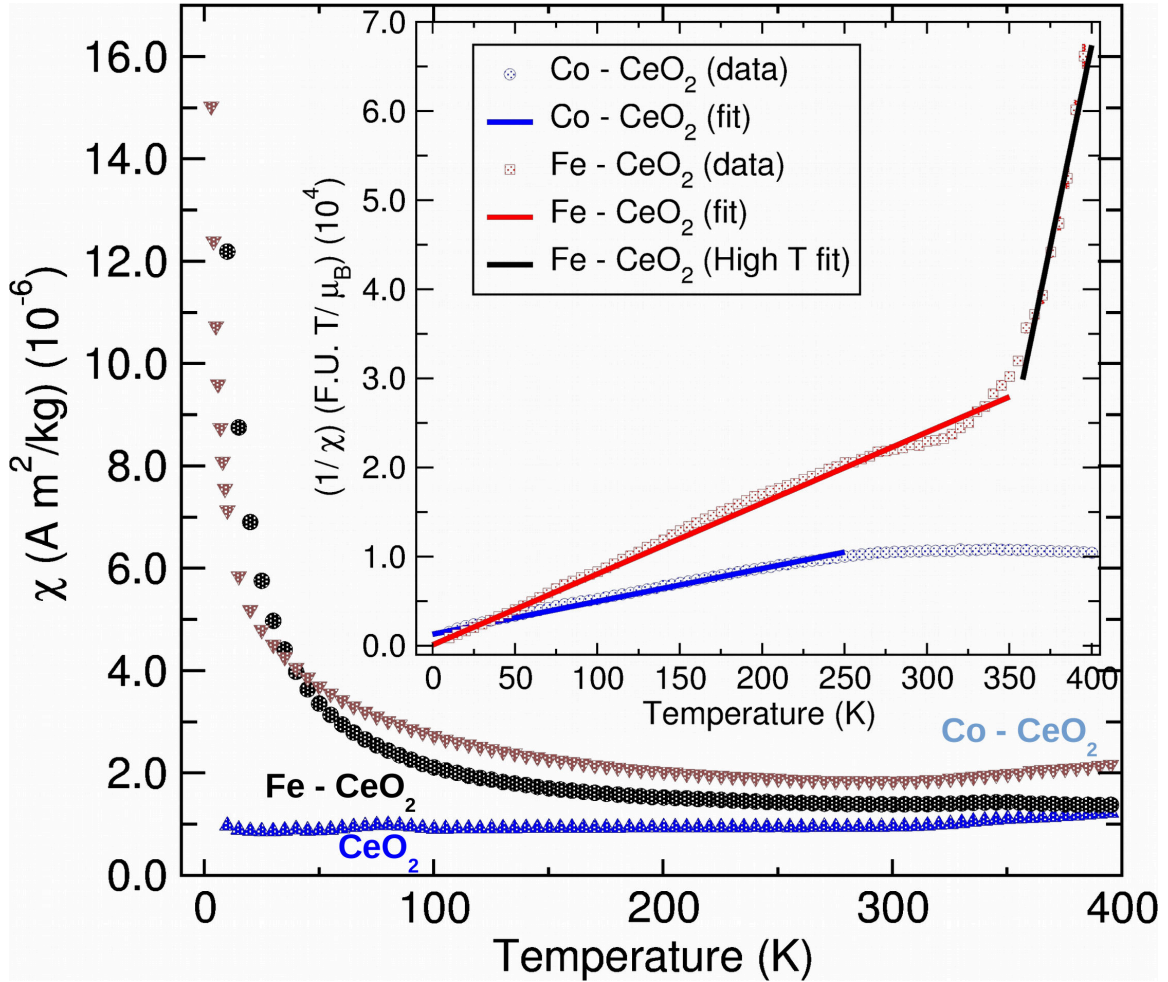


Figure 5.6: $\chi(T)$ of CeO_2 , $\text{Fe} - \text{CeO}_2$, and $\text{Co} - \text{CeO}_2$ nanocrystallites measured in $\mu_0 H = 2.5$ mT are presented. The inset shows $\chi(T)^{-1}$ data and Curie Weiss model fits (solid lines) of $\text{Fe} - \text{CeO}_2$ and $\text{Co} - \text{CeO}_2$ nanoparticles after subtracting CeO_2 background. $\text{Fe} - \text{CeO}_2$ and $\text{Co} - \text{CeO}_2$ nanocrystallites $1/\chi(T)$ data is divided into two regions as discussed in the text. For $\text{Fe} - \text{CeO}_2$ the high temperature component (> 350 K) is fit to Curie Weiss model and for $\text{Co} - \text{CeO}_2$ the high temperature (> 250 K) component is temperature independent.

($t_{2g} \downarrow$) configuration, resulting a low spin Fe^{3+} with net spin of $S = 1/2$ and μ_{eff} of Fe^{3+} as $1.73 \mu_B$. Together the effective magnetic moment of Fe is: $(0.30 \times 4.89) + (0.70 \times 1.73) = 2.68 \mu_B$, consistent with the above Curie-Weiss analysis (see table 5.2).

In the same manner, in the high temperature region the decrease in moment is due

to the following reason. In Fe²⁺ the first three electrons occupy t_{2g} state with parallel spin ($3t_{2g} \uparrow$) and the remaining three electrons occupy t_{2g} state with anti-parallel spin ($3t_{2g} \downarrow$), giving a low spin Fe²⁺ with a net spin of $S = 0$ and $\mu_{eff} = 0$; as described above the low spin Fe³⁺ moment is $1.73 \mu_B$. Collectively, the effective magnetic moment of Fe in the high temperature region is $1.23 \mu_B$, in agreement with the Curie-Weiss analysis (see table 5.2).

Similarly, in the Co - CeO₂ nanoparticles the XAS measurements identified 33% Co²⁺ T_d and 67% Co³⁺ O_h. The Co³⁺ in O_h coordination have no magnetic moment, whereas, Co²⁺ in T_d have a spin moment of $3.87 \mu_B$. Overall the magnetic moment of 33% Co²⁺ and 67% Co³⁺ amounts an effective magnetic moment of $1.29 \mu_B$ comparable to μ_{eff} obtained by the Curie-Weiss analysis. With an increase in temperature, the susceptibility is temperature independent. Unlike Fe; Co has a large spin-orbit coupling[151]; the observation that the contribution is temperature independent is as a result of the energy difference between the ground and excited orbital states being larger than $k_B T$.

5.3.2 Field dependent magnetic response of CeO₂, Fe and Co decorated CeO₂ nanocrystallites

To further probe the overall magnetic response, M versus $\mu_0 H$ were collected between 2 and 300 K in a ± 5 T field (figures 5.7(a)-(f)). A linear paramagnetic component is removed for all the samples from the data. Figure 5.7a shows the $M(\mu_0 H)$ curves measured at 2 - 300 K of CeO₂ nanocrystallites. It is clear from the $M(\mu_0 H)$ measurements that in the low temperatures (2, 5, and 10 K) the magnetization is relatively

large compared to the 100, 200, and 300 K data, and all loops saturated at ~ 3 T. At 2 K nanoscale CeO₂ has a magnetic saturation (M_s) of 0.60 A m²/kg, whereas with increasing temperature the M_s values further decreases to 0.35 and 0.10 A m²/kg at 5 and 10 K respectively. Figure 5.7b shows the $M(\mu_0 H)$ curves measured at 100, 200, and 300 K of CeO₂ nanocrystallites. The M_s values are much reduced from that of low temperatures. At 100, 200, and 300 K the M_s values are 0.25×10^{-3} , 0.10×10^{-3} , and 0.05×10^{-3} A m²/kg respectively, and all loops saturated at ~ 0.5 T.

Figure 5.7c shows the $M(\mu_0 H)$ curves measured at 2 – 300 K of Fe – CeO₂ nanocrystallites. Similar to CeO₂, the $M(\mu_0 H)$ measurements in the low temperatures (2, 5, and 10 K) the magnetization is relatively large compared to the 100, 200, and 300 K data and all loops saturated at ~ 3 T. Interestingly, at 2, 5, and 10 K the M_s values are 0.60, 0.35 and 0.10 A m²/kg respectively; all similar to CeO₂ nanocrystallites. Figure 5.7d shows the $M(\mu_0 H)$ curves measured at 100, 200, and 300 K of Fe – CeO₂ nanocrystallites. Unlike CeO₂ (M_s values are temperature dependent) for Fe – CeO₂ nanocrystallites at 100, 200, and 300 K the M_s is athermal in nature with a value of 0.20×10^{-3} A m²/kg. Additionally, at high temperatures the loops are saturated at ~ 0.5 T.

$M(\mu_0 H)$ curves measured at 2 – 300 K of Co – CeO₂ nanocrystallites are shown in Fig. 5.7e. Similar to CeO₂ and Fe – CeO₂, the $M(\mu_0 H)$ measurements in the low temperatures (2, 5, and 10 K) saturated at ~ 3 T. The M_s values at 2, 5, and 10 K are 0.30, 0.15 and 0.07 A m²/kg respectively; comparatively smaller than both CeO₂ and Fe – CeO₂ nanocrystallites. The $M(\mu_0 H)$ loops measured at 100, 200, and 300 K clearly identify that M_s is temperature dependent with values 0.45×10^{-3} A m²/kg,

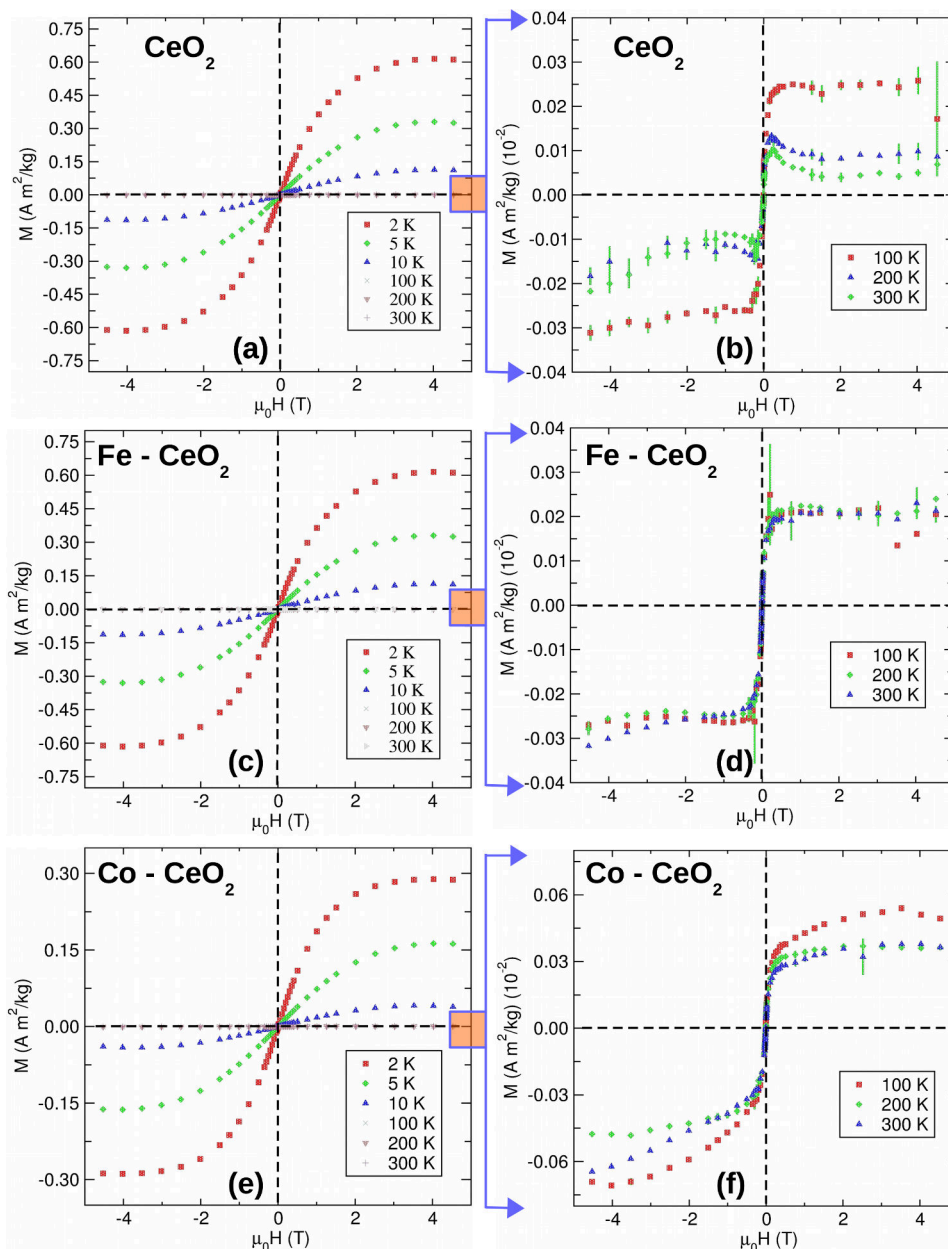


Figure 5.7: (a, c, e) Magnetization curves (corrected for diamagnetic background) for CeO_2 , $\text{Fe} - \text{CeO}_2$, and $\text{Co} - \text{CeO}_2$ are presented at 2, 5, 10, 100, 200, and 300 K. (b) In CeO_2 the magnetic saturation (M_s) values are relatively comparable at 100, 200 and 300 K. (d) In $\text{Fe} - \text{CeO}_2$ at 100, 200, and 300 K the M_s values are temperature independent. (f) In $\text{Co} - \text{CeO}_2$ at 200 and 300 K the magnetization curves are temperature independent.

$0.30 \times 10^{-3} \text{ A m}^2/\text{kg}$ and $0.30 \times 10^{-3} \text{ A m}^2/\text{kg}$ respectively, all comparable to CeO_2 and $\text{Fe} - \text{CeO}_2$ nanocrystallites.

Overall the magnetometry results are clearly indicating that all samples are saturated above 3 T below 10 K and 0.5 T above 100 K. To gain insights into the microscopic origins of the magnetism of Ce, Fe and Co cations, and oxygen vacancies, electronic structure and element specific magnetism measurements were performed.

5.4 Local Environment and Electronic Structure

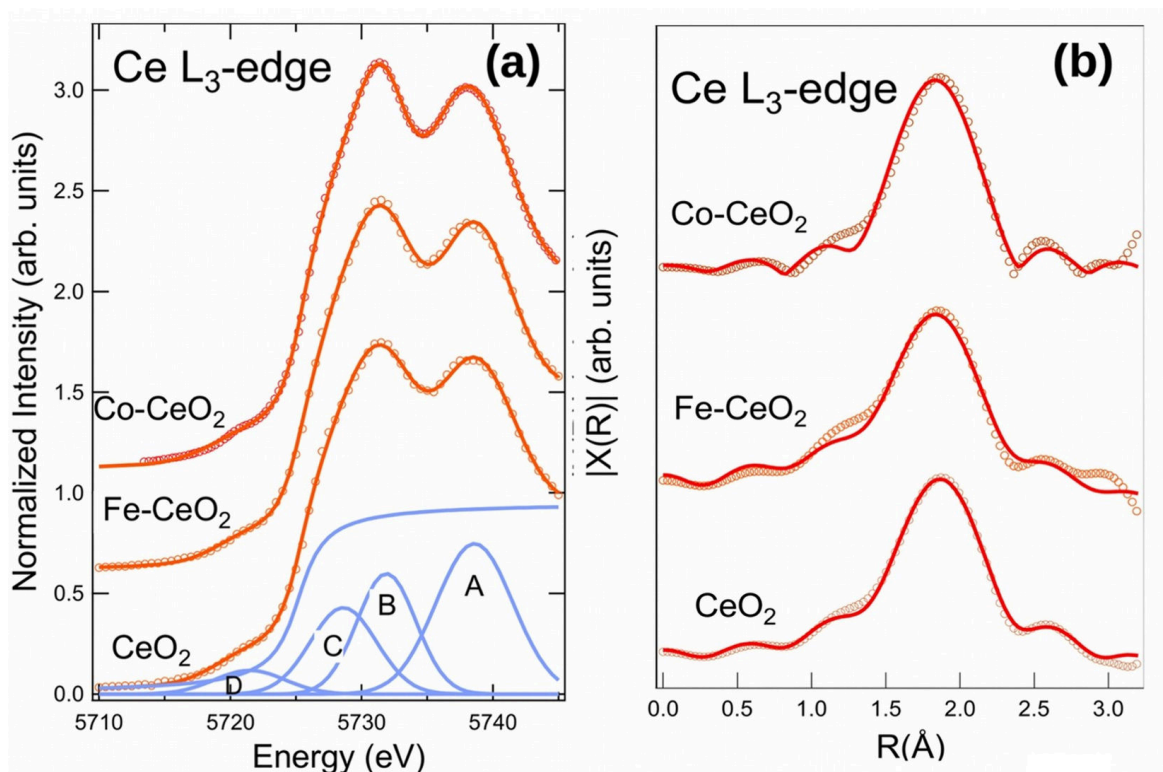


Figure 5.8: (a) The normalized XANES spectra were fitted with Gaussian functions. To exclude the effects of the edge jump from fits, an arctan function was included, as shown. (b) Fourier transforms represent raw data without correcting for phase shifts. Theoretical fits are the solid lines.

Because the electronic and magnetic properties of Ce ions depend strongly on the localized and delocalized $4f$ electron states, x-ray absorption near edge structure (XANES) experiments were performed to identify and quantify the oxidation state of Ce ions in nanoceria, Fe-decorated nanoceria (Fe- CeO_2) and Co-decorated nanoceria (Co- CeO_2).

5.4.1 Concentration of Ce^{3+} content

As shown in figure 5.8a, XANES spectra exhibit a doublet due to the interaction between the $4f$ orbitals of the Ce atoms and $2p$ orbitals of oxygen ligands. The peculiar doublet consists of four observed peaks[152; 153; 154]. Component A is assigned to the transition from the Ce $2p$ shell to $5d$ shell (final state $2p\underline{4}f^05d^1$ with no f electrons) while component B is assigned to the excitation from the $2p$ shell to $5d$ shell along with an electron being excited from the O $2p$ shell to the Ce $4f$ shell, thus leaving a hole in the valence band (final state $2p\underline{4}f^15d^1v$; v is the hole). Component C is assigned to Ce^{3+} , and component D is assigned to the $2p_{\frac{3}{2}} \rightarrow 4f$ quadrupole transition that is a consequence of $5d$ admixtures to the $4f$ states[155]. The concentrations of Ce^{3+} from spectral weighting were estimated to be $20 \pm 2\%$. In nanoceria each Ce atom ($[Xe]4f^15d^16s^2$) can donate four electrons to bonding orbitals with two O ($1s^22s^22p^4$) atoms. When an oxygen vacancy is formed, the two electrons previously occupying p orbitals of the O atom are free to distribute. The localized electrons around Ce atoms changes the oxidation state from Ce^{4+} to Ce^{3+} . The constant concentration of $Ce^{3+}(4f^1)$ is as expected since the Fe and Co ions are surface decorating the nanoceria (i.e. Fe and Co ions distributed randomly on the

Table 5.3: Parameters from the shell fitting of Ce *L*₃ edge EXAFS analysis of CeO₂, Fe-CeO₂ and Co-CeO₂ nanocrystallites.

sample	<i>N</i>	<i>E</i> ₀ (eV)	$\sigma_{Ce-O_1}^2$ (Å ²)	<i>R</i> _{Ce-O₁} (Å)
CeO ₂	5(1)	6(1)	0.001(1)	2.32(2)
Fe-CeO ₂	7(2)	5(2)	0.005(4)	2.30(4)
Co-CeO ₂	8(1)	4(1)	0.007(2)	2.31(4)

surface of the nanoceria crystallites, bonding covalently through available O ions, as shown experimentally in References [52; 53]).

5.4.2 Identifying the local environment of Ce, Fe and Co

In order to gain insights into the local environment around Ce ions, we examined the extended x-ray absorption fine structure (EXAFS). Fourier transformed data and the corresponding EXAFS oscillations are shown in figure 5.8b.

All spectra were analyzed using the ATHENA and ARTEMIS software programs[70]. The theoretical calculation of the phase shifts and backscattering amplitudes for specific atom pairs were obtained using the FEFF program[71] based on the crystallographic data of CeO₂. EXAFS of CeO₂ was fitted to its crystal structure to obtain the amplitude reduction factor (S_0^2). EXAFS analysis at the Ce *L*₃ edge includes only the shell of the Ce – O single scattering path due to the small energy separation between *L*₃ and *L*₂ edges.

Spectral fits identify that the bond distances of first shell Ce – O systems are of 2.31 ± 0.04 Å. The coordination number and structural disorder around Ce (identified by Debye-Waller factors) increases in Fe-CeO₂ and Co-CeO₂. In addition to Ce

L_3 edge EXAFS measurements, we also performed EXAFS on Fe and Co K edge to identify the local environment around Fe and Co ions. EXAFS shell fitting results illustrate that Fe neighbours are O atoms(Fig. 5.9). Similarly, Co first neighbors are O atoms, second and third neighbors are Co atoms(Fig. 5.9). The Ce L_3 edge XAS results show that for all systems, the Ce sites exist between Ce^{3+} ($4f^1 \underline{v}$) and Ce^{4+} ($4f^0$) character, with a hole (\underline{v}) in the O $2p$ valence band.

Further XAS measurements on Fe L_3 and Co L_3 edges were performed to quantify the oxidation state and coordination Fe and Co ions. Figure 5.10a shows the experimental spectrum and simulations of Fe L_3 edge in two different coordinations: $Fe^{3+} O_h$ and $Fe^{2+} T_d$. The simulations are good agreement with experimental data for 30% Fe^{2+} in O_h and 70% Fe^{3+} in O_h . Similarly, Fig. 5.10b shows the Co L_3 edge experimental spectrum and simulations. The spectra are simulated with 33% $Co^{2+} T_d$ and 67% $Co^{3+} O_h$ environments.

5.4.3 Determining the oxidation state and local environment of Fe

Mössbauer spectroscopy measurements were performed at room temperature to identify the oxidation state and local environment of Fe ions. The Mössbauer spectrum consists of a doublet with no signature of a hyperfine field. The absence of the hy-

Table 5.4: Parameters from the shell fitting of Fe K edge EXAFS analysis of Fe- CeO_2 .

Shell	N	E_0 (eV)	$\sigma^2(\text{\AA}^2)$	R (\AA)
Fe – O	3(1)	-5(2)	0.008(2)	1.97(2)

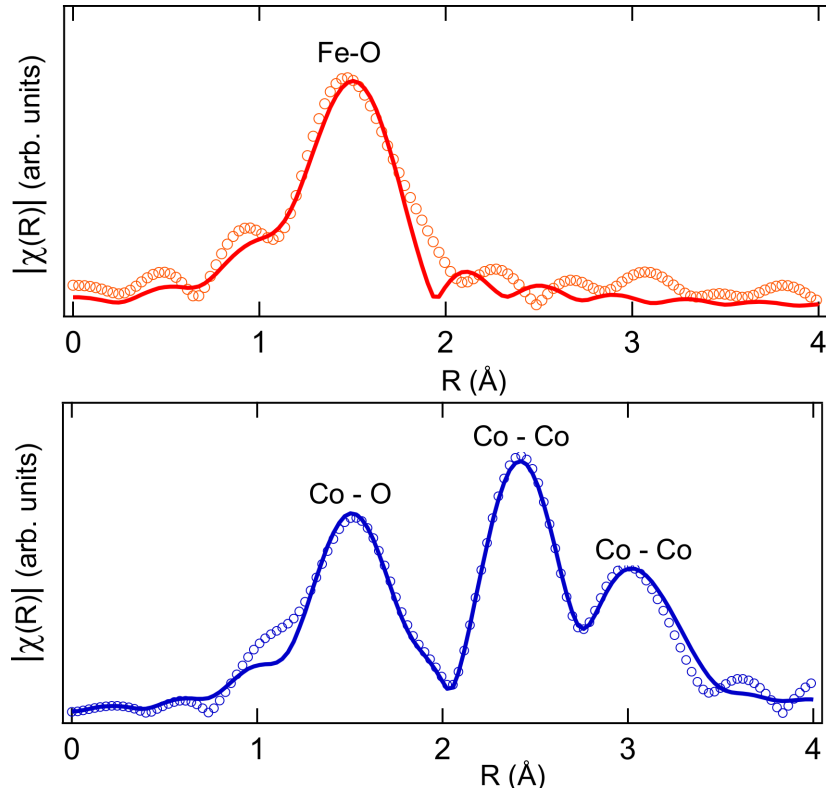


Figure 5.9: Fourier transformed magnitudes and fits of $\text{Fe}-\text{CeO}_2$ and $\text{Co}-\text{CeO}_2$ EXAFS data is shown.

perfine field (B_{hf}) is indicative of no secondary oxide phase formation. Two sites are identified; site-I with smaller isomer shift (δ_1) and larger quadrupole shift (Δ_1), site-II with larger δ_2 and smaller Δ_2 (Table 5.6). A higher Δ_2 is indicative of a more

Table 5.5: Parameters from the shell fitting of Co K edge EXAFS analysis of $\text{Co}-\text{CeO}_2$.

Shell	N	E_0 (eV)	$\sigma^2(\text{\AA}^2)$	R (\AA)
$\text{Co}_{O_h} - \text{O}$	8(1)	-5.7(8)	0.0020(9)	1.925(8)
$\text{Co}_{O_h} - \text{Co}_{T_d}$	8(1)	-5.7(8)	0.0049(9)	2.867(1)
$\text{Co}_{T_d} - \text{Co}_{T_d}$	19(2)	-5.7(8)	0.0049(9)	3.35(2)

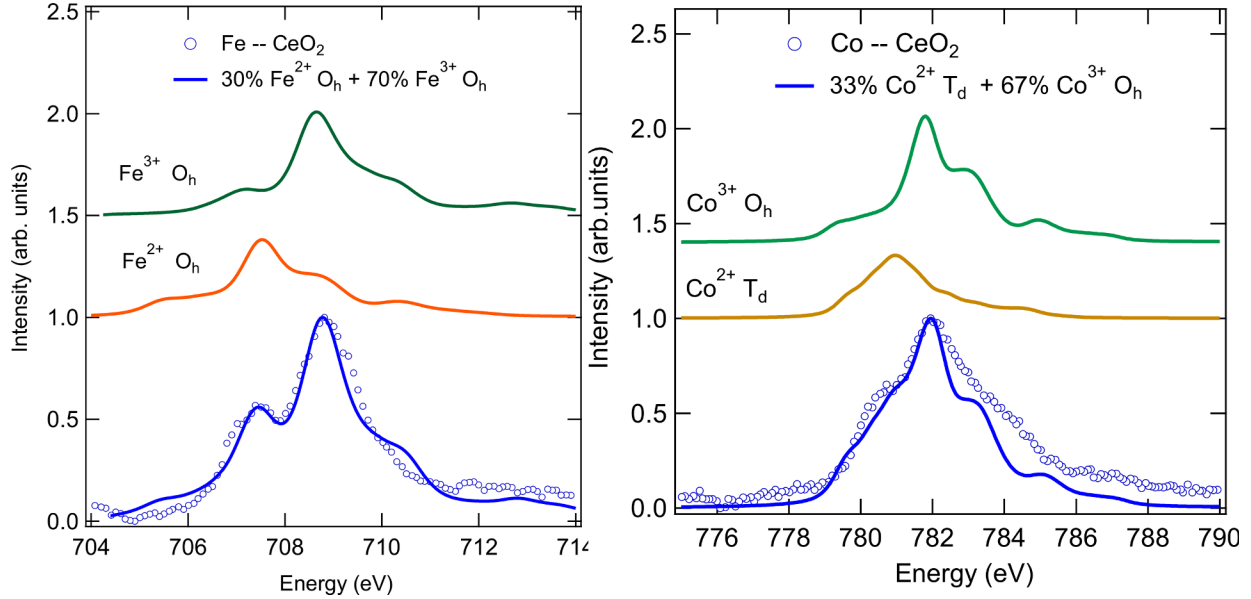


Figure 5.10: Fe L_3 edge XAS experimental spectra and simulations of Fe – CeO_2 nanoparticles. The calculated Fe^{2+} (O_h) and Fe^{3+} (T_d) components of the XAS spectra and theoretical resulting summed spectrum are shown. (b) Co L_3 edge XMCD experimental spectrum and simulations are shown. Co ions exist in Co^{2+} T_d and Co^{3+} O_h environments.

Table 5.6: Mössbauer hyperfine parameters (line width (Γ), isomer-shift (δ) and quadrupole splitting (Δ)) are presented.

Sample	Γ (mm/s)(± 0.02)	δ_1 (mm/s) (I)	Δ_1 (mm/s) (I)	Area ₁ (%)	δ_2 (mm/s) (II)	Δ_2 (mm/s) (II)	Area ₂ (%)
Fe- CeO_2	0.22	0.36 ± 0.01	0.74 ± 0.06	70 ± 10	0.36 ± 0.01	1.14 ± 0.07	30 ± 10

distorted electron charge distribution around the Fe nuclei, whereas lower Δ_1 is characteristic of a relatively undistorted Fe electric field distribution. The values of site-I are due to distorted Fe^{3+} and site-II reflects the undistorted Fe^{3+} ions.

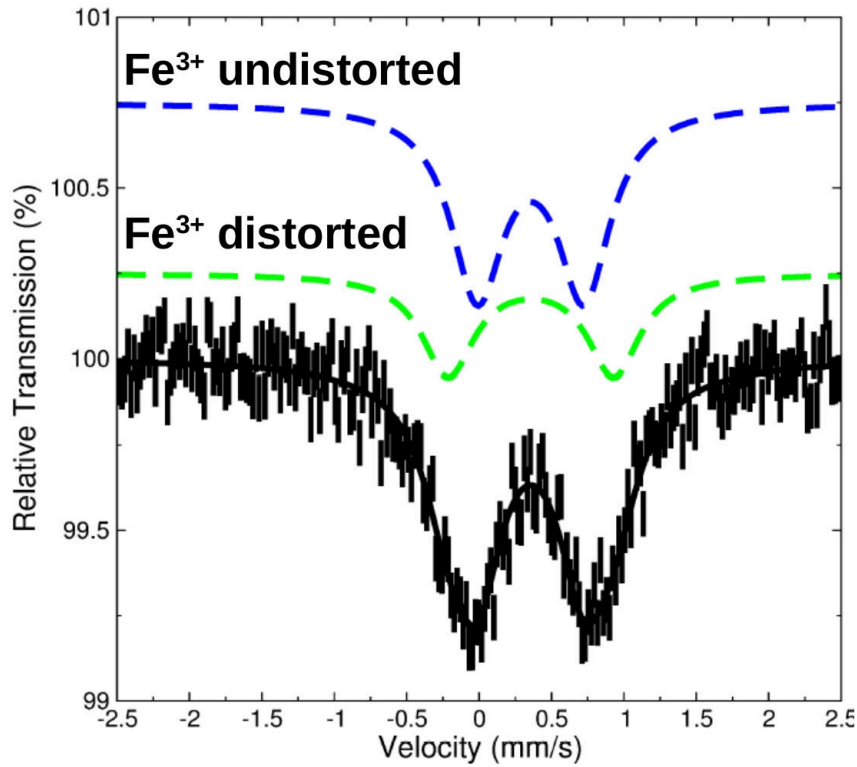


Figure 5.11: Mössbauer spectra of Fe-decorated CeO_2 systems. The solid lines represent the fitted spectra (left) and subspectra components (right) used for the undistorted (site-I) and distorted (site-II) are shown. As identified by the ICP wt% the Fe decorations are very low and which is why the statistics are poor.

5.4.4 Quantifying the f electron occupancy

To describe the f electrons, their occupancy, and electronic structure at the Ce sites, we used the Ce $M_{4,5}$ edge XAS (probes directly the valence $4f$ states by exciting electrons from $3d$ core orbitals, and gives insights to the ground state) in combination with atomic multiplet calculations based on a simplified Anderson impurity model[62; 91]. The $M_{4,5}$ edge XAS spectra (Fig. 5.13a) of nanoceria consists of main peaks at 884.6 and 902.4 eV and additional weaker satellite peaks at 889.8 and 908.0 eV. The

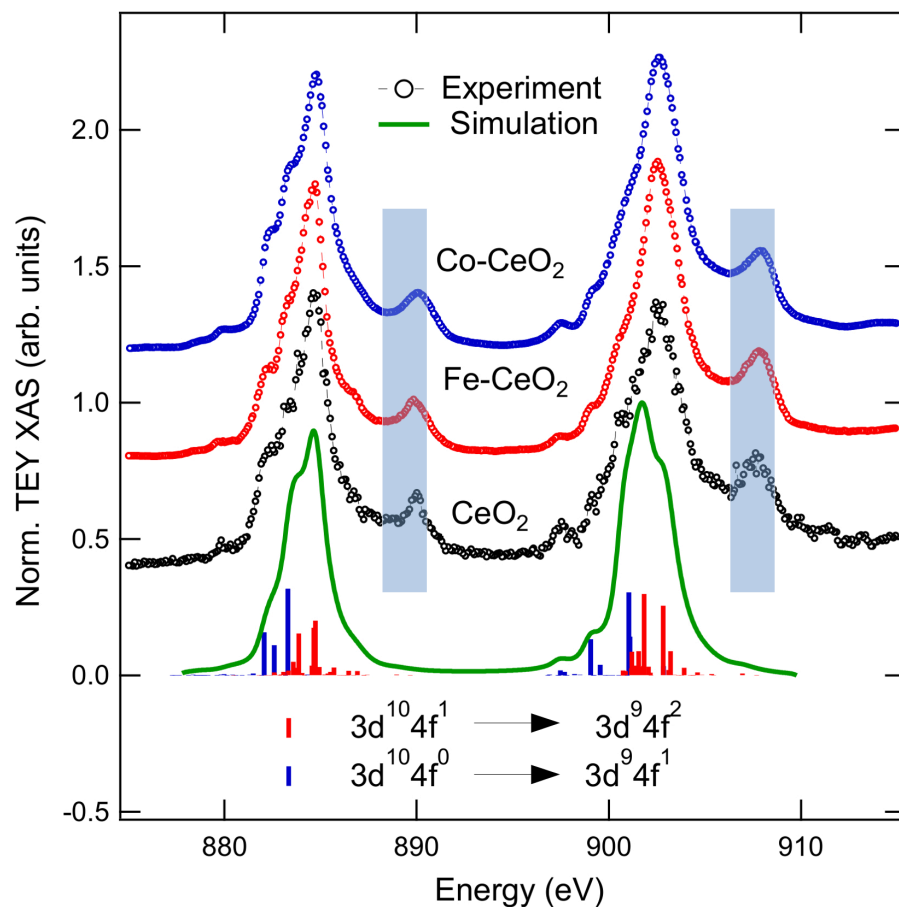


Figure 5.12: Ce $M_{4,5}$ edge XAS data and simulation with ionic limit. Higher energy satellite peaks region is shaded to show that the spectra could not be modeled successfully with $3d^{10}4f^0$ (initial) and $3d^9 4f^1$ (final) states and charge-transfer effects needs to be included.

energy splitting between Ce $M_{4,5}$ edges is due to the spin-orbit coupling with the $3d_{5/2}$ and $3d_{3/2}$ core-holes.

The primary features of the Ce $M_{5,4}$ edge XAS spectra originate from electric-dipole allowed transitions from $3d^{10}4f^n \rightarrow 3d^9 4f^{n+1}$ [91]. For nanoceria, experimental spectra are simulated including Coulomb, exchange, and spin-orbit interactions by considering only $3d^{10}4f^0 \rightarrow 3d^9 4f^1$ and $3d^{10}4f^1 \rightarrow 3d^9 4f^2$ configurations.

XAS simulations of Ce $M_{5,4}$ edge $3d^{10}4f^1 \rightarrow 3d^94f^2$ transitions were simulated using CTM4XAS 5.5 with Slater integrals F_{ff} at 79%, F_{df} and G_{df} at 100%, atomic values and $3d$ spin-orbit coupling at 98%. A Gaussian broadening of 0.20 eV was applied to account for instrumental broadening, and Lorentzian broadening of 0.4 eV and 0.2 eV were applied for the M_5 and M_4 edges, respectively. Results indicated that if we assumed only oxygen vacancies and the ground states were due to $4f^0$ and $4f^1$ atomic-like multiplets, the experimental spectra could not be modeled successfully (Fig. 5.12) by the atomic(ionic) limit; charge transfer effects need to be considered.

Charge transfer simulations for $3d^{10}4f^0 + 3d^{10}\underline{L}4f^1 \rightarrow 3d^94f^1 + 3d^9\underline{L}4f^2$ (\underline{L} is the hole in the O $2p$ band) were implemented using the command-line (as described in the CTM4XAS manual). For this configuration, Δ_{IS} was set to 2.0 eV, $\Delta_{FS} = -2.5$ eV, and $T_{IS} = T_{FS} = 0.77$ eV. Gaussian broadening of 0.20 eV was applied to account for instrumental broadenings and Lorentzian broadenings of 0.50 and 0.60 eV were applied to the M_5 and M_4 edges, respectively.

In order to understand the Ce $M_{4,5}$ edge XAS spectra, especially the origin of the higher energy satellites, we focus on the ligand hole contribution to the $3d^{10}4f^0$ ground state (from charge fluctuations in initial and final states due to hole on oxygen ligand). A schematic representation of a cluster consisting of a Ce ion surrounded by eight O ions is shown in Fig. 5.13b. Because of the strong Ce $4f$ - O $2p$ hybridization, the initial state of the transition is described by $3d^{10}4f^0 + 3d^{10}\underline{L}4f^1$ and the final state by $3d^94f^1 + 3d^9\underline{L}4f^2$ (where \underline{L} describes a hole in the O $2p$ band[156]). The two configurations in the final state form bonding ($3d^94f^1$) and antibonding ($3d^9\underline{L}4f^1$) orbital combinations. Four additional terms ΔE_{gs} , T_{gs} , ΔE_{fs} ,

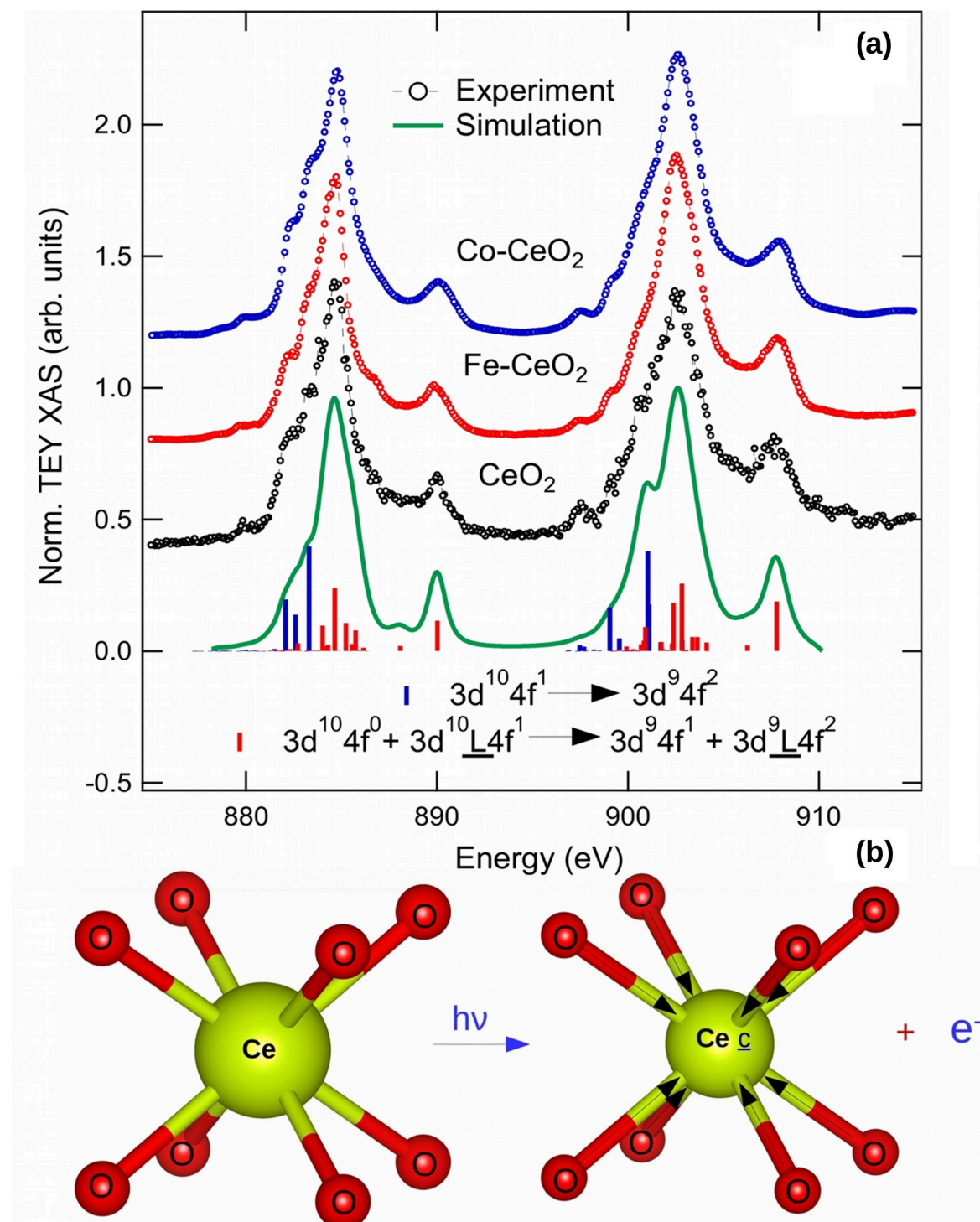


Figure 5.13: (a) Ce $M_{4,5}$ edge XAS data and the simulation. Charge transfer effects with $4f^0+4f^1 \underline{L}$ ground and $4f^1+4f^2 \underline{L}$ final states are included in order to match the experimental spectra as discussed in the text. (b) Representation of charge transfer effect between O 2p ligand and Ce 4f are shown; \underline{c} is core hole on Ce.

and T_{fs} are defined to describe the relative energies and interactions of these initial and final states[91]. Here $\Delta E_{gs} = E(3d^{10}\underline{L}4f^1) - E(3d^{10}4f^0)$ is the charge transfer energy between two ground states, and $T_{gs} = \langle(3d^{10}\underline{L}4f^1)|H|(3d^{10}4f^0)\rangle$ is the effective hopping-integral connecting the two ground state configurations. Similarly $\Delta E_{fs} = E(3d^9\underline{L}4f^2) - E(3d^94f^1)$ and $T_{fs} = \langle(3d^9\underline{L}4f^2)|H|(3d^94f^1)\rangle$ are charge transfer and hopping integrals of the final state. Our simulation was modelled with 77% $3d^{10}4f^0$ and 23% $3d^{10}\underline{L}4f^1$ ground state configuration and $\Delta E_{gs} = 2.0$ eV and $T_{gs} = 0.77$ eV. The ΔE_{fs} is defined as the sum of $\Delta E_{gs} + U_{ff} - U_{fd}$, where U_{ff} represent the Coulomb repulsion and U_{fd} the core-valence repulsion integrals. Our simulation agrees best with the experimental data with $\Delta E_{fs} = -2.5$ eV. For a purely Ce⁴⁺ based system the Ce $M_{4,5}$ edge $\Delta E_{fs} = -1.5$ eV[157]. In lanthanides it is expected that $U_{ff} > U_{fd}$ due to the smaller orbital radius[62]. However, in nanoceria, $U_{fd} > U_{ff}$ indicates that the charge transfer energy is reduced due to covalent Ce $4f - O 2p$ states in this mixed valency system. Earlier, on the basis of band-structure calculations it was shown that ceria is less ionic[158].

Oxygen K edge provide further insights into the bonding between oxygen and Ce ions. Because Ce $M_{5,4}$ simulations establish less ionic nature of Ce, consequently O K edge probes the $1s-2p$ electronic transition and provides information on the antibonding part due to hybridization. Oxygen K edge of CeO₂, Fe - CeO₂, and Co - CeO₂ are shown in figure 5.14. We can differentiate two parts in these spectra: the first one, below 540 eV, called edge region, display three main features labelled $4f$ (~ 531 eV), e_g (~ 533 eV), and t_{2g} (~ 538 eV). The second part (above 540 eV) with three low intense peaks peaks around ~ 543 eV, ~ 548 , and ~ 553 eV. The absorption

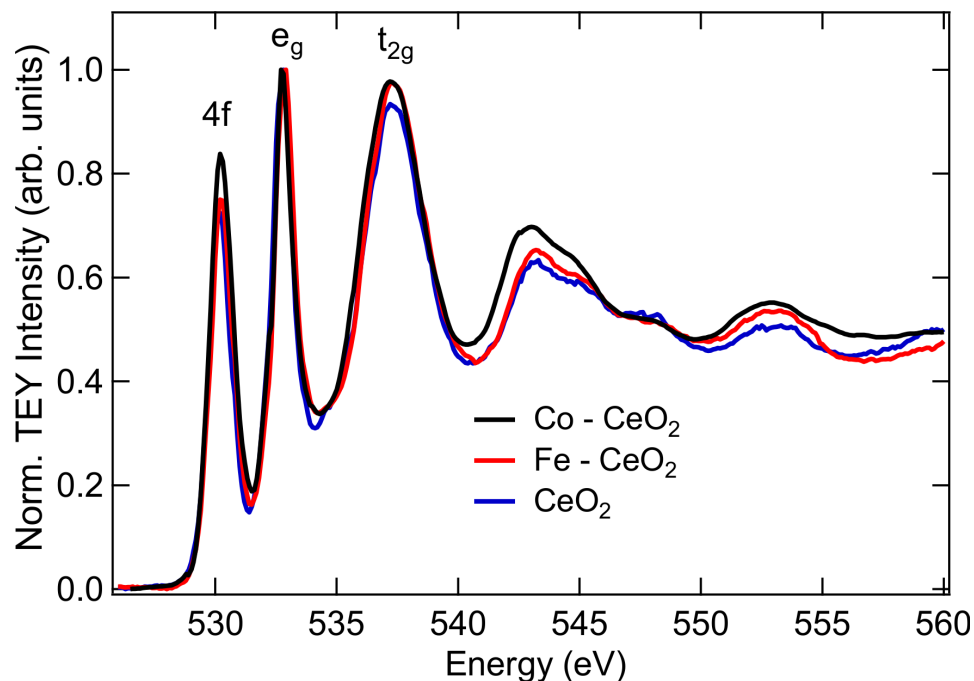


Figure 5.14: Oxygen K edge XAS spectra of the nanoscale CeO_2 , $\text{Fe} - \text{CeO}_2$, and $\text{Co} - \text{CeO}_2$ nanoparticles are shown. The three main transitions are due to $\text{O } 2p$ hybridized with the $4f$, $5de_g$, and $5dt_{2g}$ states are shown.

at ~ 531 eV is due to the transition from $\text{O } 1s$ to $\text{Ce } 4f$ state[159; 160], and the peaks at ~ 533 eV and the peaks at ~ 533 eV and ~ 538 eV are due to transition into $5de_g$ and $5dt_{2g}$ states. Dipole selection rules allows the transition from s to p states, however, the observation that we see transitions from s to f and p is an evidence of hybridization between the states.

Covalent orbitals play a major role in understanding the origin of magnetism. In trivalent Ce compounds such as CeRh_3B_2 and CeCuSi the magnetism is due to highly localized $4f$ electrons. By contrast in tetravalent α -cerium compounds CeFe_2 or CeCo_5 , the magnetism is from hybridization between $4f$ and conduction electrons[161]. The results of density functional theory calculations (LDA+U, LSDA+U,

LDA/GGA + U) of nanoceria are controversial. Some studies support charge localization in the oxygen vacancies[38; 39] as the source of the magnetism. Other studies identify Ce vacancies[162; 163] as responsible for ferromagnetism (via superexchange between localized electrons in vacancies and neighbouring Ce sites). Finally, some challenge both arguments[164], leaving the question unresolved.

5.5 Elemental and Overall Magnetism

Identifying the origin of magnetism in nanoceria (via bulk magnetization techniques such as magnetometry and susceptometry) is complex due to the challenges in decoupling the contributions from Ce mixed valence states and oxygen vacancies. X-ray magnetic circular dichroism (XMCD) is a sensitive tool to investigate the source of magnetism at an elemental atomic level via the excitation of core level electrons to unoccupied states above the Fermi level (E_F). XMCD experiments have the advantage of being site and orbital selective due to the electric (or quadrupole) selection rules. To gain insights into the role of the $4f$ electrons' contribution (conduction or hybridized) we performed surface and bulk sensitive XMCD measurements simultaneously using total electron yield (TEY) and total fluorescence yield (TFY) over the $M_{4,5}$ edges; TEY probes the first ~ 2 nm of the surface while TFY measures the complete sample but is prone to self-absorption effects[165]. In Fig. 5.15a we present the 10 K artifact free⁵ ± 5 T XMCD spectra. The TEY Co-CeO₂ Ce $M_{5,4}$ XMCD is most representative due to the least amount of surface charging. Note that ceria is

⁵The XMCD spectra were obtained as the difference of the corrected x-ray-absorption spectra for both left and right circularly polarizations. To make sure that the final XMCD spectra were free of experimental artifacts, such as those from charging effects, spectra were also collected for the opposite applied field direction.

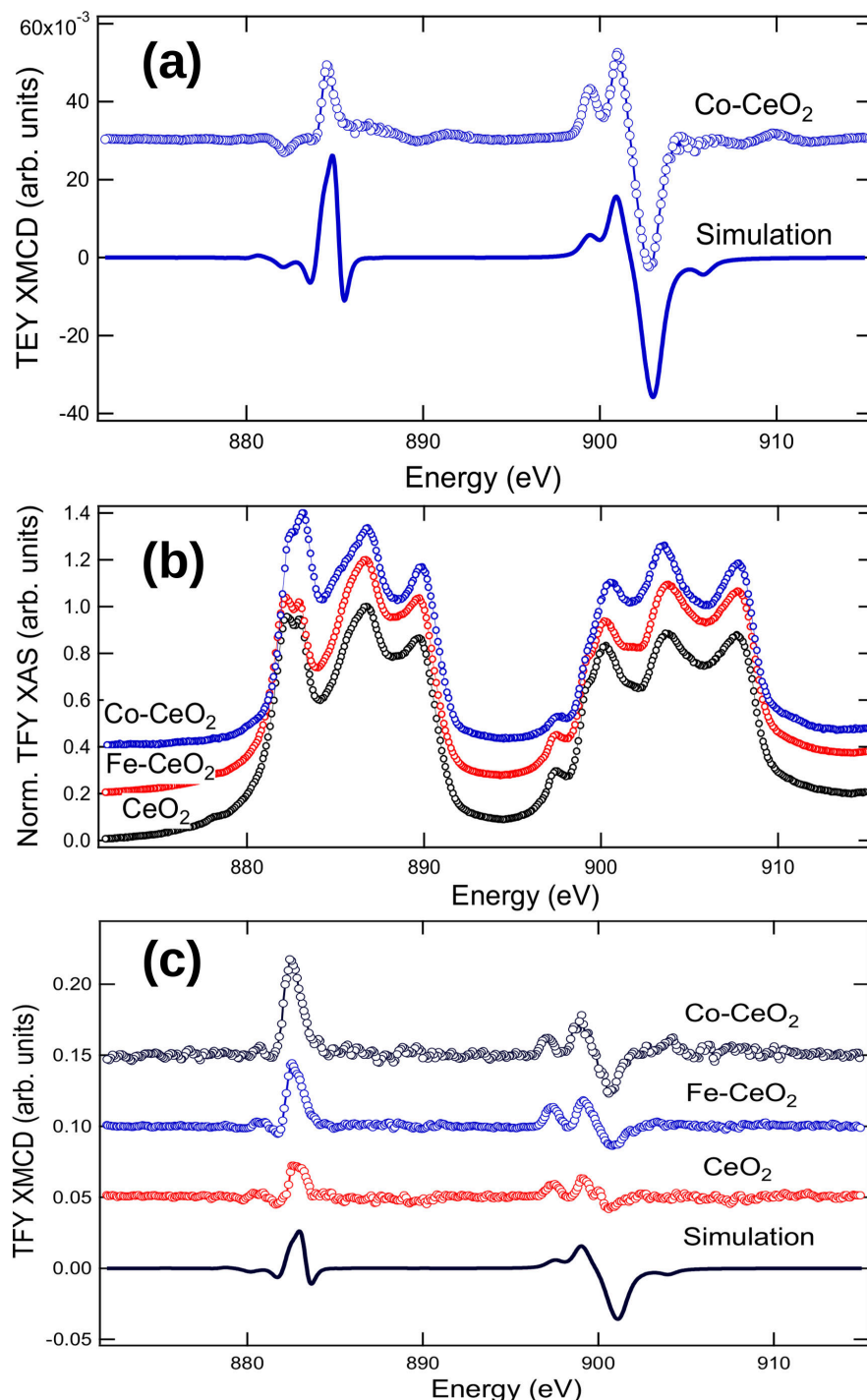


Figure 5.15: Ce $M_{5,4}$ TEY(surface) and TFY(bulk) XMCD spectra evidencing the magnetic moment at Ce $4f$ sites. (a) Co-CeO₂ TEY XMCD and simulation are shown. The absence of the negative peak ~ 886 eV in the experiment is an indication that $4f$ electrons are hybridized as discussed in the text. (b,c) A comparison of Ce $M_{5,4}$ XAS and XMCD is shown. The origin of the energy axis of the simulated spectra has been chosen to align with the maximum intensity peak of the M_5 edge and the simulated spectra is reduced by a factor of twelve to match the experimental intensity of nanocerium.

	Co-CeO ₂	CeO ₂	Fe-CeO ₂	Co-CeO ₂
	TEY/surface	TFY	TFY	TFY
$\langle L_z \rangle (\hbar)$	-0.24(1)	-0.24(1)	-0.36(2)	-0.48(2)
$\langle S_z \rangle (\hbar)$	0.03(1)	0.03(1)	0.05(1)	0.06(2)
$\langle J_z \rangle (\hbar)$	-0.21(1)	-0.21(1)	-0.32(2)	-0.42(2)
$\langle L_z \rangle / \langle S_z \rangle$	-8	-8	-7.2	-8

Table 5.7: Contributions of the z-component of the orbital and spin magnetic moments obtained from the TEY (surface) XMCD simulations of Co-CeO₂ and TFY (bulk) XMCD of CeO₂, Fe-CeO₂ and Co-CeO₂ nanocrystallites.

a poor conductor, and Co-CeO₂'s conductivity is high compared to that of Fe-CeO₂ and CeO₂ which made it difficult to measure clean XMCD spectra in TEY for the Fe-CeO₂ and CeO₂ samples. Overall both TEY and TFY XMCD spectra clearly identify that the Ce 4*f* electrons unambiguously carry a magnetic moment on both the surface and in the bulk.

5.5.1 Quantifying the spin and orbital magnetic moments

To quantify the magnetic moment, XMCD spectra were simulated using Xclaim^[63] for the $3d^{10}4f^1 \rightarrow 3d^94f^2$ transition in the atomic limit. The contributions of the XMCD spectral orbital and spin magnetic moments obtained from the surface and bulk contributions are in table 5.7. This dichroic signal is explicit evidence of Ce sites carrying magnetizable moments. In general, the spectral shape of the Ce $M_{4,5}$ edges are indicative of a ground state total angular momentum ($J = \frac{5}{2}$ for a pure state $4f^1$ state). Any changes in the XMCD spectral shape can be attributed to different

values of J contributing to the ground state[161; 166]. It is important to note that the simulated spectra (Fig. 5.15) are for a pure $J = \frac{5}{2}$ state are not in complete agreement with experiment (for example, the absence of the negative peak around ~ 886 eV in the XMCD experimental spectrum compared to the simulation is an indication that Ce $4f$ electrons are hybridized as discussed below). Interestingly, nanoceria's Ce $M_{4,5}$ XMCD spectral line shape is different from CeRh₃B₂ and CeCuSi[161] (where the ground state is pure $J = \frac{5}{2}$ and magnetism is due to $4f$ conduction electrons) but quite similar to the XMCD spectra of CeFe₂ and a Ce/Fe multilayer (ground state is a mixture of $J = \frac{5}{2}$ and $J = \frac{7}{2}$ [161; 167]). This is indicative of Ce $4f$ electrons being strongly hybridized with the O $2p$ valence band. At the M edges, although the TFY XAS signal is distorted[168] because of self absorption (Fig. 5.15b) the TFY XMCD (Fig. 5.15c) signal is similar to TEY XMCD (surface). The TFY XMCD magnitude increases in the order of CeO₂ < Fe-CeO₂ < Co-CeO₂. Results identify that foreign ions with intrinsic moments (such as Fe and Co) enhances the overall magnetic moment at Ce $4f$ increases (Table. 5.7).

5.6 Conclusions

In this Chapter, we studied structure, composition, local environment, electronic structure and magnetism of nanoscale CeO₂, Fe and Co decorated CeO₂ systems. XRD refinements, TEM and Mössbauer spectroscopy analysis identify that the systems are phase pure with identical $Fm\bar{3}m$ space group and crystallite sizes are of ~ 20 nm. Ce $L_3/M_{4,5}$, Co and Fe K edges show the presence of mixed valent Ce³⁺/Ce⁴⁺ ions and Ce $4f - O 2p$ hybridization. Collectively XMCD and SQUID magnetome-

try measurements performed on the systems show that Ce 4*f* sites carry a magnetic moment and the moment at Ce 4*f* sites can be enhanced via neighbouring transition metal ions such as Fe and Co. Additionally surface and bulk magnetism compared between XMCD and SQUID magnetometry shed light on the role of the oxygen vacancy orbitals and Ce 4*f* – O 2*p* hybridized states in the *d*⁰ magnetism.

Chapter 6

Discussion

The nanoscale metal oxides systems (Fe_3O_4 , CoFe_2O_4 , CeO_2 , $\text{Fe} - \text{CeO}_2$, and $\text{Co} - \text{CeO}_2$) studied in the thesis are classified into non- d^0 and d^0 magnetic oxides.

6.1 Fe_3O_4 and CoFe_2O_4 Nanoparticles

Fe_3O_4 and CoFe_2O_4 are rich in d electrons. Fe and Co atoms donate electrons to complete the $2p$ shells of oxygen atoms (O^{2-} anions). The electronic structure and element specific magnetism of the nanoparticles were investigated by the x-ray absorption fine structure spectroscopy (section 3.3), x-ray absorption spectroscopy (section 3.4), x-ray magnetic circular dichroism (section 3.4), and Mössbauer spectroscopy (section 3.5) techniques. The x-ray spectroscopy and Mössbauer spectroscopy results quantified the fraction of cation occupancies of Fe_3O_4 and CoFe_2O_4 as $(\text{Fe}_{0.90(6)}^{3+})[\text{Fe}_{1.11(6)}^{3+}\text{Fe}_{0.99(6)}^{2+}]\text{O}_4$ and $(\text{Co}_{0.20(2)}^{2+}\text{Fe}_{0.80(4)}^{3+})[\text{Co}_{0.60(4)}^{2+}\text{Co}_{0.20(2)}^{3+}\text{Fe}_{0.88(4)}^{3+}\text{Fe}_{0.32(4)}^{2+}]\text{O}_4$.

Our nanoscale Fe_3O_4 is an inverse spinel with $\text{Fe}^{3+} \text{O}_h \uparrow - \text{O} - \text{Fe}^{3+} \text{T}_d \downarrow$ coupled antiferromagnetically via superexchange interaction and $\text{Fe}^{3+} \text{O}_h \uparrow - \text{O} - \text{Fe}^{2+} \text{O}_h \uparrow$ coupled ferromagnetically via double exchange as shown in figure 6.1. The nanoscale CoFe_2O_4 is a mixed spinel, in addition to Fe^{3+} in T_d , and Fe^{3+} and Fe^{2+} in O_h , Co^{2+} occupy the T_d and O_h sites, and Co^{3+} occupy O_h sites. XMCD sum rule analysis performed on the Fe $L_{3,2}$ edges of Fe_3O_4 (Fig. 3.8) and CoFe_2O_4 (Fig. 3.11a) are clear indication that the ratio of orbital to spin angular momentum (L_z/S_z) are 0.16 and -0.10, respectively. The change of the sign is evidence that the overall orbital and spin moment of Fe are antiparallel to each other in CoFe_2O_4 . Similarly, the Co $L_{3,2}$ (Fig. 3.11b) edge results show that the ratio of L_z/S_z is 0.46, twice as large as Fe; the Co cations possess larger orbital momenta. The intense XMCD signal of the Co L_3

edge compared to L_2 is a further indication of strong orbital magnetism (consistent with similar studies on Fe doped CoFe_2O_4 thin films[169] and $\gamma\text{-Fe}_2\text{O}_3/\text{CoO}$ core shell nanoparticles[170]).

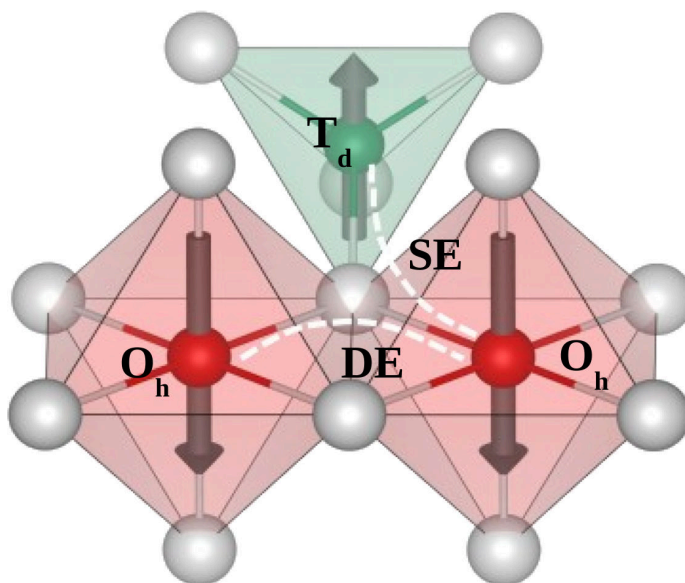


Figure 6.1: A schematic diagram of superexchange (SE) and double exchange (DE) interactions are shown. SE is mediated between tetrahedral (T_d) and octahedral (O_h) sites via central lattice oxygen, and DE is mediated between two O_h sites via lattice oxygen as shown[65].

6.1.1 Quantifying the e_g and t_{2g} orbital fraction

Figures 6.2a,b shows the oxygen K edge XAS spectrum of Fe_3O_4 and CoFe_2O_4 , respectively. The shaded area of the spectrum is due to the oxygen p character in the transition metal $3d$ band, and the broader band peaks are assigned to oxygen p character in the metal $4s$ and $4p$ orbitals[100]. Figures 6.2c,d focus on the transitions corresponding to O $2p$ states that are hybridized with the $3d$ states localized on the Fe and Co sites of the Fe_3O_4 and CoFe_2O_4 nanocrystallites. Our spectra show a clear

splitting of the peaks due to the local electrostatic interaction of the O $2p$ orbitals with the Fe and Co $3d$ orbitals[101]. Note that the peak splitting of Fe_3O_4 (Fig. 6.2c) is not very well-resolved compared to $\alpha\text{-Fe}_2\text{O}_3$ (see Fig. 1b of Ref. [100]). The reasoning is as follows: In $\alpha\text{-Fe}_2\text{O}_3$, Fe exists in $\text{Fe}^{3+} O_h$ state, whereas in Fe_3O_4 , Fe exists in three different states ($\text{Fe}^{3+} T_d$, $\text{Fe}^{3+} O_h$, and $\text{Fe}^{2+} O_h$). Because each site is associated with its respective $e_g - t_{2g}$ splitting, their overlap is responsible for the loss of resolution[101]. The area of t_{2g} and e_g are related to the number of $3d$ holes and hybridization effects. To gain further insights into the changes in e_g and t_{2g} orbitals population of Fe_3O_4 (Fig. 6.2c) and CoFe_2O_4 (Fig. 6.2d) spinels we performed peak fitting analysis of the two systems.

In Fe_3O_4 ¹, the t_{2g} ² and e_g ³ orbitals are populated at 23% and 77%, respectively. Interestingly, in the CoFe_2O_4 , where⁴ some of the Fe ions are replaced by Co ions, the area of the t_{2g} component increased to 39% and e_g decreased to 61%, indicating that overall Co substitution pulls the d orbitals away from the O $2p$ orbitals, making the hybridization with $3d$ ions weaker. Overall results show that mixed spinel CoFe_2O_4 has $\sim 16\%$ more electrons in t_{2g} orbitals than the inverse spinel Fe_3O_4 . The increase in the fraction of t_{2g} orbitals suggests that Co substitution in Fe_3O_4 impacts the crystal field energies and pulls the Fe/Co $3d$ orbitals away from the O $2p$ ligands. The direction in which $3d$ ions point towards the O $2p$ orbital play a key role in the magnetism because of their electronic interactions (especially exchange interactions).

¹ $(\text{Fe}_{0.90(6)}^{3+})[\text{Fe}_{1.11(6)}^{3+}\text{Fe}_{0.99(6)}^{2+}]\text{O}_4$

² $3d$ orbitals point away from oxygen $2p$ ligands

³ $3d$ orbitals point towards the oxygen $2p$ ligands

⁴ $(\text{Co}_{0.20(2)}^{2+}\text{Fe}_{0.80(4)}^{3+})[\text{Co}_{0.60(4)}^{2+}\text{Co}_{0.20(2)}^{3+}\text{Fe}_{0.88(4)}^{3+}\text{Fe}_{0.32(4)}^{2+}]\text{O}_4$

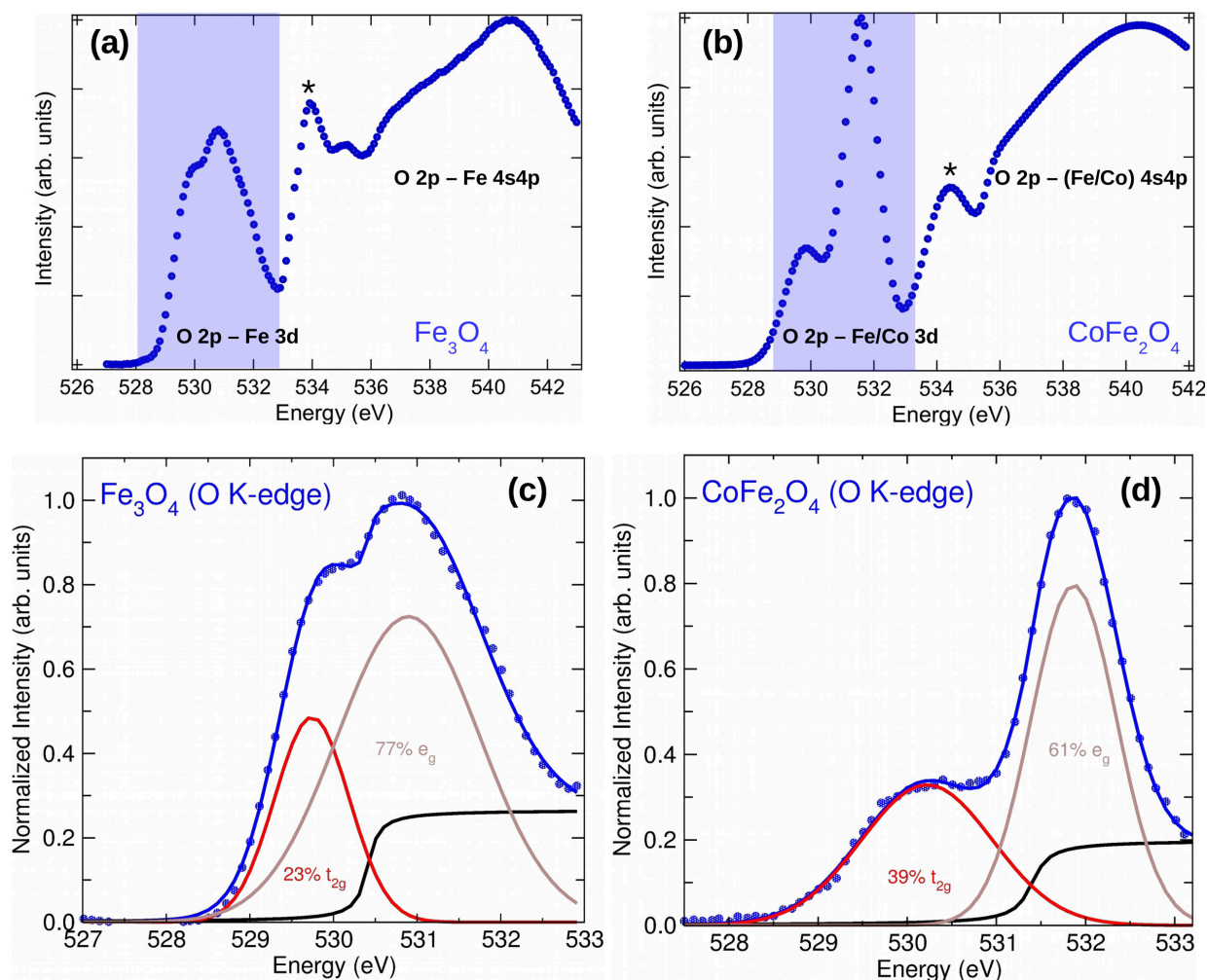


Figure 6.2: Oxygen K edge of (a) Fe_3O_4 and (b) CoFe_2O_4 are shown. The hybridization region of O $2p$ - Fe $3d$ (Fe_3O_4) and O $2p$ - Fe/Co $3d$ (CoFe_2O_4) are shaded in blue, * at 535 eV is due to vicinal oxygen from carbon conductive tape[102] and the broad peaks above 536 eV are due to O $2p$ - Fe/Co $4s4p$ orbitals. The normalized XAS spectra were fitted with Gaussian functions to quantify the e_g and t_{2g} orbitals occupancy. To exclude the effects of the edge jump from fits, an arctan function was included for Fe_3O_4 and CoFe_2O_4 , as shown. Solid lines are fit to the O K edge XAS data. (c) Oxygen K edge of Fe_3O_4 is fit with two components: 23% t_{2g} and 77% e_g . (d) CoFe_2O_4 is fit with 39% t_{2g} and 61% e_g . The change in area of O K edge prepeak is an indication that in CoFe_2O_4 the $3d$ ions are pointing away from O $2p$ orbitals as discussed in the text.

6.1.2 *In-situ* magnetic susceptibility measurements identify the magnetic exchange pathways

Oxygen interaction with $3d$ ions are essential (as shown in Figs. 3.14 and 3.15) to the magnetism. The magnetic susceptibility measurements $\Delta\chi_{FC-ZFC}$ in O_2 rich and O_2 deficient environments showed significant differences (Fig. 3.17e,f) in the Fe_3O_4 and $CoFe_2O_4$ nanoparticles. In the O_2 rich environment, the samples are under constant interaction with O_2 gas molecules whereas in O_2 deficient environment samples, they are under active pumping with a He sweep. One advantage with this approach is it permits one to quantify the magnetism due to strongly bound O $2p$ – Fe $3d$ and weakly bound O $2p$ – Fe $3d$ bonds.

In order to understand the origin of differences, we compared the $\Delta\chi_{FC-ZFC}$ (Fig. 6.3a,b) difference plots of O_2 rich - O_2 deficient systems (Fig. 6.3c). $\Delta\chi$ (O_2 rich - O_2 deficient) of Fe_3O_4 is negative whereas $CoFe_2O_4$ is positive. At first, the reason behind the differences are puzzling because both systems have identical spinel structures. However, a close look at the cation distributions, the sign of the magnetic moments identified by XAS and XMCD, and the fraction of t_{2g} and e_g populations allows elucidation of this issue.

In Fe_3O_4 the cation distributions are identified as 30% $Fe^{3+} T_d |\uparrow\rangle$, 37% $Fe^{3+} O_h |\downarrow\rangle$, and 33% $Fe^{2+} O_h |\downarrow\rangle$ ions (see Fig. 3.7), where $|\downarrow\rangle$ and $|\uparrow\rangle$ represent the direction of spin magnetic moments. Because Fe^{3+} in T_d and O_h sites are opposite in direction with equal magnitudes, their moments cancel with each other and the net moment is obtained⁵ as $5.44 \mu_B/f.u.$ In O_2 rich systems, because the surface is loaded with oxy-

⁵The net moment is due to $(12.5\% Fe^{3+} O_h + 87.5\% Fe^{2+} O_h) |\downarrow\rangle$

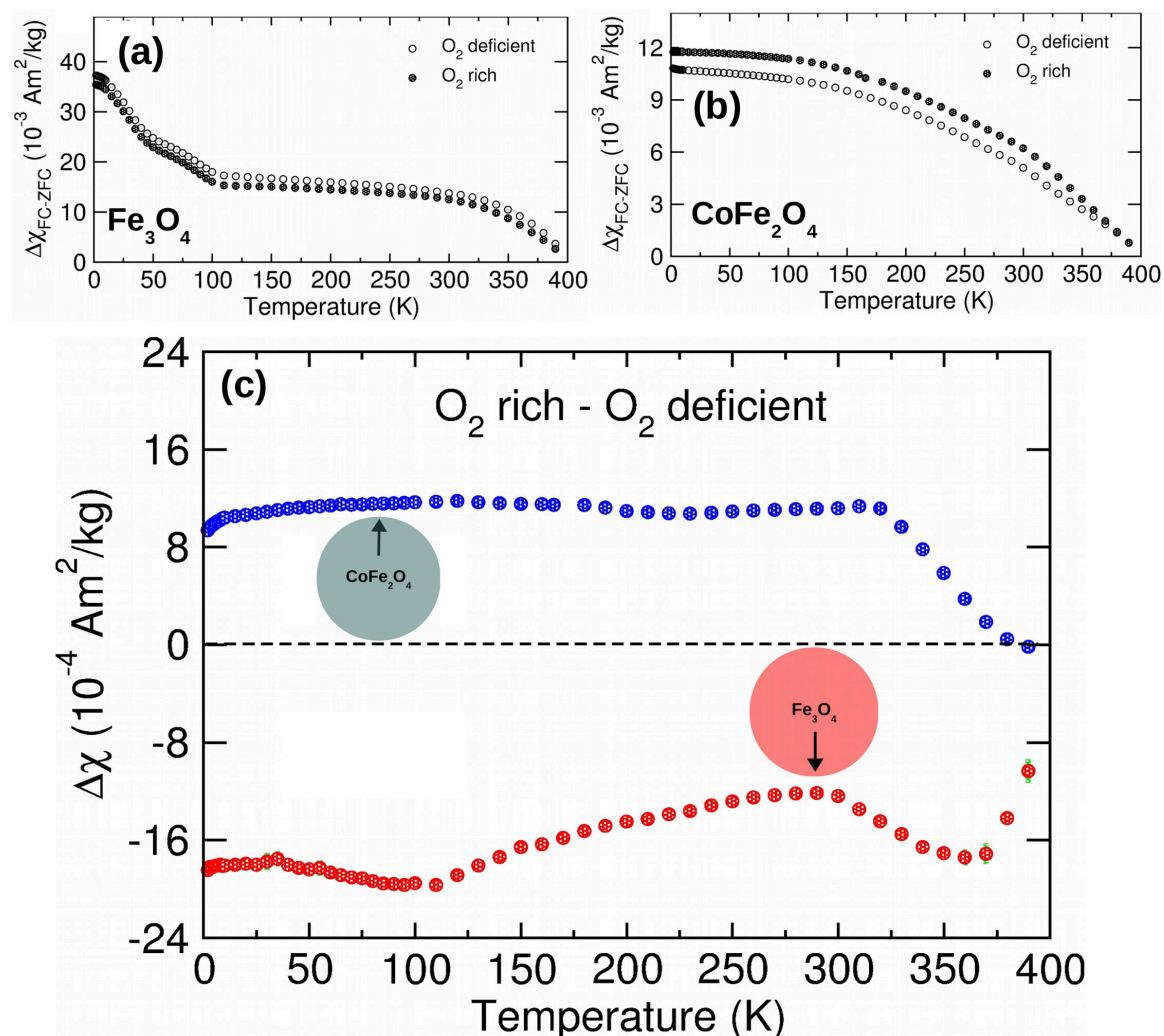


Figure 6.3: (a) $\Delta\chi_{FC-ZFC}$ of Fe_3O_4 in O_2 rich and O_2 deficient conditions (b) $\Delta\chi_{FC-ZFC}$ of CoFe_2O_4 in O_2 rich and O_2 deficient conditions (c) Difference in O_2 rich and O_2 deficient magnetic susceptibility of $\Delta\chi_{FC-ZFC}$ of Fe_3O_4 and CoFe_2O_4 are shown.

gen, the fraction of Fe ions are intrinsic to the system, whereas, O_2 deficient system lacks surface oxygen and oxygen vacancies are responsible for changing the oxidation state of Fe. The reason behind the $\Delta\chi(T)$ (O_2 rich - O_2 deficient) < 0 in Fe_3O_4 is due to the electron hopping mechanism from Fe^{2+} to Fe^{3+} states. Note that the magnetic

moment of $\text{Fe}^{3+} > \text{Fe}^{2+}$, this hopping mechanism due to oxygen vacancies increases the population of Fe^{3+} in O_2 deficient systems.

In CoFe_2O_4 the situation is more complex because now Co^{2+} and Co^{3+} ions also occupies O_h and T_d sites. The cation distributions of Co and Fe ions are identified as 60% $\text{Co}^{2+} \text{O}_h |\downarrow\rangle + 20\% \text{Co}^{3+} \text{O}_h |\downarrow\rangle + 20\% \text{Co}^{2+} \text{T}_d |\uparrow\rangle$ and 40% $\text{Fe}^{3+} \text{T}_d |\uparrow\rangle + 44\% \text{Fe}^{3+} \text{O}_h |\downarrow\rangle + 16\% \text{Fe}^{2+} \text{O}_h |\downarrow\rangle$ respectively (see Figs. 3.9 and 3.10). Considering that ions with opposite moments cancel with each other the net moment of CoFe_2O_4 is calculated⁶ as $5.15 \mu_B/\text{f.u.}$ In the case of CoFe_2O_4 because now Fe ions also occupy O_h sites, due to its relatively higher electronegativity of Co with respect to Fe, the Co^{2+} is reluctant to transfer electron to the Fe^{3+} sites (to become Co^{3+}). Rather, the delocalized electrons on the Co^{3+} ions change the electronic state from Co^{3+} to Co^{2+} and resulting in $\Delta\chi(T)$ (O_2 rich - O_2 deficient) > 0 for CoFe_2O_4 as observed in Fig. 6.3c. The increase in fraction of t_{2g} orbitals and decrease in fraction of e_g orbitals (in Fe_3O_4 compared to CoFe_2O_4) is further indication that the bonding of oxygen $2p$ orbitals with $3d$ metal ions are relatively weaker in CoFe_2O_4 compared Fe_3O_4 and further suggests that O_2 rich and O_2 deficient measurements can probe the redox mechanism/magnetism and their connection with oxygen vacancies on the surface and bulk.

The intrinsic oxygen ions that are responsible for the change in the magnetism are quantified by the difference in susceptibility from O_2 rich and O_2 deficient measurements in the range of 2 – 300 K (Fig. 6.3c). The total $\Delta\chi_{\text{Fe}_3\text{O}_4}$ and $\Delta\chi_{\text{CoFe}_2\text{O}_4}$ are $-0.00151(3)$ and $0.00113(1) \text{ A m}^2/\text{kg}$, respectively. Oxygen has a $^3\Sigma$ ground state with $S = 1$, so the effective spin only moment is $2.828 \mu_B$. From the $\Delta\chi_{\text{Fe}_3\text{O}_4}$

⁶The net moment is due to (50% $\text{Co}^{2+} \text{O}_h + 25\% \text{Co}^{3+} \text{O}_h + 5\% \text{Fe}^{3+} \text{O}_h + 20\% \text{Fe}^{2+} \text{O}_h$) $|\downarrow\rangle$

and $\Delta\chi_{CoFe_2O_4}$ the intrinsic oxygen amounts are calculated⁷ as -1.84×10^{16} O₂/g and 4.29×10^{16} O₂/g respectively. Note that here the negative sign means, the magnetism is reduced by increasing the superexchange couplings, and the positive sign refers to an increase in magnetization with a decrease in superexchange couplings as described above. The results are compared to NO_x gas reduction catalysis (section 3.7.1) measurements where the system with $\Delta\chi_{CoFe_2O_4} > 0$ shows higher catalytic activity and $\Delta\chi_{Fe_3O_4} < 0$ shows no activity indicating that O₂ rich and O₂ deficient magnetism measurements play a significant role in quantifying the surface oxygen and exchange interactions. The partial pressure of the oxygen (O₂ rich and O₂ deficient environments) is responsible for switching the oxidation state between Fe²⁺/Fe³⁺ and Co²⁺/Co³⁺.

Like nanoscale Fe₃O₄ and CoFe₂O₄; nanoscale CeO₂ is a mixed valent system (Ce³⁺ ↔ Ce⁴⁺) where the oxygen vacancy formation is relatively easy and there are no unpaired *d* electrons[171]. To gain further insights into magnetism and the impact of lattice oxygen and oxygen vacancies on metal oxide systems, we turn our attention to *d*⁰ systems.

6.2 CeO₂ Nanoshapes

Nanoscale CeO₂ is oxygen vacancy rich system, where the Ce³⁺ ↔ Ce⁴⁺ redox reaction favours creation and removal of oxygen vacancies depending on the system environment is O₂ rich or O₂ deficient. In CeO₂ the defect formation is explained by the reaction $4Ce^{4+} + O^{2-} \rightarrow 2Ce^{4+} + 2Ce^{3+} + \square + \frac{1}{2}O_2$, where \square is an oxygen

⁷1 A m²/g = 1 emu/g = $\mu_B / (0.9274 \times 10^{-20} \text{ g})$

vacancy and O^{2-} and O_2 represent lattice and molecular oxygen, respectively[108]. Oxygen vacancy defects in nanoscale CeO_2 (nanoceria) are of special importance because of their impact on the structure and electronic properties of the surface. To gain insights into the role of oxygen vacancies and lattice oxygen dynamics, we performed O_2 deficient and O_2 rich magnetometry measurements on CeO_2 nanocubes, nanorods, and nanospheres (section 4.3).

6.2.1 Nanoceria shapes surface Ce^{3+} concentration

Nanoshapes provide variation of surface Ce^{3+} by varying the amount of exposed surface terminations. To this end, the most efficient way (in the case of nanoceria) to vary the surface termination is morphology. It is an efficient way to vary the Ce:O coordination and thereby changing the number of oxygen vacancy defects and Ce^{3+} . XRD refinements and TEM results identified the three different shaped nanoceria have identical CeO_2 cubic $Fm\bar{3}m$ structures; nanocubes exposed (100) and (110) surface planes, nanorods exposed (100) and (111) planes, and nanospheres exposed all planes (section 4.2).

From the Rietveld refinements of the x-ray diffraction patterns, the cubes, rods, and spheres preferred orientations and their relative phase fractions were determined. The fraction of preferred surface planes of a structure (i.e. cube, rod or sphere) multiplied by the number of surface vacancies per Ce ion (from the coordination numbers over a unit cell) provides an average of the total number of surface vacancies associated with each Ce ion on a surface.

Nanocube surfaces are 64% (100) and 36% (110) crystal plane terminated, and

there are 2.50 and 2.25 surface vacancies per Ce for those (100) and (110) planes, respectively. This indicates that $(0.64 \times 2.50 + 0.36 \times 2.25) = 2.41$ total vacancies per surface Ce ion are present on the nanocube surface. The $\sim 25 \times 25 \times 25 \text{ nm}^3$ cubes consist of 98,680 units cells $(\frac{25^3 \text{ nm}^3}{0.541^3 \text{ nm}^3})$, and this holds $\sim 394,720$ Ce atoms. The total number of surface Ce atoms are $\sim 25,137$. Since each surface Ce contributes 2.41 vacancies, this results in $\sim 60,580$ total oxygen vacancies per nanocube. From the stoichiometry of CeO_2 , each oxygen vacancy is responsible for reducing two Ce^{3+} ions, and this indicates that $\sim 31\%$ of the Ce^{3+} ions are on a nanocube's surface $(\frac{2 \times 60,580}{394,720} \frac{\text{Ce}^{3+}}{\text{Ce}^{3+} + \text{Ce}^{4+}}$ per nanocube).

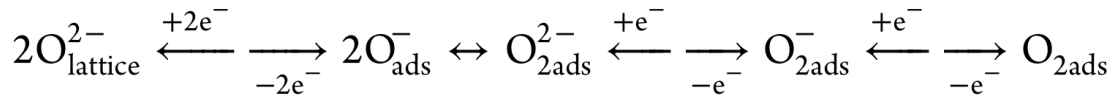
Nanorods are surface terminated by 90% (100) and 10% (111) crystal planes, with 2.50 and 1.25 surface vacancies per Ce ion, respectively. $(0.90 \times 2.50 + 0.10 \times 1.25) = 2.38$ total vacancies per surface Ce ion are present on the nanorod surface. The $\sim 50 \times 8 \times 8 \text{ nm}^3$ rods consist of 20,700 units cells $(\frac{50 \times 8 \times 8 \text{ nm}^3}{0.541^3 \text{ nm}^3})$, and this shape holds $\sim 82,800$ Ce atoms. The total number of surface Ce atoms is $\sim 10,511$. Since each surface Ce contributes 2.38 vacancies, this results in $\sim 24,990$ total oxygen vacancies per rod. Since each oxygen vacancy is responsible for reducing two Ce^{3+} ions, $\sim 60\%$ of the Ce^{3+} are present on the surface of a nanorod $(\frac{2 \times 24,990}{82,800} \frac{\text{Ce}^{3+}}{\text{Ce}^{3+} + \text{Ce}^{4+}}$ per nanorod).

Nanospheres are (111) crystal plane surface terminated so that 1.25 total vacancies per surface Ce ion should be present on the sphere's surfaces. The $\sim 2 \text{ nm}$ diameter nanospheres have ~ 120 Ce atoms, and accounting for the surface terminations, the total number of surface Ce atoms are ~ 30 . Since each surface Ce contributes 1.25 vacancies, this results in ~ 38 total oxygen vacancies per sphere. As each oxygen vacancy is responsible for reducing two Ce^{3+} ions, it follows that $\sim 63\%$ Ce^{3+} are

on the surface for the nanospheres ($\frac{2 \times 38}{120} \frac{\text{Ce}^{3+}}{\text{Ce}^{3+} + \text{Ce}^{4+}}$ per sphere). Overall, results show that $\sim 31\%$, $\sim 60\%$, $\sim 63\%$ Ce^{3+} ions are present at the surface of nanocubes, nanorods and nanospheres respectively.

6.2.2 Lattice oxygen and adsorbed surface oxygen dynamics in nanoceria

Measurement of $\chi(T)$ for nanoceria in an oxygen deficient (Fig. 6.4a) environment clearly indicates that $\text{Ce}^{3+} \leftrightarrow \text{Ce}^{4+}$ redox reactions result in an intrinsic supply of reactive lattice oxygen that combine to produce $\text{O}_{2,\text{ads}}$. In nanoceria each Ce atom ($[\text{Xe}]4f^15d^16s^2$) can donate four electrons to the bonding orbitals with two O ($1s^22s^22p^4$) atoms. When a \square is formed, the two electrons freely wander in the solid, reducing $\text{O}_{\text{lattice}}$ to $\text{O}_{2,\text{ads}}$ in the following way:



A similar mechanism was proposed previously to describe oxidation catalysis on nanoceria[172]. This $\chi(T)$ data also shows that nanoceria releases $\text{O}_{\text{lattice}}$ due to the gradient in chemical potential with the surroundings and that the $\text{O}_{2\text{ads}}$ is weakly bound to the lattice, in agreement with previous neutron scattering experiments[23].

The $\text{O}_{2\text{ads}}$ of ceria observed here is not the same as that detected by gas flow temperature programmed reaction techniques, which do not observe lattice oxygen release until[173] ~ 1000 K, in the absence of an external reductant. Instead, the intrinsic oxygen identified by its magnetism is due to the gradient in concentration with the

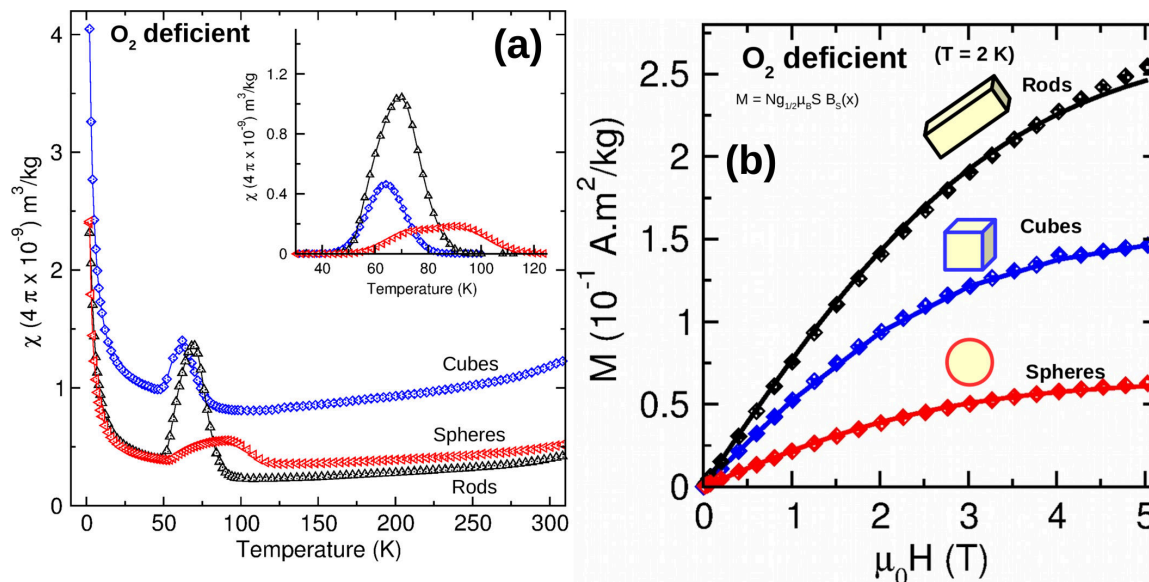


Figure 6.4: (a) Temperature dependence of magnetic susceptibility for O_2 deficient systems are shown. The inset shows the magnitude of the temperature dependent magnetism due to the released oxygen from the system (intrinsic CeO_2 $\chi(T)$ subtracted data) of the O_2 deficient environment. (b) M vs $\mu_0 H$ curve of O_2 deficient systems at 2 K with Brillouin function fits to calculate the number of Ce^{3+}/g .

surroundings. Neutron diffraction measurements by Mamontov et al.[23] suggested that it is more energetically favorable for adsorbed oxygen ions (O_2^{2-} and O^-) in reduced ceria to occupy spacious octahedral sites rather than the vacant tetrahedral sites. The identified intrinsic oxygen is presumably a result of the transformation between $O_{lattice}^{2-}$ to O_{2ads} at a given chemical potential. A more detailed quantitative analysis can be performed in the region of the O_2 magnetic transition to obtain the transition temperature and amount of adsorbed oxygen. We determined $d\chi(T)/dT$ for each (Fig. 6.5) of the different shapes; ceria nanospheres have $T_{N_{O_2}} \sim 80$ K, nanorods have $T_{N_{O_2}} \sim 70$ K, and nanocubes have a $T_{N_{O_2}} \sim 60$ K.

The shape of $\chi(T)$ around the maximum and the temperature range over which

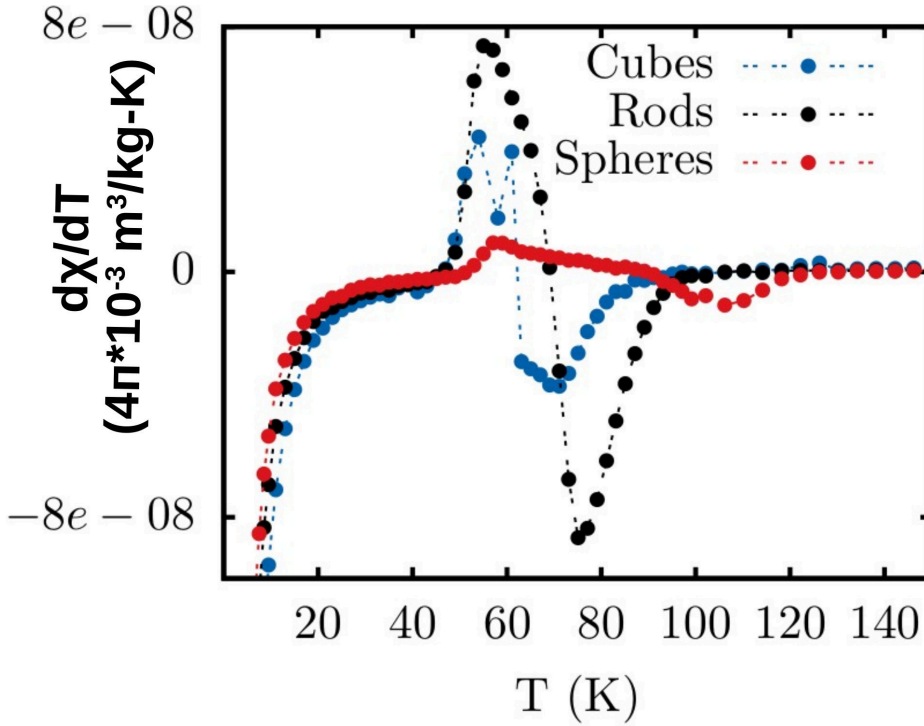


Figure 6.5: $d\chi/dT$ vs T of O_2 deficient cubes, rods, and spheres.

it spans tracks with the O_{2ads} coverage, and the variations in T_{NO_2} for the different shapes (a measure of the O–O antiferromagnetic exchange strength) are clear indications of the impact of the preferentially exposed surface planes of the different shapes. These observations are also in agreement with the abundance of O_{2ads} on the surfaces expected from BET analysis areal densities with respect to the preferentially exposed planes of the different shapes.

6.2.3 Quantifying the intrinsic oxygen storage capacity and defects

The integrated area of $\chi(T)$ over the O_{2ads} affected region (inset of Fig. 6.4a) was ascertained, incorporating the intrinsic susceptibility derived under oxygen deficient conditions. In the oxygen deficient systems, the $\chi(T)$ response due to the dissipated

Table 6.1: O₂ deficient systems' data: Number of Ce³⁺ identified by the 2 K M vs $\mu_0 H$ data and excess Ce³⁺ ions from $\chi_{FC-ZFC}(T)$ along with the % of \square , Frenkel pair defects and Ce³⁺/nm².

shape	Ce ³⁺ /g (2 K)	Ce ³⁺ /g (χ_{FC-ZFC})	\square (%)	Frenkel (%)	Ce ³⁺ /nm ²
Nanocubes	$1.65 \pm 0.01 \times 10^{19}$	$0.40 \pm 0.01 \times 10^{19}$	32	68	0.147
Nanorods	$2.62 \pm 0.02 \times 10^{19}$	$1.13 \pm 0.02 \times 10^{19}$	88	12	0.095
Nanospheres	$0.68 \pm 0.01 \times 10^{19}$	$0.56 \pm 0.02 \times 10^{19}$	53	47	0.019

O₂ molecules can be described in a way similar to the Curie constant (C). A comparison has been made to identify and quantify the oxygen in and on the different shapes. Oxygen has a ³Σ ground state with $S = 1$, so the number of O_{2ads}/g is obtained by the expression

$$N_{O_{2ads}}/g = (3kC)/(\mu_B^2[4S(S+1) + \Lambda^2]) \quad (6.1)$$

where Λ is the angular momentum quantum of molecular oxygen[8]. The order in which the amount of O_{2ads}/g is reacted from the different shapes is rods > cubes > spheres. Quantified intrinsic oxygen storage capacity in $\mu\text{mol O}_2/\text{g}$ are in the decreasing order of rods (20.1 $\mu\text{mol O}_2/\text{g}$) to cubes (8.3 $\mu\text{mol O}_2/\text{g}$) to spheres (7.1 $\mu\text{mol O}_2/\text{g}$). A similar order of the dynamic oxygen storage capacity has been reported by Trovarelli et al.[174] in Ce_xZr_(1-x)O₂ solid solutions. The identified intrinsic oxygen is due to the Frenkel and \square defects. In the anion Frenkel pair defects, O²⁻ is displaced from its lattice to an interstitial site, and in \square formation, O²⁻ is removed. In general, the Frenkel pair defect does not result in the Ce³⁺ formation. In \square defect, the stoichiometry indicates that for removal of one O²⁻ (or formation of $\frac{1}{2}\text{O}_2$), two Ce³⁺

and one \square should result. The M vs $\mu_0 H$ (2 K) data of oxygen deficient nanoceria was used to ascertain the number of Ce^{3+}/g ; since the ground state level is populated by $J_z = \pm 1/2$, the data is fit to the Brillouin function $M = Ng_{1/2}S\mu_B B_S(x)$, and the fits further confirm that the order of Ce^{3+}/g and $\text{O}_{2\text{ads}}$ is rods $>$ cubes $>$ spheres under oxygen-deficient conditions (Fig. 6.4b).

Further to the above analysis, to quantify the available excess Ce^{3+} ions we used $\chi_{FC/ZFC}$ measurements in oxygen deficient atmospheric conditions (section 4.3). The $\chi_{FC}(T)$ measurements identify (shown in Fig. 6.6) that T_N is suppressed, and $\chi_{FC}(T)$ for temperatures below T_N was increased significantly, demarking the increased number of Ce^{3+} ions able to provide a measurable magnetization after the $\text{O}_{\text{lattice}}$ migration to $\text{O}_{2\text{ads}}$ during the $\chi_{ZFC}(T)$ measurement. The difference between the $\chi_{FC}(T)$ and $\chi_{ZFC}(T)$, $\Delta\chi_{FC-ZFC}(T)$, is shown in Fig. 6.6. The increase in Ce^{3+}/g tracks with the oxygen release as a function of temperature, which is consistent with an activated energy process (Arrhenius relation) corresponding to that of oxygen migration from the lattice to the surface. Ce^{3+}/O formation (Fig. 6.7) as a function of temperature to ascertain the activation energies for the different nanoceria shapes are given below. The activation energies from linear fits of $\log_e(\Delta\text{Ce}^{3+})$ vs T of the cubes, rods, and spheres are ~ 8 , ~ 6 , and ~ 6 meV, respectively.

We find that the nanoceria cubes require $\sim 30\%$ more energy to produce Ce^{3+} and release $\text{O}_{\text{lattice}}$ than do the nanorods or nanospheres, which involve similar energies. The observed excess Ce^{3+} and identified $\chi_{ZFC}(T)$ maximum between 50 and 110 K gives a unique way to distinguish the fraction of oxygen vacancy and Frenkel pair defects. If Frenkel pair defects do not result in Ce^{3+} formation, then the observed

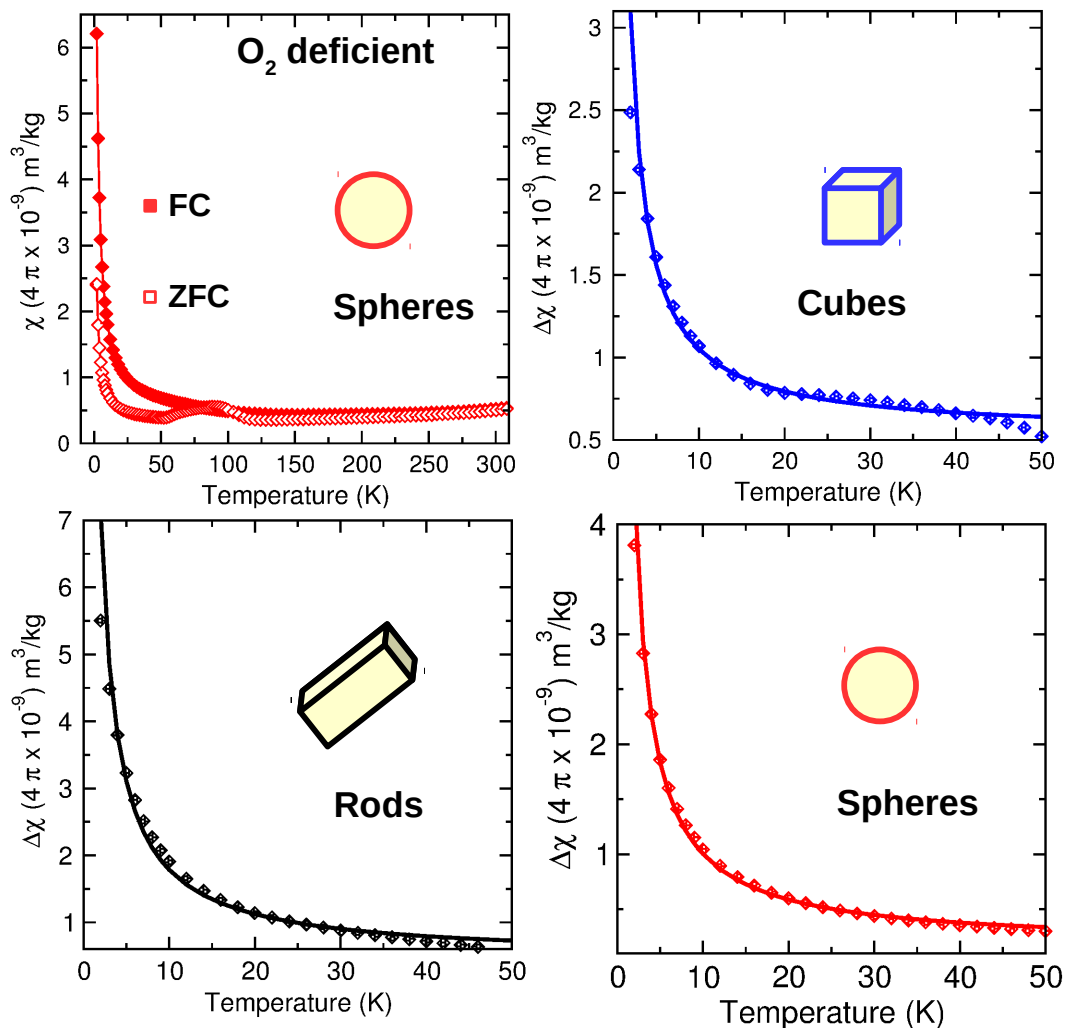


Figure 6.6: Temperature dependence of field cooled ($\chi_{FC}(T)$) and zero field cooled ($\chi_{ZFC}(T)$) magnetic susceptibility for O_2 deficient nanospheres is shown. With the FC measurement ($\mu_0 H = 10$ mT) the magnetic signature from the O_2 is removed in all shape dependent ceria nanoparticles. The $\Delta\chi_{FC-ZFC}$ vs T susceptibility of cubes, rods, and spheres identify the number of available excess Ce^{3+} ions due to the released oxygen as described in the text.

excess Ce^{3+} is exclusively due to oxygen vacancy defect formation. The $\chi_{ZFC}(T)$ maximum between 50 and 110 K describes the total intrinsic oxygen present in the system (due to Frenkel and oxygen vacancy defects) the difference between FC and

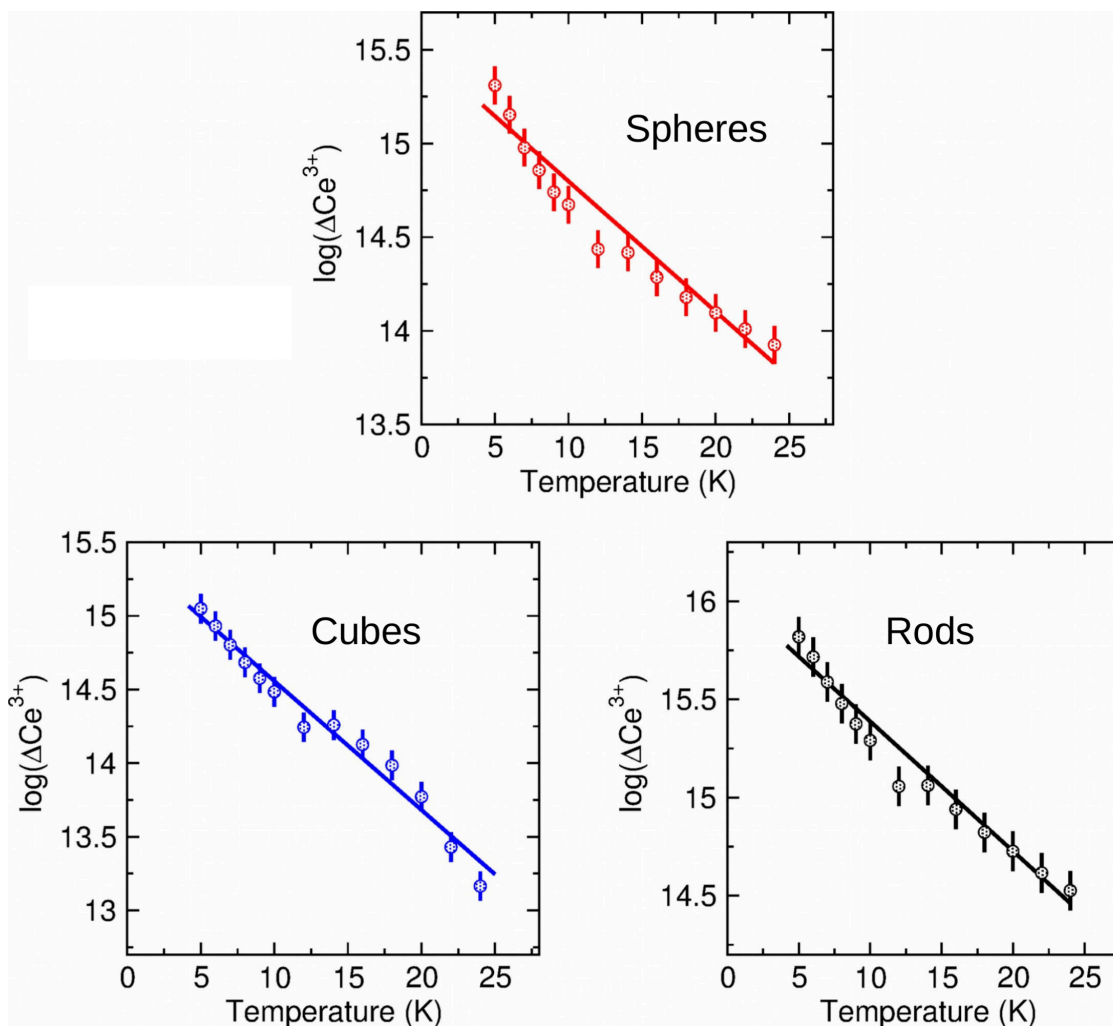


Figure 6.7: Ce^{3+}/O formation as a function of temperature.

ZFC $\chi(T)$ identifies the amount of released oxygen due to the excess Ce^{3+} (oxygen vacancy defects) by stoichiometry, the results identify the fraction of defects due to Frenkel pairs to be 68%, 47 %, and 12 % of the cubes, spheres, and rods, respectively (Table 6.1). To further understand the relation between defects and surface Ce^{3+} , we compared our results with the catalytic activity. Our results identified that catalytic activity is not necessarily related to the total number of defects (Fig. 6.8a), but rather

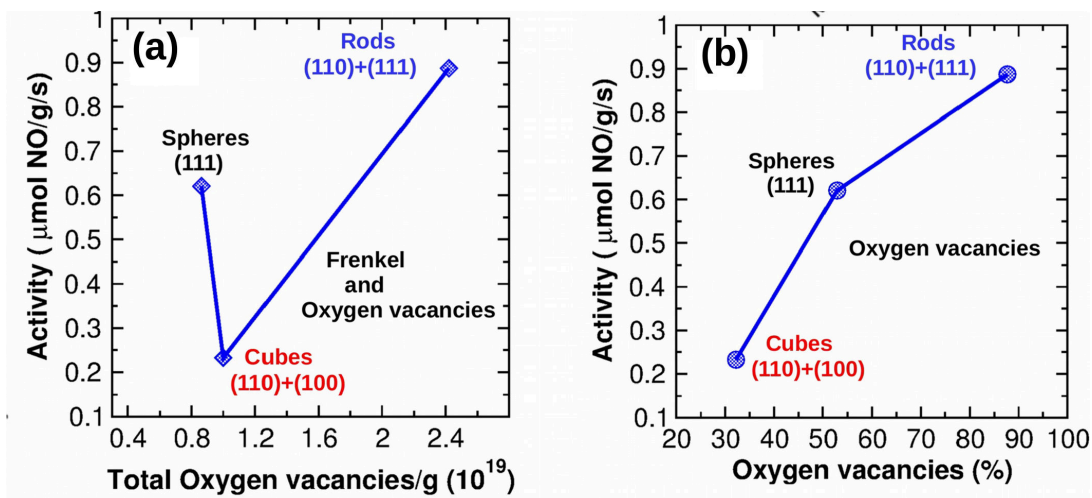


Figure 6.8: (a) Activity ($\mu\text{mol/g/s}$) as a function of Frenkel and oxygen vacancies. (b) Activity as a function of oxygen vacancies.

scales qualitatively with the fraction of the defects that are due to oxygen vacancies (Fig. 6.8b), with both measures in the order rods > spheres > cubes.

6.2.4 Surface localized Ce^{3+} is the key to catalytic activity

Keeping in mind that catalysis is a surface phenomenon, only defects near the surface would be expected to be kinetically relevant. Earlier positron annihilation experiments[125] in ceria nanorods indicated that \square 's are coupled with the adjacent Ce^{3+} to promote catalytic reactivity. Therefore, we calculate the number of Ce^{3+} that exist at the surface due to \square , and normalize this value by the total specific surface area (SSA), presented in table 6.1 (calculations are shown below).

Ce³⁺ surface density calculations

The surface Ce³⁺ ions are identified by accounting for the relative number of Ce³⁺ ions in proportion to the surface oxygen vacancies, and the SSA normalized Ce³⁺ ions for each shape. The number of Ce³⁺ ions is ascertained from the oxygen deficient (open system) M vs $\mu_0 H$ (2 K) and the surface coverage of Ce³⁺ is as follows:

Cubes:

- From the magnetometry, the total number of Ce³⁺ per gram is $1.65 \pm 0.01 \times 10^{19}$ Ce³⁺/g. Thus, the number of surface Ce³⁺ per gram is 30.7% of this value, i.e. 5.07×10^{18} Ce³⁺/g.
- Normalizing the number of surface Ce³⁺ per gram to the SSA indicates a Ce³⁺ ion coverage:

$$(5.07 \times 10^{18} \text{ Ce}^{3+}/\text{g}) \times \frac{1}{35 \text{ m}^2/\text{g}} = 0.147 \text{ Ce}^{3+}/\text{nm}^2$$

Rods:

- The number of Ce³⁺ per gram is $2.62 \pm 0.02 \times 10^{19}$ Ce³⁺/g from the magnetometry. Therefore, the number of surface Ce³⁺ per gram is 60.4% of this value, i.e. 1.58×10^{19} Ce³⁺/g.
- Normalizing to the number of surface Ce³⁺ per gram to the SSA indicates a Ce³⁺ ion coverage:

$$(1.58 \times 10^{19} \text{ Ce}^{3+}/\text{g}) \times \frac{1}{167 \text{ m}^2/\text{g}} = 0.095 \text{ Ce}^{3+}/\text{nm}^2$$

Spheres:

- From the magnetometry, the number of Ce^{3+} per gram is $6.75 \pm 0.01 \times 10^{18} \text{ Ce}^{3+}/\text{g}$ which tells us that the number of surface Ce^{3+} per gram is $4.27 \times 10^{18} \text{ Ce}^{3+}/\text{g}$ (i.e. 63.3% of the total number of Ce^{3+} per gram in the nanosphere sample).
- Normalizing with respect to the SSA indicates that the surface Ce^{3+} per gram is:

$$(4.27 \times 10^{18} \text{ Ce}^{3+}/\text{g}) \times \frac{1}{214 \text{ m}^2/\text{g}} = 0.019 \text{ Ce}^{3+}/\text{nm}^2$$

We find that the total number of Ce^{3+} ions identified by the surface termination calculations (i.e. the idealized situation) are significantly larger than the total surface Ce^{3+} ions determined from the measurements. This suggests that perhaps not all the surface terminations with their different nearest neighbor configurations identified by first principle calculations are involved in the reduction (i.e. formation of Ce^{3+}). For the cubes it is suggested that perhaps only $\sim 0.5\%$ of the available surface Ce^{3+} ions are involved, in the rods $\sim 0.8\%$ of the available surface Ce^{3+} are involved, and for the spheres, $\sim 0.2\%$ of the available surface Ce^{3+} are engaged in the redox transformation. The order of Ce^{3+} observed in these systems is consistent with the susceptibility experiments of 4 nm CeO_2 nanoparticles (the localized Ce^{3+} is $\sim 0.4\%$ [42]).

Figure 6.9 shows the specific surface area (SSA) normalized catalytic activities against the surface densities of defects, and a strong linear correlation is seen. Incorporating the relative percents of Ce^{3+} ions, we *quantitatively* correlate to the SSA normalized Ce^{3+} ions. The Ce^{3+} surface density determined under oxygen deficient conditions is related to the nitric oxide (NO) reduction catalytic activity. The solid line is a straight line fit to the data and the intercept indicates the SSA normalized

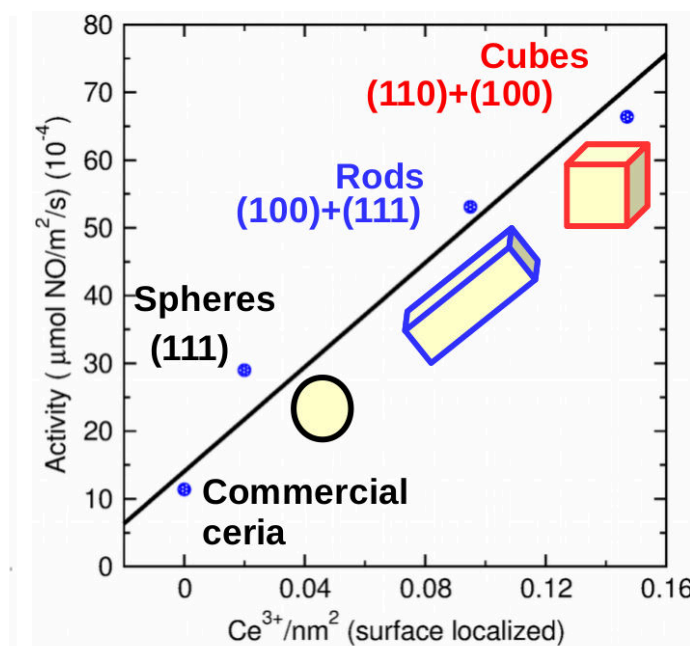


Figure 6.9: SSA-normalized activity as a function of the surface density of Ce^{3+} sites determined by the magnetic susceptibility analysis in O_2 deficient conditions. The solid line is a straight line fit to the data (slope = $0.038 \pm 0.008 \frac{\mu mol NO/m^2/s}{Ce^{3+}/nm^2}$; intercept = $0.0014 \pm 0.0005 \mu mol NO/m^2/s$) as described in the text.

activity due to the absence of surface localized Ce^{3+} . Thus, the high reactivity of the nanocubes on this basis is not due to the reactivity of the (110) and (100) surface planes per se, but rather because these surfaces result in a high surface density of Ce^{3+} defects that are produced due to the intrinsic oxygen.

6.3 CeO_2 d^0 Magnetism

One of the fundamental challenge with the origin of ferromagnetism in oxygen vacancy rich d^0 systems like nanoscale CeO_2 is where does the spin reside and how is the oxygen responsible for the ferromagnetism? Additionally, it has been widely reported

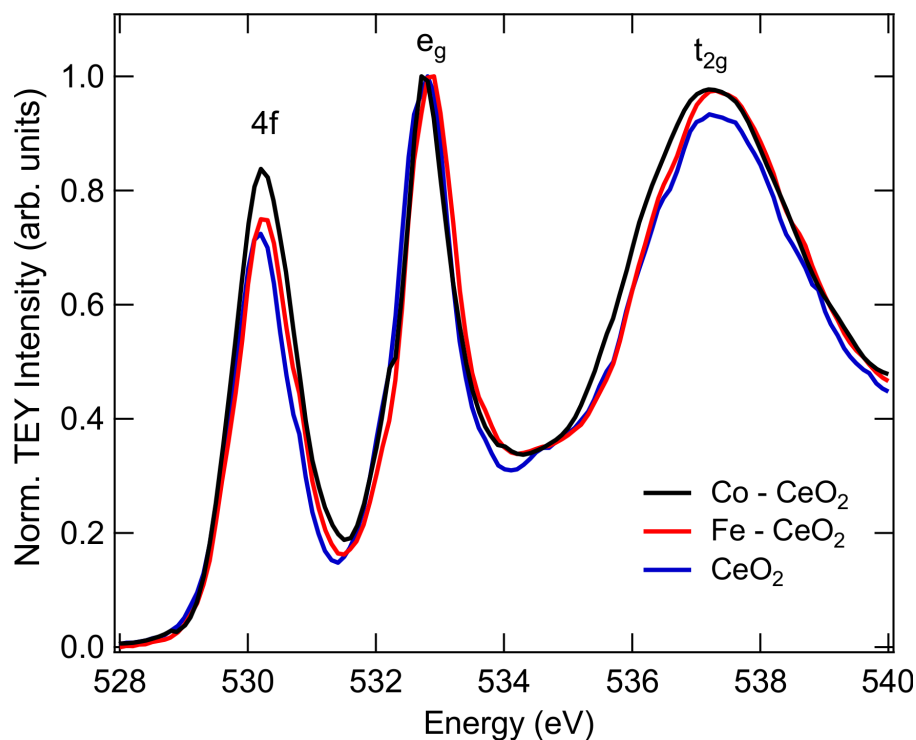


Figure 6.10: O K -edge XAS of the CeO_2 , Fe – CeO_2 , Co – CeO_2 nanocrystallites are shown. The three main peaks are due to hybridized O $2p$ – Ce $4f$, O $2p$ – Ce $5de_g$, and O $2p$ – Ce $5dt_{2g}$ states.

that the sintering nanoparticles in O_2 environment removes the magnetism[35; 109]. Nanoscale CeO_2 , Fe- and Co-decorated CeO_2 nanoparticles were studied using XRD, TEM, HAADF, ICP, BET, XANES, EXAFS, and Mössbauer spectroscopy to confirm the phase purity of nanocrystallites (Chapter 5).

6.3.1 Ce $4f$ – O $2p$ hybridization role in the d^0 magnetism

XAS measurements of Ce $M_{5,4}$ unambiguously showed a strong Ce $4f$ – O $2p$ hybridization in the nanoparticles (section 5.4.4). Figure 6.10 shows the O K edge measurements of the CeO_2 , Fe – CeO_2 and Co – CeO_2 nanoscale systems. The peak

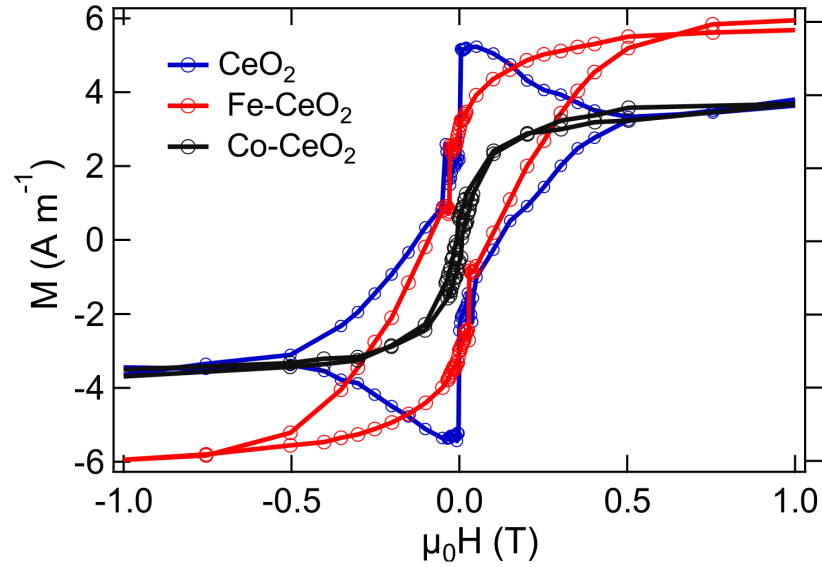


Figure 6.11: $M(\mu_0H)$ of CeO_2 , Fe-CeO_2 and Co-CeO_2 nanocrystallites measured at room temperature. $M(\mu_0H)$ of nanocerria shows a coercivity of ~ 50 mT and saturation magnetization (M_s) of ~ 4 Am^{-1} . Fe-CeO_2 and Co-CeO_2 nanocrystallites shows coercivity of ~ 50 mT and ~ 0 mT and M_s ' were ~ 7 Am^{-1} and ~ 4 Am^{-1} .

at ~ 531 eV is attributed to the $\text{O } 1s \rightarrow \text{O } 2p$ electrons hybridized with Ce $4f$ electrons. We saw that, with Fe and Co decoration, the $4f$ peak intensity increases, clearly indicating that the transition metal Fe and Co ion enhances the $\text{O } 2p$ hybridization with Ce $4f$ in the order of $\text{CeO}_2 < \text{Fe} - \text{CeO}_2 < \text{Co} - \text{CeO}_2$. The peaks at ~ 533 eV and ~ 538 eV are due to the transitions into double-degenerate $5de_g$ ($d_{x^2-y^2}$ and d_z^2) and triple-degenerate $5dt_{2g}$ (d_{xy} , d_{yz} , and d_{zy}) states. The measured peak intensity of the t_{2g} peak ($\text{CeO}_2 < \text{Fe} - \text{CeO}_2 < \text{Co} - \text{CeO}_2$) is evidence that the increase in Ce $5d - \text{O } 2p$ and Fe/Co $3d - \text{O } 2p$ mixing.

To investigate the impact of the $\text{O } 2p - \text{Ce } 4f$ hybridization on the magnetism, XMCD measurements (elemental magnetism) at Ce $M_{5,4}$ edge were compared with the overall magnetism from SQUID magnetometry. From XMCD the average magnetic

moment identified from XMCD is $0.18 \mu_B/\text{Ce}$ ⁸ (see table 5.7 for $\langle L_z \rangle$ and $\langle S_z \rangle$). A ~ 20 nm ceria crystallite has a volume of $4.2 \times 10^{-24} \text{ m}^3$. From density⁹ and molecular weight this consists of $\sim 10^5$ Ce atoms ($N = \frac{N_A \times \rho_{\text{CeO}_2} \times V}{M_{\text{CeO}_2}}$; where $N_A = 6.023 \times 10^{23}$ Ce atoms/mol, $\rho_{\text{CeO}_2} = 7.1 \text{ g/cm}^3$ and $M_{\text{CeO}_2} = 172.12 \text{ g/mol}$). If one assumes all Ce $4f$ states are responsible for the magnetism, that places an upper bound on the moment at $\sim 2 \times 10^4 \mu_B/\text{crystallite}$. In nanoceria, each Ce atom can donate four electrons to bonding orbitals with two O atoms. When an oxygen vacancy (V_O) is formed, the two electrons previously occupying p orbitals of the O atom are free to distribute. The localized electrons around Ce atoms changes the oxidation state from Ce^{4+} to Ce^{3+} (charge neutralization expression can be written as $2\text{Ce}^{4+} + V_O^{2-} \leftrightarrow 2\text{Ce}^{3+}$). This suggests that each V_O is responsible for the creation of two Ce^{3+} ions. Ce L_3 edge XANES analysis quantify (see Fig. 5.8a) the concentrations of Ce^{3+} and V_O as $\sim 20\%$ and $\sim 10\%$ respectively. Based on these results, even if one considers only the Ce $4f$ sites that are neighbouring V_O 's are responsible for the ferromagnetism, that puts a lower bound on the moment at $\sim 2 \times 10^3 \mu_B/\text{crystallite}$. SQUID magnetometry provides a measure of all magnetic components (i.e. not site or element specific). The saturation magnetization of nanoceria is 4 A/m . This magnetization is equivalent to $\sim 6 \times 10^{16} \mu_B/\text{g}$ ¹⁰ which corresponds to each ceria crystallite having a moment of $\sim 2 \mu_B$.

⁸Total moment = $\langle m_{tot}^z \rangle = \frac{-\mu_B}{\hbar} (g_s \langle S_z \rangle + g_l \langle L_z \rangle)$; g -factor $g_s = 2$ with the spin moment and $g_l = 1$ with the orbital moment [65]

⁹C.I. Kasei Co., Ltd. NanoTek powder.

¹⁰ $1 \text{ Am}^{-1} = (10^{-3} \text{ emu/cm}^3) / (7.1 \text{ g/cm}^3 \times 0.9274 \times 10^{-20} \text{ emu}/\mu_B)$

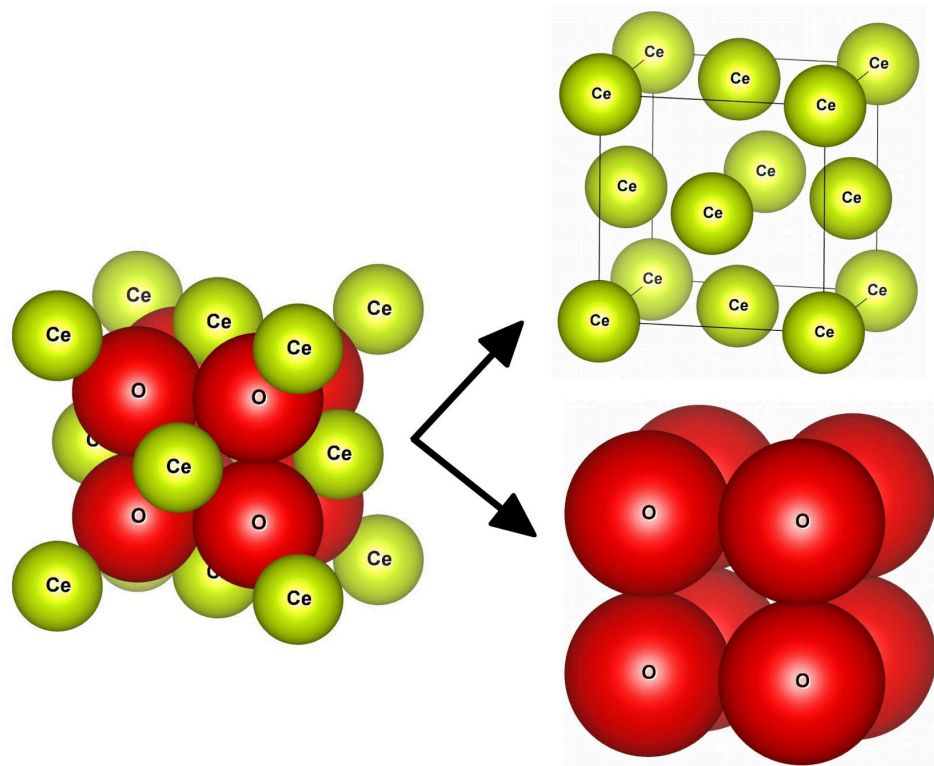


Figure 6.12: CeO_2 crystal structure is shown in space filling style. Ce-lattice is FCC and V_{orb} -lattice is simple cubic. Each Ce-lattice consists of 4 Ce's per unit cell and V_{orb} -lattice consists of 1 V_{orb} per unit cell.

6.3.2 Vacancy orbitals are the key to understand d^0 magnetism

Combinedly XMCD and SQUID magnetometry results show that the ferromagnetic volume fraction is between 0.1 – 0.01%. Clearly, not all Ce $4f$ states are involved in the magnetism; only the fraction associated with the V_{orb} and/or hybridization (it follows that because of the low fraction, only Ce $4f - \text{O } 2p$ hybridized states that are captured in the delocalized V_{orb} are associated) are responsible.

Given the concentration of V_{orb} from Ce L_3 edge XANES, the radius of V_{orb} can be estimated[175]. In CeO_2 each Ce ion has eight surrounding oxygen ions, and each

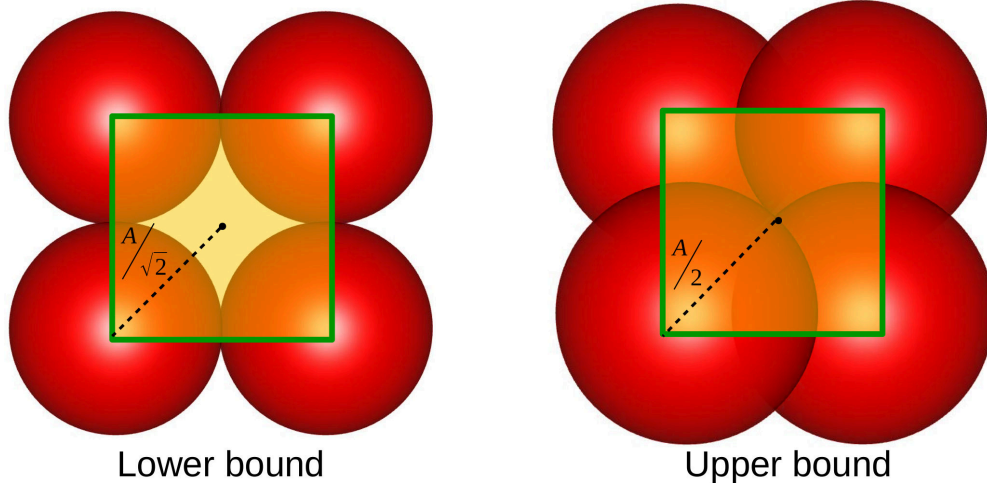


Figure 6.13: The lower and upper bounds of V_{orb} are shown. In the lower bound the radius of V_{orb} is defined as the distance at which neighboring atoms. Upper bound is the distance at which the V_{orb} fills all space.

oxygen has four neighboring Ce ions (Fig. 6.12). We approximate the Ce-lattice as simple face centered cubic (Fig. 6.12) with 4 Ce's per unit cell ($8 \times 1/8 + 6 \times 1/2$) and a lattice constant a . Similarly, we describe the V_{orb} lattice as simple cubic (Fig. 6.12) with 1 V_{orb} per unit cell ($4 \times 1/4$) with a lattice constant A .

The V_{orb} concentration is $x = \frac{N_{V_{orb}}}{N_{Ce}}$, where $N_{V_{orb}}$ ($=1/A^3$) and N_{Ce} ($=4/a^3$) are the density of V_{orb} and Ce respectively, the relationship between lattice constants is $A = a \times (\frac{1}{4x})^{\frac{1}{3}}$.

With the relation between x , a , and A , we can estimate the upper and lower bounds of the V_{orb} radius by considering two simple cases, as shown in Fig. 6.13. For V_{orb} lower bound ($V_{l,b}$) we take radius as the distance at which the orbitals just touch each other. This results in $V_{l,b} = (1/\sqrt{2}) \times (\frac{1}{4x})^{\frac{1}{3}}a$. For the upper bound we take the radius as the distance at which there is no void, and $V_{u,b} = (1/2) \times (\frac{1}{4x})^{\frac{1}{3}}a$. Ce L_3 edge

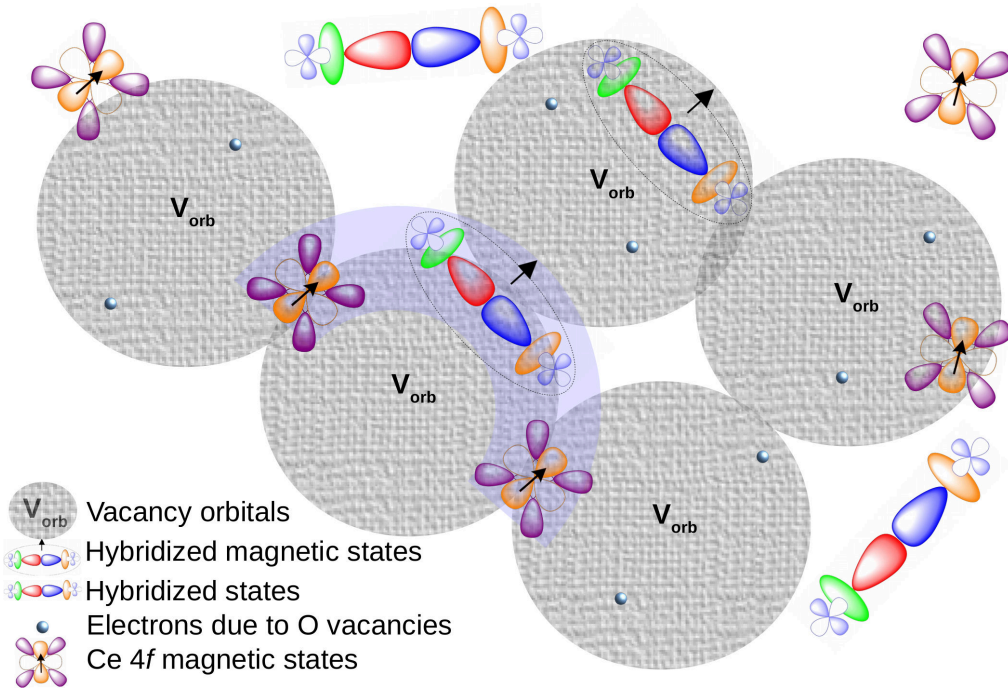


Figure 6.14: Graphical illustration of the magnetic model. Ce 4*f* magnetic states, V_{orb} , and hybridized Ce 4*f* and O 2*p* states are shown. Ce 4*f* states captured in the V_{orb} polarizes the hybridized states and provides a channel to mediate the ferromagnetism. Shaded region illustrates the magnetic exchange process as discussed in the text.

XANES analysis gives the vacancy fraction at $x = 0.1$ ($2\text{Ce}^{4+} + V_{\text{O}}^{2-} \leftrightarrow 2\text{Ce}^{3+}$) and x-ray diffraction refinements identify the lattice constant, $a \sim 5.412\text{\AA}$ (see table. 5.1), so V_{orb} is between ~ 0.5 nm and ~ 0.8 nm in diameter.

The radial extent of Ce 4*f* orbitals[176] is very small (0.54 Å) and that limits the Ce 4*f* – O 2*p* covalent mixing to be relatively low as supported by various DFT/LDA/GGA calculations[171]. However, the size (0.5 to 0.8 nm diameter) of the V_{orb} are large and less localized compared to the Ce 4*f* states. This is consistent with first principle calculations that found the size of V_{orb} is ~ 1.0 nm[175]. Note that only the trapped Ce 4*f* states in the V_{orb} can polarize spin moments (due to their

delocalized nature) on the hybridized states and be responsible for the long-range ferromagnetic order. The residual $4f$ states that are not in the vicinity of V_{orb} cannot contribute to the ferromagnetism due to the lack of the hybridized magnetic states. If the number of V_{orb} are constant, introducing foreign transition metal ions (Fe or Co) impacts Ce $4f - O 2p$ hybridization and further promotes a robust, yet weak, ferromagnetism. Figure 6.14 shows the illustration of this microscopic model. This description is consistent with the observation that air or O_2 annealed d^0 nanoscale magnetic oxides exhibit reduced or annihilated magnetism[37; 177; 33], as O_2 fills the vacancies resulting in a deficiency of V_{orb} coupling channels.

Collectively, our work showed that lattice oxygen plays a crucial role in the magnetism of oxide systems. In d electron rich oxides such as Fe_3O_4 and $CoFe_2O_4$ nanoscale systems the lattice oxygen mediates the magnetism by changing the superexchange interactions on the surface of nanoparticles. In d^0 systems such as nanoscale CeO_2 shapes, Fe and Co decorated CeO_2 systems the lattice oxygen/vacancies are responsible for the magnetism. In d^0 systems, in addition to defects, disorder/non-stoichiometry, hybridization of O $2p$ states with $4f/3d$ plays a critical role in understanding the ferromagnetism of these systems.

Chapter 7

Conclusions and Future work

Understanding the nature of bonding between metal ions and oxygen is central to engineering a variety of interesting properties, such as metal-to-insulator transitions, optical, and magnetic behavior in oxides. In this dissertation, we endeavored to gain insights into the role of the oxygen on the magnetism of the nanoscale oxides Fe_3O_4 , CoFe_2O_4 , CeO_2 shapes, and Fe decorated and Co decorated CeO_2 nanoparticles. In this Chapter, we will review our principal findings, discuss the contributions this work makes to the field, and explore future avenues for research.

We began with the goal of how oxygen rich and oxygen deficient surfaces alter the magnetic susceptibility measurements in the nanoscale oxides Fe_3O_4 and CoFe_2O_4 . Using electronic structure and probes of magnetism we quantified the cation occupancies of Fe_3O_4 and CoFe_2O_4 as $(\text{Fe}_{0.90(6)}^{3+})[\text{Fe}_{1.11(6)}^{3+}\text{Fe}_{0.99(6)}^{2+}]\text{O}_4$ and $(\text{Co}_{0.20(2)}^{2+}\text{Fe}_{0.80(4)}^{3+})[\text{Co}_{0.60(4)}^{2+}\text{Co}_{0.20(2)}^{3+}\text{Fe}_{0.88(4)}^{3+}\text{Fe}_{0.32(4)}^{2+}]\text{O}_4$, respectively. Fe_3O_4 is a normal spinel and CoFe_2O_4 is a mixed spinel. X-ray spectroscopy measurements identified that in CoFe_2O_4 the fraction of t_{2g} orbitals are 16% higher (because Co is doping in Fe_3O_4 , with increasing the number of d electrons the fraction of t_{2g} orbitals increased in CoFe_2O_4). The oxygen rich and oxygen deficient *in-situ* magnetic susceptibility measurements showed that the magnetism is enhanced in CoFe_2O_4 evidencing that the oxygen storage capacity of CoFe_2O_4 is higher by affecting the Fe/Co $3d - \text{O } 2p$ hybridization. Both Fe_3O_4 and CoFe_2O_4 nanostructures are d electron rich systems where the magnetism is due to the spin angular momentum of unpaired electrons.

We then carried out the oxygen rich and oxygen deficient *in-situ* magnetic susceptibility measurements on the nanoscale CeO_2 cubes, rods, and spheres (all are d^0 systems). Nanostructured CeO_2 shapes magnetic susceptibility measurements in

oxygen rich and oxygen deficient environments opened a new possibility to quantify the intrinsic oxygen storage capacity and defects in these systems[84]. These systems showed an antiferro-to-paramagnetic transition in oxygen-rich systems and the intrinsic oxygen tracked with the surface localized Ce^{3+} sites and catalytically active sites. The new insights into nanoceria catalysis are enabled by quantifying the defects for different ceria nanoparticle shapes (and thus surface terminations) and O_2 partial pressure. We then find a linear correlation between catalytic rates and the number of oxygen lattice vacancies generated under reducing conditions. This correlation demonstrated that the observed enhancement of reactivity for ceria nanocubes and nanorods is due to the increased ease of generating lattice defects in these materials. These results evidenced that surface oxygen, vacancies and Ce^{3+} ions play a significant role in the magnetism of these nanoscale d^0 systems.

We next investigated the origins behind the ferromagnetism in oxygen vacancy rich system. We choose nanostructured CeO_2 , Fe- decorated CeO_2 and Co- decorated CeO_2 systems. The surfaces are decorated with Fe and Co to alter the oxygen bonding with the Ce $4f$ states to identify the sources of magnetism. Employing a combination of complementary techniques (electronic structure, element and bulk sensitive) and modelling we showed that in addition to defects/disorder and non-stoichiometry, O $2p$ – Ce $4f$ hybridization is the missing link to understand the magnetism in d^0 systems[109]. Further, we also proposed a model to explain the origin of ferromagnetism in nanoscale CeO_2 via vacancy orbitals. The size of the vacancy orbitals are estimated to be of the order of ~ 1 nm in diameter, and they are essential for the spin polarization of the magnetic moments on the hybridized states and responsible

for the long-range ferromagnetic order.

Nanoscale oxides of specific shapes, and therefore surface terminations, have seen enormous synthetic success, and are important materials for fundamental study as well as practical application. In spite of the success in synthesis of the nanomaterials, the formation of defects and their impact on the surface chemistry and magnetism remains unclear. This work began the process of answering open questions in the field about the role of oxygen in the magnetism of d electron rich and d^0 systems. The magnetic susceptibility techniques developed[83] in this thesis opened a new window of opportunity to quantify the intrinsic oxygen and defects to study the magnetism of d electron rich and d^0 systems.

Extending the oxygen rich and oxygen deficient *in-situ* magnetic susceptibility measurements to a wide class of redox-active nanoscale oxide materials such as Co_3O_4 , MnFe_2O_4 , NiFe_2O_4 , and ZnFe_2O_4 spinels and correlating their t_{2g}/e_g occupancy (using O K-edge XAS measurements) trends with oxygen storage capacity may shine light on the relation between strength of hybridization and defects/intrinsic oxygen. Athermal hysteresis in nanoscale CeO_2 is an interesting result that deserves further attention. It has been reported that the prototypical d^0 system's (nanoscale CeO_2) magnetic saturation is temperature independent[42]. Such a trend is also observed for Fe-decorated CeO_2 nanocrystallites (above 100 K). The current existing models of superparamagnetism, Heisenberg superexchange, Zener double exchange, Stoner ferromagnetism, modulated ferromagnetism, giant orbital paramagnetism all fail to explain the phenomenon[33]. The idea of vacancy orbitals polarizing spin moments on the hybrid states is an elegant solution to understanding the origin of d^0 magnetism.

To extend the validity of the model to other d^0 systems, additional temperature-dependent XAS and XMCD measurements on Ce M_{5,4} and O K edge are necessary. Further, XAS and XMCD measurements should be performed on γ -Al₂O₃, ZnO, In₂O₃, and SnO₂ nanocrystallites transition metal ions and O K edges to identify the universality of the phenomenon.

Bibliography

- [1] Bruce M Moskowitz. Hitchhiker's guide to magnetism. In *Environmental Magnetism Workshop (IRM)*, volume 279, page 48. Inst. for Rock Magnetism Univ. of Minn., Minneapolis, Minn, 1991.
- [2] Steven H Simon. *The Oxford Solid State Basics*. Oxford University Press, 2013.
- [3] Robert M White, Robert M White, and Bradford Bayne. *Quantum theory of magnetism*, volume 1. Springer, 1983.
- [4] John Hasbrouck Van Vleck. Handbook of optics: The theory of electric and magnetic susceptibilities. 1965.
- [5] R. J. Elliott and K. W. H. Stevens. A preliminary survey of the paramagnetic resonance phenomena observed in rare earth ethyl sulphates. *Proceedings of the Physical Society. Section A*, 64:205, 1951.
- [6] G. S. Bogle, A. H. Cooke, and S. Whitley. Paramagnetism of cerium ethyl-sulphate at low temperatures. *Proceedings of the Physical Society. Section A*, 64:931, 1951.
- [7] P. Dutta, S. Pal, M. S. Seehra, Y. Shi, E. M. Eyring, and R. D. Ernst. Con-

- centration of Ce^{3+} and oxygen vacancies in cerium oxide nanoparticles. *Chem. Mater.*, 18:5144, 2006.
- [8] A. Morrish. *The Physical Principles of Magnetism*. Wiley-IEEE Press, 1965.
- [9] Louis Néel. Thermoremanent magnetization of fine powders. *Reviews of Modern Physics*, 25(1):293, 1953.
- [10] William Fuller Brown Jr. Relaxational behavior of fine magnetic particles. *Journal of Applied physics*, 30(4):S130–S132, 1959.
- [11] Robert D Cowan. *The theory of atomic structure and spectra*. Number 3. Univ of California Press, 1981.
- [12] Nevill F Mott. The basis of the electron theory of metals, with special reference to the transition metals. *Proceedings of the Physical Society. Section A*, 62(7):416, 1949.
- [13] J Zaanen, GA Sawatzky, and JW Allen. Band gaps and electronic structure of transition-metal compounds. *Physical Review Letters*, 55(4):418, 1985.
- [14] P Olalde-Velasco, J Jiménez-Mier, JD Denlinger, Z Hussain, and WL Yang. Direct probe of mott-hubbard to charge-transfer insulator transition and electronic structure evolution in transition-metal systems. *Physical Review B*, 83(24):241102, 2011.
- [15] Robert Green. *Transition Metal Impurities in Semiconductors: Induced Magnetism and Band Gap Engineering*. PhD thesis, Citeseer, 2013.

-
- [16] JMD Coey, M Venkatesan, and Hongjun Xu. Introduction to magnetic oxides. *Functional metal oxides: New science and novel applications*, pages 1–49, 2013.
- [17] Gerald F Dionne. *Magnetic oxides*, volume 14. Springer, 2009.
- [18] John B Goodenough. *Magnetism and chemical bond*, volume 1. Interscience Publ., 1963.
- [19] Clarence Zener. Interaction between the d-shells in the transition metals. ii. ferromagnetic compounds of manganese with perovskite structure. *Physical Review*, 82(3):403, 1951.
- [20] Jose Luis G Fierro. *Metal oxides: chemistry and applications*. CRC press, 2005.
- [21] Jacques C Vedriner. *Metal Oxides in Heterogeneous Catalysis*. Elsevier, 2018.
- [22] Paidi et al. Surface termination and promotor ion cooperation maximize NO_x reduction: The case of nanoceria supported Fe oxide catalysts (un published).
- [23] E. Mamontov and T. Egami. Structural defects in a nano-scale powder of CeO₂ studied by pulsed neutron diffraction. *J. Phys.Chem. Solids*, 61:1345, 2000.
- [24] Tiziano Montini, Michele Melchionna, Matteo Monai, and Paolo Fornasiero. Fundamentals and catalytic applications of CeO₂ based materials. *Chemical Reviews*, 116(10):5987–6041, 2016.
- [25] Alberto P Guimarães and Alberto Passos Guimaraes. *Principles of nanomagnetism*, volume 7. Springer, 2009.

- [26] Qing Zhao, Zhenhua Yan, Chengcheng Chen, and Jun Chen. Spinels: controlled preparation, oxygen reduction/evolution reaction application, and beyond. *Chemical Reviews*, 117(15):10121–10211, 2017.
- [27] Sukon Phanichphant et al. Cellulose-precursor synthesis of nanocrystalline $\text{Co}_{0.5}\text{Cu}_{0.5}\text{Fe}_2\text{O}_4$ spinel ferrites. *Materials Research Bulletin*, 47(2):473–477, 2012.
- [28] Safia Anjum, G Hassnain Jaffari, Abdul K Rumaiz, M Shahid Rafique, and S Ismat Shah. Role of vacancies in transport and magnetic properties of nickel ferrite thin films. *Journal of Physics D: Applied Physics*, 43(26):265001, 2010.
- [29] Xu Zuo, Aria Yang, Soack-Dae Yoon, Joseph A Christodoulides, Vincent G Harris, and Carmine Vittoria. Large induced magnetic anisotropy in manganese spinel ferrite films. *Applied Physics Letters*, 87(15):152505, 2005.
- [30] Xu Zuo, Aria Yang, Soack-Dae Yoon, Joe A Christodoulides, Vincent G Harris, and Carmine Vittoria. Magnetic properties of manganese ferrite films grown at atomic scale. *Journal of Applied Physics*, 97(10):10G103, 2005.
- [31] F Eskandari, SB Porter, M Venkatesan, P Kameli, K Rode, and JMD Coey. Magnetization and anisotropy of cobalt ferrite thin films. *Physical Review Materials*, 1(7):074413, 2017.
- [32] Xiao Shi, Steven L Bernasek, and Annabella Selloni. Formation, electronic structure, and defects of Ni substituted spinel cobalt oxide: a DFT+U study. *The Journal of Physical Chemistry C*, 120(27):14892–14898, 2016.

-
- [33] Karl Ackland and JMD Coey. Room temperature magnetism in CeO_2 – a review. *Physics Reports*, 2018.
- [34] JMD Coey. Magnetism in d^0 oxides. *Nature Materials*, 18(7):652, 2019.
- [35] A. Sundaresan, R. Bhargavi, N. Raangarajan, U. Siddesh, and C. N. R. Rao. Ferromagnetism as a universal feature of nanoparticles of the otherwise non-magnetic oxides. *Phys. Rev. B*, 74:161306, 2006.
- [36] V Fernandes, P Schio, RJO Mossaneck, AJA De Oliveira, WA Ortiz, Dominique Demaille, F Vidal, Y Zheng, P Fichtner, L Amaral, et al. Anisotropy of magnetization and nanocrystalline texture in electrodeposited CeO_2 films. *Electrochemical and Solid-State Letters*, 14(3):P9–P11, 2011.
- [37] A Sundaresan, R Bhargavi, N Rangarajan, U Siddesh, and CNR Rao. Ferromagnetism as a universal feature of nanoparticles of the otherwise nonmagnetic oxides. *Physical Review B*, 74(16):161306, 2006.
- [38] M. Y. Ge, H. Wang, E. Z. Liu, J. F. Liu, J. Z. Jiang, Y. K. Li, Z. A. Xu, and H. Y. Li. On the origin of ferromagnetism in CeO_2 nanocubes. *Appl. Phys. Lett.*, 20:062505, 2008.
- [39] Xiaoping Han, Jaichan Lee, and Han-Ill Yoo. Oxygen-vacancy-induced ferromagnetism in CeO_2 from first principles. *Physical Review B*, 79(10):100403, 2009.
- [40] Yinglin Liu, Zainovia Lockman, Azizan Aziz, and Judith MacManus-Driscoll. Size dependent ferromagnetism in cerium oxide (CeO_2) nanostructures indepen-

- dent of oxygen vacancies. *Journal of Physics: Condensed Matter*, 20(16):165201, 2008.
- [41] Mingjie Li, Shihui Ge, Wen Qiao, Li Zhang, Yalu Zuo, and Shiming Yan. Relationship between the surface chemical states and magnetic properties of CeO₂ nanoparticles. *Applied Physics Letters*, 94(15):152511, 2009.
- [42] Michael Coey, Karl Ackland, Munuswamy Venkatesan, and Siddhartha Sen. Collective magnetic response of CeO₂ nanoparticles. *Nature Physics*, 12(7):694, 2016.
- [43] Novica Paunović, Zorana Dohčević-Mitrović, Rareş Scurtu, Sonja Aškračić, Marija Prekajski, Branko Matović, and Zoran V Popović. Suppression of inherent ferromagnetism in Pr-doped CeO₂ nanocrystals. *Nanoscale*, 4(17):5469–5476, 2012.
- [44] Karl Ackland, Lorena MA Monzon, M Venkatesan, and JMD Coey. Magnetism of nanostructured CeO₂. *IEEE transactions on magnetics*, 47(10):3509–3512, 2011.
- [45] Shih-Yun Chen, Chi-Hang Tsai, Mei-Zi Huang, Der-Chung Yan, Tzu-Wen Huang, Alexandre Gloter, Chi-Liang Chen, Hong-Ji Lin, Chien-Te Chen, and Chung-Li Dong. Concentration dependence of oxygen vacancy on the magnetism of CeO₂ nanoparticles. *The Journal of Physical Chemistry C*, 116(15):8707–8713, 2012.
- [46] William Lee, Shih-Yun Chen, Yu-Sheng Chen, Chung-Li Dong, Hong-Ji Lin,

- Chien-Te Chen, and Alexandre Gloter. Defect structure guided room temperature ferromagnetism of Y-doped CeO₂ nanoparticles. *The Journal of Physical Chemistry C*, 118(45):26359–26367, 2014.
- [47] Dong-Ze Peng, Shih-Yun Chen, Chi-Liang Chen, Alexandre Gloter, Fei-Ting Huang, Chung-Li Dong, Ting-Shan Chan, Jin-Ming Chen, Jyh-Fu Lee, Hong-Ji Lin, et al. Understanding and tuning electronic structure in modified ceria nanocrystals by defect engineering. *Langmuir*, 30(34):10430–10439, 2014.
- [48] Zili Wu, Meijun Li, Jane Howe, Harry M Meyer III, and Steven H Overbury. Probing defect sites on CeO₂ nanocrystals with well-defined surface planes by raman spectroscopy and O₂ adsorption. *Langmuir*, 26(21):16595–16606, 2010.
- [49] H. Mai, L. Sun, Y. Zhang, R. Si, Wei Feng, H. Zhang, H. Liu, and C. Yan. Shape-selective synthesis and oxygen storage behavior of ceria nanopolyhedra, nanorods, and nanocubes. *J. Phys. Chem. B*, 109(51):24380, 2005.
- [50] VD Araujo, W Avansi, HB De Carvalho, ML Moreira, Elson Longo, C Ribeiro, and Maria Inês Basso Bernardi. CeO₂ nanoparticles synthesized by a microwave-assisted hydrothermal method: evolution from nanospheres to nanorods. *CrytEngComm*, 14(3):1150–1154, 2012.
- [51] A Bonamartini Corradi, F Bondioli, AM Ferrari, and T Manfredini. Synthesis and characterization of nanosized ceria powders by microwave–hydrothermal method. *Materials Research Bulletin*, 41(1):38–44, 2006.
- [52] Charles A Roberts, Dario Prieto-Centurion, Yasutaka Nagai, Yusaku F

- Nishimura, Ryan D Desautels, Johan Van Lierop, Paul T Fanson, and Justin M Notestein. In Situ Characterization of Highly Dispersed, Ceria-Supported Fe sites for NO reduction by CO. *The Journal of Physical Chemistry C*, 119(8):4224–4234, 2015.
- [53] Torin C Peck, Gunugunuri K Reddy, Michael Jones, and Charles A Roberts. Monolayer detection of supported Fe and Co oxides on ceria to establish structure–activity relationships for reduction of NO by CO. *The Journal of Physical Chemistry C*, 121(15):8435–8443, 2017.
- [54] Charles Kittel, Paul McEuen, and Paul McEuen. *Introduction to solid state physics*, volume 8. Wiley New York, 1976.
- [55] Juan Rodríguez-Carvajal. Recent advances in magnetic structure determination by neutron powder diffraction. *Physica B*, 192:55, 1993.
- [56] Pierre Villars. *Pearson’s crystal data®: crystal structure database for inorganic compounds*. ASM International, 2007.
- [57] P Thompson, DE Cox, and JB Hastings. Rietveld refinement of Debye–Scherrer synchrotron X-ray data from Al_2O_3 . *Journal of Applied Crystallography*, 20(2):79–83, 1987.
- [58] A. L. Patterson. The Scherrer Formula for X-Ray Particle Size Determination. *Phys. Rev.*, 56:978–982, Nov 1939.
- [59] A.C. Larson and R.B. Von Dreele. General Structure Analysis System (GSAS). *Los Alamos National Laboratory Report LAUR*, pages 86–748, 1994.

- [60] Stephen Brunauer, Paul Hugh Emmett, and Edward Teller. Adsorption of gases in multimolecular layers. *Journal of the American Chemical Society*, 60(2):309–319, 1938.
- [61] <http://xafs.org>.
- [62] Frank De Groot. Multiplet effects in x-ray spectroscopy. *Coordination Chemistry Reviews*, 249(1-2):31–63, 2005.
- [63] Javier Fernández-Rodríguez, Brian Toby, and Michel van Veenendaal. Xclaim: A graphical interface for the calculation of core-hole spectroscopies. *Journal of Electron Spectroscopy and Related Phenomena*, 202:81–88, 2015.
- [64] John C Slater and George F Koster. Simplified LCAO method for the periodic potential problem. *Physical Review*, 94(6):1498, 1954.
- [65] Joachim Stöhr and Hans Christoph Siegmann. Magnetism. *Solid-State Sciences*. Springer, Berlin, Heidelberg, 5, 2006.
- [66] G Schütz, W Wagner, Wr Wilhelm, P Kienle, R Zeller, R Frahm, and G Materlik. Absorption of circularly polarized x rays in iron. *Physical Review Letters*, 58(7):737, 1987.
- [67] BT Thole, Paolo Carra, F Sette, and Gerrit van der Laan. X-ray circular dichroism as a probe of orbital magnetization. *Physical Review Letters*, 68(12):1943, 1992.
- [68] Paolo Carra, BT Thole, Massimo Altarelli, and Xindong Wang. X-ray circular dichroism and local magnetic fields. *Physical Review Letters*, 70(5):694, 1993.

- [69] CT Chen, YU Idzerda, H-J Lin, NV Smith, G Meigs, E Chaban, GH Ho, E Pellegrin, and F Sette. Experimental confirmation of the x-ray magnetic circular dichroism sum rules for iron and cobalt. *Physical Review Letters*, 75(1):152, 1995.
- [70] Bruce Ravel and MATHENA Newville. ATHENA, ARTEMIS, HEPHAESTUS: data analysis for x-ray absorption spectroscopy using IFEFFIT. *Journal of Synchrotron Radiation*, 12(4):537–541, 2005.
- [71] John J Rehr and Robert C Albers. Theoretical approaches to x-ray absorption fine structure. *Reviews of Modern Physics*, 72(3):621, 2000.
- [72] EA Stern and SM Heald. Basic principles and applications of EXAFS, Handbook of Synchrotron Radiation, 1983.
- [73] Matthew Newville. Fundamentals of XAFS. *Reviews in Mineralogy and Geochemistry*, 78(1):33–74, 2014.
- [74] M Pompa, AM Flank, P Lagarde, JC Rife, I Stekhin, M Nakazawa, H Ogasawara, and A Kotani. Experimental and theoretical comparison between absorption, total electron yield, and fluorescence spectra of rare-earth M_5 edges. *Physical Review B*, 56(4):2267, 1997.
- [75] Rudolf L Mössbauer. Kernresonanzfluoreszenz von Gammastrahlung in Ir^{191} . *Zeitschrift für Physik*, 151(2):124–143, 1958.
- [76] Philipp Gütlich, Eckhard Bill, and Alfred X Trautwein. *Mössbauer spectroscopy*

- and transition metal chemistry: fundamentals and applications*. Springer Science & Business Media, 2010.
- [77] RD Desautels, JM Cadogan, and J van Lierop. Spin dynamics in CoFe_2O_4 nanoparticles. *Journal of Applied Physics*, 105(7):07B506, 2009.
- [78] OC Kistner and AW Sunyar. Evidence for Quadrupole Interaction of Fe^{57m} , and Influence of Chemical Binding on Nuclear Gamma-Ray Energy. *Physical Review Letters*, 4(8):412, 1960.
- [79] RJ Armstrong, AH Morrish, and GA Sawatzky. Mössbauer study of ferric ions in the tetrahedral and octahedral sites of a spinel. *Physics Letters*, 23(7):414–416, 1966.
- [80] DP Johnson. Mössbauer study of the local environments of ^{57}Fe in FeO . *Solid State Communications*, 7(24):1785–1788, 1969.
- [81] SK Banerjee, W O’reilly, and CE Johnson. Mössbauer-effect measurements in FeTi spinels with local disorder. *Journal of Applied Physics*, 38(3):1289–1290, 1967.
- [82] Robert Steven Hargrove and W Kündig. Mössbauer measurements of magnetite below the Verwey transition. *Solid State Communications*, 8(5):303–308, 1970.
- [83] Vinod K Paidi, Johan A Van Lierop, and Charles A Roberts. Method of magnetic analysis to determine the catalytic activity of metal oxides including nanoceria, January 17 2019. US Patent App. 15/646,863.

- [84] Vinod K Paidi, Louisa Savereide, David J Childers, Justin M Notestein, Charles A Roberts, and Johan Van Lierop. Predicting NO_x Catalysis by Quantifying Ce^{3+} from Surface and Lattice Oxygen. *ACS Applied Materials & Interfaces*, 9(36):30670–30678, 2017.
- [85] Koichi Momma and Fujio Izumi. VESTA 3 for three-dimensional visualization of crystal, volumetric and morphology data. *Journal of Applied Crystallography*, 44(6):1272–1276, 2011.
- [86] JA Moyer, CAF Vaz, DA Arena, D Kumah, E Negusse, and VE Henrich. Magnetic structure of Fe-doped CoFe_2O_4 probed by x-ray magnetic spectroscopies. *Physical Review B*, 84(5):054447, 2011.
- [87] H Okudera, K Kihara, and T Matsumoto. Temperature dependence of structure parameters in natural magnetite: single crystal X-ray studies from 126 to 773 K. *Acta Crystallographica Section B: Structural Science*, 52(3):450–457, 1996.
- [88] M Laarj, S Kacim, and B Gillot. Cationic Distribution and Oxidation Mechanism of Trivalent Manganese Ions in Submicrometer $\text{Mn}_x\text{CoFe}_{2-x}\text{O}_4$ Spinel Ferrites. *Journal of Solid State Chemistry*, 125(1):67–74, 1996.
- [89] Gloria Subías, Joaquín García, and Javier Blasco. Exafs spectroscopic analysis of the Verwey transition in Fe_3O_4 . *Physical Review B*, 71(15):155103, 2005.
- [90] DH Kim, HJ Lee, G Kim, YS Koo, JH Jung, HJ Shin, J-Y Kim, and J-S Kang. Interface electronic structures of $\text{BaTiO}_3@X$ nanoparticles ($X=\gamma\text{-Fe}_2\text{O}_3$,

- Fe₃O₄, α -Fe₂O₃, and Fe) investigated by XAS and XMCD. *Physical Review B*, 79(3):033402, 2009.
- [91] BT Thole, G Van der Laan, JC Fuggle, GA Sawatzky, RC Karnatak, and J-M Esteve. 3d x-ray-absorption lines and the 3d⁹4fⁿ⁺¹ multiplets of the lanthanides. *Physical Review B*, 32(8):5107, 1985.
- [92] Carolyn I Pearce, C Michael B Henderson, Richard AD Patrick, Gerrit Van Der Laan, and David J Vaughan. Direct determination of cation site occupancies in natural ferrite spinels by L_{2,3} X-ray absorption spectroscopy and X-ray magnetic circular dichroism. *American Mineralogist*, 91(5-6):880–893, 2006.
- [93] Richard AD Patrick, Gerrit Van Der Laan, C Michael B Henderson, Pieter Kuiper, Esther Dudzik, and David J Vaughan. Cation site occupancy in spinel ferrites studied by x-ray magnetic circular dichroism: developing a method for mineralogists. *European Journal of Mineralogy*, 14(6):1095–1102, 2002.
- [94] J Chen, DJ Huang, A Tanaka, CF Chang, SC Chung, WB Wu, and CT Chen. Magnetic circular dichroism in Fe 2p resonant photoemission of magnetite. *Physical Review B*, 69(8):085107, 2004.
- [95] Gerrit van der Laan, Elke Arenholz, Rajesh V Chopdekar, and Yuri Suzuki. Influence of crystal field on anisotropic X-ray magnetic linear dichroism at the Co²⁺ L_{2,3} edges. *Physical Review B*, 77(6):064407, 2008.
- [96] Reiko Nakajima, J. Stöhr, and Y. U. Idzerda. Electron-yield saturation effects

- in L-edge x-ray magnetic circular dichroism spectra of Fe, Co, and Ni. *Phys. Rev. B*, 59:6421–6429, Mar 1999.
- [97] IS Lyubutin, EA Alkaev, Yu V Korzhetskiy, CR Lin, and RK Chiang. Monitoring by Mössbauer spectroscopy the thermal reduction of hematite into magnetite: the surface effect and charge disproportionality in iron oxide nanoparticles. *Hyperfine Interactions*, 189(1-3):21–29, 2009.
- [98] GA Sawatzky, F Van Der Woude, and AH Morrish. Cation distributions in octahedral and tetrahedral sites of the ferrimagnetic spinel CoFe_2O_4 . *Journal of Applied Physics*, 39(2):1204–1205, 1968.
- [99] V Rusanov, V Gushterov, S Nikolov, and AX Trautwein. Detailed Mössbauer study of the cation distribution in CoFe_2O_4 ferrites. In *ISIAME 2008*, pages 397–404. Springer, 2009.
- [100] FMF De Groot, M Grioni, JC Fuggle, J Ghijsen, GA Sawatzky, and H Petersen. Oxygen 1s x-ray-absorption edges of transition-metal oxides. *Physical Review B*, 40(8):5715, 1989.
- [101] ZY Wu, S Gota, F Jollet, M Pollak, M Gautier-Soyer, and CR Natoli. Characterization of iron oxides by x-ray absorption at the oxygen K edge using a full multiple-scattering approach. *Physical Review B*, 55(4):2570, 1997.
- [102] Feng Lin, Dennis Nordlund, Taijun Pan, Isaac M Markus, Tsu-Chien Weng, Huolin L Xin, and Marca M Doeff. Influence of synthesis conditions on the

- surface passivation and electrochemical behavior of layered cathode materials. *Journal of Materials Chemistry A*, 2(46):19833–19840, 2014.
- [103] EJW Verwey. Electronic conduction of magnetite (Fe_3O_4) and its transition point at low temperatures. *Nature*, 144(3642):327, 1939.
- [104] TJ Daou, G Pourroy, S Bégin-Colin, Jean-Marc Grenèche, C Ulhaq-Bouillet, P Legaré, P Bernhardt, C Leuvrey, and G Rogez. Hydrothermal synthesis of monodisperse magnetite nanoparticles. *Chemistry of Materials*, 18(18):4399–4404, 2006.
- [105] JB Yang, XD Zhou, William B Yelon, William Joseph James, Qingsheng Cai, KV Gopalakrishnan, Satish K Malik, XC Sun, and DE Nikles. Magnetic and structural studies of the verwey transition in $\text{Fe}_{3-\delta}\text{O}_4$ nanoparticles. *Journal of Applied Physics*, 95(11):7540–7542, 2004.
- [106] K Balakrishnan, SK Arora, and IV Shvets. Strain relaxation studies of the $\text{Fe}_3\text{O}_4/\text{MgO}$ (100) heteroepitaxial system grown by magnetron sputtering. *Journal of Physics: Condensed Matter*, 16(30):5387, 2004.
- [107] J Abellán and M Ortuno. The Verwey Transition in Polycrystalline Cobalt-Iron Ferrites. *Physica Status Solidi (a)*, 96(2):581–586, 1986.
- [108] A. Trovarelli. *In Catalytic Science Series*, volume 2. Imperial College Press: London, 2002.
- [109] Vinod K Paidi, Dale L Brewé, John W Freeland, Charles A Roberts, and Johan

- van Lierop. Role of Ce 4*f* hybridization in the origin of magnetism in nanoceria. *Physical Review B*, 99(18):180403, 2019.
- [110] C. T. Campbell. Waltzing with O₂. *Science*, 299:357, 2003.
- [111] Charles T Campbell and Charles HF Peden. Oxygen vacancies and catalysis on ceria surfaces. *Science*, 309(5735):713–714, 2005.
- [112] F. Esch, S. Fabris, L. Zhou, T. Montini, C. Africh, P. Fornasiero, G. Comelli, and R. Rosei. Electron localization determines defect formation on ceria substrates. *Science*, 309:752, 2005.
- [113] HC Yao and YF Yu Yao. Ceria in automotive exhaust catalysts: I. oxygen storage. *Journal of Catalysis*, 86(2):254–265, 1984.
- [114] Javier Guzman, Silvio Carrettin, and Avelino Corma. Spectroscopic evidence for the supply of reactive oxygen during CO oxidation catalyzed by gold supported on nanocrystalline CeO₂. *Journal of the American Chemical Society*, 127(10):3286–3287, 2005.
- [115] Yu. A. Teterin, A. Yu. Teterin, A. M. Lebedev, and I. O. Utkin. The XPS spectra of cerium compounds containing oxygen. *J. Electron Spectroscopy and Related Phenomena.*, 88:275, 1998.
- [116] F. Zhang, P. Wang, J. Koberstein, S. Khalid, and S. Chan. Cerium oxidation state in ceria nanoparticles studied with x-ray photoelectron spectroscopy and absorption near edge spectroscopy. *Surface Science*, 563:74, 2004.

- [117] J. Soria, A. Martinez-Arias, and J. Conesa. Spectroscopic study of oxygen adsorption as a method to study surface defects on CeO₂. *J. Chem. Soc. Faraday Trans.*, 91:1669, 1995.
- [118] Carla de Leitenburg, Alessandro Trovarelli, Jordi Llorca, Fabrizio Cavani, and Gianluca Bini. The effect of doping CeO₂ with zirconium in the oxidation of isobutane. *Applied Catalysis A: General*, 139(1):161–173, 1996.
- [119] Fatima MZ Zotin, Louise Tournayan, Jean Varloud, Vincent Perrichon, and Roger Fréty. Temperature-programmed reduction: limitation of the technique for determining the extent of reduction of either pure ceria or ceria modified by additives. *Applied Catalysis A: General*, 98(1):99–114, 1993.
- [120] M. Huang and S. Fabris. Role of surface peroxo and superoxo species in the low-temperature oxygen buffering of ceria: Density functional theory calculations. *Phys. Rev. B*, 75:081404, 2007.
- [121] Y. M. Choi, H. Abernathy, H.T. Chen, M. C. Lin, and M. Liu. Characterization of O₂—CeO₂ interactions using in situ raman spectroscopy and first-principle calculations. *Chem. Phys. Chem.*, 7:1957, 2006.
- [122] M. V. Ganduglia-Pirovano, Alexander Hofmann, and Joachim Sauer. Oxygen vacancies in transition metal and rare earth oxides: Current state of understanding and remaining challenges. *Surface Science Reports*, 62:219, 2007.
- [123] S. Yang and L. Gao. Controlled synthesis and self-assembly of CeO₂ nanocubes. *J. Am. Chem. Soc.*, 128:9330, 2006.

- [124] Y. Lin, Z. Wu, J. Wen, K. R. Poeppelmeier, and L. D. Marks. Imaging the atomic surface structures of CeO₂ nanoparticles. *Nano Lett.*, 14(1):191, 2014.
- [125] X. Liu, K. Zhou, L. Wang, B. Wang, and Y. Li. Oxygen vacancy clusters promoting reducibility and activity of ceria nanorods. *J. Am. Chem. Soc.*, 131:3140, 2009.
- [126] Shilpa Agarwal, Leon Lefferts, Barbara L Mojet, DAJ Ligthart, Emiel JM Hensen, David RG Mitchell, Willem J Erasmus, Bruce G Anderson, Ezra J Olivier, Johannes H Neethling, et al. Exposed surfaces on shape-controlled ceria nanoparticles revealed through ac-tem and water-gas shift reactivity. *Chem. Sus. Chem*, 6(10):1898–1906, 2013.
- [127] S. Tsunekawa, K. Ishikawa, Z Q Li, Y Kawazoe, and A Kasuya. Origin of anomalous lattice expansion in oxide nanoparticles. *Phys. Rev. Lett.*, 85:3440, 2000.
- [128] X. D. Zhou and W. Huebner. Size-induced lattice relaxation in CeO₂ nanoparticles. *Appl. Phys. Lett.*, 79:3512, 2001.
- [129] M Veronica Ganduglia-Pirovano, Alexander Hofmann, and Joachim Sauer. Oxygen vacancies in transition metal and rare earth oxides: Current state of understanding and remaining challenges. *Surface science reports*, 62(6):219–270, 2007.
- [130] Koichi Momma and Fujio Izumi. Vesta 3 for three-dimensional visualization of

- crystal, volumetric and morphology data. *Journal of applied crystallography*, 44(6):1272–1276, 2011.
- [131] P. Dutta, P. Burgardt, and M. S. Seehra. Magnetic susceptibility of iron pyrite (FeS_2) between 4.2 and 620 K. *Solid State Comm.*, 22:153, 1977.
- [132] I. Das and E. V. Sampathkumaran. Magnetic ordering in Ce_2RhSi_3 . *J. Magn. Magn. Mater.*, 137:L239, 1994.
- [133] N. Kase, T. Muranaka, and J. Akimitsu. Antiferromagnetic kondo-lattice system with moderate heavy-fermion behavior. *J. Magn. Magn. Mater.*, 321:3380, 2009.
- [134] Jon Lawrence. Speculations on the critical behavior of reduced moment antiferromagnetic cerium compounds. *Journal of Applied Physics*, 53(3):2117–2121, 1982.
- [135] S. Chen, C. Tsai, M. Huang, D. Yan, T. Huang, A. Gloter, C. Chen, H. Lin, C. Chen, and C. Dong. Concentration dependence of oxygen vacancy on the magnetism of CeO_2 nanoparticles. *J. Phys. Chem. C*, 116:8707, 2012.
- [136] G. C. DeFotis. Magnetism of solid oxygen. *Phys. Rev. B*, 23:4714, 1981.
- [137] S. Gregory. Magnetic susceptibility of oxygen adsorbed on graphite. *Phys. Rev. Lett.*, 40:723, 1978.
- [138] D. D. Awschalom, G. N. Lewis, and S. Gregory. Melting and wetting behavior in oxygen films. *Phys. Rev. Lett.*, 51:586, 1983.

- [139] U. Kobler and R. Marx. Susceptibility study of physisorbed oxygen layers on graphite. *Phys. Rev. B*, 35:9809, 1987.
- [140] H. Kanoh and K. Kaneko. Magnetic spin clusters of O₂ confined in a slit-shaped graphitic nanospace at low temperature. *Chem. Phys. Lett.*, 237:329, 1995.
- [141] Y. Murakami. Magnetic and structural phase transitions of physisorbed oxygen layers. *J Phys. Chem. Solids*, 59:467, 1998.
- [142] K. Kawamura and Y. Suzuki. Magnetic susceptibility of oxygen adsorbed by type a bead like zeolite. *Jpn. J. Appl. Phys.*, 46:1009, 2007.
- [143] Dario Prieto-Centurion, Todd R Eaton, Charles A Roberts, Paul T Fanson, and Justin M Notestein. Catalytic reduction of NO with H₂ over redox-cycling Fe on CeO₂. *Applied Catalysis B: Environmental*, 168:68–76, 2015.
- [144] TXT Sayle, SC Parker, and CRA Catlow. The role of oxygen vacancies on ceria surfaces in the oxidation of carbon monoxide. *Surface Science*, 316(3):329–336, 1994.
- [145] Michael Nolan, Stephen C Parker, and Graeme W Watson. The electronic structure of oxygen vacancy defects at the low index surfaces of ceria. *Surface Science*, 595(1):223–232, 2005.
- [146] M Venkatesan, CB Fitzgerald, and JMD Coey. Thin films: unexpected magnetism in a dielectric oxide. *Nature*, 430(7000):630, 2004.
- [147] Nguyen Hoa Hong, Joe Sakai, Nathalie Poirot, and Virginie Brizé. Room-

- temperature ferromagnetism observed in undoped semiconducting and insulating oxide thin films. *Phys. Rev. B*, 73:132404, Apr 2006.
- [148] Chaitanya Das Pemmaraju and S. Sanvito. Ferromagnetism Driven by Intrinsic Point Defects in HfO_2 . *Phys. Rev. Lett.*, 94:217205, Jun 2005.
- [149] David W Abraham, Martin M Frank, and Supratik Guha. Absence of magnetism in hafnium oxide films. *Applied Physics Letters*, 87(25):252502, 2005.
- [150] VK Paidi, NS Ferreira, D Goltz, and J van Lierop. Magnetism mediated by a majority of $\text{Fe}^{3+} + \text{V}_\text{O}^{2-}$ complexes in Fe-doped CeO_2 nanoparticles. *Journal of Physics: Condensed Matter*, 27(33):336001, 2015.
- [151] WC Martin. Table of Spin-Orbit Energies for p -Electrons in Neutral Atomic (core) np Configurations. *J. Res. Natl. Bur. Stand*, pages 109–111, 1971.
- [152] H Dexpert, RC Karnatak, J-M Esteve, JP Connerade, M Gasgnier, PE Caro, and L Albert. X-ray absorption studies of CeO_2 , PrO_2 , and TbO_2 . ii. Rare-earth valence state by L_{III} absorption edges. *Physical Review B*, 36(3):1750, 1987.
- [153] G Kaindl, G Schmiester, EV Sampathkumaran, and P Wachter. Pressure-induced changes in L_{III} x-ray-absorption near-edge structure of CeO_2 and CeF_4 : Relevance to $4f$ -electronic structure. *Physical Review B*, 38(14):10174, 1988.
- [154] AV Soldatov, TS Ivanchenko, S Della Longa, A Kotani, Y Iwamoto, and A Bianconi. Crystal-structure effects in the Ce L_3 -edge x-ray-absorption spectrum of CeO_2 : Multiple-scattering resonances and many-body final states. *Physical Review B*, 50(8):5074, 1994.

- [155] TK Sham, RA Gordon, and SM Heald. Resonant inelastic x-ray scattering at the Ce L₃ edge of CePO₄ and CeO₂: Implications for the valence of CeO₂ and related phenomena. *Physical Review B*, 72(3):035113, 2005.
- [156] Butorin et al. Resonant x-ray fluorescence spectroscopy of correlated systems: A probe of charge-transfer excitations. *Physical Review Letters*, 77(3):574, 1996.
- [157] Löble et al. Covalency in Lanthanides. An X-ray Absorption Spectroscopy and Density Functional Theory Study of LnCl₆^{x-} (x = 3, 2). *Journal of the American Chemical Society*, 137(7):2506–2523, 2015.
- [158] DD Koelling, AM Boring, and JH Wood. The electronic structure of CeO₂ and PrO₂. *Solid State Communications*, 47(4):227–232, 1983.
- [159] Akio Kotani, T Jo, and JC Parlebas. Many-body effects in core-level spectroscopy of rare-earth compounds. *Advances in Physics*, 37(1):37–85, 1988.
- [160] L Douillard, M Gautier, N Thommat, M Henriot, MJ Guittet, JP Duraud, and G Tourillon. Local electronic structure of Ce-doped Y₂O₃: An XPS and XAS study. *Physical Review B*, 49(23):16171, 1994.
- [161] J Ph Schillé, F Bertran, M Finazzi, Ch Brouder, JP Kappler, and G Krill. 4f orbital and spin magnetism in cerium intermetallic compounds studied by magnetic circular x-ray dichroism. *Physical Review B*, 50(5):2985, 1994.
- [162] V Fernandes, RJO Mossaneck, P Schio, JJ Klein, AJA De Oliveira, WA Ortiz, N Mattoso, J Varalda, WH Schreiner, M Abbate, et al. Dilute-defect mag-

- netism: Origin of magnetism in nanocrystalline CeO_2 . *Physical Review B*, 80(3):035202, 2009.
- [163] Lu Zhan-Sheng, Ma Dong-Wei, Zhang Jing, Xu Guo-Liang, and Yang Zong-Xian. First principles study of the magnetism driven by cation defects in CeO_2 : the important role of O $2p$ states. *Chinese Physics B*, 21(4):047505, 2012.
- [164] PRL Keating, DO Scanlon, and GW Watson. Intrinsic ferromagnetism in CeO_2 : Dispelling the myth of vacancy site localization mediated superexchange. *Journal of Physics: Condensed Matter*, 21(40):405502, 2009.
- [165] WT Fuhrman, JC Leiner, JW Freeland, M van Veenendaal, SM Koohpayeh, W Adam Phelan, TM McQueen, and C Broholm. Magnetic dichroism in the Kondo insulator SmB_6 . *Physical Review B*, 99(2):020401, 2019.
- [166] G Van der Laan, BT Thole, GA Sawatzky, JC Fuggle, and R Karnatak. Identification of the relative population of spin-orbit split states in the ground state of a solid. *Journal of Physics C: Solid State Physics*, 19(5):817, 1986.
- [167] M Finazzi, FMF De Groot, A-M Dias, B Kierren, F Bertran, Ph Sainctavit, J-P Kappler, O Schulte, W Felsch, and G Krill. Direct evidence of the role of hybridization in the x-ray magnetic circular dichroism of α -Ce. *Physical Review Letters*, 75(25):4654, 1995.
- [168] SM Butorin, DC Mancini, J-H Guo, N Wassdahl, and J Nordgren. On the hybridization of Ce $4f$ states in CeF_3 and CeO_2 : A near-threshold excitation

- X-ray fluorescence study. *Journal of Alloys and Compounds*, 225(1-2):230–233, 1995.
- [169] JA Moyer, CAF Vaz, E Negusse, DA Arena, and VE Henrich. Controlling the electronic structure of $\text{Co}_{1-x}\text{Fe}_{2+x}\text{O}_4$ thin films through iron doping. *Physical Review B*, 83(3):035121, 2011.
- [170] E. Skoropata, R. D. Desautels, C.-C. Chi, H. Ouyang, J. W. Freeland, and J. van Lierop. Magnetism of iron oxide based core-shell nanoparticles from interface mixing with enhanced spin-orbit coupling. *Phys. Rev. B*, 89:024410, Jan 2014.
- [171] Joachim Paier, Christopher Penschke, and Joachim Sauer. Oxygen defects and surface chemistry of ceria: quantum chemical studies compared to experiment. *Chemical reviews*, 113(6):3949–3985, 2013.
- [172] A. Trovarelli. Catalytic properties of ceria and CeO_2 -containing materials. *Catal. Rev. Sci. Eng.*, 38:439, 1996.
- [173] E.S. Putna, J.M. Vohs, and R.J. Gorte. Evidence for weakly bound oxygen on ceria films. *J. Phys. Chem.*, 100:17862, 1996.
- [174] Alessandro Trovarelli, Francesca Zamar, Jordi Llorca, Carla De Leitenburg, Giuliano Dolcetti, and Janos T Kiss. Nanophase fluorite-structured $\text{CeO}_2\text{-ZrO}_2$ catalysts prepared by high-energy mechanical milling. *Journal of Catalysis*, 169(2):490–502, 1997.
- [175] TS Heng, D-C Qi, T Berlijn, JB Yi, KS Yang, Y Dai, YP Feng, I Santoso,

- C Sánchez-Hanke, XY Gao, et al. Room-temperature ferromagnetism of Cu-doped ZnO films probed by soft x-ray magnetic circular dichroism. *Physical Review Letters*, 105(20):207201, 2010.
- [176] Zoila Barandiarán and Luis Seijo. Quantum chemical analysis of the bond lengths in f^n and $f^{n-1}d^1$ states of Ce^{3+} , Pr^{3+} , Pa^{4+} , and U^{4+} defects in chloride hosts. *The Journal of Chemical Physics*, 119(7):3785–3790, 2003.
- [177] Nguyen Hoa Hong, Nathalie Poirot, and Joe Sakai. Evidence for magnetism due to oxygen vacancies in Fe-doped HfO_2 thin films. *Applied physics letters*, 89(4):042503, 2006.